LBNL-39513
UC-413

ERNEST ORLANDO LAWRENCE
BERKELEY NATIONAL LABORATORY

I. Mass Asymmetric Fission Barriers for ^{98}Mo
II. Synthesis and Characterization of Actinide-Specific Chelating Agents

Alan Charles Veeck
Nuclear Science Division

August 1996
Ph.D. Thesis

LBNL-39513

I. Mass Asymmetric Fission Barriers for ^{98}Mo.

II. Synthesis and Characterization of Actinide-Specific Chelating Agents.

Charles Veeck, Jr.

Ph.D. Thesis

Department of Chemistry
University of California
Berkeley, CA 94720

and

Glenn T. Seaborg Institute for Transactinium Science
Lawrence Livermore National Laboratory
Livermore, CA 94551

and

Nuclear Science Division
Lawrence Berkeley National Laboratory
Berkeley, CA 94720

This research was supported by the Glenn T. Seaborg Institute for Transactinium Science, Lawrence Livermore National Laboratory, by the U.S. Department of Energy under Contract No. W-7405-ENG-48, and by the Office of Energy Research of the U.S. Department of Energy at Lawrence Berkeley National Laboratory, under Contract No. DE-AC03-76SF00098.

I. Mass Asymmetric Fission Barriers for ^{98}Mo.
II. Synthesis and Characterization of Actinide-Specific Chelating Agents.

by

Alan Charles Veeck

B.S. (The College of William and Mary in Virginia) 1991

A dissertation submitted in partial satisfaction of the

requirements for the degree of

Doctor of Philosophy

in

Chemistry

in the

GRADUATE DIVISION

of the

UNIVERSITY of CALIFORNIA at BERKELEY

Committee in charge:

Professor Darleane C. Hoffman, Chair
Professor Kenneth N. Raymond
Professor Stanley G. Prussin

1996

I. Mass Asymmetric Fission Barriers for ^{98}Mo
II. Synthesis and Characterization of Actinide-Specific Chelating Agents

by

Alan Charles Veeck

I. Mass Asymmetric Fission Barriers for ^{98}Mo. II. Synthesis and Characterization of Actinide-Specific Chelating Agents.

Alan Charles Veeck

Abstract

I. From the realm of Fundamental Nuclear Chemistry:

Excitation functions have been measured for complex fragment emission from the compound nucleus ^{98}Mo, produced by the reaction of ^{86}Kr with ^{12}C. Mass asymmetric fission barriers have been obtained by fitting the excitation functions with a transition state formalism. The extracted barriers are $\sim$ 5.7 MeV higher, on average, than the calculations of the Rotating Finite Range Model (RFRM). These data clearly show an isospin dependence of the conditional barriers when compared with the extracted barriers from ^{90}Mo and ^{94}Mo.

II. From the realm of Applied Nuclear and Synthetic Chemistry:

Eleven different liquid/liquid extractants were synthesized based upon the chelating moieties 3,2-HOPO and 3,4-HOPO; additionally, two liquid/liquid extractants based upon the 1,2-HOPO chelating moiety were obtained for extraction studies. The extractants were rendered organophilic by the attachment of long alkane side chains of varying length to the chelating moiety. Synthesis of the 3,2-HOPOs was achieved with greater ease, higher yield, and greater purity than synthesis of the 3,4-HOPOs.

A spectrophotometric titration of 3,2-HOPO-propylamide with Th(IV) gave a formation constant of $\log \beta_{140} = 38.3 \pm 0.3$. This formation constant compares favorably with the other measured formation constants for the chelate groups 1,2-HOPO and 3,4-HOPO.

Measurements of the fraction of uncomplexed ligand in the aqueous phase

showed that the majority of the extractants remained in the organic phase, and only three extractant/organic phase pairs showed significant ligand solubility in the aqueous phase.

The Fe(III) extractions indicated three general trends: first, the 1,2-HOPO extractants performed the best, followed closely by the 3,2-HOPOs, with the 3,4-HOPOs extracting very poorly; second, extraction from the higher ionic strength aqueous phase was favored over extraction from the lower ionic strength aqueous phase; third, extraction into the organic phase when 1-octanol was the solvent was much greater and proceeded more rapidly than when methyl isobutyl ketone (MIBK) was the solvent. For all conditions, however, the 1,2-HOPO extractants performed very well, extracting $> 99\%$ of the Fe(III).

The Pu(IV) extractions, quite surprisingly, yielded results that were very different from the Fe(III) extractions. The first trend remained the same: the 1,2-HOPOs were the best extractants, followed closely by the 3,2-HOPOs, followed by the 3,4-HOPOs; but in these Pu(IV) extractions the 3,4-HOPOs performed much better than in the Fe(III) extractions. There was a reversal in the organic solvent ordering, with MIBK, in general, performing better as the organic phase than 1-octanol. The difference in extraction between the high ionic strength aqueous phase and the low ionic strength aqueous phase was less, but the high ionic strength phase still showed higher extraction. As with the Fe(III) extractions, the 1,2-HOPOs performed extremely well under all conditions tested, extracting $> 99\%$ of the Pu(IV). The kinetics for the Pu(IV) extractions were 10–12 minutes faster than for the Fe(III) extractions. The percent extraction showed no significant dependence on the length of the organophilic side chain.

Since the 1,2-HOPOs performed so well in both metal extractions, 1,2-HOPO-octylamide in MIBK was chosen to test some additional extraction properties. This extractant was able to remove 95–100% of the Pu(IV) in competition studies with 100:1 Fe(III) (D.F. = 325), 1000:1 Fe(III) (D.F. = 60), and 3:1 EDTA (D.F. = 490). Concentration studies with this extractant support the hypothesis that a species other than ML_4 can be extracted into the organic phase. 1,2-HOPO-octylamide forms such a strong plutonium complex that the Pu(IV) could not be stripped away from it

by an aqueous phase reducing agent; only $\sim$ 40 % could be stripped by concentrated (15.8 M) nitric acid.

Dedication

To the memory of Alan Campbell-Ling,
who brought my interest in nuclear chemistry to life

and

To my beautiful wife Michelle,
and to Emily.

Acknowledgments

The work presented in a doctoral thesis is the collaborative output of many minds. Because this thesis consists of two very different projects, the number of people involved in bringing it to fruition is very large. Foremost amongst these people are those who are most important to me in this world: my mother, Lucinda, my father, Al, my brother, Jason, my wonderful first wife, Michelle, and our beautiful itty-bitty, Emily.

My decision to enter the discipline of chemistry as an undergraduate was cemented by a number of excellent mentors and professors: David Thompson, William Starnes, Brenda Wojciechowski, Gary Hollis, and Alan Campbell-Ling.

During my early graduate school years, spent in building 71B with the Moretto group, I was taught the basic skills of nuclear physics by a very talented and fun bunch of people: Nicola Colonna, Karl Hanold, Dimitri Delis, Kin Tso, Kexing Jing, Wojtek Skulski, Bruce Libby, Qu Sui, Larry Phair, Dick McDonald, Bryan Bandong, Gordon Wozniak, and Luciano Moretto. As my first advisor, Luciano taught me, by his example, how to be a cautious, discerning, and rational scientist. When I left his group, he helped me understand what my personal strengths are, and how to best use those attributes for future success.

I joined the Hoffman and Raymond groups in late 1993, and I am very thankful for how easily and kindly both groups assimilated me into their cultures. The members of the Hoffman group, both at Lawrence Berkeley National Laboratory and Lawrence Livermore National Laboratory, continued my education as a nuclear and radiochemist: Nancy Stoyer, Mary Neu, Bobby Kadkhodayan, Vadim Romanovski, Patrick Allen, Eric Hudson, Linda Marquez, Dave Wruck, Pi-Hong Zhou, Reggie Gaylord, Eric Sylwester, Mike Lane, Chris Kacher, Dawn Keeney, Melissa Hendricks, Dan Strellis, Phil Wilk, Laurance Beauvais, Eric Osterrieder, Greg Klunder, Diana Lee, Ken Gregorich, and Darleane Hoffman. The members of the Raymond group taught me all I know about synthetic inorganic chemistry and how to run the NMR: Donald Whisenhunt, Xu Jide, David White, Ryan Powers, Klaus Langemann, Jason

Telford, Sonja Franklin, Barb Bryan, Chris Sunderland, Zhiguo Hou, Bill Fuller, Jim McCormick, Rolf Moors, Bert Kersting, Thomas Beissel, Michel Myers, Carmen Barnes, Seth Cohen, Shannon Halkyard, Dana Caulder, Sharad Hajela, Inger Coble, and Ken Raymond. Thank you, Darleane and Ken, for allowing me to work on such a fun and exciting project.

The Bay Area was a wonderful place to live for five years while obtaining my degree, and Michelle and I have made many lasting friendships with some of this earth's nicest people: Bill and Doralece Dullaghan, Rick Chamberlain, Maria Rzeznik, Lee Loughnane and Cindy Fay, Scott and Sarah Auerbach (and Madeline!), Donald and Mindy Whisenhunt (and Alexandra!), Meg Thomas, Harry Beal, Jeff Gammon, George Lucier, Leon Newton, Stan Prussin, Wendy and Peter Andersen, Maureen Tortorelli, Marc Schrier, and The Black Mask.

Contents

List of Tables

List of Figures

Part I

Mass Asymmetric Fission Barriers for ^{98}Mo

Chapter 1

Introduction

> "AMONG the preceding experiments, some were prepared on Wednesday the 26 and Thursday the 27 of February, and, as on those days the sun appeared only intermittently, I held back the experiments that had been prepared, and returned the plate-holders to darkness in a drawer, leaving the lamellas of the uranium salt in place. As the sun still did not appear during the following days, I developed the photographic plates on the first of March, expecting to find very weak images. To the contrary, the silhouettes appeared with great intensity."
>
> Henri Becquerel, 1896 [1]

In 1896, exactly one-hundred years ago, the phenomenon of radioactivity was discovered by Henri Becquerel in Paris. Becquerel, conducting experiments on x-ray emissions from uranium ores, noticed that when potassium uranyl sulfate was placed next to a photographic plate in a dark enclosure, the ore caused a darkening of the photographic plate. This was the first observation of alpha radioactivity. In 1909, Ernest Rutherford, the First Baron Rutherford of Nelson, was the first to recognize alpha radioactivity as the emission of a light charged particle, $^4He^{2+}$. Rutherford and his coworkers, and a growing legion of scientists around the world, labored to understand the nature of alpha particle emission. This type of decay was classified as light particle emission; when the light particle is a neutron or proton, its emission is termed *evaporation*, because of its similarity to the evaporation of a molecule from a liquid.

Then, in Germany in 1938, Otto Hahn and Fritz Strassmann were the first to recognize nuclear fission as the splitting of a very heavy nucleus into two smaller nuclear fragments. Lise Meitner and Otto Frisch theorized that the heavy nucleus could exist in a lower energy configuration by splitting into two roughly equal halves, after traversing a potential energy barrier that was determined by the shape and size of the nucleus as it deformed into two halves [2]. The discovery of nuclear fission ranks as one of the greatest scientific discoveries of this century, and it led to an intense study of nuclear processes, along with the development of nuclear power generators and the nuclear bomb. As a nuclear decay process, however, fission was viewed as being completely distinct from light particle evaporation. The former results in the creation of two nuclear fragments of roughly equal size with the emission of a large amount of energy ($\sim$ 200 MeV), while the latter results in the creation of a very small nuclear fragment, an alpha particle, and a large residual nucleus, with the liberation of only a relatively small amount of energy ($\sim$ 5 MeV).

In the 1960s and 1970s, scientists began to notice a type of decay that bridged the gap between light particle evaporation and fission. This type of decay was dubbed *complex fragment emission*, because it involved the low cross section emission of a nuclear fragment with a mass somewhere between that of a light charged particle and a fission fragment [2]. A team at Lawrence Berkeley Laboratory in 1971 was the first to systematically study complex fragment emission (Figure 1.1), using the reaction of 5.5 GeV protons on a natural uranium target [3]. These "complex" nuclear fragments could not be explained by the models which described light particle evaporation or nuclear fission.

At the University of California, Berkeley, in 1975, Luciano Moretto published an article that joined light particle evaporation and fission into a single, unified theoretical framework that was able to account for complex fragment emission [4]. The theoretical framework recognizes that light particle evaporation and fission are the main modes of decay available to a compound nucleus; they can be considered as the two limiting forms of a common process whose underlying connection is provided by the mass asymmetry coordinate. The mass asymmetry coordinate describes the degree of asymmetry that is achieved when a nuclear system divides into two parts,

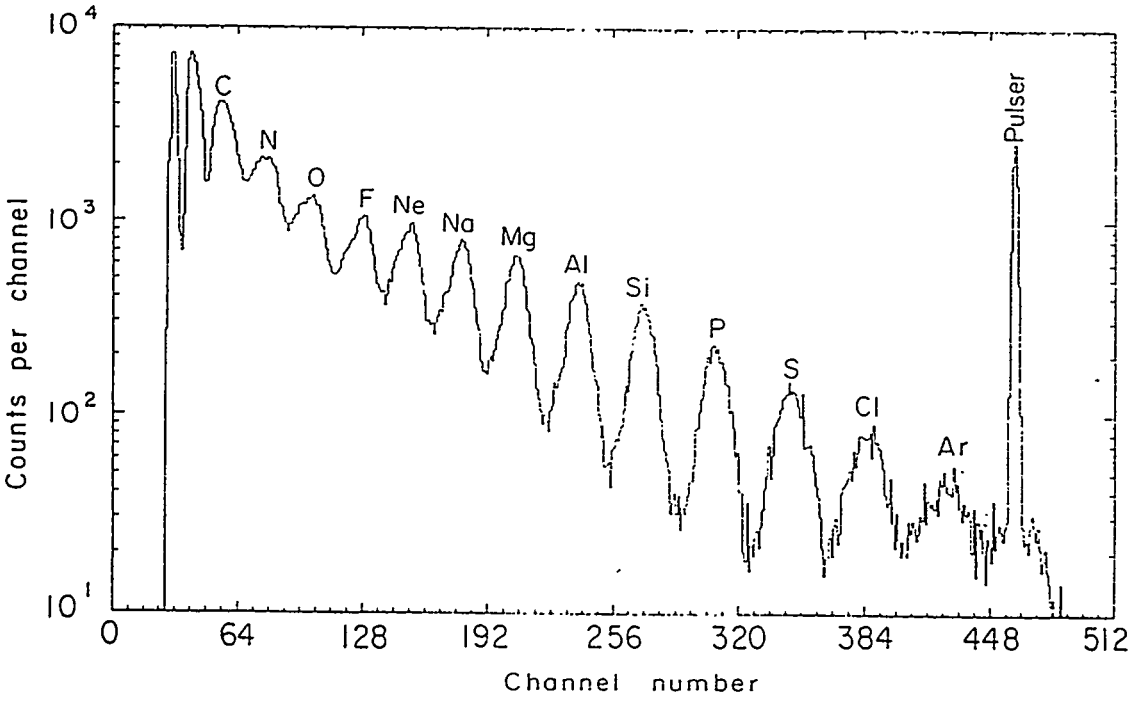

Figure 1.1: Complex fragment emission from the reaction of 5.5 GeV protons on a natural uranium target; notice the decreasing yield with increasing atomic number.

and is defined as

$$Z_{asymm} = Z_{frag}/Z_{CN}, \tag{1.1}$$

where Z_{frag} is the atomic number of one of the fragments, and Z_{CN} is the atomic number of the decaying nucleus (compound nucleus). Light particle evaporation involves large mass asymmetries (i.e., a small-mass alpha particle plus a relatively heavy residual nucleus), while nuclear fission involves division into two relatively equal sized fragments, at small mass asymmetry. It is decay at intermediate mass asymmetries that leads to the emission of complex fragments.

The probability for the decay of a nuclear system at a particular mass asymmetry is governed by the potential energy barrier associated with that mass asymmetry. The height of the energy barrier is determined by a number of parameters, but predominantly by the size and shape of the decaying nucleus at its saddle configuration (the saddle configuration is the nuclear shape when it crosses the saddle point in the nuclear potential energy surface) (Figure 1.2). The conditional saddles for all mass asymmetries are the maxima of all the individual barriers heights, and they form a "ridge line" on the potential energy surface of the decaying nucleus (this is shown in three dimensions in Figure 1.3). A compound nucleus, confronted with this potential energy ridge, can choose any asymmetry through which to decay. A continuum of trajectories can be envisioned, originating in the compound nucleus region, which climb the slope of the potential barrier and then descend toward the product region once over the ridge. Quite obviously, the statistically favored trajectories are those which pass over the lowest points in the ridge line. For all but the heaviest nuclei, the nuclear shape at the saddle is very indented, and once a conditional saddle is negotiated, the mass asymmetry should remain constant until scission. Thus, the mass distributions which result from a binary decay are a direct fingerprint of the probabilities (and hence the barrier heights) of overcoming the ridge at the various mass asymmetries. The relationship between the yield (Y) and the barrier heights (B_Z) for a given complex fragment is given approximately by

$$Y \propto \exp(-B_Z/T), \tag{1.2}$$

where T is the temperature of the decaying nucleus. Put simply, *the dependence of*

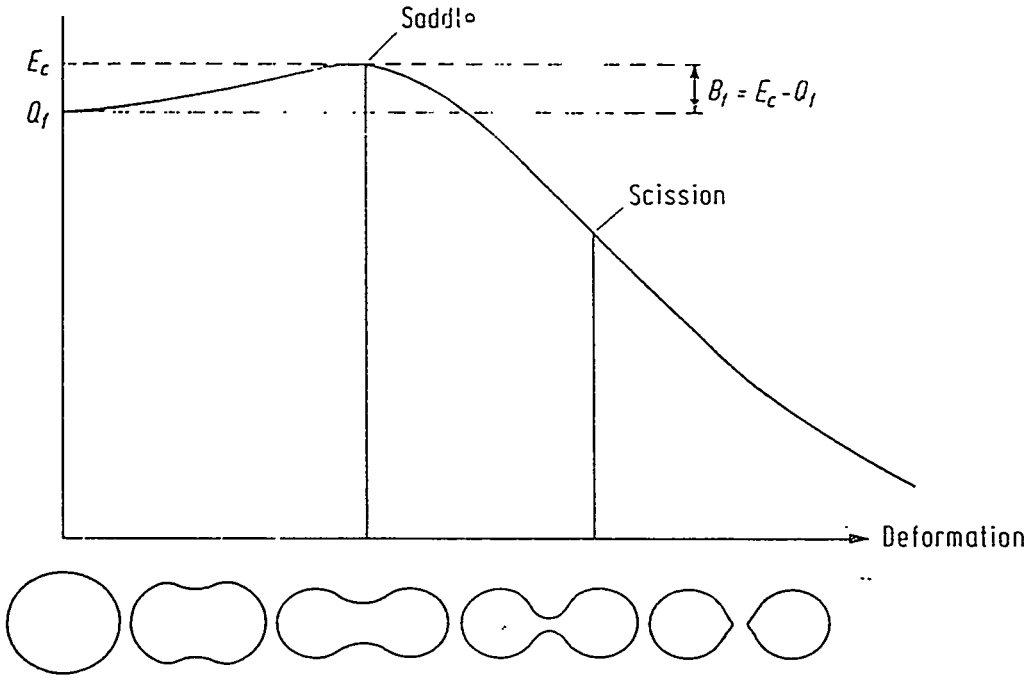

Figure 1.2: A fission barrier diagram in two dimensions, with the x-axis representing deformation along the fission coordinate, and the y-axis representing relative energy. The saddle point is the energetic maximum, with scission occurring at a much lower energy.

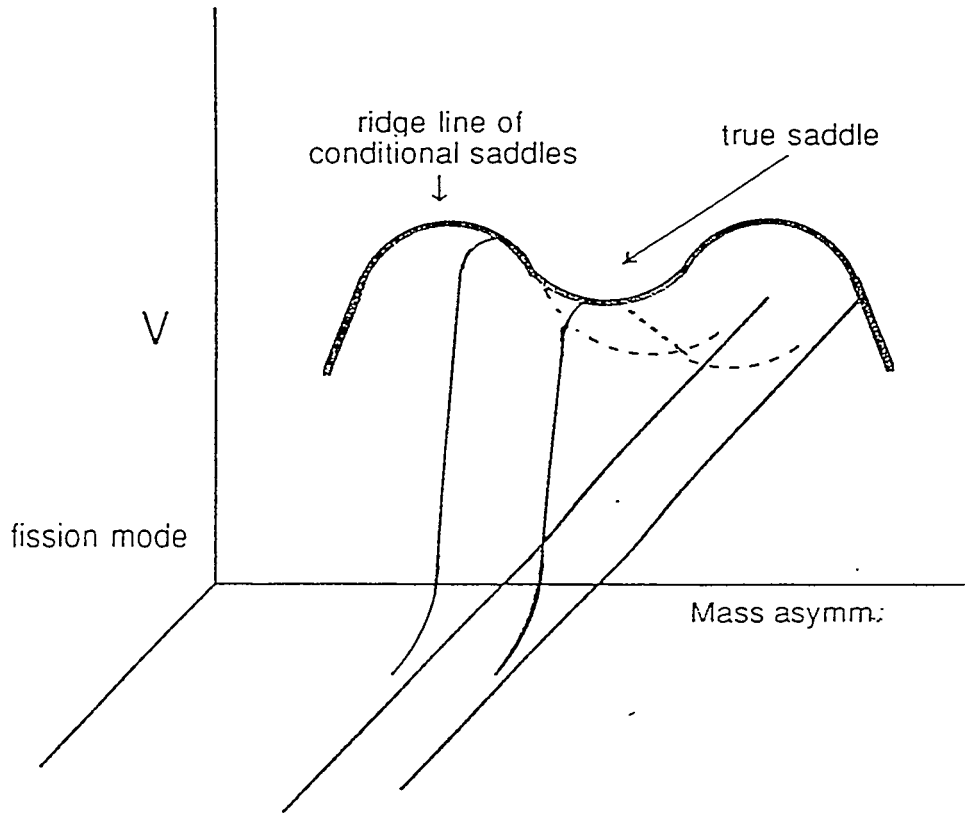

Figure 1.3: A fission barrier diagram, now including a third dimension, the mass asymmetry axis; the maxima of all the individual barriers form a "ridge line".

the barrier height on the asymmetry of the binary division is what determines the charge and mass distributions of the emitted complex fragments.

This decay scenario has a corollary in chemical reactions, in which the Arrhenius equation describes the rate of reaction:

> *rate of reaction = (rate of collision of two molecules) × (probability that collision carries enough energy to ascend potential barrier).*

To translate the Arrhenius equation into nuclear terms:

> *rate of fission = (rate of deforming nuclear oscillations) × (probability that deformed nucleus has enough energy to ascend fission barrier).*

The shape of the ridge line depends on the magnitude of the fissility parameter, x [5]:

$$x = E_C/2E_s, \tag{1.3}$$

where E_C and E_s represent the Coulomb energy term and the surface energy term, respectively, from the liquid drop model equation. Depending upon whether the fissility parameter lies above or below the Businaro-Gallone [6, 7] point (in the liquid drop model of the nucleus, the fissility parameter at the Businaro-Gallone point has a value $x_{BG} = 0.396$, for zero angular momentum [8]), the ridge line will have a shape similar to either an "M" or a "∩" (with the corresponding fragment yield having either a "W" or a "U"-type shape, respectively). This is shown graphically in Figure 1.4, where the height of the potential barrier and the yield are plotted on two different y-axes, versus the mass asymmetry parameter (Z_{asymm}). For heavy nuclei (case (a)), well above the Businaro-Gallone point, the ridge line presents a deep minimum at symmetry ($Z_{asymm} = 0.5$). This means there is a low barrier to fission for symmetric division, giving rise to the well-known fission peak in the mass distribution. Notice, too, that the ridge line also reaches a minimum at the largest mass asymmetries, producing the other well-known decay mode, light particle evaporation. However, for light nuclei (case (b)), which lie below the Businaro-Gallone point (like ^{98}Mo, the nucleus of interest to this study, with $x \approx 0.359$), there is no longer a minimum in the ridge line for symmetric division; the potential energy increases monotonically along

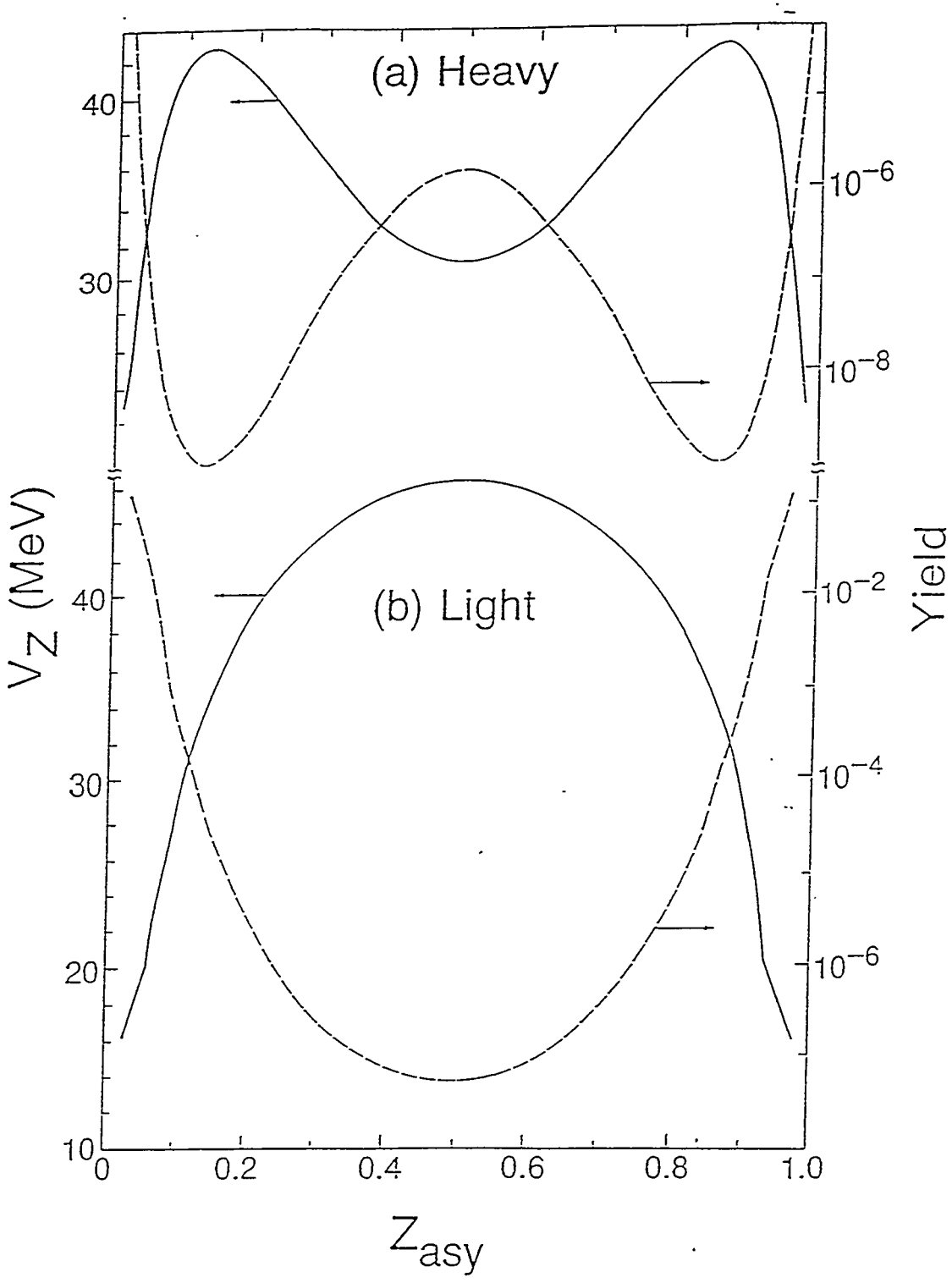

Figure 1.4: Theoretical shape of the ridge lines (solid) and corresponding yields (dashed) for all mass asymmetries, for heavy (a) and light (b) fissioning systems.

the ridge line as the division approaches symmetry, meaning that fission can no longer compete with light particle evaporation as an energetically viable decay process.

The determination of the precise form of the ridge line, which is the dependence of the fission barriers upon the mass asymmetry (Figure 1.4), requires the measurement of the entire mass distribution at various bombarding energies. By measuring the mass distributions at various energies, experimental excitation functions can be constructed. By fitting the excitation functions with model equations which containing the barrier height as a variable, the experimental barrier heights (which compose the ridge line) can be determined. In light systems, these measurements are difficult because of the expected low yield for symmetric decay of the compound nucleus at the lowest excitation energies. Furthermore, verification that the reaction occurs through the compound nucleus mechanism, and that the desired and expected compound nucleus is being produced, is required.

This study is important because it increases the experimental information available to theorists who rely on such information for the formation and refinement of nuclear models. Previous experiments [9–11] involving the determination of symmetric fission barriers have played an essential role in the establishment of key features of nuclear models. For example, the ambiguity between the surface (E_s) and Coulomb energy (E_C) in the liquid drop model has been resolved by simultaneously fitting both the ground state and saddle point masses in heavy nuclei [12], where there is a large and obvious distinction between these two terms. In another example, the contribution of shell effects to the ground state and saddle nuclear configurations was elucidated by investigation of the fission barriers for nuclei near closed shells (large shell effects) [11] and nuclei in the actinide region (small shell effects) [13].

The rotating liquid drop model (RLDM) [14] for nuclear fission is one of the simplest theoretical models used to predict fission barriers. As its name suggests, it is a model which likens a fissioning nucleus to a rotating drop of liquid, and it uses existing parameters from the well-known liquid drop model, and modifies them for a rotating, fissioning system. In a number of studies [15–19] that compared experimental fission excitation functions with predictions of the RLDM, it was found that the predicted fission barrier heights were too large. A reduction in the predicted barrier

heights was provided with a newer, more inclusive model, the rotating finite range model (RFRM) [20, 21]. The RFRM depicts a fissioning nucleus more realistically than the RLDM, by including:

1. Energy contributions from the proximity of the nuclear surfaces on either side of the "neck" of a fissioning nucleus at its saddle point configuration (so-called "finite-range" effects; see Figure 1.5).

2. A description of the nuclear surface as diffuse ("fuzzy"), rather than sharply defined (Figure 1.5).

3. A more realistic shape parameterization.

The barriers predicted by the RFRM are lower than those predicted by the RLDM because the added effects in the RFRM stabilize the nuclear saddle point configuration. In light fissioning nuclei, where the fissility parameter, x, is small, the nuclear indentation at the saddle configuration is very pronounced, and the difference between the predictions of the RFRM and the RLDM are large. However, as the nuclear mass increases, x increases, and the less pronounced indentation of the heavier fissioning nuclei decreases the difference between the predictions of the two models (Figure 1.6). The same difference between the two models is observed as the angular momentum is increased (Figure 1.7); the surface diffuseness and finite-range effects contribute less to the RFRM as the nuclear configuration is separated in space across a longer "neck".

The RFRM has been quite successful in reproducing the fission barriers determined in heavy-ion reactions ($A > 100$) [22, 23]. Additionally, in two studies conducted by this research group, the RFRM model was able to reproduce the measured barriers for a very light system, ^{75}Br [24, 25], and a slightly heavier one, $^{110-112}$In [26]. When inspected more closely, however, the modeling has failed to take into account the shell effect in the ground state nuclear masses. When the shell effect corrections are made to the conditional barrier heights (Figure 1.8), the RFRM tends to underestimate the fission barriers. While the RFRM predictions of the barriers for $^{110-112}$In are about 1.5 MeV lower than the experimental data, the discrepancy in

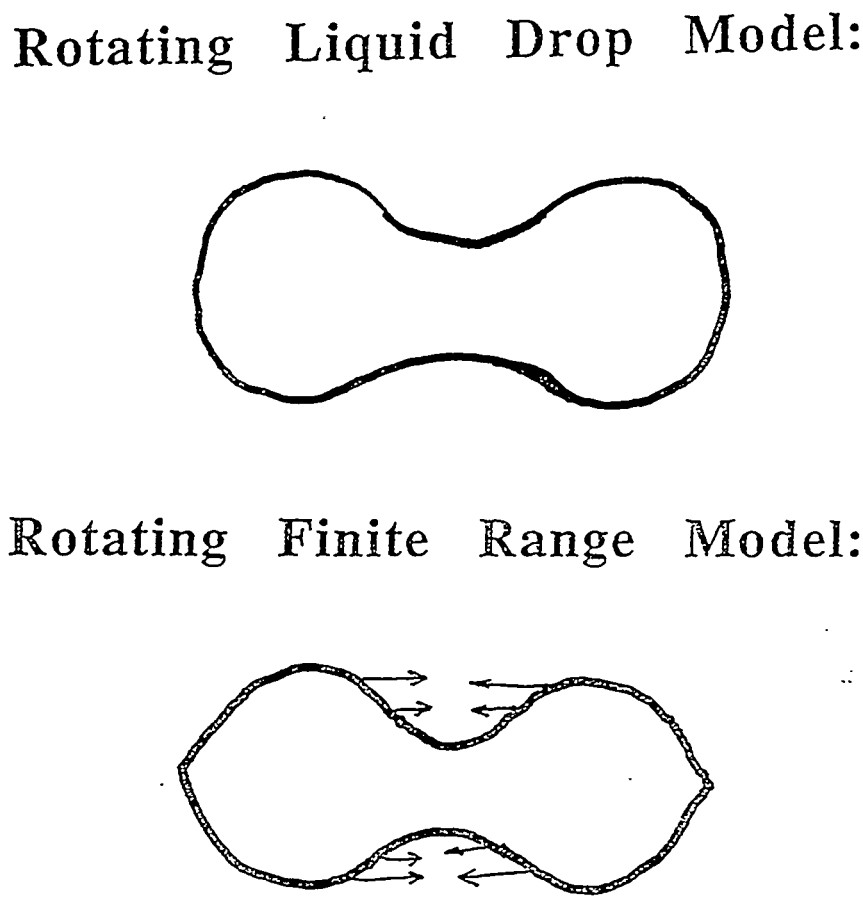

Figure 1.5: Cartoon to illustrate some differences between the Rotating Liquid Drop Model (RLDM) and the Rotating Finite Range Model (RFRM).

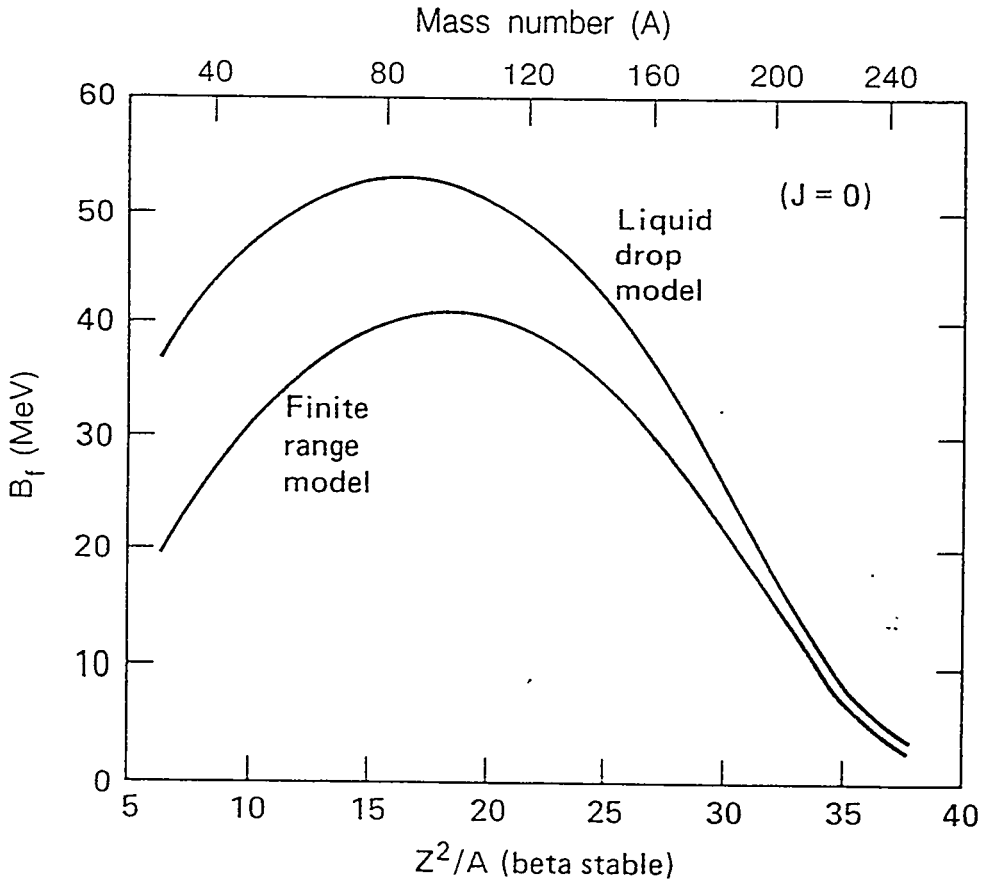

Figure 1.6: Fission barriers for symmetric division of non-rotating nuclei as a function of Z^2/A, along the line of beta stability.

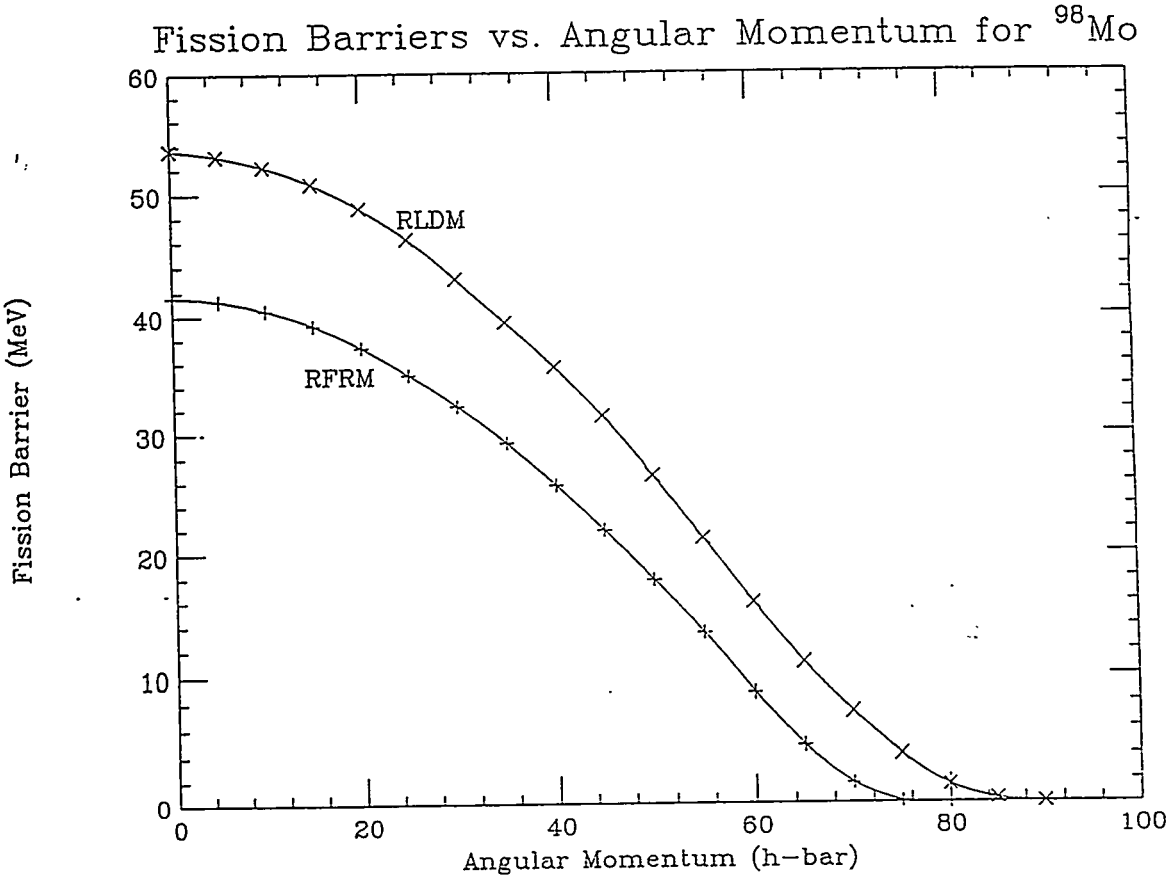

Figure 1.7: Liquid drop (RLDM) and rotating finite range model (RFRM) calculations of the fission barrier heights for symmetric division of ^{98}Mo, and their dependence on angular momentum.

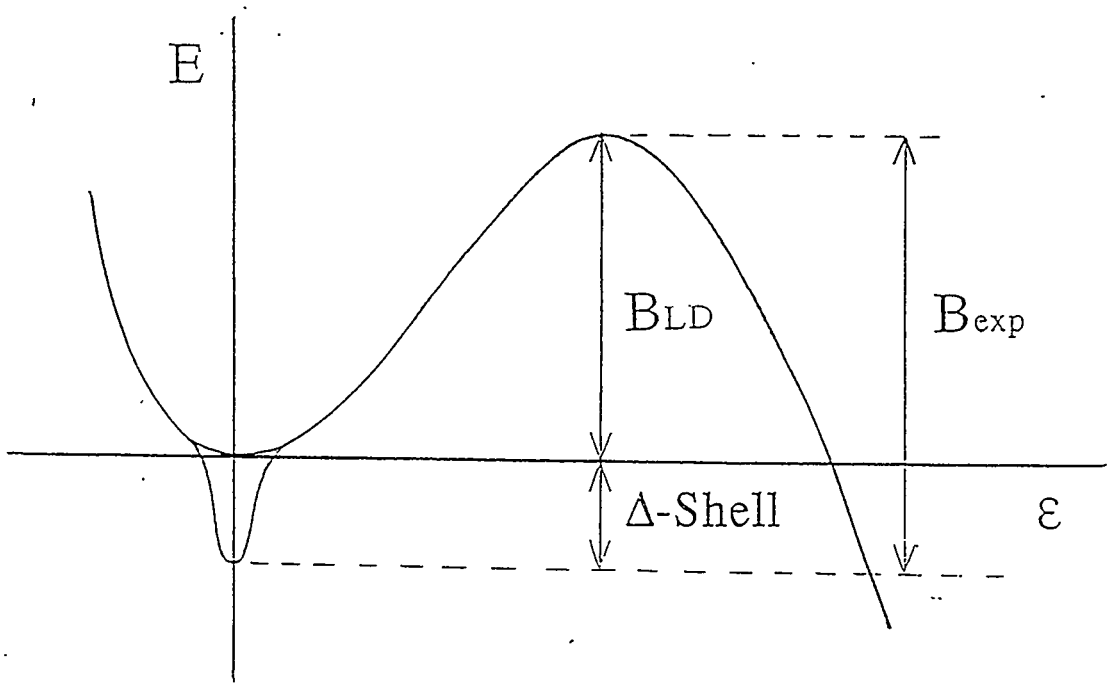

Figure 1.8: Fission barrier heights with shell corrections included.

the case of ^{75}Br becomes as large as 4.5 MeV, on average. It must be stressed that without taking the shell effects into account, direct comparison between experimental data and the macroscopic model calculations may result in false agreement or disagreement (see, for example, [27, 28]). Boger and Alexander [29] report conditional barriers for the compound nucleus ^{149}Tb, produced by the reaction:

$$^{86}\mathrm{Kr} + {}^{63}\mathrm{Cu} \longrightarrow {}^{149}\mathrm{Tb}$$

Their experimental barriers lie between the calculations of the RFRM and the RLDM and show a sizable disagreement with both. These results may suggest the need for refinement of the RFRM constants in order to explain the data in the medium mass region.

Additionally, in both the RFRM and the RLDM, the surface energy (E_s) calculation contains a neutron-to-proton (n/p) asymmetry term. The constant of this asymmetry term is not well determined, due to the limited range of asymmetries previously explored in measured fission barriers. Measuring the fission barriers of isotopes with very different neutron-to-proton ratios should allow a significant improvement in the value of the surface asymmetry constant.

Finally, in a recently developed Thomas-Fermi model of nuclear properties [30], extra binding energy has been assigned to pairs of nucleons which have wave functions with congruent nodal structures, and which consequently have an overlap that is greater than average. The characteristic features of this "congruence energy" are:

1. A dependence on the absolute magnitude of the relative neutron excess, $(N - Z)/A$.
2. A doubling of the extra binding energy when a nucleus is divided into two non-communicating pieces (such a process is approximated by the fission of light nuclei that proceed through a strongly necked-in fission saddle point shape).

A detailed comparison of the experimentally measured fission barriers in the $A = 90$

region with the Thomas-Fermi model calculations should provide evidence for the presence, or lack of, the additional binding energy.

The major objective of the present work is to provide a complete set of experimental mass asymmetric barriers for a single isotope, against which macroscopic models, and especially their surface asymmetry term, can be compared. This study presents a nearly complete experimental ridge line of the conditional barriers for the compound nucleus ^{98}Mo, with $n/p = 1.33$. These barriers, in concert with the barriers for ^{90,94}Mo ($n/p = 1.14$ and 1.24, respectively) which were measured in another experiment by this group [31], should provide a strong measurement of the n/p dependence of the conditional barriers, and allow an improvement in the determination of the surface asymmetry constant in the nuclear mass formula. This experiment measures the complex fragments emitted from the reverse kinematics reaction

$$^{86}\mathrm{Kr} + {}^{12}\mathrm{C} \longrightarrow {}^{98}\mathrm{Mo},$$

and the barriers are obtained by fitting the experimental excitation functions with a transition state method following the Bohr-Wheeler formalism [32, 5].

Chapter 2

Experiment

The experiment was conducted at Lawrence Berkeley Laboratory's 88-Inch Cyclotron ($K = 140$), with the assistance of the following Moretto research group members: Kexing Jing, Nicola Colonna, Karl Hanold, Kin Tso, Wojtek Skulski, Dimitri Delis, Qu Sui, Gordon Wozniak, and Luciano Moretto. Krypton gas, isotopically enriched with ^{86}Kr, was introduced into the Advanced Electron-Cyclotron-Resonance (AECR) source [33], where krypton atoms were ionized to high charge states. The ionized atoms were extracted from the AECR, injected into the cyclotron, and accelerated to one of seven desired energies, from 7.71 to 12.94 MeV/$\dot{A}$. Rapid beam energy changes were accomplished by accelerating different charge states at the same cyclotron mainfield setting [34].

A 1.0 mg/cm^2 thick ^{12}C target was bombarded with ^{86}Kr projectiles. The target thickness was chosen to give a large enough cross section for the compound nucleus of interest, yet thin enough to ensure that the energy loss of the fragments produced in the target was small. Two detector units, named *Faith* and *Hope* (constructed by Dr Robert *Charity*), were positioned on either side of the path of the beam inside a large-volume 60-inch evacuated scattering chamber. Each detector unit contained four separate telescopes, and each telescope was composed of a ΔE gas detector and an E solid-state silicon detector. The gas detector measured the energy loss (ΔE) of each fragment as it traversed 7 cm of isobutane gas at 30 torr pressure; an 80 μg/cm^2 thick Mylar window maintained the gas pressure inside the

detector, yet caused minimal fragment energy loss. Each gas detector measured the horizontal position of each fragment by means of a Frish-type grid and the measured drift time of electrons to the wall of the detector. The solid-state silicon semiconductor detector, 45 mm $\times$ 45 mm, measured the total energy (E) of each fragment as it was deposited into the 5 mm thick detector. These detectors measured the vertical position of each fragment using a coating of strips of low-resistivity material alternated with strips of high-resistivity material; the resistive division of the energy signal gave the position [35]. The active area of each telescope subtended 5.0°. Using these telescopes, the total energy, atomic number, in-plane angle, and out-of-plane angle could be determined for each fragment that traveled through the gas detector and was stopped in the silicon detector.

Each detector unit covered 24.8° in-plane and 5° out-of-plane, with a separation of 1.6° between individual telescopes. Measurements were initially performed with the detectors positioned to cover the angular range from 4.0° to 28.8°. The detectors were then moved by 3° to allow fragments to be detected at angles which were initially located in the dead areas between adjacent detectors. In this way, complete and continuous angular distributions were obtained with a relatively small amount of beam time and used for constructing invariant cross section diagrams.

The atomic number of each detected fragment was determined from the measured ΔE and E values. The Stopping-Power Formula [2] can be reduced to

$$Z \propto (E)(\Delta E)^{1/3}, \tag{2.1}$$

meaning that knowledge of the total energy and the energy loss of a fragment in a medium can yield the atomic number of that fragment. An example of an E versus ΔE spectrum, illustrating the range of fragments observed and the Z resolution achieved, is shown in Figure 2.1.

The energy calibration of the E and ΔE detectors was performed using the method illustrated in reference [36]. Calibration points were obtained with beams of ^{14}N, ^{28}Si, ^{35}Cl, and ^{63}Cu at 10.9 MeV/A, and ^{13}C, ^{26}Mg, ^{39}K, ^{65}Cu, and ^{78}Kr at 12.6 MeV/A, projected directly into both the E and ΔE detectors. The energy losses of calibration beams in the gas detector were measured by observing the difference

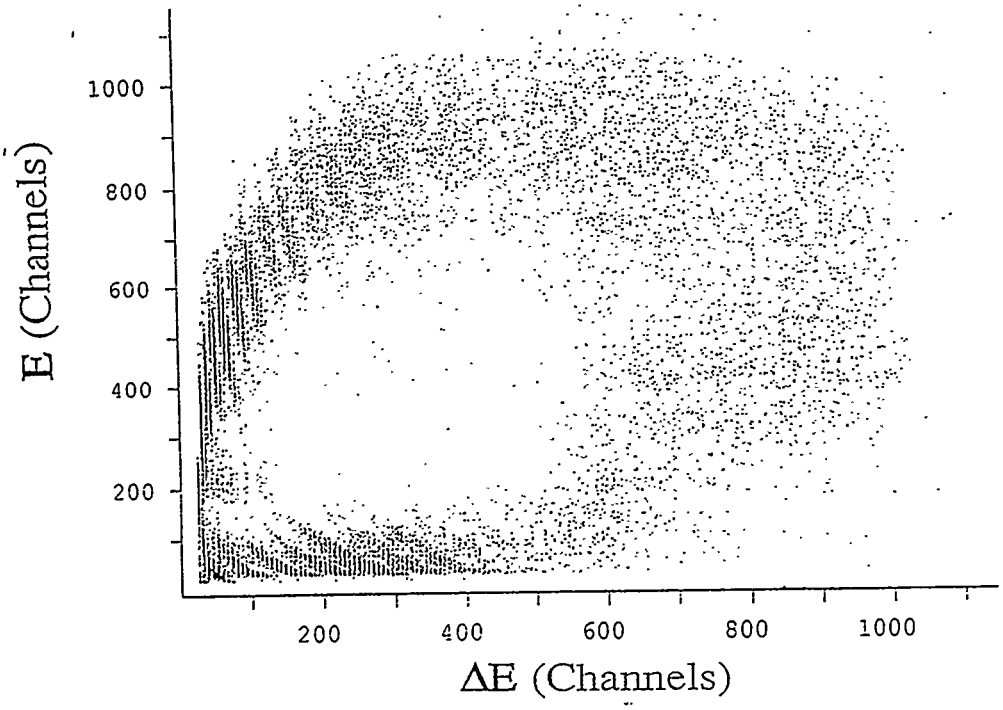

Figure 2.1: Plot of E versus ΔE for the reaction of ^{86}Kr on ^{12}C at 11.98 MeV/A.

between the E signal with and without gas in the gas detector. The intensity of these beams was attenuated to limit the counting rate to < 500 counts/sec. Corrections were made for energy loss in the Mylar entrance window of the gas detector, and in the gold foil absorber used to suppress electrons and x-rays. The pulse-height defect, which is a physical phenomenon resulting from the creation of an incredibly dense cone of ionization along the path of a heavy fragment through a solid, causing ion-pair recombination and hence a smaller pulse height, was corrected using the systematics of Moulton *et al.* [37]. The energy calibrations are accurate to $\pm 1\%$.

The out-of-plane position was calibrated with a mask, consisting of a matrix of 2.00 mm holes separated by 4.73 mm, that could be lowered into position remotely. The in-plane position, by virtue of its design previously mentioned, was self-calibrated. The typical position resolution obtained was $\pm$ 0.2°. To obtain absolute cross sections, the beam charge was collected in a Faraday cup and integrated with a charge integration module. The charge state of ^{86}Kr ions entering the Faraday cup was determined by the method of McMahan [38], or by means of Rutherford scattering from a 40 mg/cm^2 thick ^{197}Au foil.

The carbon foil used in these experiments needs to be virtually free of any low-Z impurities, because the yield of complex fragments from heavier impurities can be very large. In addition, the yield from the carbon target falls off much more rapidly with decreasing beam energy than does the yield from low-Z impurities. A calculation of the relative yields from carbon and several heavier impurities has been performed with the statistical code GEMINI [39], and is displayed in Figure 2.2. At higher energies, the yield for the reaction with sodium impurity is two orders of magnitude greater than that for the carbon; at the lowest energy, this yield differential is increased to approximately *four-and-a-half orders of magnitude.* Yields from nitrogen and oxygen impurities, while not as large as those from sodium, could also be significant sources of background reactions as well. It is for these reasons that a very pure carbon target is required for these types of experiments. The choice of the carbon target will be expanded upon in the discussion of the coincidence data, Section 3.1.

All data were recorded on magnetic tape and analyzed off-line.

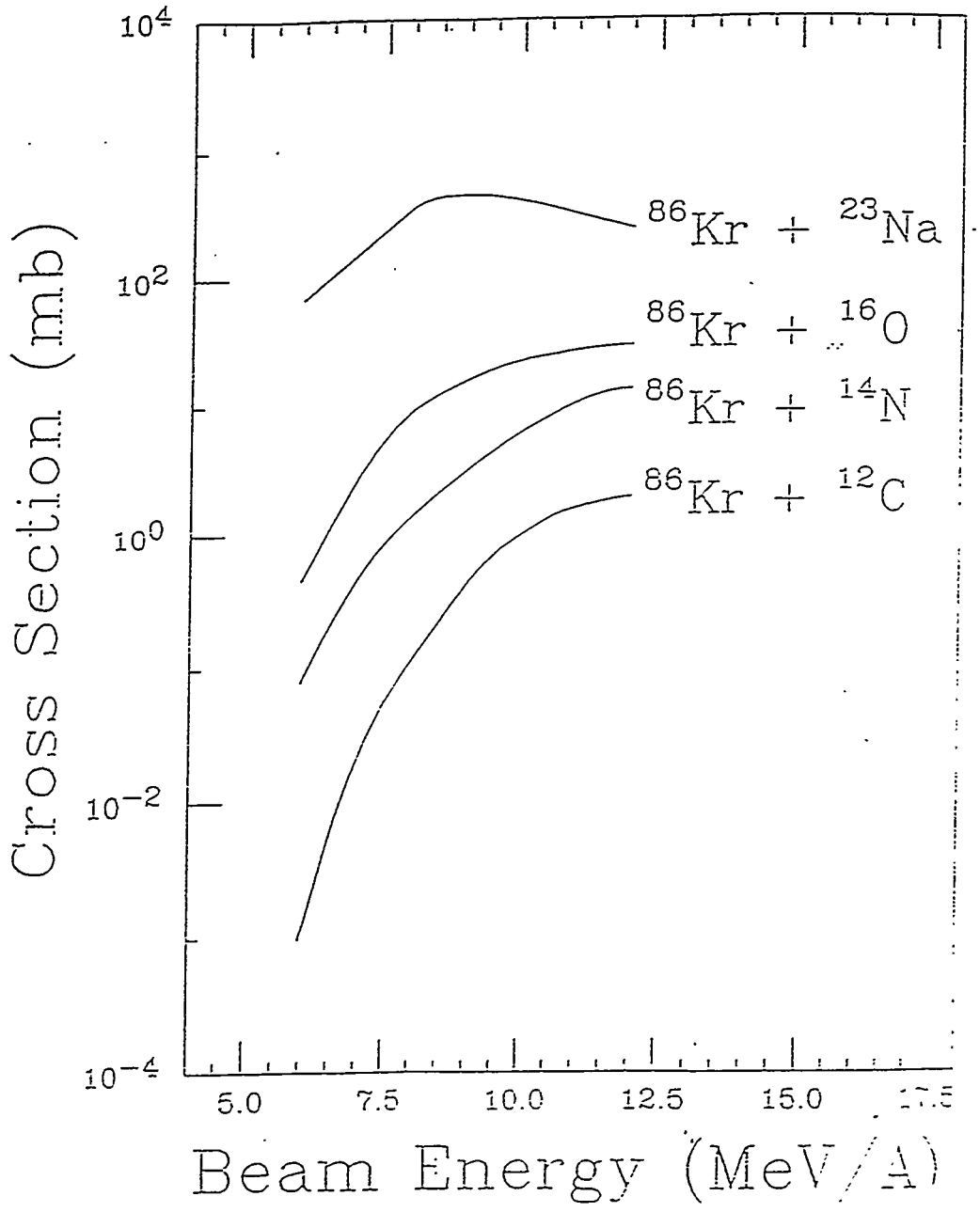

Figure 2.2: Yield of complex fragments ($14 < Z < 26$) from the reaction of ^{86}Kr with various possible target impurities, versus bombarding energy.

Chapter 3

Analysis and Discussion

In the majority of nuclear reactions studied in the laboratory, the lighter of the reacting nuclei is chosen to be the projectile, and the heavier of the pair is chosen as the target. However, for the reaction studied here, the kinematics have been reversed, meaning that the heavier nucleus is used as the projectile (^{86}Kr) and the lighter nucleus is employed as the target (^{12}C). The reverse kinematics technique has two advantages (see Figure 3.1):

1. Because the heavier nucleus is being accelerated, the resultant compound nucleus has a greater velocity relative to the normal kinematic arrangement; the increased velocity ensures that even the smallest fragments from the binary decay will have enough translational energy to exceed detector thresholds.

2. The reaction products are forward-focused by the large velocity of the compound nucleus, meaning that a greater angular range will be detected when compared with the normal kinematic arrangement.

In Figure 3.1, the velocity of the source of the complex fragments is represented by the long vector V_s. In the present reaction, V_s represents the velocity of the compound nucleus, ^{98}Mo, while V_e represents the velocity of the complex fragment emitted from the binary decay of the compound nucleus, in the center-of-mass frame. V_e has a well-defined value, determined mainly by the Coulomb repulsion between the two decay products. The loci of the emission velocities for a particular complex fragment

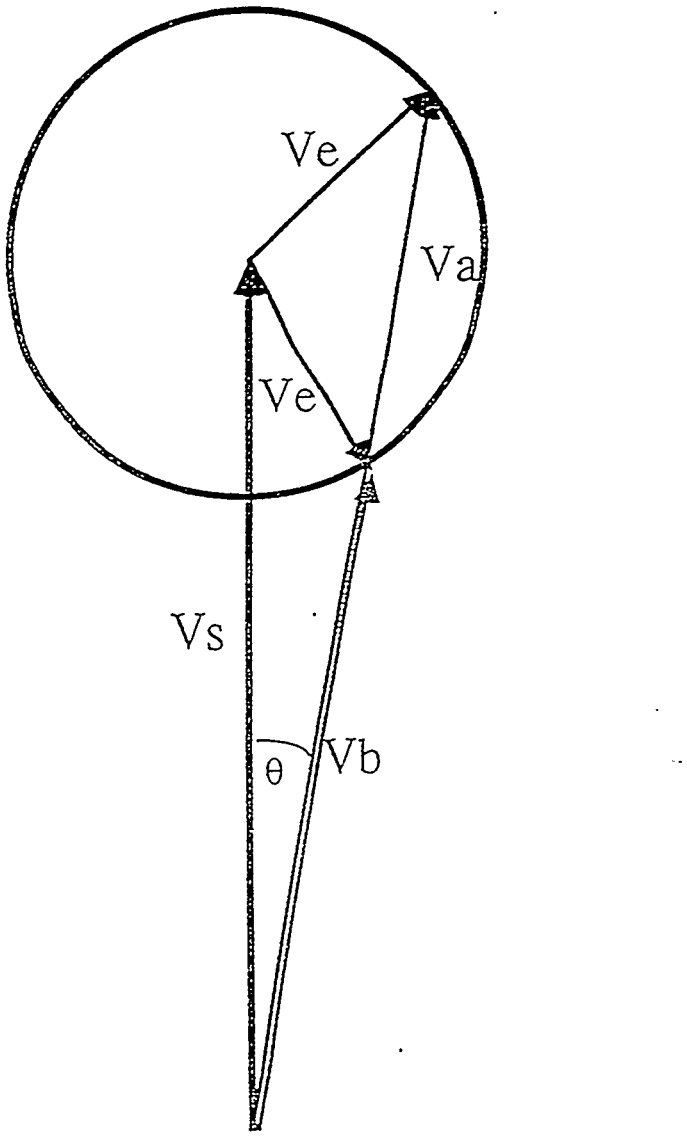

Figure 3.1: Schematic representation of the binary decay of a compound nucleus, showing velocity vectors for fragment emission.

are represented by the circle in the diagram, because the fragment vector will always be the same length, but can point in any direction in the center-of-mass frame. V_a and V_b are the velocities of the fragments observed at the laboratory angle Θ. The high (low) velocity vector V_a (V_b) corresponds to forward (backward) emission of the fragment in the center-of-mass frame. In Figure 2.1, the E versus ΔE plot that gives atomic number resolution, the two ridges associated with the forward and backward emission from the binary decay of the fast-moving compound nucleus can clearly be seen.

It is necessary to verify that the reaction under study, at the excitation energies used, did indeed produce the desired product, ^{98}Mo, via true compound nucleus formation. This was verified in three ways:

1. In coincident events, where both fragments of the binary decay were detected, the measured atomic numbers of each fragment can be summed to give the atomic number of the parent nucleus of the binary decay; for ^{98}Mo, the fragments should sum to Z_{total}=40–42 ($Z_{Mo} = 42$), accounting for the evaporation of light particles before a binary split.

2. The source of fragments, believed to be a compound nucleus, should have a velocity that is consistent with a completely fused system.

3. Angular distributions of fragments in the center-of-mass frame should be isotropic; that is, there should be an equal emission of complex fragments in the reaction plane into all angles.

The results discussed in the next sections verify that ^{98}Mo was produced via a compound nucleus reaction mechanism.

3.1 Carbon Foil Purity; Coincidence Data

Events in which coincident fragments were detected on opposite sides of the beam axis were analyzed. Essentially no coincidences between telescopes on the same side of the beam were observed, consistent with the predominantly binary nature of the complex fragment events, and conservation of momentum. Coincidence detection followed by compound nucleus reconstruction was the primary measurement used to gauge the level of purity of the carbon foils investigated [40].

A second measurement of impurities in the carbon foils was made using Rutherford Backscattering Spectrometry (RBS) [41] offered by the Surface Science Division at Lawrence Berkeley Laboratory. A beam of $^4He^{2+}$ ions was accelerated to 1.95 MeV and scattered off atoms in the carbon foils. A particle detector was set at 165° in the backscatter direction with respect to the beam. The scattering energy is related to the atomic number of the scattering nucleus, thus identifying components of the foils. To obtain a value for the concentration of impurities in the foils, the height of the impurity edges were compared with the height of the carbon edge in the spectrum; using the scattering cross section for each element gives a concentration value that contains about 10% error.

The carbon foil used in the first cyclotron experiment, Foil A [42], was produced by vacuum evaporation, which is a widely used foil preparation technique. In this procedure, a source of spectrographically pure carbon, in the form of graphite, is heated in vacuum, causing evaporation of the carbon onto a glass slide coated with a parting agent. The parting agent is used to facilitate the removal of the foil from the glass plate, typically accomplished by floating the foil onto a water surface. The manufacturer quoted impurities of $\sim 0.1\%$ and $\sim 1.0\%$ (atomic) for sodium and oxygen, respectively. The parting agent for Foil A is proprietary, but is most likely a soap or soap derivative; the manufacturer reports that the parting agent does contain sodium.

Figure 3.2 shows a plot of the number of events versus the sum of the measured atomic number (Z_{sum}) of the two coincident fragments for the first cyclotron experiment with Foil A. At the higher bombarding energy, a single peak centered at

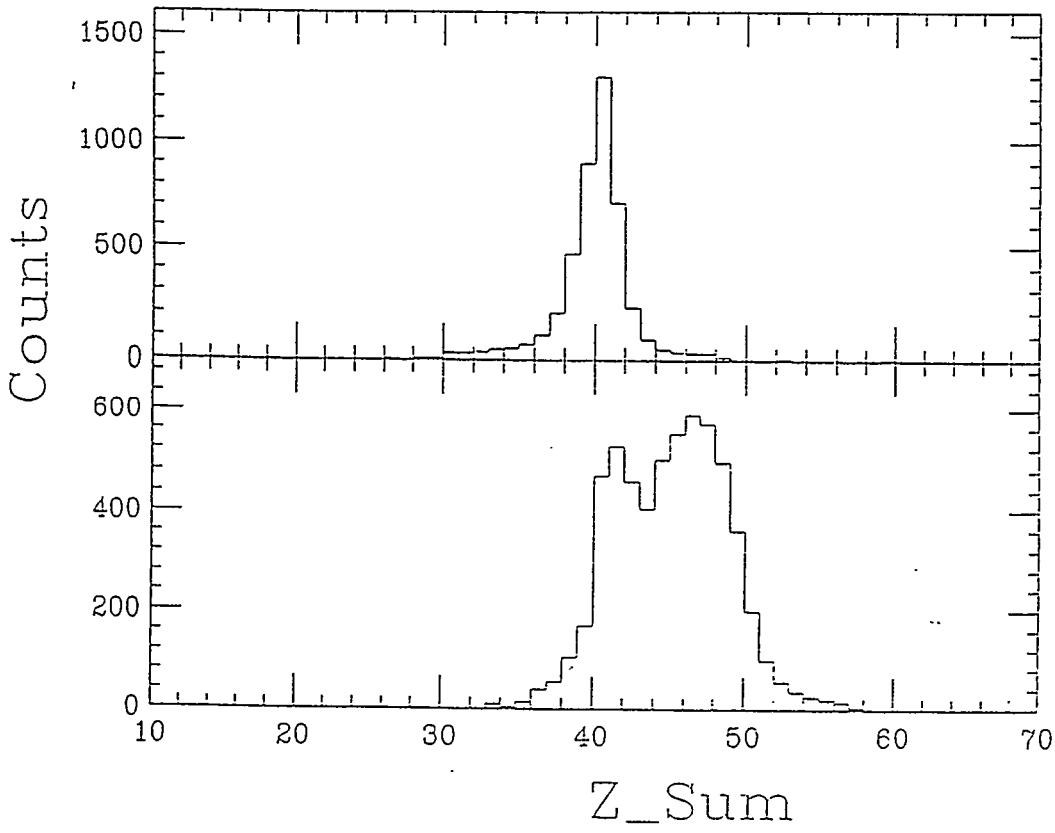

Figure 3.2: Number of coincidence events versus the sum of the measured atomic number for each fragment for Foil A, at bombarding energies of 11.98 (upper) and 7.71 (lower) MeV/A. At the lower energy, the ratio of the integrated counts for the $Z_{sum} \approx 47$ peak versus the $Z_{sum} \approx 42$ peak is 1.8 : 1.

$Z_{sum} \approx 42$ (all Z measurements carry an error of ± 1) is observed, corresponding to the fusion of krypton ($Z = 36$) and carbon ($Z = 6$); however, at the lower energy there are two peaks, a smaller one at $Z_{sum} \approx 42$ and a larger one at $Z_{sum} \approx 47$. The smaller peak corresponds to the reaction of interest, while the larger, broader peak is due to reactions with impurities in the foil heavier than carbon, with sodium being the primary culprit. The ratio of integrated counts for the $Z_{sum} \approx 47$ peak versus the $Z_{sum} \approx 42$ peak is 1.8 : 1. As the energy of the beam is decreased, the yield of fission fragments from the carbon target decreases precipitously, relative to the yield of fragments from the heavier impurities. Thus, at lower energy, the observed yield is from reactions on the impurities in the carbon target, not on carbon itself.

To measure the yield at the lowest energies, it is necessary to use a purer carbon foil. Numerous articles have been written concerning carbon foil purity and purification techniques [43–46]; however, most of the techniques discussed for purging carbon foils of their impurities do not achieve the requisite level of purity required for these experiments. Because the parting agent was the suspected cause of the impurity, the surface of the foil was washed with hydrofluoric acid, followed by a deionized water wash and drying in a vacuum oven. A second cyclotron experiment revealed that the concentration of impurities was worse, with oxygen (from the water wash) being the most concentrated impurity.

The producer of Foil A began with spectrographically pure graphite to manufacture Foil A, so it appears that the manufacturing technique, especially the use of a parting agent, was the main source of impurities in the foil. For this reason, a different foil manufacturing technique was investigated in hopes of obtaining a purer carbon foil. A promising alternative technique that does not involve a parting agent is chemical vapor deposition. In this technique, a hydrocarbon gas is "cracked" at a high temperature in an inert gas environment, and carbon is deposited onto a bed of molten metal. When the molten metal cools, the carbon foil curls off the metal surface. This technique is more expensive than vacuum evaporation, but because it avoids the parting agent, and because the foil does not need to be floated on water, the foil is relatively free of adsorbed contaminants. The second foil, Foil B [47], was prepared by this technique, and the manufacturer quoted the metallic ash impurity,

including sodium, as $\sim 5 \times 10^{-4}$% (atomic), and the total ash impurity as less than 0.001% (atomic).

Because beam time at the cyclotron is expensive, it was advantageous to have an assay of the impurities in the new foil before using it in a cyclotron experiment. RBS was used to analyze both Foil A and Foil B for impurities. A comparison of the spectra of the two foils, Figure 3.3, shows that Foil A has a greater degree of contamination, with $\sim$ 1.7% (atomic) nitrogen, $\sim$ 2.1% oxygen, and $\sim$ 0.12% sodium. The contamination level in Foil B is below the sensitivity of the technique, indicating $\leq$ 1.0% (atomic) nitrogen, $\leq$ 0.8% oxygen, and $\leq$ 0.10% sodium (see Table 3.1). Note the very large carbon edge at approximately 500 keV, and the marked nitrogen, oxygen, and sodium edges on the magnified scale.

Table 3.1: Impurities for carbon foils as determined by Rutherford Backscattering Spectrometry; impurity levels given as atomic percent.

Foil	N	O	Na
A	1.7%	2.1%	0.12%
B	$\leq$1.0%	$\leq$0.8%	$\leq$0.1%

Since the level of impurity of the foil prepared by chemical vapor deposition (Foil B) was below the limit of detection of RBS, only upper limits on the impurity were determined. However, it was sufficiently purer than the foil prepared by vacuum evaporation (Foil A) to warrant using it in a cyclotron experiment. A third, identical bombardment was done using a ^{86}Kr beam on Foil B of the same thickness as Foil A. The analysis of the two coincident fragments (lower portion of Figure 3.4) shows a single peak at $Z_{sum} \approx 42$, and the absence of any additional contamination peaks. For comparison, the spectrum from Foil A at the same energy is shown in the upper portion of the figure. Using the statistical simulation cross section data of Figure 2.2, these data indicate that the level of sodium impurity in Foil B is $\leq$ 0.02% (atomic), consistent with RBS measurement and the manufacturer's claims, and sufficiently low to measure fission cross sections at the lowest compound nucleus energies.

This study has determined that foils prepared by chemical vapor deposition

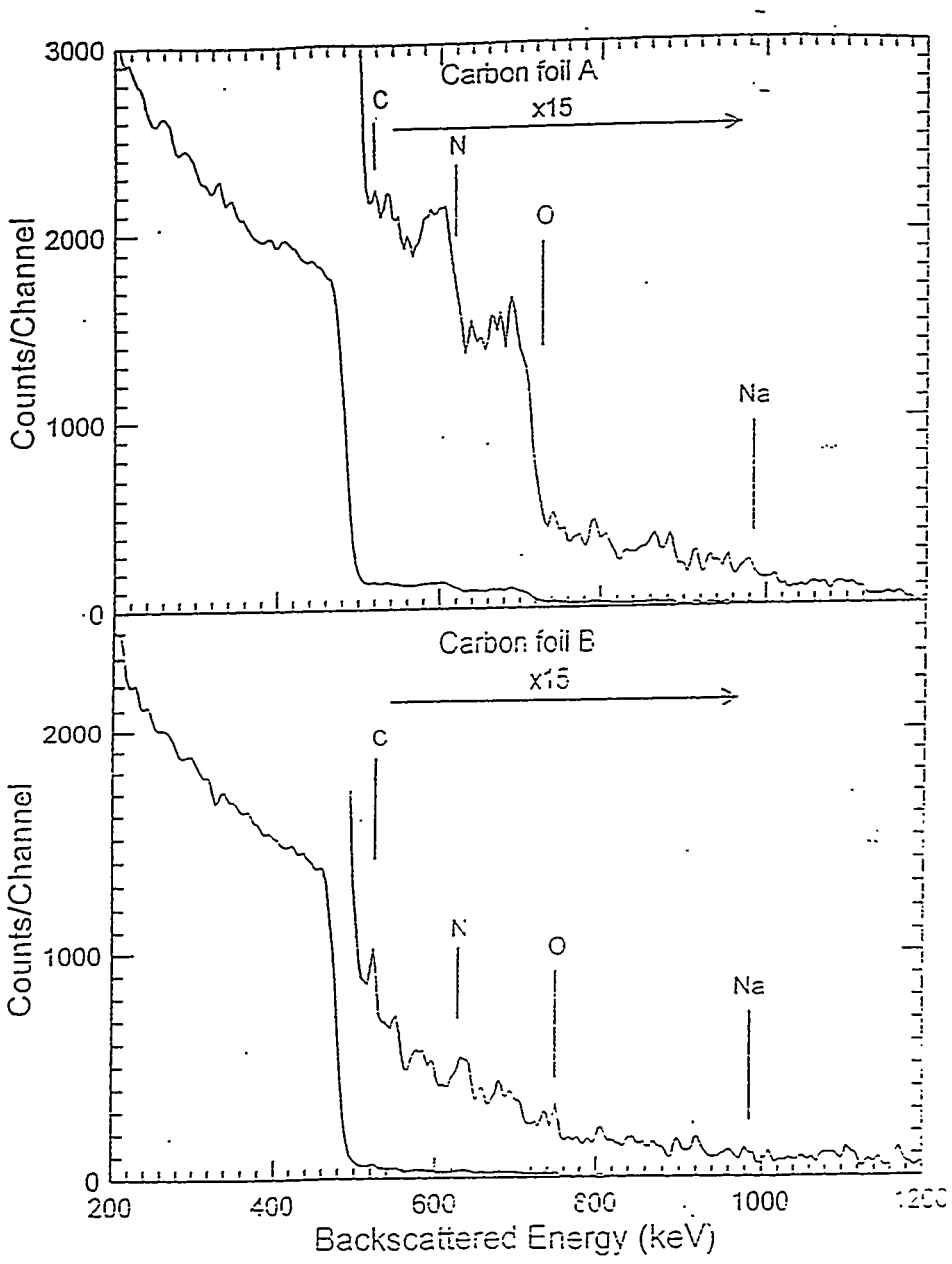

Figure 3.3: Rutherford backscattering spectrometry spectra of Foil A (upper) and Foil B (lower). Foil A shows impurity peaks for nitrogen, oxygen, and sodium, whereas Foil B shows no impurity above the limits of detection. Note scale change; position of edge due to backscattering indicated.

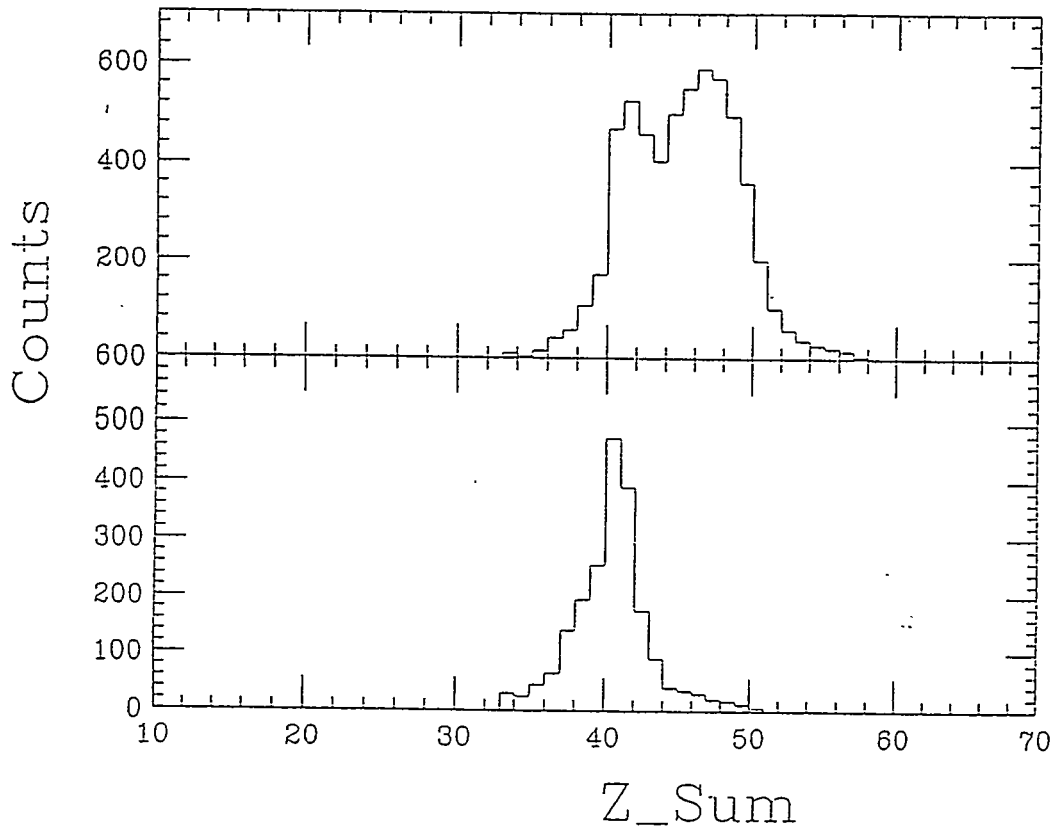

Figure 3.4: Number of coincidence events versus the sum of the measured atomic number for each fragment, for Foil A (upper) and Foil B (lower) at the same bombarding energy (7.71 MeV/A).

are purer than those prepared by vacuum evaporation onto a coated glass slide. A significant impurity in foils prepared by the latter technique is sodium. Since spectrographically pure carbon is used in both procedures, a small amount of sodium is likely introduced by the parting agent used to coat the glass slide. The foils produced by chemical vapor deposition are of sufficient purity to allow for the accurate measurement of nuclear properties at very low cross sections.

For compound nucleus reactions with no impurity present in the carbon foil, essentially all the charge of the compound nucleus (Z_{CN}) is detected in the two fragments, confirming the binary nature of the reaction. The small difference between Z_{CN} and the total detected charge ($Z_1 + Z_2 = Z_{sum}$) determines the amount of light charged particles evaporated from the hot nascent fragments. For ^{98}Mo, the average total charge loss at the highest energies is about two Z units; this charge loss appears to decrease only slightly as the excitation energy is decreased, because neutron-rich ^{98}Mo will more easily emit its surplus of neutrons than its relative dearth of protons.

3.2 Source and Emission Velocities; Coulomb Circles

To determine that the nuclear product in these reactions was indeed a true compound nucleus, the laboratory energy spectra were transformed into cross section plots in velocity space. The velocity, V, of each fragment was calculated from its measured charge and kinetic energy. The average mass, A, of each fragment, was determined using each fragment's measured atomic number (Z), and the empirical formula [48]:

$$A = 2.08Z + 0.0029Z^2. \tag{3.1}$$

This formula is valid for the low energy regime in which these reactions were studied. Figure 3.5 presents these velocity-space cross section plots for the 11.98 MeV/A reaction of ^{86}Kr on ^{12}C, with the x- and y-axes representing the fragment velocity perpendicular and parallel to the beam, respectively. For $Z > 10$, these plots show a high cross section isotropic ring (commonly called a Coulomb circle). The Coulomb circles shown are equivalent to the circle drawn in Figure 3.1, which has been overlapped with a single Coulomb circle in Figure 3.6, in order to make their relationship more clear. The width of the circle is broadened mainly by sequential evaporation of light particles, and also by small variations in the Coulomb energy near the scission point, arising from thermal fluctuations in various collective degrees of freedom [4]. The observed Coulomb circles correspond to the emission of fragments with Coulomb-like velocities from a single source which has a well-defined laboratory velocity. These circles have been previously observed [24, 39, 48–51], and are indications of fully relaxed binary decays associated with either compound nucleus emission or fully damped deep inelastic processes. The center of each circle defines the laboratory velocity of the source (compound nucleus or composite system), and the radius corresponds to the emission velocity with which the complex fragments are emitted in the source frame. For the lighter fragments (Z = 5–9), the isotropic component is visible at the forward angles; however, at the backward angles, a partially damped deep inelastic component masks the isotropic component. It is backward peaked in

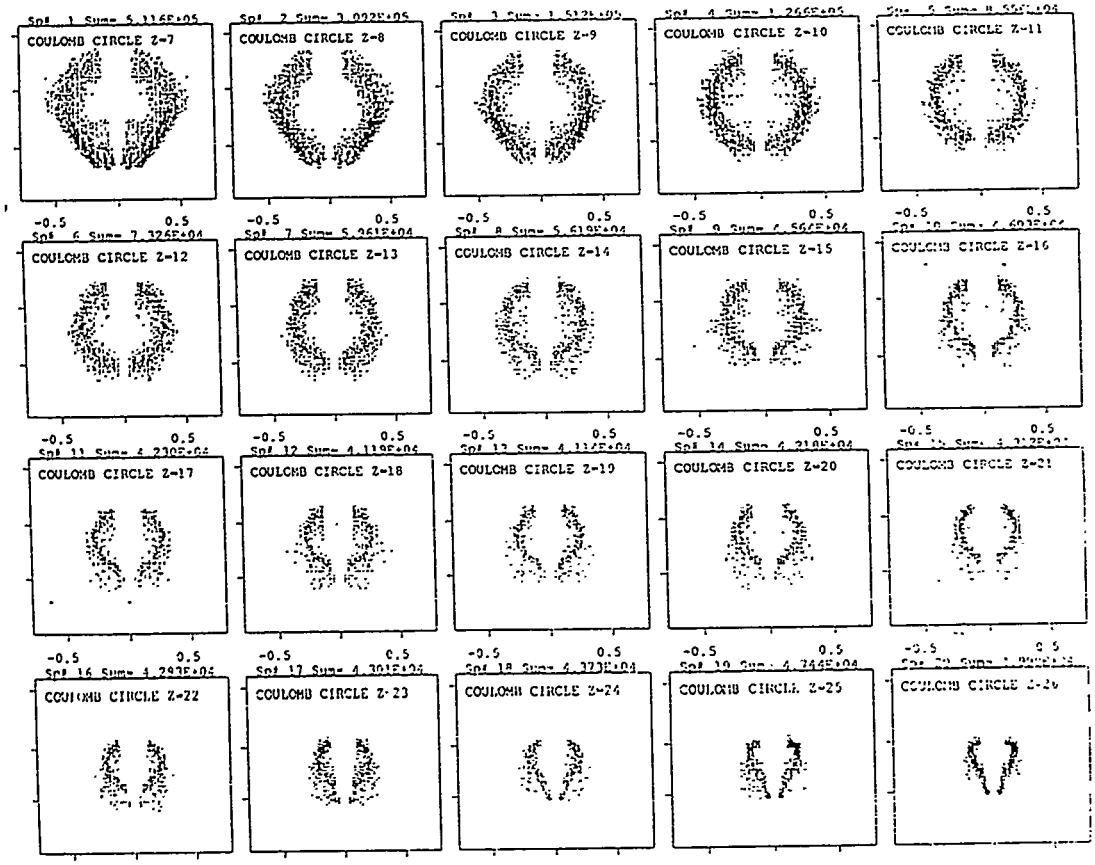

Figure 3.5: Scatter plots of Coulomb circles. The x-axis is the perpendicular velocity (relative to the beam axis) and the y-axis is the parallel velocity, for the reaction of ^{86}Kr on ^{12}C at 11.98 MeV/A.

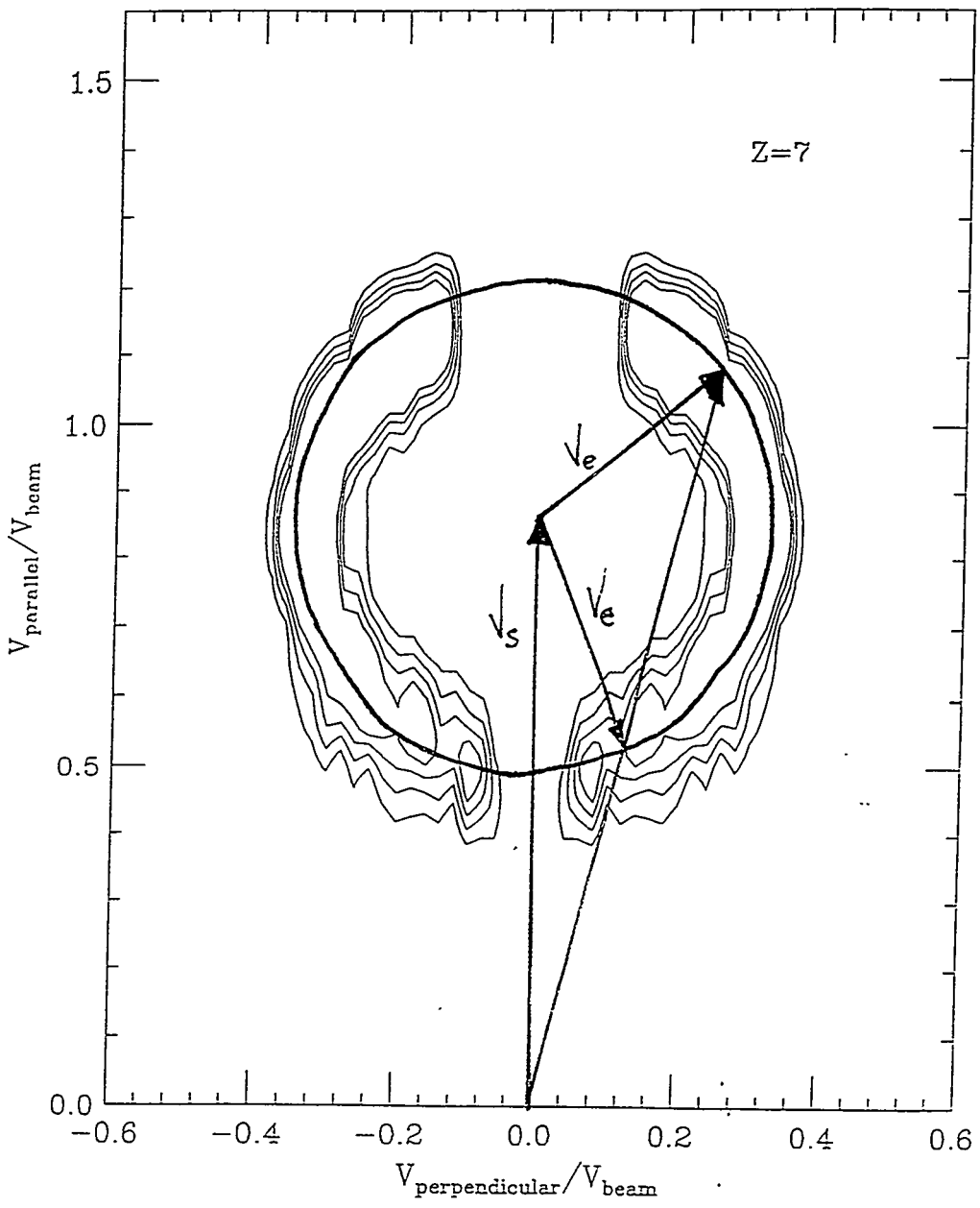

Figure 3.6: The Coulomb circle for nitrogen fragments from the reaction of ^{86}Kr on ^{12}C at 11.98 MeV/A, overlaid with the vector scheme discussed previously. Source and emission velocities, as they relate to the Coulomb circle, are illustrated.

reverse kinematics because this component is composed of target-like fragments.

The source and emission velocities for each Z are contained within the preceding Coulomb circles in Figure 3.6; they have been extracted from the Coulomb circles and presented in Figure 3.7, for the reaction of ^{86}Kr on ^{12}C at 11.98 MeV/A.

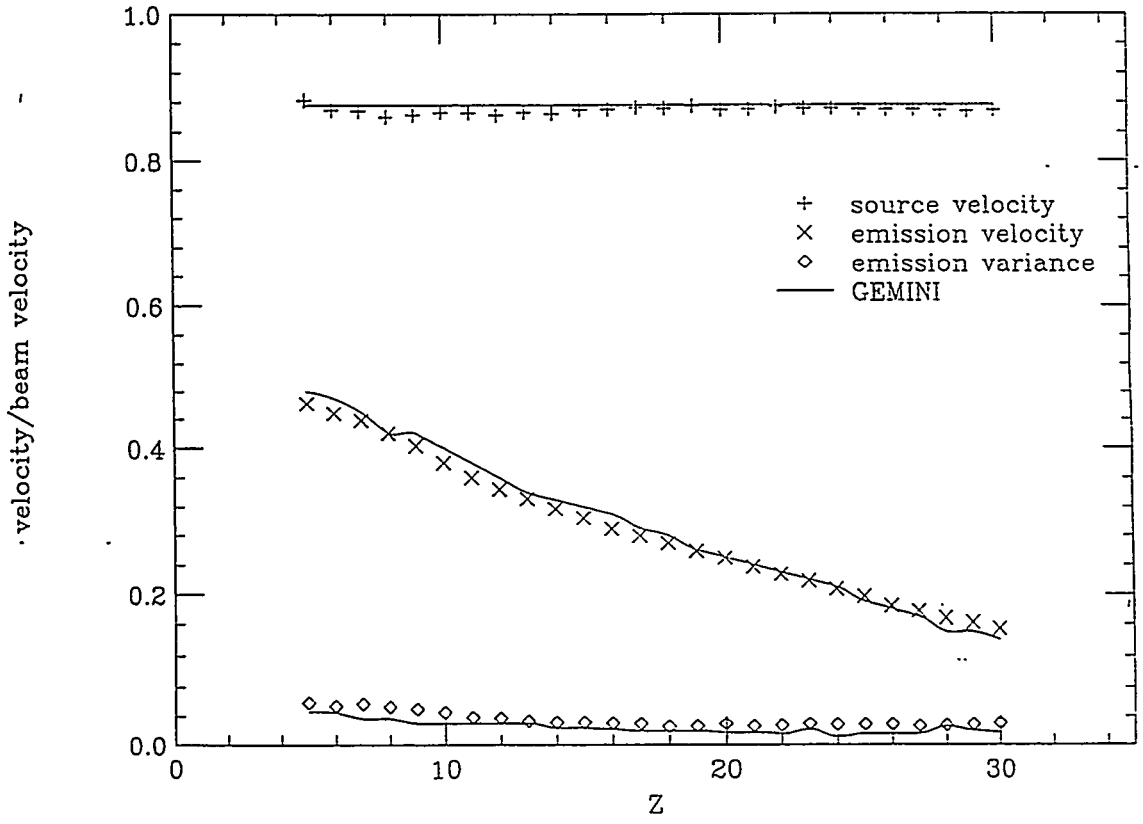

Figure 3.7: Source (upper) and emission (middle) velocities for the reaction of ^{86}Kr on ^{12}C at 11.98 MeV/A. Also shown is the variance in the fragment emission velocities (lower).

The source velocity (V_s) for each atomic number was obtained by determining the center point of each Coulomb circle. The experimental source velocities show very little variation with the fragment atomic number, confirming that all fragments are emitted by the same source. These source velocities agree closely with the velocities expected for complete fusion, which were calculated with the statistical code GEMINI [39] and are represented in Figure 3.7 by the horizontal line that overlaps

the data.

The emission velocity (V_e) for each atomic number was obtained by determining the average radius of each Coulomb circle. The Coulomb nature of these velocities can be inferred from both their magnitude and their nearly linear dependence upon the atomic number of the emitted fragment. A calculation of the Coulomb velocities, based upon Viola systematics [52] and generalized to asymmetric divisions, is shown in Figure 3.7 by the solid line that closely tracks the emission velocity data points. This calculation was performed using GEMINI, and the Coulomb energy was taken to be

$$E_{Coul} = (1.44 Z_1 Z_2)/[r_0(A_1^{1/3} + A_2^{1/3} + 2.0)], \tag{3.2}$$

where r_0 was determined by equating E_{Coul} for symmetric fission (*i.e.*, $Z_1 = Z_2$ and $A_1 = A_2$) to the value given by Viola systematics [52]. By assuming that the momentum in the center-of-mass was conserved, the emission velocities of both fragments in the binary decay can be calculated. The agreement between the data and the calculations is quite good, and confirms that the emission velocities are Coulomb-like.

Each emission velocity is associated with a distribution that arises from the width of the Coulomb circle. The variances of these distributions, which result from the sequential evaporation of light particles and from the thermal fluctuation of the Coulomb energy near the scission point, are also plotted for each fragment in Figure 3.7.

3.3 Angular Distributions

Some representative angular distributions, in the frame of the source system, are shown in Figure 3.8, for the reaction of ^{86}Kr on ^{12}C at 11.98 and 11.06 MeV/A. For intermediate Z-values, the angular distributions ($d\sigma/d\Theta$) are flat over the measured angular range, indicating that emission was isotropic in the reaction plane. However, for some Z-values there is a deep inelastic component along with the isotropic component of fragment emission (this was discussed briefly on page 33; see also references [50, 53–56]). For fragments with $Z < 10$, the distributions are peaked at backward angles (Θ_{cm} >130°)due to the presence of a target-like (light) component. The projectile-like component, which is expected to peak at forward angles for the heaviest fragments, does not appear to be present in these distributions because $Z > 24$ was not measured.

The majority of these angular distributions are flat, indicating a pure isotropic distribution. For the few Z-values which show a mixture of isotropic and anisotropic components, the anisotropic component can be subtracted away, because it appears only at the most backward angles on top of the isotropic component. With the isotropic component isolated, and with the fulfillment of the three conditions required to define our product as ^{98}Mo from ^{86}Kr on ^{12}C, via the compound nucleus reaction mechanism, the individual fragment cross sections and barrier heights are quite easily extracted.

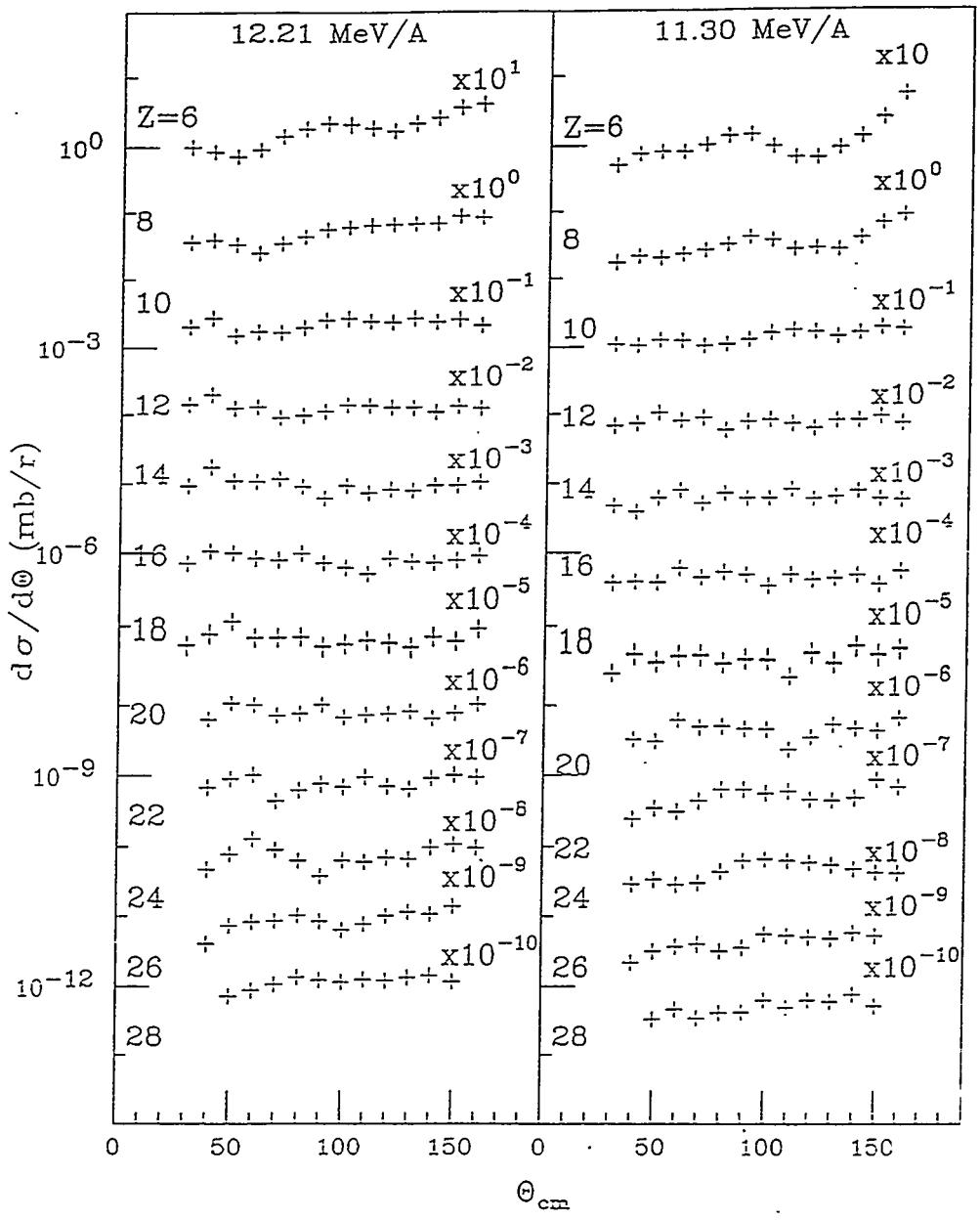

Figure 3.8: Angular distributions for the reaction of ^{86}Kr on ^{12}C at 11.98 and 11.06 MeV/A. The flat distributions for the majority of the fragments indicate that a well-equilibrated compound nucleus is their source.

3.4 Cross Sections and Excitation Functions

Because of the flat angular distributions, the cross sections can be determined by integrating the average value of $d\sigma/d\Theta$ over the angular range $\Theta_{cm} = 0°$ to 180°. With the angular distributions that peaked at the backward angles, a constant equal to the minimum value of $d\sigma/d\Theta$ was taken as an upper limit for the isotropic component, and the cross section was determined by integrating that constant over the angular range $\Theta_{cm} = 0°$ to 180°.

For all the energy points, the measured cross sections of the isotropic component are shown in Figure 3.9, and listed in Table 3.2. The measured cross sections show one-half of the characteristic "U"-shaped distribution associated with the decay of a compound system with a mass below the Businaro-Gallone point (see page 8). The change in absolute cross section, as well as the evolution of the shape of the cross section, as a function of bombarding energy, are shown very well in this figure. The flattening of the distribution with increasing energy can be understood as the leveling of the probability for decay through any given channel, which is due to an increase in the temperature of the decaying system, as predicted by Equation 1.2.

Figure 3.10 displays the excitation functions for all measured atomic numbers at all measured energies. Obviously, as the excitation energy of the system increases, the greater the likelihood (cross section) that a certain fragment will be ejected. The excitation function plots basically depict the cross section data in a slightly different way, with the excitation energy (E_x) replacing the atomic number (Z) on the x-axis.

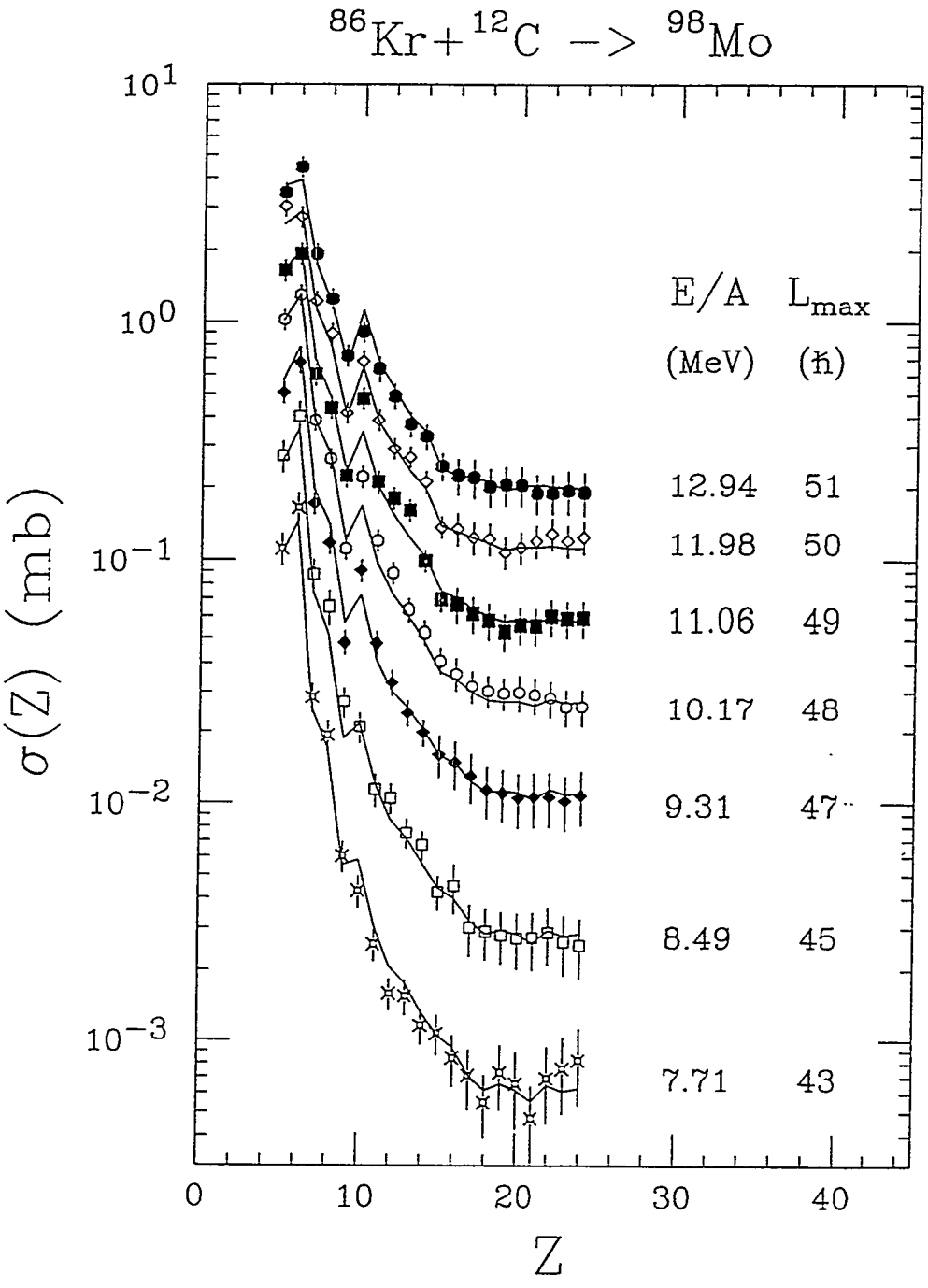

Figure 3.9: Cross sections for all fragments detected from the reaction of ^{86}Kr on ^{12}C, at all energies studied. Also listed is the ℓ_{max} used for fitting each energy in this plot (solid lines); this is discussed in Section 3.5.

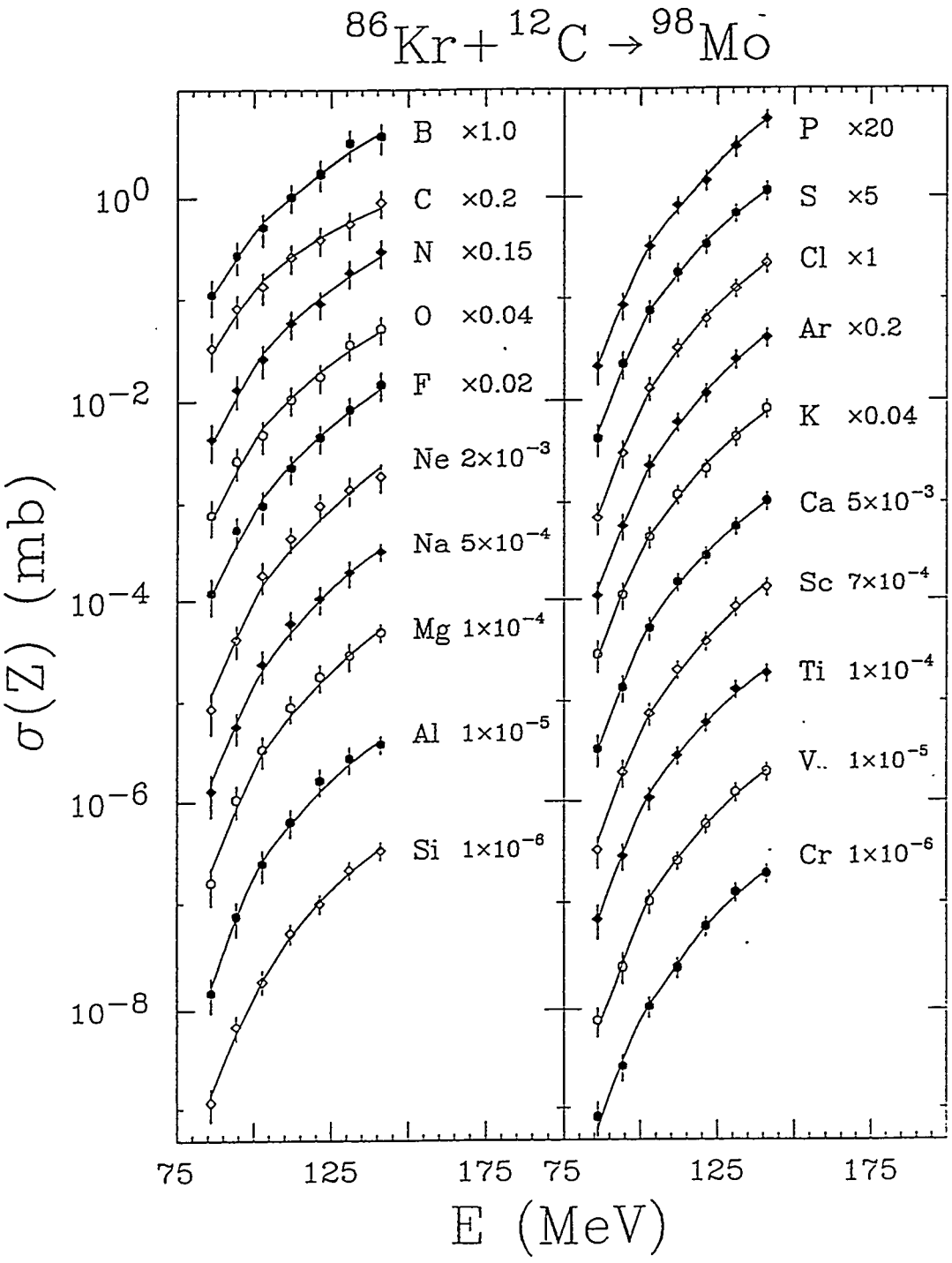

Figure 3.10: Excitation functions for fragments $5 < Z < 24$ from the reaction of ^{86}Kr on ^{12}C at all energies; the solid lines are the theoretical fits, discussed in Section 3.5.

Table 3.2: The cross section data for all the measured fragments (Z) from the reaction of ^{86}Kr on ^{12}C, for all the energies investigated. Both energy per nucleon of the projectile and excitation energy of the compound nucleus (^{98}Mo) are shown across the top.

E_{beam} (MeV/A)	12.94	11.98	11.06	10.17	9.31	8.49	7.71
E (MeV)	141.1	131.0	121.3	111.9	102.9	94.3	86.0
Z	σ_Z (mb)						
5	3.47±1.04	3.05±0.91	1.66±0.50	1.02±0.31	0.51±0.18	0.27±0.09	0.11±0.04
6	4.46±1.34	2.74±0.82	1.93±0.58	1.31±0.39	0.67±0.24	0.40±0.14	0.16±0.07
7	1.93±0.58	1.23±0.37	0.60±0.18	0.39±0.12	0.17±0.06	(8.7±3.1)10^{-2}	(2.9±1.1)10^{-2}
8	1.26±0.38	0.89±0.27	0.44±0.13	0.26±0.08	0.12±0.04	(6.5±2.3)10^{-2}	(1.9±0.8)10^{-2}
9	0.72±0.22	0.42±0.13	0.22±0.07	0.11±0.03	(4.8±1.7)10^{-2}	(2.7±0.9)10^{-2}	(6.0±2.4)10^{-3}
10	0.91±0.27	0.68±0.21	0.48±0.14	0.22±0.07	(9.1±3.2)10^{-2}	(2.1±0.7)10^{-2}	(4.3±1.9)10^{-3}
11	0.64±0.13	0.39±0.12	0.21±0.06	0.12±0.04	(4.8±1.7)10^{-2}	(1.1±0.4)10^{-2}	(2.6±1.2)10^{-3}
12	0.49±0.10	0.29±0.09	0.18±0.05	(8.8±2.7)10^{-2}	(3.3±1.2)10^{-2}	(1.1±0.4)10^{-2}	(1.6±0.6)10^{-3}
13	0.37±0.07	0.27±0.08	0.16±0.05	(6.4±1.9)10^{-2}	(2.4±0.9)10^{-2}	(7.5±2.6)10^{-3}	(1.5±0.6)10^{-3}
14	0.33±0.07	0.21±0.04	(9.9±2.0)10^{-2}	(5.2±1.0)10^{-2}	(2.0±0.5)10^{-2}	(6.7±2.0)10^{-3}	(1.2±0.4)10^{-3}
15	0.24±0.05	0.14±0.03	(7.0±1.4)10^{-2}	(4.1±0.8)10^{-2}	(1.6±0.4)10^{-2}	(4.2±1.3)10^{-3}	(1.1±0.4)10^{-3}
16	0.22±0.04	0.14±0.03	(6.7±1.3)10^{-2}	(3.6±0.7)10^{-2}	(1.5±0.4)10^{-2}	(4.5±1.3)10^{-3}	(8.4±3.0)10^{-4}
17	0.22±0.04	0.12±0.02	(6.2±1.2)10^{-2}	(3.2±0.6)10^{-2}	(1.3±0.3)10^{-2}	(3.0±0.9)10^{-3}	(7.1±2.5)10^{-4}
18	0.20±0.04	0.12±0.02	(5.8±1.2)10^{-2}	(3.0±0.6)10^{-2}	(1.1±0.3)10^{-2}	(2.9±0.9)10^{-3}	(5.5±1.9)10^{-4}
19	0.21±0.04	0.11±0.02	(5.3±1.1)10^{-2}	(3.0±0.6)10^{-2}	(1.1±0.3)10^{-2}	(2.8±0.8)10^{-3}	(7.3±2.6)10^{-4}
20	0.20±0.04	0.11±0.02	(5.6±1.1)10^{-2}	(3.0±0.6)10^{-2}	(1.1±0.3)10^{-2}	(2.7±0.8)10^{-3}	(6.6±2.3)10^{-4}
21	0.19±0.04	0.12±0.02	(5.6±1.1)10^{-2}	(2.9±0.6)10^{-2}	(1.1±0.3)10^{-2}	(2.7±0.8)10^{-3}	(4.7±1.7)10^{-4}
22	0.19±0.04	0.13±0.03	(6.0±1.2)10^{-2}	(2.8±0.6)10^{-2}	(1.1±0.3)10^{-2}	(2.9±0.9)10^{-3}	(6.9±2.4)10^{-4}
23	0.19±0.04	0.12±0.02	(5.9±1.2)10^{-2}	(2.6±0.5)10^{-2}	(1.0±0.3)10^{-2}	(2.6±0.8)10^{-3}	(7.6±2.7)10^{-4}
24	0.19±0.04	0.13±0.03	(5.9±1.2)10^{-2}	(2.6±0.5)10^{-2}	(1.1±0.3)10^{-2}	(2.5±0.8)10^{-3}	(8.2±2.9)10^{-4}

3.5 Barrier Heights

In order to extract the conditional barriers and examine their sensitivity to a variety of parameters, the experimental excitation functions (Figure 3.10) have been fitted with functions obtained from a transition state method following the Bohr-Wheeler formalism [4, 32, 5, 57, 58] and from the Weisskopf theory [59]. In the transition state theory, the reaction coordinate is determined at a suitable point in coordinate space (typically at the saddle point in the case of fission), and the decay rate is equated with the phase space flux across a hyperplane in phase space passing through the saddle point and perpendicular to the fission direction. The decay width for first chance emission of a fragment of charge Z is expressed as

$$\Gamma_Z = \frac{1}{2\pi\rho(E - E_r^g)} \int_0^{E-B_Z^{eff}} \rho(E - B_Z^{eff} - \varepsilon)d\varepsilon, \tag{3.3}$$

where $\rho(E - E_r^g)$ is the compound nucleus level density, $\rho(E - B_Z^{eff} - \varepsilon)$ is the level density at the conditional saddle with the kinetic energy ε in the fission mode, and B_Z^{eff} is the effective fission barrier defined as

$$B_Z^{eff} = B_Z + E_r^s, \tag{3.4}$$

with B_Z being the conditional barrier for zero angular momentum. E_r^g and E_r^s are the energy of the rotating ground state relative to the non-rotating macroscopic sphere and the rotational energy of the saddle point, respectively. The neutron and proton decay widths can be written as

$$\Gamma_n = \frac{2mR^2g'}{\hbar^2 2\pi\rho(E - E_r^g)} \int_0^{E-B_n^{eff}} \varepsilon\rho(E - B_n^{eff} - \varepsilon)d\varepsilon, \tag{3.5}$$

and

$$\Gamma_p = \frac{2mR^2g'}{\hbar^2 2\pi\rho(E - E_r^g)} \int_{\varepsilon_C}^{E-B_p^{eff}} \varepsilon(1 - \frac{\varepsilon_C}{\varepsilon})\rho(E - B_p^{eff} - \varepsilon)d\varepsilon, \tag{3.6}$$

respectively, where $\rho(E - B_n^{eff} - \varepsilon)$ and $\rho(E - B_p^{eff} - \varepsilon)$ are level densities of the residual nucleus after neutron and proton emission, respectively. ε is the energy of the emitted particle (neutron or proton), m its mass, g' its spin degeneracy ($g' = 2$), R the radius of the nucleus from which it has been emitted, and ε_C is the Coulomb

barrier for proton evaporation which is evaluated in this study with the empirical formula given by Parker *et al.* [60]. The effective neutron barrier (B_n^{eff}) and proton barrier (B_p^{eff}) are defined as

$$B_n^{eff} = B_n + E_r^g \tag{3.7}$$

and

$$B_p^{eff} = B_p + E_r^g, \tag{3.8}$$

where B_n is the last neutron binding energy and B_p is the last proton binding energy.

As shown in Equation 3.3, the angular momentum dependence of Γ_Z is accounted for by the addition of the rotational energy

$$E_r^s = \frac{\hbar\ell(\ell+1)}{2\Im_{saddle}} \tag{3.9}$$

to the conditional barrier for zero angular momentum (B_Z), where $\Im_{saddle}$ is the moment of inertia about the axis perpendicular to the symmetry axis of the nucleus at the conditional saddle point. Such treatment of the angular momentum is adequate since the calculated moment of inertia of the saddle point is virtually constant [61] over the range of angular momentum considered here.

The formalism presented above requires the use of a specific level density expression in the widths of Γ_n, Γ_p, and Γ_Z. It is mainly in these quantities that all of the physical information concerning the nucleus at the saddle point, and the residual nucleus after light particle evaporation, is contained. For the level density, the standard Fermi gas expression

$$\rho(E) \propto \exp[2(aE)^{1/2}] \tag{3.10}$$

has been used, where E is the thermal excitation energy of the system and a is the energy level parameter.

The maximum angular momentum (ℓ_{max}) used in the calculations was not treated as a free parameter for each individual fit (each Z); instead, ℓ_{max} was calculated with the Bass model [62, 63], and adjusted within 1.5 $\hbar$ of the Bass model predictions to minimize the χ^2 of all the fits simultaneously. Both the ℓ_{max} values used in the fits and the ℓ_{max} values predicted by the Bass model are listed in Table 3.3.

The angular momentum distribution of the fusion cross section (σ_ℓ) was parametrized using a Fermi distribution [22, 64]

$$\sigma_\ell = \frac{(\lambda^2/4\pi)(2\ell+1)}{1+\exp[(\ell-\ell_{max})/\delta\ell]}, \tag{3.11}$$

where $\delta\ell$ determines the diffuseness of the distribution and ℓ_{max} is the maximum angular momentum. The value of $\delta\ell$ was chosen to be 1; the fitting was not very sensitive to the specific value of $\delta\ell$. The expression used in evaluating the cross section for a given fragment is given by:

$$\sigma_Z = \sum_0^{\ell_{max}} \sigma_\ell P_Z(\ell), \tag{3.12}$$

where $P_Z(\ell)$ is the probability of emitting a complex fragment. In the expression used for $P_Z(\ell)$, second and third chance emission (emission of a fragment after the initial emission of one or two protons and/or neutrons) have been included. The probability for the first chance emission is Γ_Z/Γ_T, where Γ_T is the total decay width taken to be

$$\Gamma_T = \Gamma_n + \Gamma_p + \Gamma_Z. \tag{3.13}$$

Notice that Γ_T is almost independent of Z since

$$\Gamma_n + \Gamma_p \gg \sum_{Z\geq 2} \Gamma_Z \tag{3.14}$$

holds true in the mass region and excitation energy range studied in the present work.

The excitation functions were fitted with two free parameters:

1. The conditional fission barrier, B_Z.
2. The ratio of the level density parameter at the saddle point divided by that of the residual nucleus after neutron decay (a_Z/a_n).

A level density parameter of $a = a_n = A/8$ for the residual nucleus after neutron or proton emission was assumed in the fitting. The fits are excellent for all mass asymmetries and the entire excitation energy range explored, as shown in Figure 3.10 by the solid lines. This rigorous consistency with the transition state theory provides the

strongest evidence for the compound nucleus mechanism of the isotropic component in the angular distributions (Section 3.3). It also undermines the claims [65, 66] of the existence of transient time effects, as has been pointed out by Moretto *et al.* [67].

The extracted conditional barriers and the ratio of level density parameters are shown in Figure 3.11; for reference, the extracted barriers for ^{94}Mo and ^{90}Mo are also shown [31]. The conditional barriers extracted contain uncertainties from several sources; however, the most significant error is due to the sensitivity of the barriers to the level density parameter a_n. This parameter has not yet been established experimentally for the excitation energy region well above the last neutron binding energy. This study used $a_n = A/8$, which results in excellent fits for all the excitation functions. It should be noted that a decrease in the level density parameter from $A/8$ to $A/9$ will result in an increase in the value of the extracted barriers by ~ 1.1 MeV, and an increase in a_Z/a_n of $\sim 1.2\%$, without compromising the quality of the fits. This dependence of the barriers on the level density parameter is encoded in the specific form of the Fermi gas level density (Equation 3.10) which was used in the fitting. Therefore, when quoting experimental values for the barrier heights, it is important to also make reference to the level density parameter used to extract the barriers.

Another source of uncertainty in the extracted barrier heights arises from the energy of the rotating ground state (E_r^g), as calculated with the RFRM. The rotational energy of the saddle point (E_r^s) was calculated by assuming a configuration of two spheres separated by 2 fm. If the saddle shape given by the RFRM were used instead to compute the rotational energy, the extracted barriers would shift by -0.24 MeV on average (-0.5 MeV maximum). In addition, a change of the diffuseness parameter ($\delta\ell$) within acceptable values (between 0 and 3) causes a change in the height of the barriers by ± 0.35 MeV. An overall uncertainty in the extracted barrier heights, without including the contribution from the level density parameter (a_n), amounts to $\sim 3\%$.

The extracted barriers are internally consistent, meaning that they increase as a function of fragment atomic number, peak at symmetric division ($Z = 21$), and

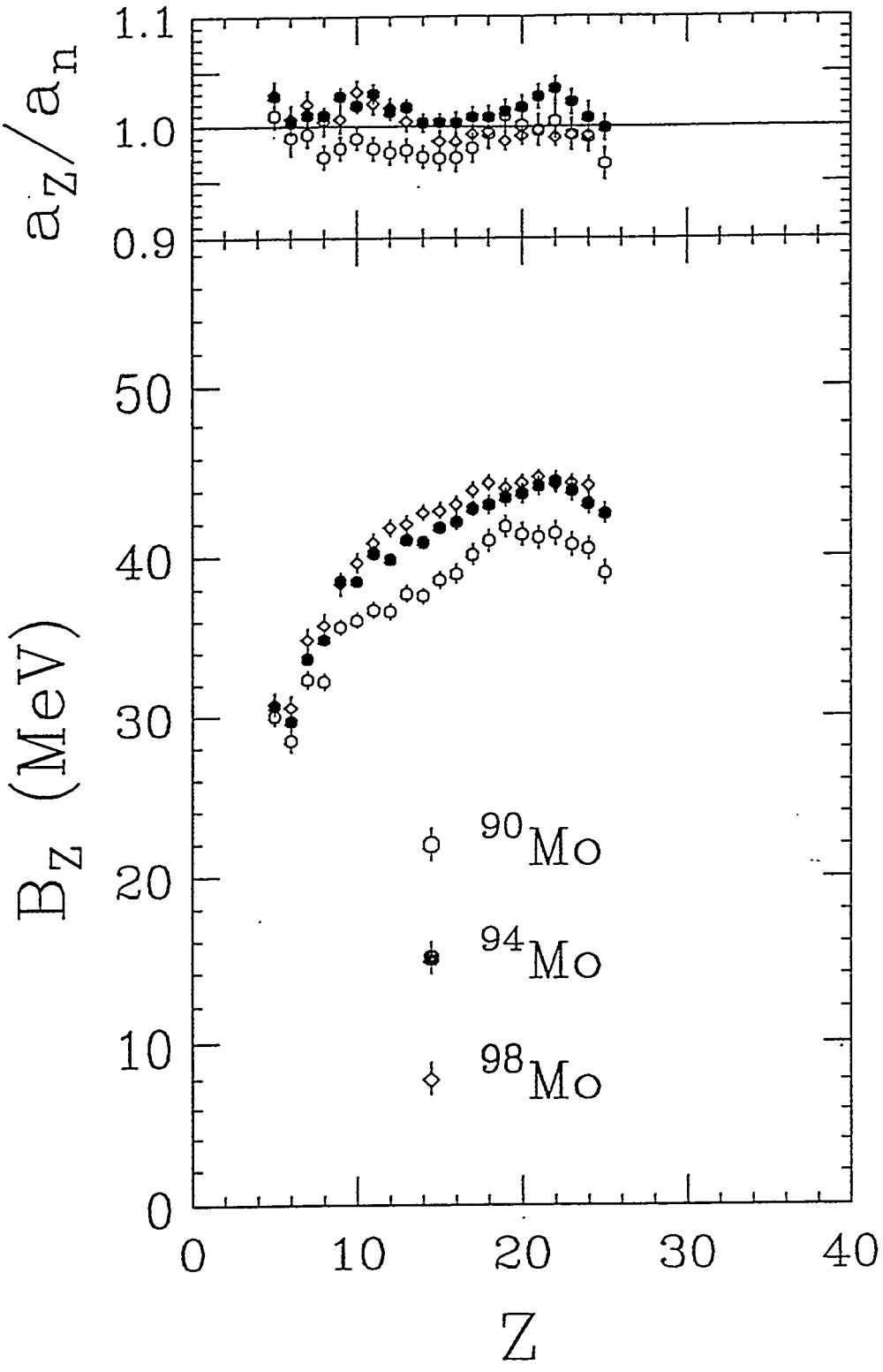

Figure 3.11: Extracted conditional fission barriers for fragments $5 < Z < 24$ from the compound nucleus ^{98}Mo; also plotted are the extracted barriers for ^{94}Mo and ^{90}Mo, for reference, and the value of a_Z/a_n for each barrier.

then fall off. This is the trend expected for ^{98}Mo, with fissility parameter $x \approx 0.359$, below the Businaro-Gallone point. The slight disagreement between the barriers for complementary Z values near symmetric fission can be understood as due mainly to the poorer atomic number identification for the heavier fragments.

Sierk, using the RFRM, has computed the conditional barriers for fragments from the excited compound nucleus ^{98}Mo. His method is to calculate the difference between the mass of the macroscopic sphere and the mass of the saddle point shape, not taking into account the ground state shell effects (see Figure 1.8). In the case of ^{90}Mo and ^{94}Mo, , the shell effects are small enough to be negligible (~ -0.1 MeV), so the experimentally measured barriers can be compared directly with the RFRM calculations. For ^{98}Mo, however, shell effects are $\sim +3.1$ MeV, and must be added to the measured barriers to make them comparable with the model calculations. In Figure 3.12, the shell-corrected experimental data are plotted along with the RFRM and RLDM predictions. The experimental barriers for ^{98}Mo are ~ 5.7 MeV higher, on average, than the predictions of the RFRM. The barrier data are substantially lower than the RLDM predictions, and the difference between the data and the RLDM is even larger than that between the data and the RFRM. The shape of the measured ridge lines are also slightly different from those of the RFRM and RLDM. These results suggest the need for refinements of both the RFRM and RLDM constants, and perhaps even modifications of the models themselves.

The RFRM calculations also predict the dependence of the conditional barriers for ^{98}Mo, along with the experimental barriers for ^{90,94}Mo [31], upon the n/p ratio of the compound nucleus. These experimental data give an even stronger isospin dependence than the model predicts. The isospin dependence is easily rationalized: *the more neutrons that an excited nucleus has, the easier it is for that nucleus to de-excite via neutron emission, leading to higher barriers, and consequently smaller cross sections for the emission of complex fragments.* The compound nucleus with the smallest number of neutrons, ^{90}Mo, has the lowest conditional barriers for complex fragment emission, because its neutron decay channel is narrower, by comparison, with the more neutron-rich isotopes of molybdenum. Conversely, ^{98}Mo, with more neutrons, has a wider neutron decay channel, and a more constricted channel for

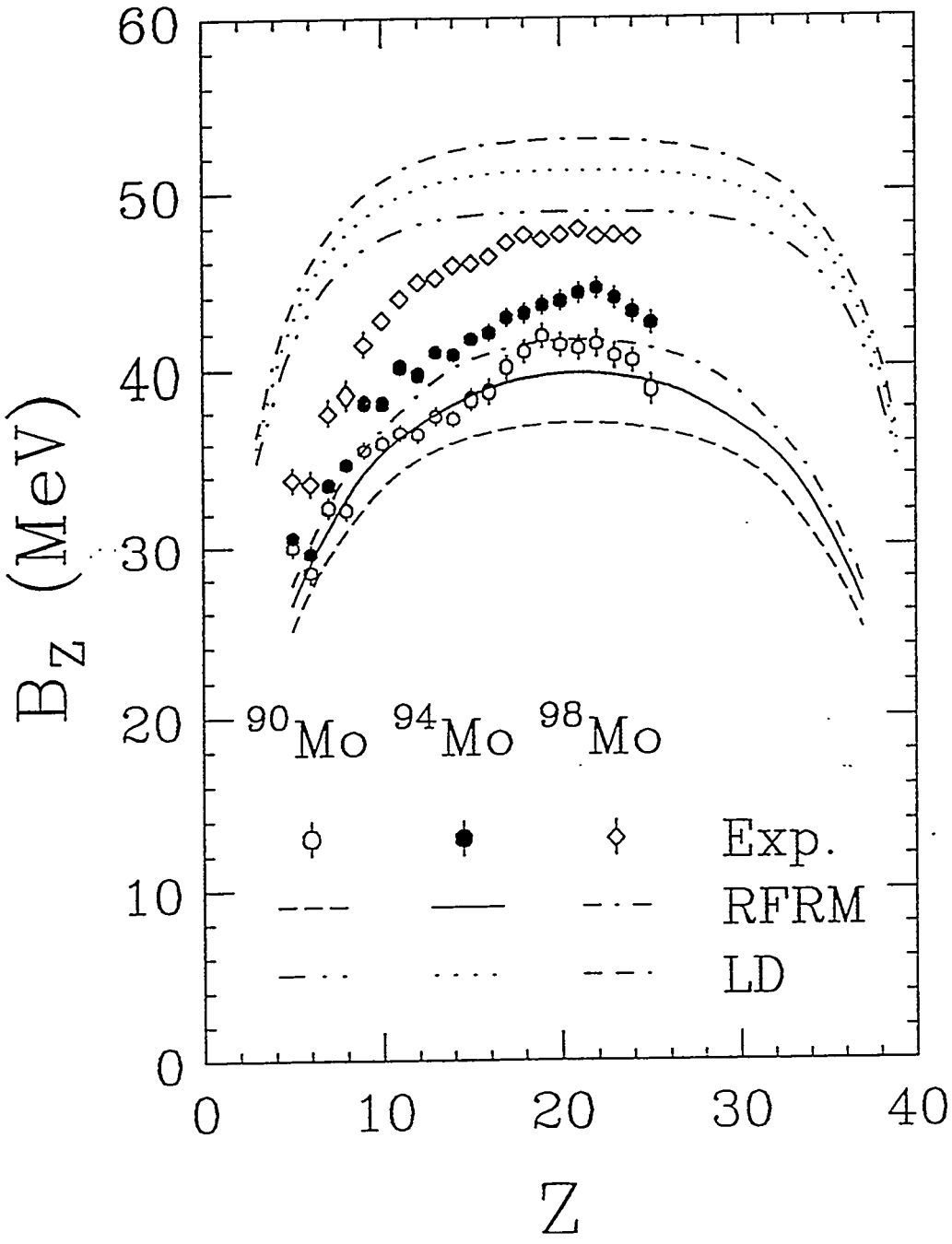

Figure 3.12: The shell-corrected experimental mass asymmetric fission barriers for ^{90}Mo, ^{94}Mo, and ^{98}Mo, along with the RFRM and RLDM predictions. The experimental barriers for ^{98}Mo are $\sim$ 5.7 MeV higher, on average.

complex fragment emission (higher barriers). These data should aid in improving the theoretical nuclear models which depend upon a n/p ratio term.

Table 3.3: The ℓ_{max} values predicted by the Bass model for $^{86}Kr + ^{12}C$, and the ℓ_{max} values used in the fit to minimize the χ^2. Values are given for each energy investigated.

E_{beam} (MeV/A)	ℓ_{max} ($\hbar$) (Bass)	ℓ_{max} ($\hbar$) (Fits)
12.94	49.7	51
11.98	49.7	50
11.06	49.7	49
10.17	49.4	48
9.31	47.2	47
8.49	44.9	45
7.71	42.7	43

Table 3.4: The experimental mass asymmetric barrier heights (B_Z) and a_Z/a_n for each fragment from the decay of the compound nucleus ^{98}Mo.

Z	B_Z (MeV)	a_Z/a_n
5	30.80±0.70	1.029±0.012
6	30.60±0.71	1.007±0.012
7	34.85±0.72	1.020±0.013
8	35.77±0.71	1.004±0.012
9	38.34±0.71	1.007±0.013
10	39.66±0.57	1.032±0.010
11	40.83±0.55	1.021±0.009
12	41.76±0.52	1.017±0.009
13	42.00±0.53	1.004±0.009
14	42.71±0.46	1.003±0.008
15	42.82±0.48	0.987±0.008
16	43.21±0.47	0.986±0.008
17	44.02±0.47	0.994±0.008
18	44.46±0.45	0.996±0.008
19	44.18±0.49	0.987±0.008
20	44.46±0.47	0.992±0.008
21	44.80±0.44	0.997±0.008
22	44.35±0.47	0.991±0.008
23	44.45±0.48	0.992±0.008
24	44.32±0.48	0.992±0.008

3.6 Conclusions

Excitation functions have been measured for complex fragment emission from the compound nucleus ^{98}Mo, produced by the reaction of ^{86}Kr with ^{12}C. Mass asymmetric fission barriers have been obtained by fitting the excitation functions with a transition state formalism. The extracted barriers are $\sim$ 5.7 MeV higher, on average, than the calculations of the Rotating Finite Range Model (RFRM). These data clearly show an isospin dependence of the conditional barriers when compared with the extracted barriers from ^{90}Mo and ^{94}Mo [31].

The results of this measurement are consistent with previous measurements for ^{75}Br, $^{110-112}$In, and ^{149}Tb. These results indicate that the RFRM systematically underestimates the mass asymmetric fission barriers for nuclei in the mass region A=75–146.

Part II

Synthesis and Characterization of Actinide-Specific Chelating Agents

Chapter 4

Introduction

4.1 Radioactivity in the Environment

In this one-hundredth anniversary year of the discovery of radioactivity by Henri Becquerel in Paris, it is quite interesting to review the historical course of the public perception of radioactivity. In 1896, immediately after Becquerel's discovery of radioactive emissions from uranium ore (see page 2), scientists were very excited about the new prospective fields of nuclear chemistry and nuclear physics. Countless scientific articles were written concerning the subject of radioactivity, and many general-interest articles were written in newspapers and periodicals for public consumption and stimulation. But even as early as the turn of the century, just a few years after Becquerel's discovery, journalists began to use the subject of radioactivity as tool to instill fear in their readers. In the *St Louis Post-Dispatch* of October 4, 1903, an article speculated on the inconceivable new power that was contained in radioactive nuclei (especially radium, which was one of the more publicly popular radioactive nuclei), and discussed the possible use of radioactivity in war, and how it could be used as a means to destroy the world [68]. Articles of this type probably did little but entertain the public, until 1945, when these fears were realized in the actual destruction of much of a city — Hiroshima, Japan — by atomic bombs that used nuclear fission to generate its amazing energy output, and produced a large amount of radioactivity in the process. Ever since this use of radioactivity for destructive

purposes, the public opinion of radioactivity has been one of fear and skepticism.

The public attitude toward radioactivity has only worsened in the last three decades, and pessimism is not limited to the destructive uses of radioactivity. The use of radioactivity for the generation of electricity has fallen out of favor with the public in most of the world, because of accidents at nuclear power plants, the most serious being in Chernobyl, Ukraine. Ever since the April 26, 1986, accident at the fourth reactor at Chernobyl, public opinion concerning the peaceful use of radioactivity for nuclear power has dwindled to tolerance, at best. Even the use of radioactivity for medical purposes has suffered in the public eye, e.g., the renaming of Nuclear Magnetic Resonance (NMR), as it applies to medicine, to Magnetic Resonance Imaging (MRI), in order to completely avoid the word "nuclear". The popular press has seized upon the public fear of radioactivity with a vengeance, and has capitalized on it with article titles such as:

- "The 'glow-in-the-dark' farmer's tale" [69]
- "At an old atomic waste site, the only sure thing is peril" [70]
- "Nuclear hazard festers years after alarm (nuclear waste remains a time bomb at Hanford site)" [71]
- "4 decades of bungling at bomb plant" [72]
- "Facing a nightmare of poisoned earth" [73]
- "Generations of poison and lies" [74]

In the last few years, the public's fear of radioactivity has centered around two main issues: terrorism and nuclear waste disposal. The popular press is still sensationalizing these issues in order to sell their publications and further their own political agenda, as the following quotation from the August 19, 1994, editorial entitled, "The New Threat That Must Unite the World", so aptly illustrates [75]:

> "A highly radioactive element that did not so much as exist before nuclear technology first produced it in the 1940s, plutonium is one of the

> most toxic substances known to science. One ten-thousandth of a gram, inhaled, can cause cancer. A few ounces in an urban water reservoir could cause hundreds of thousands of deaths. And plutonium-239, an isotope of the element, is a key ingredient in nuclear bombs. "

This quotation is filled with *four* blatantly incorrect statements about the nature of radioactivity and its possible use to instill terror in society. A few articles have been written by scientists to approach these problems in a level-headed manner [76, 77], but it will take a much greater effort to educate the public on these issues. To be sure, nuclear terrorism and nuclear waste disposal are extremely important issues that will face society for years to come. But unless so-called "alternative" energy sources are greatly improved, large-scale nuclear power will become a necessity within the next century as the reserves of fossil fuels become scarce. The education of the public concerning radioactivity and its inherent benefits when used in a safe, responsible manner, is absolutely crucial.

There are significant numbers of countries around the world that rely on nuclear power to satisfy a portion of their energy requirements. France generates about 70% of its electrical power with nuclear reactors, and supports a very advanced scientific program to study radioactive waste management. The French program reprocesses much of the radioactive waste that it generates, and is constantly designing and developing more efficient reactors that generate less radioactive waste. Japan produces approximately 30% of its electricity with nuclear reactors, and the Japanese government has sponsored a national advertising campaign to inform its citizenry about the safe generation of nuclear power. The Former Soviet Union (FSU) relies heavily on the nuclear generation of electricity, but they have often used much less sophisticated approaches to dealing with the waste. Very recently [78], the FSU has been internationally criticized for their past practice of burying uncontained radioactive waste. Unfortunately, this method of waste disposal has been utilized by many countries, including the United States, although not to such an extent as seen in the FSU.

In the United States, there are many sites around the country with radioactive waste. All of the large sites are managed by the government, through the

Department of Energy (DOE), and are mostly the result of the building and maintenance of the nuclear weapons program that began in the 1940s. The biggest sites with defense-related waste, and the amount of waste they store, are [79]:

- Hanford Site: 254,000 m^3
- Savannah River Site: 132,000 m^3
- Idaho National Engineering Laboratory: 12,000 m^3
- Oak Ridge National Laboratory: 1,230 m^3

Additionally, there is a large amount of civilian nuclear waste, primarily from the nuclear power industry, that the DOE will assume ownership of at the end of this century. All of this radioactive nuclear waste will need to be remediated and disposed of in some fashion, and this issue is receiving a lion's share of attention by the DOE. A description of two of these sites, the Hanford Site and the Oak Ridge National Laboratory Site, is given below, because application of the waste remediation technology discussed in this study is likely to occur on low concentration actinide solutions found at these two sites.

4.1.1 Hanford Engineering Works

In the early 1940s, when the Second World War was being waged around the globe, much United States governmental attention and resource was being focused on the development of a new weapon based upon nuclear fission. The Manhattan Project, as the atomic bomb program was known, involved hundreds of thousands of scientists, engineers, and others in the construction of a weapon to help win, or in any case, to prevent the loss, of the war.

The Hanford Engineering Works (HEW) was established in 1943 by the United States Department of Energy (DOE) for the purpose of generating a supply of weapons-grade plutonium for use in the nascent national nuclear arsenal. The project was very successful, for within two years enough high-purity plutonium had been generated to manufacture the nuclear bomb known as "The Fat Man". This device was detonated over Nagasaki, Japan, on August 9, 1945, and along with the uranium fission-based nuclear bomb used on Hiroshima ("The Little Boy"), it was largely responsible for the end of World War II. Hanford continued to produce plutonium after 1945 for national defense during the Cold War, but in 1990, with the peaceful end of the Cold War, the country had no further need for large quantities of plutonium. The unfortunate legacy that Hanford leaves as a result of its successes is an almost unimaginable amount of unremediated waste [80, 81]:

- a total of 1,377 waste sites spread throughout the reservation
- more than 1 billion metric tons of contaminated soil and groundwater
- underground plumes of hazardous materials such as carbon tetrachloride
- 15 metric tons of cesium and strontium capsules
- 61 million gallons of mixed waste (hazardous and radioactive) contained in 177 underground tanks
- approximately 150 million Ci of total radioactivity

The Hanford reservation contains one-third of all of DOE's waste sites, one-half of DOE's transuranic waste, and two-thirds of DOE's high-level waste. These numbers are staggering, but even more remarkable is that the U.S. Government is under binding agreements with the state of Washington to have the waste remediated by the year 2020 [80].

The Hanford Tank Farm (HTF) is called a "farm" because of the large number of underground tanks lined into rows on the very large site. The tanks were first built in the late 1940s, and were intended to provide permanent storage for the waste generated at the site. Of the 177 tanks, 149 tanks are of a single-shell design — they provide only primary containment for the waste with a single outer wall constructed of carbon steel backed with thick concrete. The tanks are 75 feet in diameter, and have a capacity of about one million gallons. Approximately one-half of the single-shell tanks are presumed to have leaked, a conclusion based upon a decrease in the monitored level of waste in the tanks. Because of the leaks, a second generation of tanks has been built at the site. Beginning in the 1970s, double-shell tanks were constructed to hold waste transferred from the single-shell tanks that leaked the worst. The double-shell tanks provide secondary containment of the waste in the event of a leak, by surrounding the entire inner shell (composed of carbon steel backed by concrete) with an air space and an outer shell of the same construction.

The composition of the waste in the tanks is very poorly known because there was no accurate record-keeping of what was placed in the tanks in the early years of the site. To describe the 177 tanks in a very general way, all of them appear to have stratified into three or four main layers [81]:

sludge The bottom-most layer in each of the tanks, it has been described as "having the consistency of peanut-butter" [80]. This layer is composed mostly of metals and their hydroxides.

supernatant The largest volume of the waste, this layer is an aqueous solution saturated with nitrate; it also contains carbonate, phosphate, and sulfate.

salt cake Most of the tanks have a thick, crusty solid above the supernatant that is

composed of solid salts that have dried from the saturated supernatant below it.

organic A few of the tanks have an organic layer. This layer is the result of incomplete separation during liquid/liquid extraction.

This is a very general picture; each of the tanks has its own individual composition which is very difficult to ascertain. Overall, the inventory of major components in the tanks is estimated to be [81]:

- 840,000 kg uranium (5500 kg ^{235}U)
- 240 kg plutonium
- 13,000 kg thorium
- EDTA, HEDTA, citric acid
- Fe(III)
- PO_4^{3-}, CO_3^{2-}, SO_4^{2-}

To understand why and how this waste was generated at Hanford, one needs to look a little more closely at the separations processes used at Hanford to manufacture weapons-grade plutonium. Plutonium, element number 94, was first synthesized in the laboratory in 1941 by Dr Glenn T. Seaborg and coworkers at the University of California, Berkeley. The half-life of its longest-lived isotope, ^{244}Pu, is 8.0×10^7years (for the half-lives and energies of all the radioactive isotopes mentioned in this chapter, see Table 4.1 [82]); this half-life is about fifty times shorter than the age of the earth, so the plutonium that existed on earth immediately after its creation has decayed away to a minuscule amount, and any large quantities of plutonium existent on earth today are man-made (with the exception of plutonium that was found in the natural nuclear reactor at Oklo, Gabon, West Africa [2]). The first plutonium isotope made in the laboratory was ^{239}Pu, which is created from the decay of ^{239}Np (see the reaction below); however, the half-life of this isotope of plutonium was too long

Table 4.1: Half-lives and energies for the radioactive isotopes discussed in this chapter.

Isotope	Type of Decay †	Half-life ($t_{1/2}$	Energy (MeV) †
^{233}U	α	1.59×10^{5}y	4.824
^{235}U	α	7.04×10^{8}y	4.400
^{238}U	α	4.47×10^{9}y	4.197
^{239}U	$\beta-$	23.5 m	1.21
^{239}Np	$\beta-$	2.35 d	0.438
^{238}Pu	α	87.7 y	5.4992
^{239}Pu	α	2.41×10^{4}y	5.156
^{240}Pu	α	6.56×10^{3}y	5.1683
^{241}Pu	$\beta-$	14.4 y	0.0208
^{242}Pu	α	3.75×10^{5}y	5.4901
^{241}Am	α	432.7 y	5.4857

† — Only primary decay type is listed, with primary energy.

to accurately measure [83]. ^{238}Pu, with a much shorter half-life (estimated as $\sim$ 50 years in 1940), was the first to be discovered in the laboratory, and it was instantly recognized as a very important element because of its fissile properties [84, 85]. It is more fissile than ^{235}U and its synthesis and purification are, in many ways, easier than those for ^{235}U [86]. For this reason, when the United States began its nuclear weapons program during World War II, plutonium was on its short-list of important ingredients.

Plutonium was generated at Hanford using what are known as the "pile reactions" [87]:

$$^{235}\mathrm{U} + \mathrm{n} \longrightarrow \text{fission products} + 2.5\mathrm{n} + \sim 200\ \mathrm{MeV}$$

$$^{238}\mathrm{U} + \mathrm{n} \longrightarrow {}^{239}\mathrm{U}\ (\beta\text{-}, 23.5\ \mathrm{min}) \longrightarrow {}^{239}\mathrm{Np}\ (\beta\text{-}, 2.35\ \mathrm{days}) \longrightarrow {}^{239}\mathrm{Pu}$$

These are called "pile reactions" because they are nuclear reactions that were first used in a reactor made of stacked graphite blocks, called a "pile", built by Enrico Fermi and his coworkers at the University of Chicago in 1942 [88]. Neutrons from the spontaneous fission of ^{235}U are used to transmute ^{238}U into ^{239}U (this is actually

a nuclear process, not "almost magic", as conjured by a journalist for *The New York Times*), which beta-decays with a half-life of 23.5 min to ^{239}Np; ^{239}Np beta-decays with a half-life of 2.35 days to ^{239}Pu. This isotope of plutonium is long-lived. After a sufficient amount of time in the reactor, the irradiated uranium fuel rods are removed and processed to extract the plutonium from the uranium and fission products.

There are many ways to separate plutonium from uranium, and the separation is made possible because of the myriad oxidation states that both elements allow. In solution, plutonium has oxidation states from +2 to +7, and uranium from +2 to +6. When certain oxidizing or reducing conditions are applied to a solution of the two elements, each can attain a different oxidation state, and in different states plutonium can be separated from uranium using liquid/liquid extraction or ion-exchange techniques. In the early years of the Hanford project, many separations processes were used that were less efficient and more waste-producing than current methods. The bismuth phosphate ($BiPO_4$) coprecipitation method [87] was used from 1944 to 1956, and was the main culprit responsible for the bulk of waste produced and stored in the tanks. This separation method did not recycle any of the uranium in the waste, and was the greatest contributor to the huge amounts of uranium in the tanks. In 1952, a new method, called REDOX (**RED**uction-**OX**idation) [87], was introduced, which relied upon methyl isobutyl ketone (MIBK) to extract plutonium, and significantly reduced the amount of waste generated. Then in 1956, REDOX was replaced by a new process, called PUREX (**P**lutonium **U**ranium **R**eduction **EX**traction) [87], that was used from 1956 until 1990, when the separations processes were halted. The ratio of waste generated by these three processes was 35:10:1 ($BiPO_4$:REDOX:PUREX). At many stages in these complex processes, different chemicals were used: EDTA, sodium bismuthate, sodium dichromate, hydrofluoric acid, carbonate, citrate, nitrate, nitrite, formate, acetate, oxalate, ferricyanide; the list is lengthy.

4.1.2 Oak Ridge National Laboratory

Another very important facet of the Manhattan Project was to perfect a way to separate massive quantities of ^{235}U from its more stable isotope, ^{238}U (^{235}U is fissile material that can be used in the design of a fission bomb). This "uranium enrichment" part of the overall project was intended to compete with another part of the Manhattan Project, the "plutonium separation" part (see Section 4.1.1). The organizers of the Manhattan Project were not sure which isotope could be separated and purified in the shortest amount of time; when the race was over, however, it was a virtual tie. Of the two bombs dropped on Japan in 1945, one was a uranium bomb and the other was a plutonium bomb. (Another instance of the Manhattan Project leaders hedging their bets — they were not certain whether either bomb would work, scientifically or technically; hence one of each.)

In February 1943, the Manhattan Project bought 54,000 acres of land just outside of Knoxville, Tennessee, in the small town of Clinton [89]. The majority of work on the "uranium enrichment" side of the project was conducted at this location, then called the Clinton Engineer Works, now known as the Oak Ridge National Laboratory (ORNL). This part of the project involved an incredible number of workers and scientists, and significant costs as well — by the end of WWII, the Clinton Engineer Works had cost the United States 544 million dollars. (These costs amount to $\sim$ 5.48 billion 1996 dollars, which pales in comparison with the 30 billion dollars estimated for remediaion; these costs did have a significant result, though, providing the enriched ^{235}U for the first fission bomb, the "Little Boy", dropped on Hiroshima, Japan, on August 6, 1945.) At the Clinton Engineer Works, there were two promising technologies being investigated to effect the enrichment of uranium: electromagnetic separation and gaseous diffusion.

The first process, electromagnetic separation, was the brainchild of Ernest O. Lawrence, who proposed that his invention, the cyclotron, could be used as a gigantic mass separator to separate two isotopes of sufficiently different masses. He had done some preliminary investigations into the process at the University of California's Radiation Laboratory, and was convinced that it could be scaled into a large process

to separate enough enriched ^{235}U for the construction of an atomic bomb. There were many scientists who did not share Lawrence's optimism, however. Dr George T. Felbeck, a scientist who was working on the competing technology, gaseous diffusion, said of electromagnetic separation, "...it is like trying to find needles in a haystack while wearing boxing gloves" [89]. Electromagnetic separation uses the large size of a cyclotron to separate ^{235}U from ^{238}U by means of the "cyclotron equation", which mathematically shows that the radii of two ions of different masses will describe different paths when accelerated in a very large magnetic field. Lawrence called the big cyclotrons, "CalUtrons", since they were developed at laboratories at the University of California, Berkeley.

The first pilot plants using the electromagnetic separation technique were constructed at the Clinton Engineer Works in September 1942 [90]. It was soon discovered that the process is very inefficient and wasteful, separating only about 10% of the uranium feedstock and spraying the rest on the walls of the "racetrack", as the large calutrons were nicknamed. Since wartime uranium was in short supply, workers had to separate the magnets in the calutrons and remove and recycle the unseparated uranium every few hours. To improve efficiency, two types of calutrons were built:

α-calutrons Primary stage, could enrich ^{235}U to 10–15%.

β-calutrons Secondary stage, could enrich ^{235}U up to 90%.

Uranium was injected into the calutrons as uranium tetrachloride, UCl_4, then vaporized and dissociated to elemental uranium. Ionization was accomplished by electron bombardment, and then the ions were cycled around the calutron a number of times until the two isotopes were sufficiently separated in space to collect them in different copper pockets within the machine. After the pilot plant proved the process feasible, five calutrons were constructed, beginning in February 1943. They were operating by August 1943, but because of various difficulties (mostly magnet problems), they were not producing separated uranium until November 1944. Once in full operation, however, the calutrons could separate 100g of 90% ^{235}U per day.

The controls for the calutrons were operated by a staff of about 13,000 women from the local area, all trained to control a very small piece of the mammoth calutrons (i.e., a magnet or a valve); the uranium recovery and recycling teams were 10,000 men strong.

The second process used to enrich ^{235}U at the Clinton Engineer Works was called gaseous diffusion [90]. The gaseous diffusion plant proved to be the most reliable source of enriched uranium at the lowest cost, and was operated until very recently. The idea behind the process was not thought of until early 1942, so it lagged behind the electromagnetic separation process. The gaseous diffusion process utilized the mass dependence of diffusion of a gas through a permeable membrane. The gas used was uranium hexafluoride, UF_6 (a corrosive gas that gave the process development team much trouble), and the diffusion barriers were made of powdered nickel. Since each individual barrier only provided about 0.4% enrichment of the uranium gas, nearly 4000 barrier stages were required to enrich to 90%. In January 1945, three years after the technology was only an idea, it took 20,000 construction workers to assemble the half-mile long process plant from its individual components. By May 1946, approximately nine months after the war was over, the plant was producing 1kg of 90% enriched ^{235}U per day, and was designated as the sole supplier of enriched uranium for the country's defense effort.

The result of all this toil and expense to enrich ^{235}U was the first fission bomb ever used in wartime – the bomb nicknamed "Little Boy" that was dropped on Hiroshima on 6 August 1945. Another result was the accumulation of several tankfuls of waste solution. The tanks are called "gunite" tanks, and after exhaustive research, the meaning of the term "gunite" has been found [91]:

(1) a mixture of portland cement, sand, and water, applied by pneumatic pressure through a specially adapted hose, and used as a fireproofing agent and as a sealing agent to prevent weathering of mine timbers and roadways; synonymous with shotcrete

(2) a phrase of courteous parting to be used during nocturnal hours

I knew the second definition, but had never heard of the first.

The gunite tanks at Oak Ridge National Laboratory contain liquid waste resulting from the uranium enrichment work that began at the laboratory during the war. This work continued until the late 1980s, but the enrichment process was improved over the years of its operation so as to minimize the amount of waste generated. There are twelve tanks of varying size, the smallest having diameters of eight feet, and the largest having diameters of fifty feet and volumes of 150,000 gallons. The waste level in each of the tanks varies as well, from one foot to ten feet. Overall, the tanks contain 466,000 gallons of supernatant and sludge, with approximately 10% sludge by volume. The sludge in most of the tanks, which is composed of hydrolysis products and other particulates, is fairly soft, while in a few tanks it is hard, and in a single tank is completely absent. The liquid supernatant in most of the tanks is pale yellow, but two of the tanks have bright yellow supernatant, perhaps indicating the presence of a uranyl species in solution in these tanks. The temperature in all the tanks is a relatively constant 18–20°C. A comprehensive report of all the tanks was completed by the laboratory at the end of 1994 [92]. The report indicates the presence of low levels of plutonium, primarily in the sludge (due to the high pH), which is why this waste stream might prove ideal for the extractant ligands discussed in this study.

4.2 Actinide-Specific Chelating Agents

Ken Raymond and his research group at the University of California, Berkeley, entered the field of actinide chelation in the late 1960s, studying organometallic complexes of the lanthanides and actinides. Actinide chelation research, principally *in-vivo* chelation, grew naturally as an extension of the group's iron sequestration research, because Fe(III) shares many similar chemical properties with the actinide(IV) elements, especially Pu(IV) [93]. Both Fe(III) and Pu(IV) are "hard" Lewis acid metal cations, carrying a large amount of charge and having a relatively small ionic radius (see Figure 4.1). They also both behave similarly in water, displaying large

$$\text{Fe(III): } \frac{charge}{radius} = \frac{3}{0.65} = 4.6$$

$$\text{Pu(IV): } \frac{charge}{radius} = \frac{4}{0.96} = 4.2$$

$$Fe^{3+} + 3OH^- \longrightarrow Fe(OH)_3;\ K = 10^{38}$$

$$Pu^{4+} + 4OH^- \longrightarrow Pu(OH)_4;\ K = 10^{55}$$

Figure 4.1: A comparison of Fe(III) and Pu(IV), showing the many similar characteristics that the two metals share. For the charge-to-radius comparison, charge is in atomic units (Z) and radius is in angstrom (Å).

hydrolysis equilibrium constants. They are both readily bound by basic ligands that can provide negative charge, such as oxo-donors; however, because of its larger size and charge, Pu(IV) is eight-coordinate instead of six-coordinate, like Fe(III). Additionally, in the blood plasma of mammals, Pu(IV) is transported as a complex of transferrin, and binds at the same site that normally binds Fe(III).

Much of the early research in the Raymond group that preceded actinide-specific chelation research involved the study of a class of naturally occurring biomolecules called siderophores. Siderophores [from the Greek *sideros* (iron) + *pherein* (to bear)] are produced in nature by microorganisms to sequester iron from the environment, in order to promote growth. Siderophores function with an incredible

degree of efficiency and selectivity, and bind Fe(III) more strongly than any other class of iron chelators. It is because of the strong Lewis-acidic nature of Fe(III) that the hexadentate siderophores, with their very Lewis-basic oxo-chelating groups, are able to bind so strongly and selectively to Fe(III). Figure 4.2 shows the structures of two siderophores, enterobactin and desferrioxamine B (DFO), which have large formation constants (K_f) with Fe(III). The siderophore enterobactin is produced by

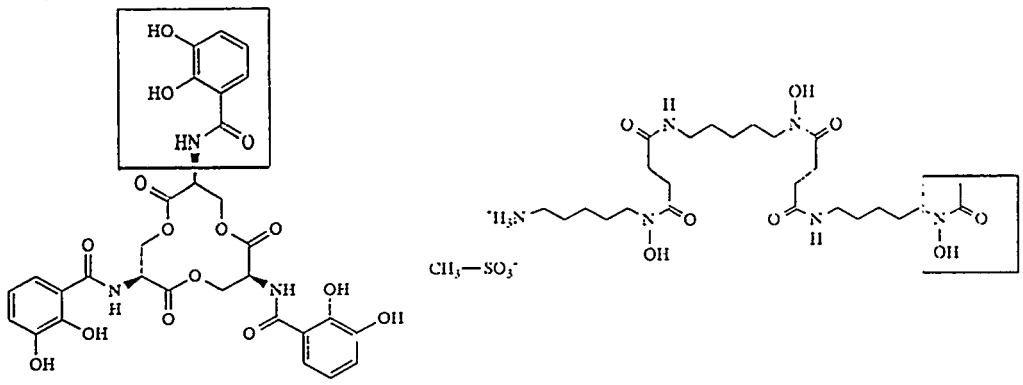

Enterobactin
$\log K_f = 49.0$

Desferrioxamine B (Desferal^R)
$\log K_f = 30.6$

Figure 4.2: Two siderophores, enterobactin and desferrioxamine B (DFO), and their formation constants (K_f) with Fe(III).

enteric bacteria such as *Escherichia coli*, for the purpose of solubilizing and transporting Fe(III). It has three catecholamide groups attached to a central trilactone ring of *L*-serine, and metal coordination occurs through the three bidentate catechol moieties. Its formation constant with Fe(III) is $\sim 10^{49}$, which is notable as the most stable complex of Fe(III) known. DFO, with an Fe(III) formation constant of $\sim 10^{31}$, is a drug used for the treatment of iron overload, and is known by the trade name Desferal. DFO achieves its metal coordination through three bidentate hydroxamate groups [94].

In the design of actinide chelators, and chelators of Pu(IV) in particular, the research goal has been to follow the biomimetic approach — that is, to design chelators like those found in nature. Choosing the right chelating groups is perhaps

the most important aspect of ligand design. The correct choice will give a ligand not only strength to bind a metal ion, but also specificity to bind one metal ion preferentially over another. Over the years of research that have been conducted in this group, a folktale has arisen to describe the way in which the group arrived at the best possible actinide chelating groups — the folktale is the chemical corollary to "Goldilocks and the Three Bears" [95]:

> ONCE UPON A TIME, there was a graduate student who roamed the halls of Latimer Hall, and he decided to join the Raymond group. As his research project, he was told to design the best actinide chelator. He knew it had to be an octadentate molecule, but what were the best chelating groups to put on this molecule? He went into laboratory #511, and spent a year synthesizing a ligand that had four catechol binding groups. He knew that enterobactin, a siderophore, was the strongest Fe(III) complexer known; he thought a tetracatechol ligand would be the best chelator for Pu(IV). But when he measured the stability constant of his new ligand with Pu(IV), he found that catechol is too basic a ligand for Pu(IV)...

Goldilocks found the porridge in the big bowl *too hot*...

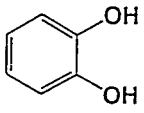

catechol

$pK_a = 13.0$

Then the graduate student went into laboratory #542, and spent a year synthesizing a ligand that had four pyrazine dione binding groups; he thought, "If catechol is too basic, then I'll just choose a more acidic

chelator." But he found that the pyrazine dione ligand was too acidic...

...and she found the medium-size chair was *too soft*...

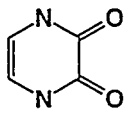

pyrazine dione

$pK_a = 1.6$

Then the graduate student went into laboratory #502 (he was feeling very smart now, because he had just passed his prelims!), and spent a year synthesizing a ligand that had four hydroxypyridinone (HOPO) chelating groups. When he went to measure the stability constant of this ligand with Pu(IV), he found that this ligand was neither too basic, nor too acidic, but just right...

...but the small bed was *just right*!

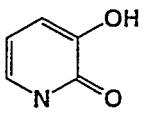

3-hydroxy-2-pyridinone

$pK_a = 8.7$

The story above outlines why HOPOs tend to be the best actinide chelators: they balance the need for a ligand that is basic enough to donate sufficient negative charge to a metal cation, with the need for a ligand that is acidic enough to deprotonate its binding group at a reasonable pH. Compared to catechol, a HOPO ligand not only has a lower pK_a, but also has one less dissociable proton. Additionally, the HOPO chelators used in this study have an added structural feature: the amide proton can hydrogen-bond to the ortho-hydroxyl oxygen on the HOPO ring. This gives the metal complex a degree of preorganization and structural rigidity that makes it more stable. For these reason, HOPOs have been used extensively by this group in the design of actinide chelators [96–99].

One example of the successful use of the HOPO chelating group is found in the design of an *in-vivo* actinide chelator, H(2,2)Me-3,2-HOPO (Figure 4.3). This

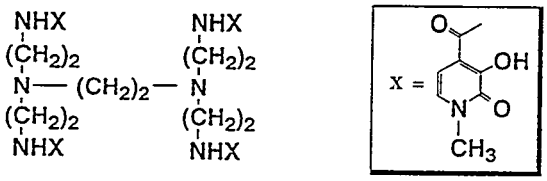

H(2,2)-Me-3,2-HOPO

Percentage plutonium removed:

	Injected Activity	Oral Activity
H(2,2)-Me-3,2-HOPO	82%	76%
DTPA	66%	14%

Figure 4.3: An *in-vivo* chelator, H(2,2)-Me-3,2-HOPO; the X in the molecular formula represents the position of attachment for the 3,2-HOPO moiety. Also listed are data concerning the efficacy of this ligand in removing Pu(IV) from mice.

ligand is based upon the siderophore model, as illustrated in Figure 4.2. It has a central backbone that arranges the chelating HOPO groups in space in such a way as to aid in metal coordination. In order to be effective at binding Pu(IV), though, the standard siderophore model has been modified to include a fourth bidentate chelating

group, in order to saturate the octadentate coordination sphere of Pu(IV). This ligand is much more effective than the current FDA-approved actinide decorporation drug, DTPA; note that its oral activity eclipses that of DTPA [100].

The focus of this study is not actinide decorporation agents, but instead actinide-specific chelating agents that are very effective at removing actinide(IV) metals (especially Pu(IV)) from the various nuclear wastes discussed above. The transition from *in-vivo* chelating agents to those that work well in solutions of nuclear waste is a difficult one. The requirements for a Pu(IV) *in-vivo* chelator include:

- It must work well at pH = 7.4, in a solution of constant ionic strength.
- It must be non-toxic.
- It must have a high affinity for Pu(IV), but a low affinity for Ca(II), Zn(II), Mg(II), etc.
- It must be a stronger chelator of Pu(IV) than transferrin.

For a Pu(IV) chelator that is meant to treat waste solutions like those at the Hanford Site or the Oak Ridge National Laboratory Site, the requirements are a little different:

- It must work well through a range of pHs, and in solutions of widely varying ionic strength (mostly high).
- It must be hydrolytically and radiolytically stable.
- It must have a higher affinity for Pu(IV) than for many other metals, especially Fe(III).
- It must be a stronger chelator than other chelators in the waste solution (*i.e.*, EDTA).
- It must be separable from the waste solution once it has coordinated Pu(IV).

To satisfy the last condition in the list above, this study examines the synthesis and characterization of liquid/liquid extractants based upon the HOPO chelating moiety. When dealing with liquid/liquid extraction, there are three additional criteria placed upon the extractant [101, 102]:

1. The extractant must form an uncharged, extractable complex *in the aqueous phase.*

2. The resulting complex must have a high distribution constant for extraction into the organic phase.

3. The extracted complex must interact well with the organic phase.

The liquid/liquid extractants discussed in this study have been designed with these elements from extraction theory in mind. The extractant needs to be organophilic, in order to extract into the organic phase, but it also needs to have some small solubility in the aqueous phase, so as to retrieve the metal. This is a very difficult balance to achieve; in this study, many extractants have been synthesized with different chelate groups and side chains in order to find the optimal arrangement needed for effective Pu(IV) extraction.

The Raymond group has synthesized and characterized a number of other types of actinide-specific chelating agents — more octadentate siderophore analogs [103], uranyl "cap" ligands [104], solid/liquid extractants [105], and the liquid/liquid extractants described here. The bidentate extractant ligands discussed in this study are synthesized from three different HOPO moieties: 3,4-HOPO, 3,2-HOPO, and 1,2-HOPO. All of the chelating groups are made organophilic by the synthetic attachment of a long alkane chain (from C_6 to C_{18}) or other organophilic side chain (such as phenylpropylamine) to the carboxyl functionality of each HOPO. Liquid/liquid extractants of the same design, but with catecholamide and terephthalamide chelate moieties, have also been studied in this group [104], but generally performed less well than the HOPO extractants because of their very basic nature and their double negative charge upon deprotonation.

4.3 Remediation

> The single most important challenge facing the nuclear field (commercial and defense) is what to do with the nuclear waste.
>
> National Research Council report, 1996 [79]

The quotation above is more a reflection of what the public perceives to be the biggest challenge facing the nuclear field, rather than the reality. The science required to accomplish the task of remediation is well-known; it is the politics of remediation that remain the most important challenge. The remediation plan that is currently envisioned by the DOE for all its waste is composed of two parts. First, to save the cost of long-term storage of large volumes of waste, the high level waste (HLW and transuranics (TRUs)) will be separated from the much larger volume of low level waste (LLW; short-lived radioactive species and hazardous chemicals). This will require some powerful and selective separation techniques, which are currently being developed (this study is one example). In the second step, the LLW will be disposed of using low-cost waste handling techniques, and the HLW will be prepared for long-term storage. The current baseline approach is to encapsulate the HLW in glass "logs" (log-shaped glass capsules encased by carbon steel; the HLW is incorporated into the glass matrix), and store the logs in a repository that is geologically stable.

Since the actinide waste at the sites mentioned above (Sections 4.1.1, 4.1.2) is predominantly in the sludge layer (because the pH of the waste has been raised), a pretreatment method is needed to redissolve the actinides into a treatable solution. Three types of pretreatment are currently under investigation [106]:

1. A simple washing of the sludges with dilute NaOH.
2. Caustic leaching and washing to remove certain sludge components.
3. Dissolving the sludges in acid and separating key radionuclides.

The differences between these three methods mainly concerns what degree of waste separation they achieve, and how much they cost. The method which is finally chosen

must strike a balance between the cost of pretreatment (separation) and the cost of long-term storage. In general, the least expensive pretreatment methods (*i.e.*, washing and leaching) result in the largest volume of HLW for long-term storage. Since long-term storage is so expensive, money can be saved by performing some separations to reduce the HLW volume; *but the savings must be greater than the cost to implement the separation technique.*

This study examines a new separation technology for Pu(IV), but there are many other technologies that currently exist for separating Pu(IV) and other transuranic metals (TRUs) from aqueous solutions. The most well-known and often used Pu(IV) separation technique is the PUREX process. PUREX [87] uses a $\sim 30\%$ solution of tributyl phosphate (TBP) in kerosene to extract uranium and plutonium from nitric acid solutions. It works well with high ionic strength aqueous phases, and typically achieves decontamination factors (D.F.; see page 149) between 10^3 and 10^4.

A second Pu(IV) separation technique, developed recently, is known as the TRUEX process [107]. It exists in two versions, each version using a slightly different organophosphorous compound to extract Pu(IV). One uses derivatives of the ligand carbamoylmethylphosphineoxide (CMPO) in a hydrocarbon solvent, and the second uses a phosphonate called CMP in a hydrocarbon solvent [79]. TRUEX effects very large Pu(IV) decontamination factors, but has one drawback — it is very difficult to strip the Pu(IV) away from the extractant, because of the strong nature of the bond. This process is still being investigated [106], and it holds promise for future waste remediation.

Yet another Pu(IV) separation technique worthy of mention is the DIAMEX process [108, 109]. DIAMEX was developed in France and has received considerable attention recently [79]; like the previous two processes mentioned, it extracts Pu(IV) from nitric acid with large decontamination factors, but instead of organophosphorous compounds, it uses amides such as dimethyldibutyltetradecylmethylamide (DMDBT-DMA) in hydrocarbon solvents to effect the separation. The big advantage of this process is that the organic phase can be incinerated completely, generating no hazardous waste, while the other two processes contain phosphorous, which is a difficult waste to handle after incineration.

There are many other separation schemes that are not based on liquid/liquid extraction methods which could be used to remediate Pu(IV) contaminated waste. Many are still in early stages of development. Just a few of the newer, more interesting techniques are:

Magnetically Assisted Chemical Separation (MACS) This technique uses polymer coated ferromagnetic particles with an adsorbed layer of CMPO and TBP to remove low levels of Pu(IV) from waste solutions. For separation, magnets are used to collect the ferromagnetic particles [110].

Photochemical Valence Adjusting (PVA) This technique uses the same chemicals as PUREX to complex Pu(IV), but uses a mercury lamp to adjust the oxidation state of the complexed metals and gain a separation [111].

Polymer-Immobilized Liquid Membrane (PILM) This technique uses a thin extractant-impregnated membrane between two aqueous phases to extract Pu(IV) from one aqueous phase in an uphill manner into the other aqueous phase [112].

Phyto-remediation This novel technique uses certain plants, such as Bermuda grass, corn, and Indian mustard, to extract large quantities of toxic metals from the ground and waste solutions [113].

The bad news about the current status of most of the remediation projects run by the DOE is that they are proceeding very slowly. First, there is still much confusion about what type of waste solution will be remediated, and this is the first, most basic question that must be answered in any remediation scheme. For this project, the waste could be acidic or alkaline, it could be at any degree of ionic strength, and could contain any number of competing metals or other extractants. Part of this problem is fundamental, in that some of the characteristics of the waste are not known because inadequate records have been kept and waste sampling has not been conducted. But another part of the problem is due to lack of action; there is nobody willing to make the hard decisions about how the waste remediation should

proceed. Second, most researchers cannot obtain samples of real waste to use in tests of different separation schemes. This makes accurate testing of the various separation schemes nearly impossible.

The good news about waste remediation in this country is that even though it is proceeding slowly, it is proceeding. Many small nuclear waste sites, like one in West Valley, NY, are moving ahead with their delayed waste encapsulation projects [114]. The newly-constructed vitrification plant at the Savannah River Site is currently encapsulating HLW from their storage tanks into glass "logs" [115]. And it is with these small beginnings that the difficult task of remediation, after five decades of nuclear waste neglect, is beginning.

Chapter 5

Experimental

5.1 Synthesis

All chemicals were used as obtained without further purification, unless otherwise noted. 2-methyl-3-benzyloxy-4-pyridinone-N-methylcarboxylic acid (the starting 3,4-HOPO chelating moiety) was synthesized by Dr Linda Uhlir [116]; N-methyl-3-benzyloxy-2-pyridinone-4-carboxylic acid (the starting 3,2-HOPO chelating moiety) was provided by Dr Xu Jide [117, 100]. Proton (^{1}H) NMR spectra were measured with a Bruker 300 MHz superconducting FT spectrometer in the UCB NMR Laboratory; carbon (^{13}C) NMR spectra were measured with a Bruker 400 MHz superconducting FT spectrometer in the UCB NMR Laboratory. Elemental analyses were determined by the Microanalytical Laboratory at the University of California, Berkeley, College of Chemistry.

Figure 5.1 shows the chemical structures of some of the reagents used in these syntheses. All of the referenced NMR spectra from this section are contained in Appendix A.

5.1.1 Ligand Synthesis: 3,4-HOPOs

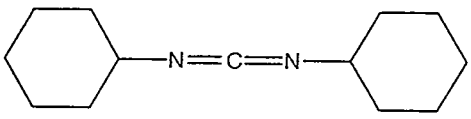

dicyclohexylcarbodiimide (DCC)

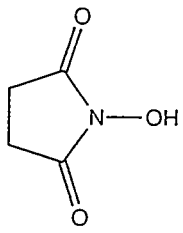

N-hydroxysuccinimide (NHS)

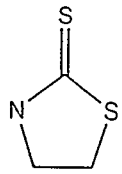

2-mercaptothiazolide

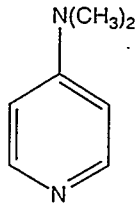

4-dimethylaminopyridine (DMAP)

Figure 5.1: Chemical structures of some of the reagents used in these syntheses.

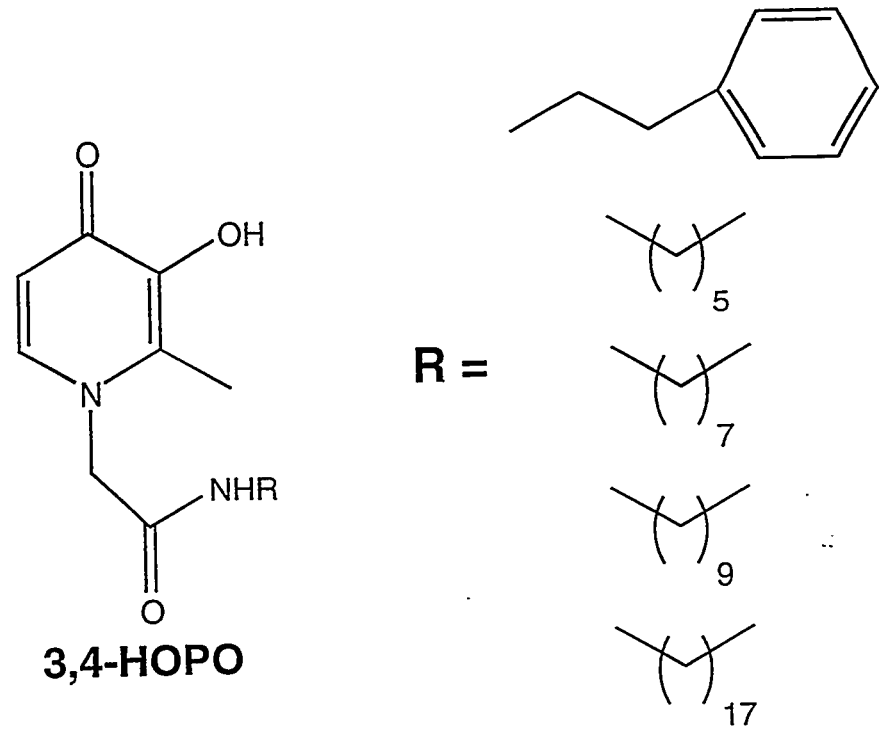

Figure 5.2: The 3,4-HOPO chelating moiety, and the side chains used to render it organophilic.

2-methyl-3-benzyloxy-4-pyridinone-N-methyl- N′-phenylpropylcarboxamide
(1d) (Figure 5.3).

2-methyl-3-benzyloxy-4-pyridinone-N-methylcarboxylic acid [116] (1a) (1.20 g, 4.63mmol) was dried in a vacuum oven at 70°C overnight, because the first step of this synthesis, the formation of the "activated ester", is very moisture sensitive. Additionally, all of the glassware used in the first synthetic step was dried in an oven, and the reaction was performed under dry nitrogen. Dry pyridine (20ml) was added to compound 1a in a dry 50ml single-neck round-bottom flask, and dissolved by stirring and heating the solution with a mantle until all of the solid was in solution. The solution was slowly cooled to room temperature, and some of compound 1a came back out of solution. Both N-hydroxysuccinimide (NHS) (0.58g, 5.00mmol) and dicyclohexylcarbodiimide (DCC) (1.03g, 5.00mmol) were added, and the solution was stirred for 4h at room temperature. The reaction was followed by silica TLC, but the results were often inconsistent; by experience, 4h is typically enough time for the formation of the activated ester (1b).

Phenyl-1-propylamine (1c) (0.71 ml, 5.00 mmol) was added, dropwise, directly to the stirring solution of the activated ester. The solution was stirred overnight, and silica TLC revealed a primary product spot plus 3–4 sideproducts. The solution was filtered over a M-grade glass frit to remove dicyclohexylurea (DCU) solids from the solution. The pyridine was evaporated using a rotary evaporator, and a thick, dark orange oil remained. The oil was dissolved in methylene chloride (20ml), and impurities were extracted with two basic extractions (1M KOH, saturated with NaCl) followed by one acidic extraction (1M HCl). The methylene chloride was evaporated to leave a beige, crusty solid, compound 1d (1.64g, 4.20mmol). Yield: 91%.

^{1}H NMR (300 MHz, $CDCl_3$) (Figure A.1): 1.87ppm (quin, 2H, CH_2-*CH_2*-CH_2), 2.42 (sing, 3H, HOPO-*CH_3*), 2.65 (trip, 2H, CH_2-*CH_2*-phenyl), 3.27 (quart, 2H, NH-*CH_2*-CH_2), 5.10 (sing, 2H, O-*CH_2*-Bn), 5.18 (sing, 2H, HOPO-N-*CH_2*-CO), 7.11-7.25 (mult, 5H, phenyl), 7.26 (sing, $CDCl_3$), 7.31 (sing, 5H, Bn), 7.69 (doub, 1H, HOPO ring H), 8.12 (doub, 1H, HOPO ring H), 8.77 (trip, 1H, CO-*NH*-CH_2).

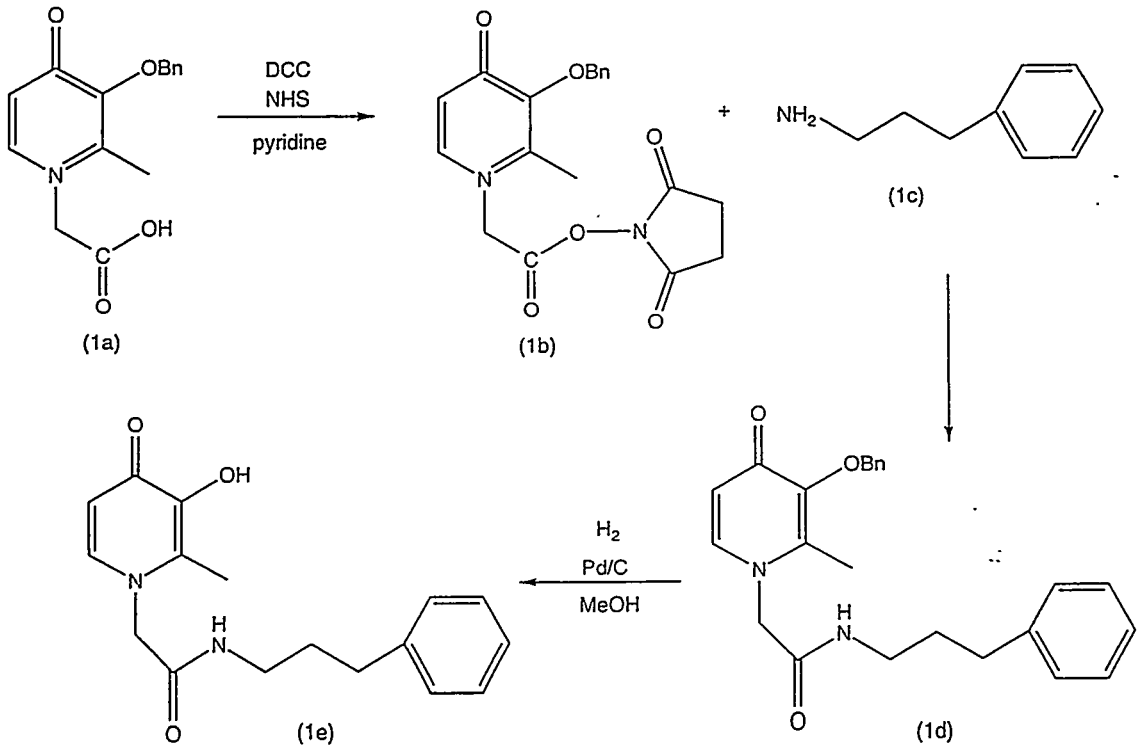

Figure 5.3: Schematic diagram of the synthetic route to 3,4-HOPO-phenylpropylamide, showing both the protected ligand (1d) and the deprotected ligand (1e).

2-methyl-3-hydroxy-4-pyridinone-N-methyl- N′-phenylpropylcarboxamide (1e) (Figure 5.3).

Compound 1d was deprotected quite easily by hydrogenation. Compound 1d was dissolved in methanol (20ml) in a small Schlenk tube, along with 10% Pd/C catalyst (0.15g). The tube was purged three times with H_2, then allowed to react overnight under H_2 with vigorous stirring. The catalyst was filtered with a F-grade glass frit, and the methanol was evaporated from the white foam product, compound 1e (1.06g, 3.54mmol). The product was dissolved in basic (NaOH) water, filtered on a M-grade glass frit, and then acidified with HCl until the product precipitated from solution. The basic solution was placed in a cold-room (4°C), and later the product was filtered and washed with acidic (HCl) water. The product was dried overnight in a vacuum oven at room temperature. Yield: 84%.

^{1}H NMR (300 MHz, DMSO) (Figure A.2): 1.73ppm (quin, 2H, CH_2-*CH_2*-CH_2), 2.27 (sing, 3H, HOPO-*CH_3*), 2.504 (mult, DMSO), 2.60 (trip, 2H, CH_2-*CH_2*-phenyl), 3.12 (quart, 2H, NH-*CH_2*-CH_2), 4.92 (sing, 2H, HOPO-N-*CH_2*-CO), 6.74 (doub, 1H, HOPO ring H), 7.15-7.31 (mult, 5H, phenyl), 7.88 (doub, 1H, HOPO ring H), 8.53 (trip, 1H, CO-*NH*-CH_2).

Elemental analysis for $C_{17}H_{19}N_2O_3 \cdot 3H_2O$ (353.39g/mol) calc%(found%): C 57.77 (57.94), H 7.13 (7.04), N 7.93 (7.94).

2-methyl-3-benzyloxy-4-pyridinone-N-methyl- N′-hexylcarboxamide (2d) (Figure 5.4).

2-methyl-3-benzyloxy-4-pyridinone-N-methylcarboxylic acid [116] (2a) (1.14 g, 4.40mmol) was dried in a vacuum oven at 70°C overnight, because the first step of this synthesis, the formation of the "activated ester", is very moisture sensitive. Additionally, all of the glassware used in the first synthetic step was dried in an oven, and the reaction was performed under dry nitrogen. Dry pyridine (10ml) was added to compound 2a in a dry 50ml single-neck round-bottom flask, and dissolved by stirring and heating the solution with a mantle until all of the solid was in solution. The solution was slowly cooled to room temperature, and some of compound 2a

came back out of solution. Both N-hydroxysuccinimide (NHS) (0.50g, 4.34mmol) and dicyclohexylcarbodiimide (DCC) (0.90g, 4.36mmol) were added, and the solution was stirred for 6h at room temperature. The reaction was followed by silica TLC, but the results were often inconsistent; by experience, 4h is typically enough time for the formation of the activated ester (2b).

Hexylamine (2c) (0.70 ml, 5.00 mmol) was added, dropwise, directly to the stirring solution of the activated ester. The solution was stirred overnight, and silica TLC revealed a primary product spot plus 3–4 sideproducts. The solution was filtered over a M-grade glass frit to remove dicyclohexylurea (DCU) solids from the solution. The pyridine was evaporated using a rotary evaporator, and a thick, dark orange oil remained. The oil was dissolved in methylene chloride (20ml), and impurities were extracted with two basic extractions (1M KOH, saturated with NaCl) followed by one acidic extraction (1M HCl). The methylene chloride was evaporated to leave a beige, crusty solid, compound 2d (1.26g, 3.53mmol). Yield: 80%.

^{1}H NMR (300 MHz, $CDCl_3$) (Figure A.3): 0.84ppm (trip, 3H, terminal CH_3), 1.16-1.27 (mult, 6H, alkane), 1.54 (quart, 2H, CH_2-*CH_2*-CH_3), 2.47 (sing, 3H, HOPO-methyl), 3.23 (quart, 2H, NH-*CH_2*-CH_2), 5.15 (sing, 2H, O-*CH_2*-Bn), 5.24 (sing, 2H, HOPO-N-*CH_2*-CO), 7.26 (sing, $CDCl_3$), 7.35 (sing, 5H, Bn), 7.72 (doub, 1H, HOPO ring H), 8.24 (doub, 1H, HOPO ring H), 8.65 (trip, 1H, CO-*NH*-CH_2).

2-methyl-3-hydroxy-4-pyridinone-N-methyl- N′-hexylcarboxamide (2e) (Figure 5.4).

Compound 2d was deprotected quite easily by hydrogenation. Compound 2d was dissolved in methanol (20ml) in a small Schlenk tube, along with 10% Pd/C catalyst (0.20g). The tube was purged three times with H_2, then allowed to react overnight under H_2 with vigorous stirring. The catalyst was filtered with a F-grade glass frit, and the methanol was evaporated from the white lacy product, compound 2e (0.24g, 0.90mmol). The product was dissolved in basic (NaOH) water, filtered on a M-grade glass frit, and then acidified with HCl until the product precipitated from solution. The basic solution was placed in a cold-room (4°C), and later the product

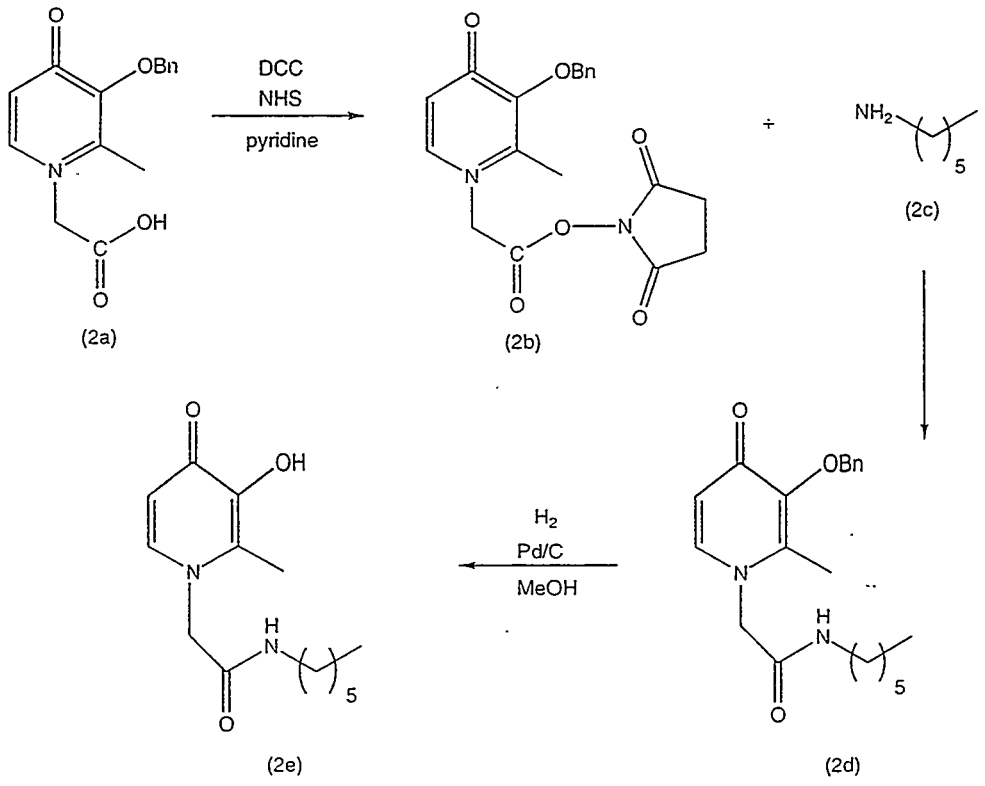

Figure 5.4: Schematic diagram of the synthetic route to 3,4-HOPO-hexylamide, showing both the protected ligand (2d) and the deprotected ligand (2e).

was filtered and washed with acidic (HCl) water. The product was dried overnight in a vacuum oven at room temperature. The yield is quite low because of large product solubility in water. Yield: 25%.

^{1}H NMR (300 MHz, DMSO) (Figure A.4): 0.86ppm (trip, 3H, terminal CH_3), 1.26 (sing, 6H, alkane), 1.41 (quart, 2H, CH_2-*CH_2*-CH_3), 2.34 (sing, 3H, HOPO-methyl), 2.504 (sing, DMSO), 3.11 (quart, 2H, NH-*CH_2*-CH_2), 5.08 (sing, 2H, HOPO-N-*CH_2*-CO), 7.18 (doub, 1H, HOPO ring H), 8.12 (doub, 1H, HOPO ring H), 8.61 (trip, 1H, CO-*NH*-CH_2).

Elemental analysis for $C_{14}H_{22}N_2O_3 \cdot 2.6H_2O$ (313.18g/mol) calc%(found%): C 53.69 (53.76), H 8.75 (7.56), N 8.95 (9.03).

2-methyl-3-benzyloxy-4-pyridinone-N-methyl- N′-octylcarboxamide (3d) (Figure 5.5).

2-methyl-3-benzyloxy-4-pyridinone-N-methylcarboxylic acid [116] (3a) (1.09 g, 4.20mmol) was dried in a vacuum oven at 70°C overnight, because the first step of this synthesis, the formation of the "activated ester", is very moisture sensitive. Additionally, all of the glassware used in the first synthetic step was dried in an oven, and the reaction was performed under dry nitrogen. Dry pyridine (10ml) was added to compound 3a in a dry 50ml single-neck round-bottom flask, and dissolved by stirring and heating the solution with a mantle until all of the solid was in solution. The solution was slowly cooled to room temperature, and some of compound 3a came back out of solution. Both N-hydroxysuccinimide (NHS) (0.48g, 4.17mmol) and dicyclohexylcarbodiimide (DCC) (0.89g, 4.31mmol) were added, and the solution was stirred for 5h at room temperature. The reaction was followed by silica TLC, but the results were often inconsistent; by experience, 4h is typically enough time for the formation of the activated ester (3b).

Octylamine (3c) (2.77 ml, 16.8 mmol) was added, dropwise, directly to the stirring solution of the activated ester. The solution was stirred overnight, and silica TLC revealed a primary product spot plus 3–4 sideproducts. The solution was filtered over a M-grade glass frit to remove dicyclohexylurea (DCU) solids from the solution.

The pyridine was evaporated using a rotary evaporator, and a thick, dark orange oil remained. The oil was dissolved in methylene chloride (20ml), and impurities were extracted with two basic extractions (1M KOH, saturated with NaCl) followed by one acidic extraction (1M HCl). The methylene chloride was evaporated to leave a beige, crusty solid, compound 3d (1.54g, 4.32mmol). Yield: 93%.

^{1}H NMR (300 MHz, $CDCl_3$) (Figure A.5): 0.85ppm (trip, 3H, terminal CH_3), 1.13-1.24 (mult, 10H, alkane), 1.54 (quart, 2H, CH_2-*CH_2*-CH_3), 2.49 (sing, 3H, HOPO-methyl), 3.23 (quart, 2H, NH-*CH_2*-CH_2), 5.14 (sing, 2H, O-*CH_2*-Bn), 5.24 (sing, 2H, HOPO-N-*CH_2*-CO), 7.26 (sing, $CDCl_3$), 7.35 (sing, 5H, Bn), 7.71 (doub, 1H, HOPO ring H), 8.38 (doub, 1H, HOPO ring H), 8.53 (trip, 1H, CO-*NH*-CH_2).

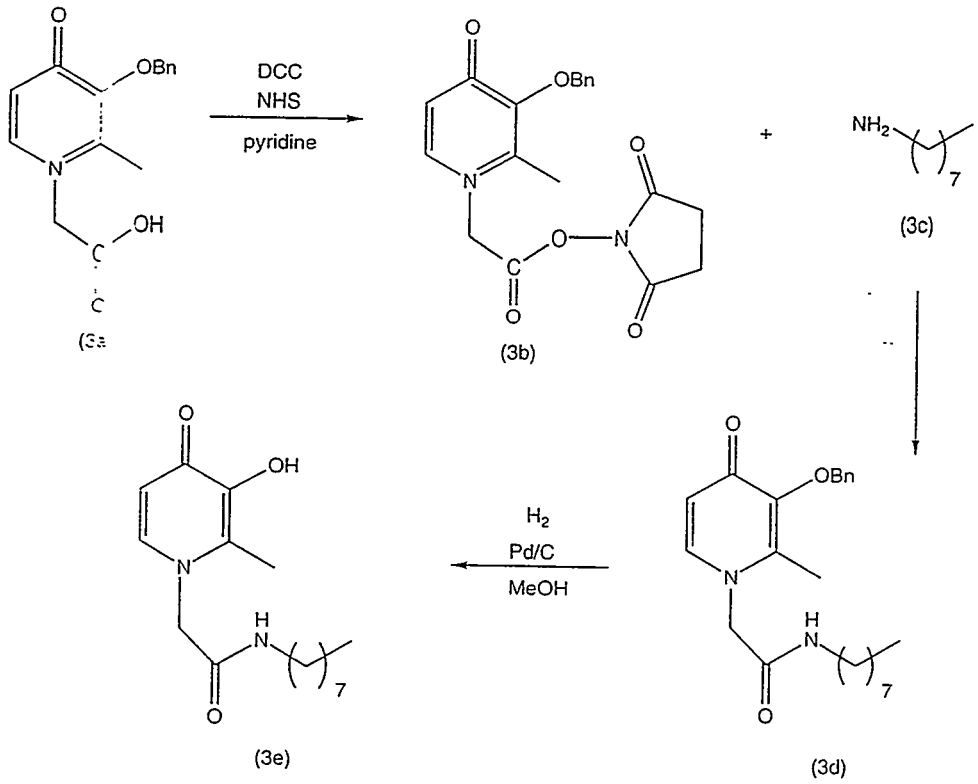

Figure 5.5: Schematic diagram of the synthetic route to 3,4-HOPO-octylamide, showing both the protected ligand (3d) and the deprotected ligand (3e).

2-methyl-3-hydroxy-4-pyridinone-N-methyl- N′-octylcarboxamide (3e) (Figure 5.5).

Compound 3d was deprotected quite easily by hydrogenation. Compound 3d was dissolved in methanol (20ml) in a small Schlenk tube, along with 10% Pd/C catalyst (0.20g). The tube was purged three times with H_2, then allowed to react overnight under H_2 with vigorous stirring. The catalyst was filtered with a F-grade glass frit, and the methanol was evaporated from the white product, compound 3e (1.04g, 3.52mmol). The product was dissolved in basic (NaOH) water, filtered on a M-grade glass frit, and then acidified with HCl until the product precipitated from solution. The basic solution was placed in a cold-room (4°C), and later the product was filtered and washed with acidic (HCl) water. The product was dried overnight in a vacuum oven at room temperature. Yield: 81%.

^{1}H NMR (300 MHz, DMSO) (Figure A.6): 0.85ppm (trip, 3H, terminal CH_3), 1.25 (sing, 10H, alkane), 1.42 (quart, 2H, CH_2-*CH_2*-CH_3), 2.24 (sing, 3H, HOPO-methyl), 2.504 (mult, DMSO), 3.09 (quart, 2H, NH-*CH_2*-CH_2), 4.88 (sing, 2H, HOPO-N-*CH_2*-CO), 6.68 (doub, 1H, HOPO ring H), 7.83 (doub, 1H, HOPO ring H), 8.46 (trip, 1H, CO-*NH*-CH_2).

Elemental analysis for $C_{16}H_{26}N_2O_3 \cdot 4.1H_2O$ (368.25g/mol) calc%(found%): C 52.18 (52.14), H 9.36 (7.71), N 7.61 (7.30).

2-methyl-3-benzyloxy-4-pyridinone-N-methyl- N′-decylcarboxamide (4d) (Figure 5.6).

2-methyl-3-benzyloxy-4-pyridinone-N-methylcarboxylic acid [116] (4a) (1.00 g, 3.86mmol) was dried in a vacuum oven at 70°C overnight, because the first step of this synthesis, the formation of the "activated ester", is very moisture sensitive. Additionally, all of the glassware used in the first synthetic step was dried in an oven, and the reaction was performed under dry nitrogen. Dry pyridine (10ml) was added to compound 4a in a dry 50ml single-neck round-bottom flask, and dissolved by stirring and heating the solution with a mantle until all of the solid was in solution. The solution was slowly cooled to room temperature, and some of compound 4a

came back out of solution. Both N-hydroxysuccinimide (NHS) (0.50g, 4.34mmol) and dicyclohexylcarbodiimide (DCC) (0.89g, 4.31mmol) were added, and the solution was stirred for 6h at room temperature. The reaction was followed by silica TLC, but the results were often inconsistent; by experience, 4h is typically enough time for the formation of the activated ester (4b).

Decylamine (4c) (1.3 ml, 6.5 mmol) was added, dropwise, directly to the stirring solution of the activated ester. The solution was stirred overnight, and silica TLC revealed a primary product spot plus 3–4 sideproducts. The solution was filtered over a M-grade glass frit to remove dicyclohexylurea (DCU) solids from the solution. The pyridine was evaporated using a rotary evaporator, and a thick, dark orange oil remained. The oil was dissolved in methylene chloride (20ml), and impurities were extracted with two basic extractions (1M KOH, saturated with NaCl) followed by one acidic extraction (1M HCl). The methylene chloride was evaporated to leave a beige, crusty solid, compound 4d (1.27g, 3.08mmol). Yield: 80%.

^{1}H NMR (300 MHz, $CDCl_3$) (Figure A.7): 0.86ppm (trip, 3H, terminal CH_3), 1.23 (sing, 14H, alkane), 1.38 (quart, 2H, CH_2-*CH_2*-CH_3), 2.48 (sing, 3H, HOPO-methyl), 3.22 (quart, 2H, NH-*CH_2*-CH_2), 5.12 (sing, 2H, O-*CH_2*-Bn), 5.28 (sing, 2H, HOPO-N-*CH_2*-CO), 7.26 (sing, $CDCl_3$), 7.34 (sing, 5H, Bn), 7.76 (doub, 1H, HOPO ring H), 8.41 (doub, 1H, HOPO ring H), 8.59 (trip, 1H, CO-*NH*-CH_2).

2-methyl-3-hydroxy-4-pyridinone-N-methyl- N′-decylcarboxamide (4e) (Figure 5.6).

Compound 4d was deprotected quite easily by hydrogenation. Compound 4d was dissolved in methanol (20ml) in a small Schlenk tube, along with 10% Pd/C catalyst (0.12g). The tube was purged three times with H_2, then allowed to react overnight under H_2 with vigorous stirring. The catalyst was filtered with a F-grade glass frit, and the methanol was evaporated from the white/yellow product, compound 4e (0.66g, 2.05mmol). The product was dissolved in basic (NaOH) water, filtered on a M-grade glass frit, and then acidified with HCl until the product precipitated from solution. The basic solution was placed in a cold-room (4°C), and later the product

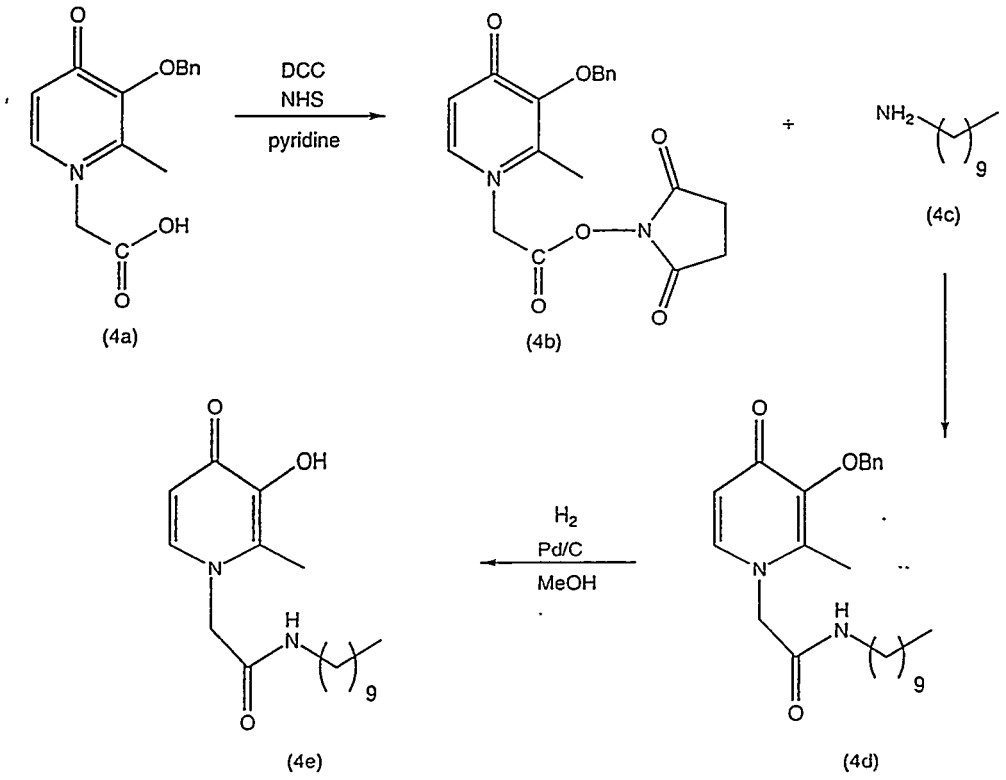

Figure 5.6: Schematic diagram of the synthetic route to 3,4-HOPO-decylamide, showing both the protected ligand (4d) and the deprotected ligand (4e).

was filtered and washed with acidic (HCl) water. The product was dried overnight in a vacuum oven at room temperature. Yield: 67%.

^{1}H NMR (300 MHz, DMSO) (Figure A.8): 0.84ppm (trip, 3H, terminal CH_3), 1.25 (sing, 14H, alkane), 1.42 (quart, 2H, CH_2-*CH_2*-CH_3), 2.26 (sing, 3H, HOPO-methyl), 2.504 (mult, DMSO), 3.09 (quart, 2H, NH-*CH_2*-CH_2), 4.90 (sing, 2H, HOPO-N-*CH_2*-CO), 6.75 (doub, 1H, HOPO ring H), 7.87 (doub, 1H, HOPO ring H), 8.45 (trip, 1H, CO-*NH*-CH_2).

Elemental analysis for $C_{18}H_{30}N_2O_3$ (322.44g/mol) calc%(found%): C 67.05 (67.01), H 9.38 (9.39), N 8.69 (8.71).

2-methyl-3-benzyloxy-4-pyridinone-N-methyl- N′-octadecylcarboxamide (5d) (Figure 5.7).

2-methyl-3-benzyloxy-4-pyridinone-N-methylcarboxylic acid [116] (5a) (1.14 g, 4.40mmol) was dried in a vacuum oven at 70°C overnight, because the first step of this synthesis, the formation of the "activated ester", is very moisture sensitive. Additionally, all of the glassware used in the first synthetic step was dried in an oven, and the reaction was performed under dry nitrogen. Dry pyridine (10ml) was added to compound 5a in a dry 50ml single-neck round-bottom flask, and dissolved by stirring and heating the solution with a mantle until all of the solid was in solution. The solution was slowly cooled to room temperature, and some of compound 5a came back out of solution. Both N-hydroxysuccinimide (NHS) (0.50g, 4.34mmol) and dicyclohexylcarbodiimide (DCC) (0.90g, 4.36mmol) were added, and the solution was stirred for 4h at room temperature. The reaction was followed by silica TLC, but the results were often inconsistent; by experience, 4h is typically enough time for the formation of the activated ester (5b).

Octadecylamine (5c) (1.08 g, 4.01 mmol) was dissolved in hexane and added, dropwise, directly to the stirring solution of the activated ester; an additional 0.4g dry amine was added after a few hours; the solution was white and milky. The solution was stirred for two days, and silica TLC revealed a primary product spot plus 3–4 sideproducts. The solution was filtered over a M-grade glass frit to remove

dicyclohexylurea (DCU) solids from the solution, but the product appeared to filter as well. The pyridine was evaporated using a rotary evaporator, and a white solid remained. The solid was dissolved in methylene chloride (20ml), and impurities were extracted with two basic extractions (1M KOH, saturated with NaCl) followed by one acidic extraction (1M HCl). The extraction was strange, with a solid white layer forming between the two liquid layers. The solid layer was discarded, and the organic layer retained. The methylene chloride was evaporated to leave a white solid, compound 5d (1.01g, 1.92mmol). Yield: 44%.

^{1}H NMR (300 MHz, DMSO) (Figures A.9, A.10): 0.85ppm (trip, 3H, terminal CH_3), 1.23 (sing, 30H, alkane), 1.42 (quart, 2H, CH_2-*CH_2*-CH_3), 2.28 (sing, 3H, HOPO-methyl), 2.504 (mult, DMSO), 3.09 (quart, 2H, NH-*CH_2*-CH_2), 5.07 (sing, 2H, O-*CH_2*-Bn + sing, 2H, HOPO-N-*CH_2*-CO), 7.33-7.44 (mult, 5H, Bn + doub, 1H, HOPO ring H), 8.30 (doub, 1H, HOPO ring H), 8.66 (trip, 1H, CO-*NH*-CH_2).

2-methyl-3-hydroxy-4-pyridinone-N-methyl- N′-octadecylcarboxamide (5e) (Figure 5.7).

Compound 5d was deprotected quite easily by hydrogenation. Compound 5d (0.90g, 1.71mmol) was dissolved in methanol (30ml) in a small Schlenk tube, along with 10% Pd/C catalyst (0.20g). The tube was purged three times with H_2, then allowed to react overnight under H_2 with vigorous stirring. The catalyst was filtered with a F-grade glass frit, and the methanol was evaporated from the white product, compound 5e (0.22g, 0.51mmol). The product was dissolved in basic (NaOH) water, filtered on a M-grade glass frit, and then acidified with HCl until the product precipitated from solution. The basic solution was placed in a cold-room (4°C), and later the product was filtered and washed with acidic (HCl) water. The product was dried overnight in a vacuum oven at room temperature. Yield: 30%.

^{1}H NMR (300 MHz, DMSO) (Figures A.11, A.12): 0.86ppm (trip, 3H, terminal CH_3), 1.24 (sing, 30H, alkane), 1.42 (quart, 2H, CH_2-*CH_2*-CH_3), 2.19 (sing, 3H, HOPO-methyl), 2.504 (mult, DMSO), 3.09 (quart, 2H, NH-*CH_2*-CH_2), 4.76 (sing, 2H, HOPO-N-*CH_2*-CO), 6.42 (doub, 1H, HOPO ring H), 7.69 (doub, 1H, HOPO ring H),

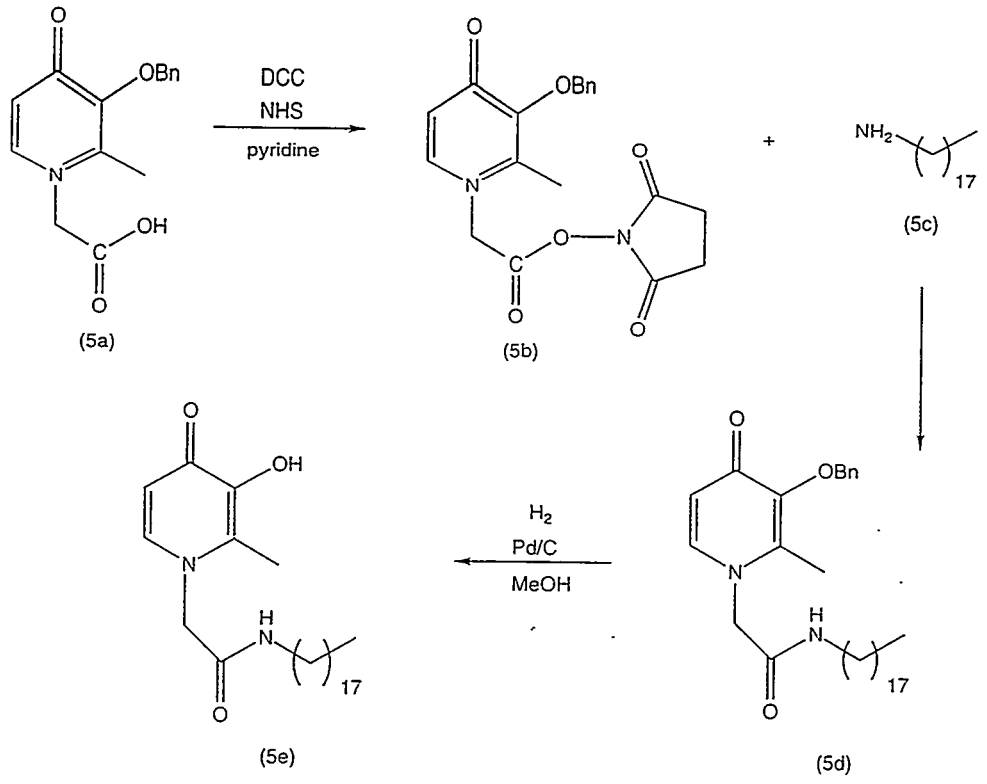

Figure 5.7: Schematic diagram of the synthetic route to 3,4-HOPO-octadecylamide, showing both the protected ligand (5d) and the deprotected ligand (5e).

8.32 (trip, 1H, CO-*NH*-CH_2).

Elemental analysis for $C_{26}H_{46}N_2O_3 \cdot 1.7H_2O$ (465.28g/mol) calc%(found%): C 67.11 (67.29), H 10.70 (10.73), N 6.02 (5.68).

5.1.2 Ligand Synthesis: 3,2-HOPOs

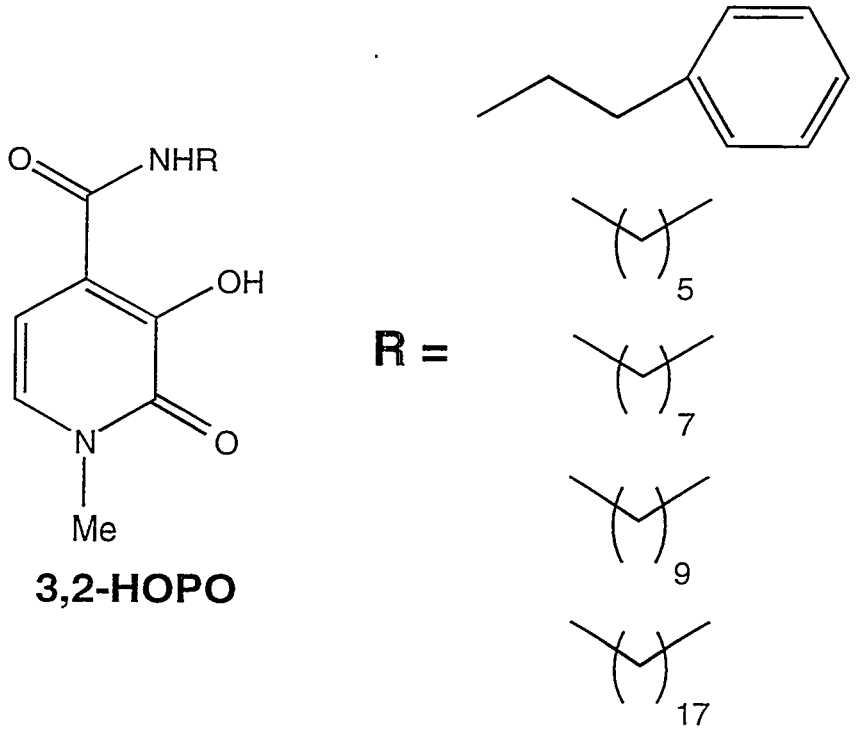

Figure 5.8: The 3,2-HOPO chelating moiety, and the side chains used to render it organophilic.

3-benzyloxy-1-methyl-2-pyridinone-4-n- propylcarboxamide (6d) (Figure 5.9).

N-methyl-3-benzyloxy-2-pyridinone-4-carboxylic acid [117, 100] (6a) (0.63g, 2.44mmol) was dissolved with stirring in a dry 100mL single-neck round-bottom flask in dry methylene chloride (75mL) along with 2-mercaptothiazoline (0.29g, 2.44mmol) and a catalytic amount of dimethylaminopyridine (DMAP) (0.04g, 0.3mmol). Dicyclohexylcarbodiimide (DCC) (0.56g, 2.73mmol) was added and the solution slowly turned yellow. The flask was wrapped in aluminum foil (compound 6b is light-sensitive) and allowed to stir overnight.

The solution was filtered on a M-grade glass frit to remove the dicyclohexylurea (DCU) solids; the solids were washed with dry methylene chloride, until

all visible yellow was rinsed through the frit, to assure high yield. Four-fifths of the methylene chloride was evaporated from the product, and then isopropanol (40mL) was added to the flask. The activated intermediate precipitated from solution in the form of bright yellow crystals. The remainder of the methylene chloride was evaporated, and the crystals in isopropanol were placed in a cold-room (4°C). The activated intermediate, compound 6b (0.70g, 2.03mmol), was filtered on a M-grade glass frit and dried in a vacuum oven overnight at room temperature. Yield: 83%.

Compound 6b (0.70g, 2.03mmol) was dissolved in dry methylene chloride (30mL). Propylamine (6c) (0.17mL, 2.03mmol), which was freshly distilled, was added dropwise to the stirring solution, and the solution gradually lost its yellow color within approximately 15 minutes. The solution was covered with aluminum foil and stirred overnight. Formation of the product can be followed with silica TLC, and the product appears as a bright blue spot under UV light.

The product was purified with one basic (1M NaOH) and one acidic (1M HCl) extraction, and then passed through a rotary silica column (Chromatotron), using methylene chloride and methanol as the stationary and mobile phases, respectively. The fractions with the benzyl-protected product were isolated and the solvent was evaporated. A thick, slightly yellow oil remained, compound 6d (0.59g, 1.96mmol). Yield: 97%.

^{1}H NMR (300MHz, $CDCl_3$) (Figure A.13): 0.79 (trip, 3H, terminal CH_3), 1.33 (sext, 2H, CH_2-*CH_2*-CH_3), 3.18 (quart, 2H, NH-*CH_2*-CH_2), 3.60 (sing, 3H, HOPO-*CH_3*), 5.38 (sing, 2H, O-*CH_2*-Bn), 6.81 (doub, 1H, HOPO ring H), 7.11 (doub, 1H, HOPO ring H), 7.26 (sing, $CDCl_3$), 7.36-7.46 (mult, 5H, Bn), 7.91 (sing, 1H, CO-*NH*-CH_2).

^{13}C NMR (400MHz, $CDCl_3$) (Figure A.14): low-field, 5C, 11.4, 20.1, 22.3, 37.7, 41.5; high-field, 10C, 105.0, 128.7, 128.8, 129.0, 130.6, 132.0, 136.2, 146.5, 159.7, 163.0.

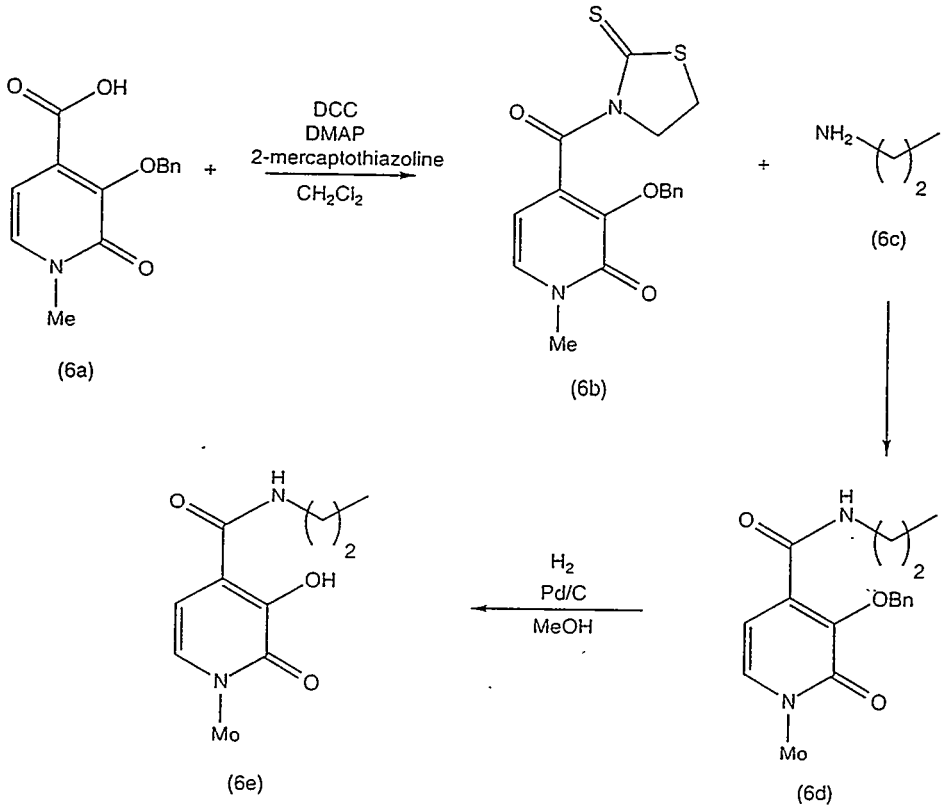

Figure 5.9: Schematic diagram of the synthetic route to 3,2-HOPO-propylamide, showing both the protected ligand (6d) and the deprotected ligand (6e).

3-hydroxy-1-methyl-2-pyridinone-4-n-propylcarboxamide (6e) (Figure 5.9).

Compound 6d was deprotected quite easily by hydrogenation. Compound 6d (0.59g, 1.96mmol) was dissolved in methanol (30ml) in a small Schlenk tube, along with 10% Pd/C catalyst (0.06g). The tube was purged three times with H_2, then allowed to react for 6h under H_2 with vigorous stirring. The catalyst was filtered with a F-grade glass frit, and four-fifths of the methanol was evaporated from the product. Ethyl acetate (30mL) was added, and after the remainder of the methanol was evaporated, white product precipitated from solution. The solution was placed in a cold-room (4°C), and later the product was filtered and washed with cold ethyl acetate. The product, compound 6e (0.18g, 0.86mmol), was dried overnight in a vacuum oven at room temperature. Yield: 44%.

^{1}H NMR (300MHz, DMSO) (Figure A.15): 0.87 (trip, 3H, terminal CH_3), 1.51 (sext, 2H, CH_2-*CH_2*-CH_3), 2.504 (mult, DMSO), 3.24 (quart, 2H, NH-*CH_2*-CH_2), 3.47 (sing, 3H, HOPO-*CH_3*), 6.52 (doub, 1H, HOPO ring H), 7.18 (doub, 1H, HOPO ring H), 8.46 (trip, 1H, CO-*NH*-CH_2).

^{13}C NMR (400MHz, DMSO) (Figure A.16): low-field, 4C, 11.3, 22.2, 36.8, 40.8; high-field, 6C, 102.4, 117.0, 127.7, 147.9, 158.0, 165.6.

Elemental analysis of $C_{10}H_{14}N_2O_3$ (210.23g/mol) calc%(found%): C 57.13 (57.14), H 6.71 (6.80), N 13.33 (13.32).

3-benzyloxy-1-methyl-2-pyridinone-4-n- phenylpropylcarboxamide (7d) (Figure 5.10).

N-methyl-3-benzyloxy-2-pyridinone-4-carboxylic acid [117, 100] (7a) (0.90g, 3.49mmol) was dissolved with stirring in a dry 100mL single-neck round-bottom flask in dry methylene chloride (75mL) along with 2-mercaptothiazoline (0.41g, 3.49mmol) and a catalytic amount of dimethylaminopyridine (DMAP) (0.04g, 0.3mmol). Dicyclohexylcarbodiimide (DCC) (0.80g, 3.90mmol) was added and the solution slowly turned yellow. The flask was wrapped in aluminum foil (compound 7b is light-sensitive) and allowed to stir overnight.

The solution was filtered on a M-grade glass frit to remove the dicyclohexylurea (DCU) solids; the solids were washed with dry methylene chloride, until all visible yellow was rinsed through the frit, to assure high yield. Four-fifths of the methylene chloride was evaporated from the product, and then isopropanol (40mL) was added to the flask. The activated intermediate precipitated from solution in the form of bright yellow crystals. The remainder of the methylene chloride was evaporated, and the crystals in isopropanol were placed in a cold-room (4°C). The activated intermediate, compound 7b (1.00g, 2.90mmol), was filtered on a M-grade glass frit and dried in a vacuum oven overnight at room temperature. Yield: 83%.

Compound 7b (1.00g, 2.90mmol) was dissolved in dry methylene chloride (30mL). Phenylpropylamine (7c) (0.41mL, 2.90mmol) was added dropwise to the stirring solution, and the solution gradually lost its yellow color within approximately 15 minutes. The solution was covered with aluminum foil and stirred overnight. Formation of the product can be followed with silica TLC, and the product appears as a bright blue spot under UV light.

The product was purified with one basic (1M NaOH) and one acidic (1M HCl) extraction, and then passed through a rotary silica column (Chromatotron), using methylene chloride and methanol as the stationary and mobile phases, respectively. The fractions with the benzyl-protected product were isolated and the solvent was evaporated. A thick, slightly yellow oil remained, compound 7d (0.95g, 2.54mmol). Yield: 88%.

^{1}H NMR (300MHz, $CDCl_3$) (Figure A.17): 1.61 (quin, 2H, CH_2-*CH_2*-CH_2), 2.50 (trip, 2H, CH_2-*CH_2*-phenyl), 3.23 (quart, 2H, NH-*CH_2*-CH_2), 3.60 (sing, 3H, HOPO-*CH_3*), 5.38 (sing, 2H, O-*CH_2*-Bn), 6.81 (doub, 1H, HOPO ring H), 7.07-7.44 (doub, 1H, HOPO ring H + sing, $CDCl_3$ + mult, 5H, Bn), 7.94 (sing, 1H, CO-*NH*-CH_2).

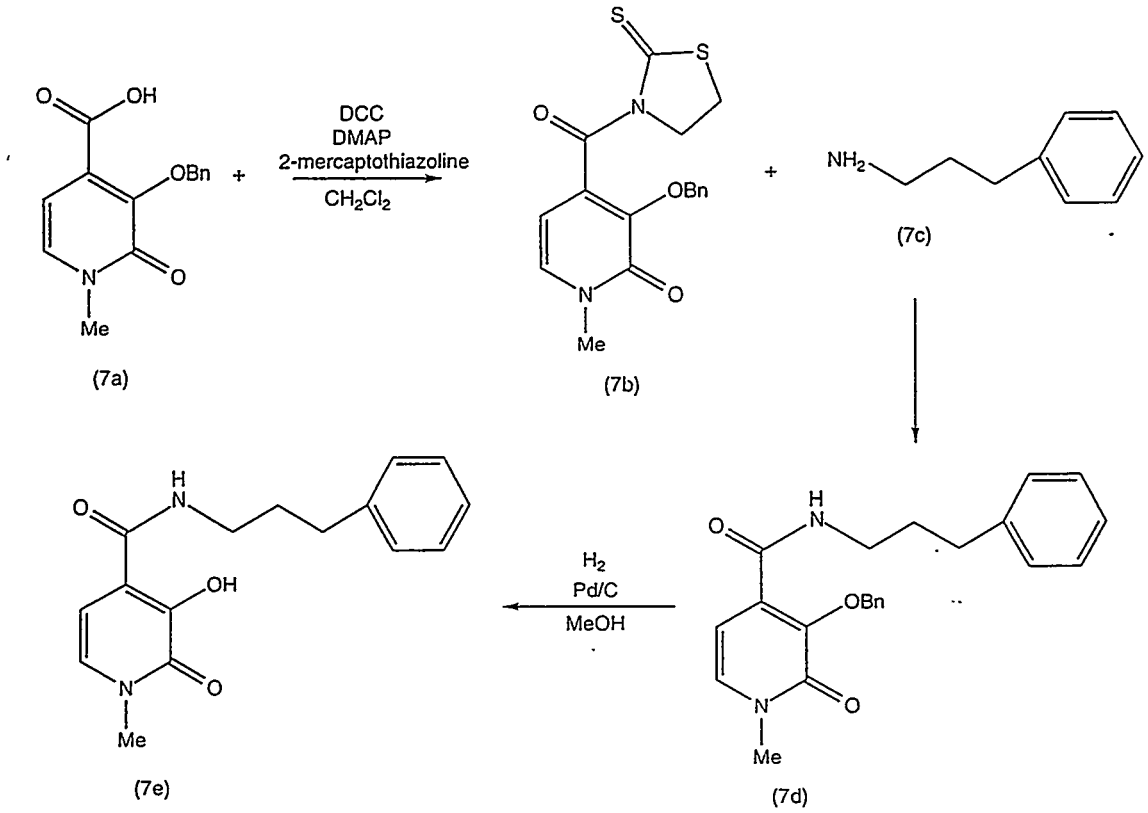

Figure 5.10: Schematic diagram of the synthetic route to 3,2-HOPO-phenylpropylamide, showing both the protected ligand (7d) and the deprotected ligand (7e).

3-hydroxy-1-methyl-2-pyridinone-4-n- phenylpropylcarboxamide (7e) (Figure 5.10).

Compound 7d was deprotected quite easily by hydrogenation. Compound 7d (0.95g, 2.54mmol) was dissolved in methanol (30ml) in a small Schlenk tube, along with 10% Pd/C catalyst (0.11g). The tube was purged three times with H_2, then allowed to react for 6h under H_2 with vigorous stirring. The deprotection was not finished after 24h (the catalyst was probably poisoned), so additional 10% Pd/C (0.20g) was added. The deprotection finished within 2h. The catalyst was filtered with a F-grade glass frit, and four-fifths of the methanol was evaporated from the product. Ethyl acetate (30mL) was added, and after the remainder of the methanol was evaporated, white product precipitated from solution. The solution was placed in a cold-room (4°C), and later the product was filtered and washed with cold ethyl acetate. The product, compound 7e (0.30g, 1.05mmol), was dried overnight in a vacuum oven at room temperature. Yield: 41%.

^{1}H NMR (300MHz, $CDCl_3$) (Figure A.18): 1.82 (quin, 2H, CH_2-*CH_2*-CH_2), 2.504 (mult, DMSO), 2.62 (trip, 2H, CH_2-*CH_2*-phenyl), 3.29 (quart, 2H, NH-*CH_2*-CH_2), 3.47 (sing, 3H, HOPO-*CH_3*), 6.51 (doub, 1H, HOPO ring H), 7.15-7.36 (doub, 1H, HOPO ring H + mult, 5H, Bn), 8.53 (trip, 1H, CO-*NH*-CH_2).

^{13}C NMR (400MHz, DMSO) (Figures A.19, A.20): low-field, 4C, 30.6, 32.5, 36.8, 38.7; high-field, 9C, 102.4, 117.1, 125.8, 127.6, 128.3, 141.5, 148.0, 158.1, 165.7.

Elemental analysis of $C_{16}H_{18}N_2O_3 \cdot 1.5H_2O$ (313.35g/mol) calc%(found%): C 61.32 (61.58), H 6.76 (5.77), N 8.94 (8.97).

3-benzyloxy-1-methyl-2-pyridinone-4-n- hexylcarboxamide (8d) (Figure 5.11).

N-methyl-3-benzyloxy-2-pyridinone-4-carboxylic acid [117, 100] (8a) (0.90g, 3.49mmol) was dissolved with stirring in a dry 100mL single-neck round-bottom flask in dry methylene chloride (75mL) along with 2-mercaptothiazoline (0.41g, 3.49mmol) and a catalytic amount of dimethylaminopyridine (DMAP) (0.04g, 0.3mmol). Dicyclohexylcarbodiimide (DCC) (0.80g, 3.90mmol) was added and the solution slowly

turned yellow. The flask was wrapped in aluminum foil (compound 8b is light-sensitive) and allowed to stir overnight.

The solution was filtered on a M-grade glass frit to remove the dicyclohexylurea (DCU) solids; the solids were washed with dry methylene chloride, until all visible yellow was rinsed through the frit, to assure high yield. Four-fifths of the methylene chloride was evaporated from the product, and then isopropanol (40mL) was added to the flask. The activated intermediate precipitated from solution in the form of bright yellow crystals. The remainder of the methylene chloride was evaporated, and the crystals in isopropanol were placed in a cold-room (4°C). The activated intermediate, compound 8b (1.00g, 2.90mmol), was filtered on a M-grade glass frit and dried in a vacuum oven overnight at room temperature. Yield: 83%.

Compound 8b (1.00g, 2.90mmol) was dissolved in dry methylene chloride (30mL). Hexylamine (8c) (0.38mL, 2.90mmol) was added dropwise to the stirring solution, and the solution gradually lost its yellow color within approximately 15 minutes. The solution was covered with aluminum foil and stirred overnight. Formation of the product can be followed with silica TLC, and the product appears as a bright blue spot under UV light.

The product was purified with one basic (1M NaOH) and one acidic (1M HCl) extraction, and then passed through a rotary silica column (Chromatotron), using methylene chloride and methanol as the stationary and mobile phases, respectively. The fractions with the benzyl-protected product were isolated and the solvent was evaporated. A thick, slightly yellow oil remained, compound 8d (0.78g, 2.29mmol). Yield: 79%.

^{1}H NMR (300MHz, $CDCl_3$) (Figure A.21): 0.82 (trip, 3H, terminal CH_3), 1.16-1.27 (mult, 8H, alkane chain H), 3.17 (quart, 2H, NH-CH_2-CH_2), 3.55 (sing, 3H, HOPO-CH_3), 5.33 (sing, 2H, O-CH_2-Bn), 6.76 (doub, 1H, HOPO ring H), 7.08 (doub, 1H, HOPO ring H), 7.26 (sing, $CDCl_3$), 7.32-7.43 (mult, 5H, Bn), 7.88 (sing, 1H, CO-*NH*-CH_2).

^{13}C NMR (400MHz, $CDCl_3$) (Figure A.22): low-field, 8C, 13.9, 22.3, 26.4, 28.8, 31.2, 37.5, 39.6, 74.7; high-field, 10C, 104.8, 128.6, 128.7, 128.9, 130.5, 131.9, 136.0, 146.3, 159.5, 162.8.

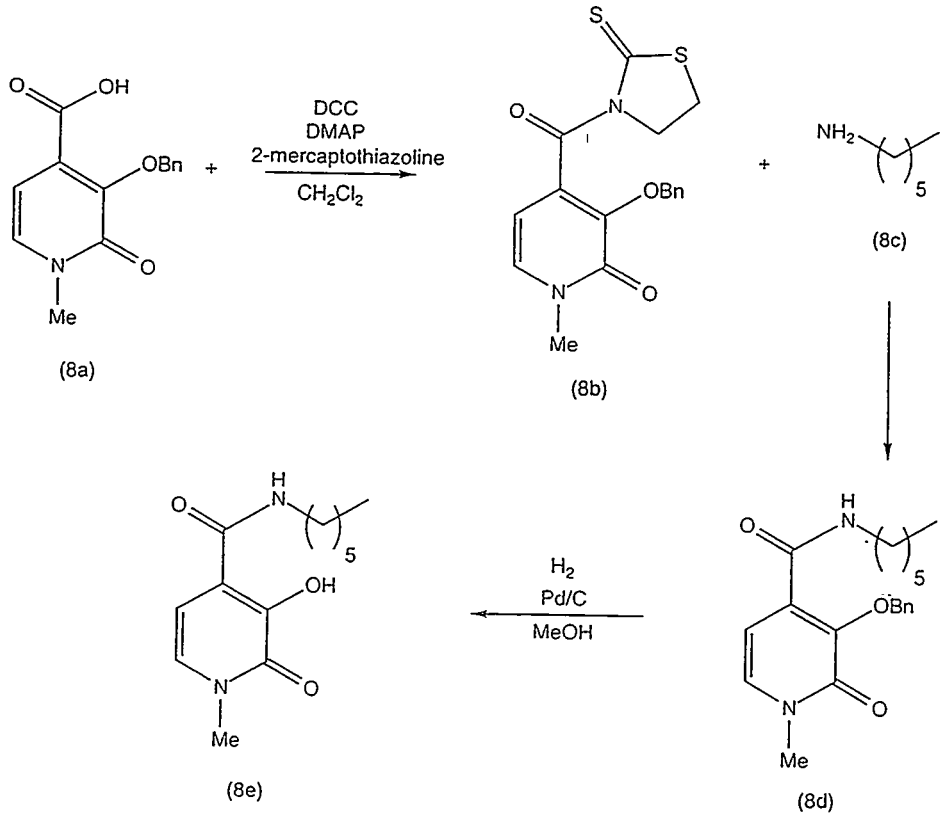

Figure 5.11: Schematic diagram of the synthetic route to 3,2-HOPO-hexylamide, showing both the protected ligand (8d) and the deprotected ligand (8e).

3-hydroxy-1-methyl-2-pyridinone-4-n-hexylcarboxamide (8e) (Figure 5.11).

Compound 8d was deprotected quite easily by hydrogenation. Compound 8d (0.78g, 2.29mmol) was dissolved in methanol (30ml) in a small Schlenk tube, along with 10% Pd/C catalyst (0.21g). The tube was purged three times with H_2, then allowed to react for 10h under H_2 with vigorous stirring. The catalyst was filtered with a F-grade glass frit, and four-fifths of the methanol was evaporated from the product. Ethyl acetate (30mL) was added, and after the remainder of the methanol was evaporated, white product precipitated from solution. The solution was placed in a cold-room (4°C), and later the product was filtered and washed with cold ethyl acetate. The product, compound 8e (0.45g, 1.78mmol), was dried overnight in a vacuum oven at room temperature. Yield: 78%.

^{1}H NMR (300MHz, DMSO) (Figure A.23): 0.85 (trip, 3H, terminal CH_3), 1.26-1.31 (sing, 6H, alkane chain H), 1.48 (quin, 2H, NH-CH_2-*CH_2*-CH_2), 2.504 (mult, DMSO), 3.26 (quart, 2H, NH-*CH_2*-CH_2), 3.46 (sing, 3H, HOPO-*CH_3*), 6.52 (doub, 1H, HOPO ring H), 7.19 (doub, 1H, HOPO ring H), 8.46 (trip, 1H, CO-*NH*-CH_2).

^{13}C NMR (400MHz, DMSO) (Figures A.24, A.25): low-field, 7C, 13.9, 22.0, 26.1, 28.8, 30.9, 36.8, 39.01; high-field, 6C, 102.3, 116.9, 127.7, 148.0, 158.0, 165.6.

Elemental analysis of $C_{13}H_{20}N_2O_3$ (252.31g/mol) calc%(found%): C 61.88 (61.67), H 7.99 (7.88), N 11.11 (10.07).

3-benzyloxy-1-methyl-2-pyridinone-4-n- octylcarboxamide (9d) (Figure 5.12).

N-methyl-3-benzyloxy-2-pyridinone-4-carboxylic acid [117, 100] (9a) (0.90g, 3.49mmol) was dissolved with stirring in a dry 100mL single-neck round-bottom flask in dry methylene chloride (75mL) along with 2-mercaptothiazoline (0.41g, 3.49mmol) and a catalytic amount of dimethylaminopyridine (DMAP) (0.04g, 0.3mmol). Dicyclohexylcarbodiimide (DCC) (0.80g, 3.90mmol) was added and the solution slowly turned yellow. The flask was wrapped in aluminum foil (compound 9b is light-sensitive) and allowed to stir overnight.

The solution was filtered on a M-grade glass frit to remove the dicyclohexylurea (DCU) solids; the solids were washed with dry methylene chloride, until all visible yellow was rinsed through the frit, to assure high yield. Four-fifths of the methylene chloride was evaporated from the product, and then isopropanol (40mL) was added to the flask. The activated intermediate precipitated from solution in the form of bright yellow crystals. The remainder of the methylene chloride was evaporated, and the crystals in isopropanol were placed in a cold-room (4°C). The activated intermediate, compound 9b (1.00g, 2.90mmol), was filtered on a M-grade glass frit and dried in a vacuum oven overnight at room temperature. Yield: 83%.

Compound 9b (1.00g, 2.90mmol) was dissolved in dry methylene chloride (30mL). Octylamine (9c) (0.48mL, 2.90mmol) was added dropwise to the stirring solution, and the solution gradually lost its yellow color within approximately 15 minutes. The solution was covered with aluminum foil and stirred overnight. Formation of the product can be followed with silica TLC, and the product appears as a bright blue spot under UV light.

The product was purified with one basic (1M NaOH) and one acidic (1M HCl) extraction, and then passed through a rotary silica column (Chromatotron), using methylene chloride and methanol as the stationary and mobile phases, respectively. The fractions with the benzyl-protected product were isolated and the solvent was evaporated. A thick, slightly yellow oil remained, compound 9d (0.81g, 2.18mmol). Yield: 75%.

^{1}H NMR (300MHz, $CDCl_3$) (Figure A.26): 0.81 (trip, 3H, terminal CH_3), 1.14-1.22 (mult, 12H, alkane chain H), 3.14 (quart, 2H, NH-CH_2-CH_2), 3.51 (sing, 3H, HOPO-CH_3), 5.30 (sing, 2H, O-CH_2-Bn), 6.71 (doub, 1H, HOPO ring H), 7.06 (doub, 1H, HOPO ring H), 7.26 (sing, $CDCl_3$), 7.29-7.39 (mult, 5H, Bn), 7.85 (sing, 1H, CO-*NH*-CH_2).

^{13}C NMR (400MHz, $CDCl_3$) (Figure A.27): low-field, 10C, 13.9, 22.4, 26.7, 28.7, 28.9, 29.0, 31.5, 37.4, 39.6, 74.6; high-field, 10C, 104.7, 128.5, 128.6, 128.7, 130.4, 131.9, 136.0, 146.1, 159.4, 162.7.

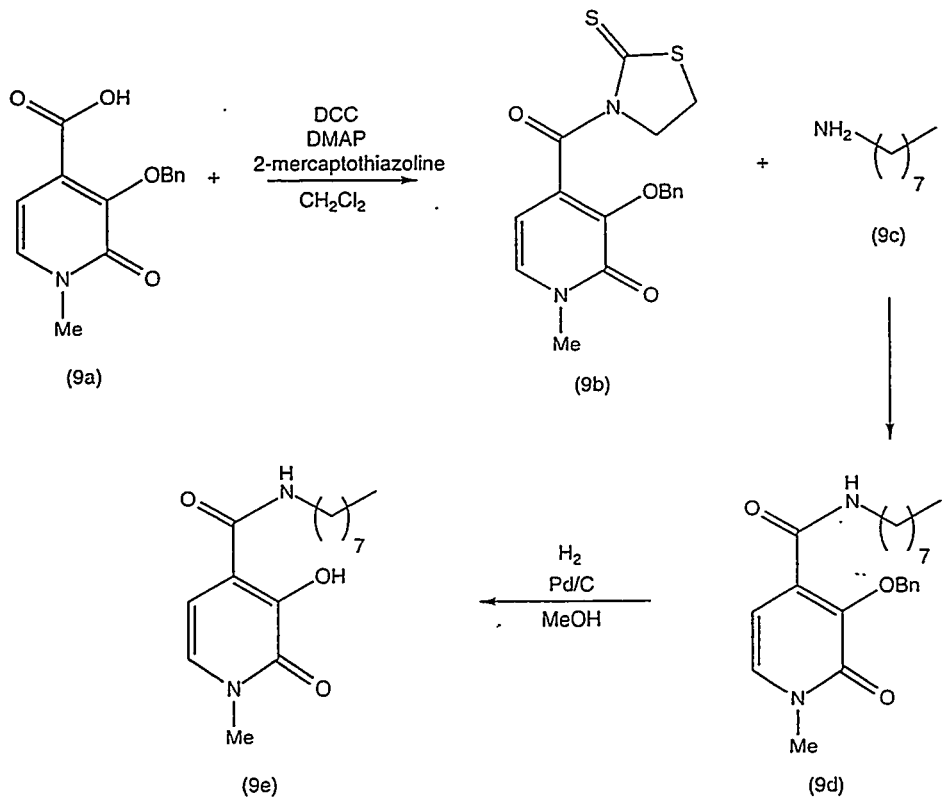

Figure 5.12: Schematic diagram of the synthetic route to 3,2-HOPO-octylamide, showing both the protected ligand (9d) and the deprotected ligand (9e).

3-hydroxy-1-methyl-2-pyridinone-4-n-octylcarboxamide (9e) (Figure 5.12).

Compound 9d was deprotected quite easily by hydrogenation. Compound 9d (0.81g, 2.18mmol) was dissolved in methanol (30ml) in a small Schlenk tube, along with 10% Pd/C catalyst (0.21g). The tube was purged three times with H_2, then allowed to react overnight under H_2 with vigorous stirring. The catalyst was filtered with a F-grade glass frit, and four-fifths of the methanol was evaporated from the product. Ethyl acetate (30mL) was added, and after the remainder of the methanol was evaporated, white product precipitated from solution. The solution was placed in a cold-room (4°C), and later the product was filtered and washed with cold ethyl acetate. The product, compound 9e (0.50g, 1.78mmol), was dried overnight in a vacuum oven at room temperature. Yield: 82%.

^{1}H NMR (300MHz, DMSO) (Figure A.28): 0.84 (trip, 3H, terminal CH_3), 1.15-1.25 (mult, 10H, alkane chain H), 1.48 (quin, 2H, NH-CH_2-*CH_2*-CH_2), 2.504 (mult, DMSO), 3.26 (quart, 2H, NH-*CH_2*-CH_2), 3.46 (sing, 3H, HOPO-CH_3), 6.52 (doub, 1H, HOPO ring H), 7.19 (doub, 1H, HOPO ring H), 8.46 (trip, 1H, CO-*NH*-CH_2).

^{13}C NMR (400MHz, DMSO) (Figures A.29, A.30): low-field, 9C, 13.9, 22.1, 26.4, 28.6, 28.7, 28.8, 31.2, 36.8, 39.0; high-field, 6C, 102.3, 116.9, 127.6, 148.0, 158.0, 165.6.

Elemental analysis of $C_{15}H_{24}N_2O_3$ (280.37g/mol) calc%(found%): C 64.25 (63.90), H 8.63 (8.53), N 9.99 (9.77).

3-benzyloxy-1-methyl-2-pyridinone-4-n- decylcarboxamide (10d) (Figure 5.13).

N-methyl-3-benzyloxy-2-pyridinone-4-carboxylic acid [117, 100] (10a) (0.90g, 3.49mmol) was dissolved with stirring in a dry 100mL single-neck round-bottom flask in dry methylene chloride (75mL) along with 2-mercaptothiazoline (0.41g, 3.49mmol) and a catalytic amount of dimethylaminopyridine (DMAP) (0.04g, 0.3mmol). Dicyclohexylcarbodiimide (DCC) (0.80g, 3.90mmol) was added and the solution slowly

turned yellow. The flask was wrapped in aluminum foil (compound 10b is light-sensitive) and allowed to stir overnight.

The solution was filtered on a M-grade glass frit to remove the dicyclohexylurea (DCU) solids; the solids were washed with dry methylene chloride, until all visible yellow was rinsed through the frit, to assure high yield. Four-fifths of the methylene chloride was evaporated from the product, and then isopropanol (40mL) was added to the flask. The activated intermediate precipitated from solution in the form of bright yellow crystals. The remainder of the methylene chloride was evaporated, and the crystals in isopropanol were placed in a cold-room (4°C). The activated intermediate, compound 10b (1.00g, 2.90mmol), was filtered on a M-grade glass frit and dried in a vacuum oven overnight at room temperature. Yield: 83%.

Compound 10b (1.00g, 2.90mmol) was dissolved in dry methylene chloride (30mL). Decylamine (10c) (0.58mL, 2.90mmol) was added dropwise to the stirring solution, and the solution gradually lost its yellow color within approximately 15 minutes. The solution was covered with aluminum foil and stirred overnight. Formation of the product can be followed with silica TLC, and the product appears as a bright blue spot under UV light.

The product was purified with one basic (1M NaOH) and one acidic (1M HCl) extraction, and then passed through a rotary silica column (Chromatotron), using methylene chloride and methanol as the stationary and mobile phases, respectively. The fractions with the benzyl-protected product were isolated and the solvent was evaporated. A thick, slightly yellow oil remained, compound 10d (0.96g, 2.41mmol). Yield: 83%.

^{1}H NMR (300MHz, $CDCl_3$) (Figure A.31): 0.88 (trip, 3H, terminal CH_3), 1.20-1.33 (mult, 16H, alkane chain H), 3.20 (quart, 2H, NH-CH_2-CH_2), 3.60 (sing, 3H, HOPO-CH_3), 5.30 (sing, 2H, O-CH_2-Bn), 6.81 (doub, 1H, HOPO ring H), 7.11 (doub, 1H, HOPO ring H), 7.26 (sing, $CDCl_3$), 7.29-7.46 (mult, 5H, Bn), 7.90 (sing, 1H, CO-NH-CH_2).

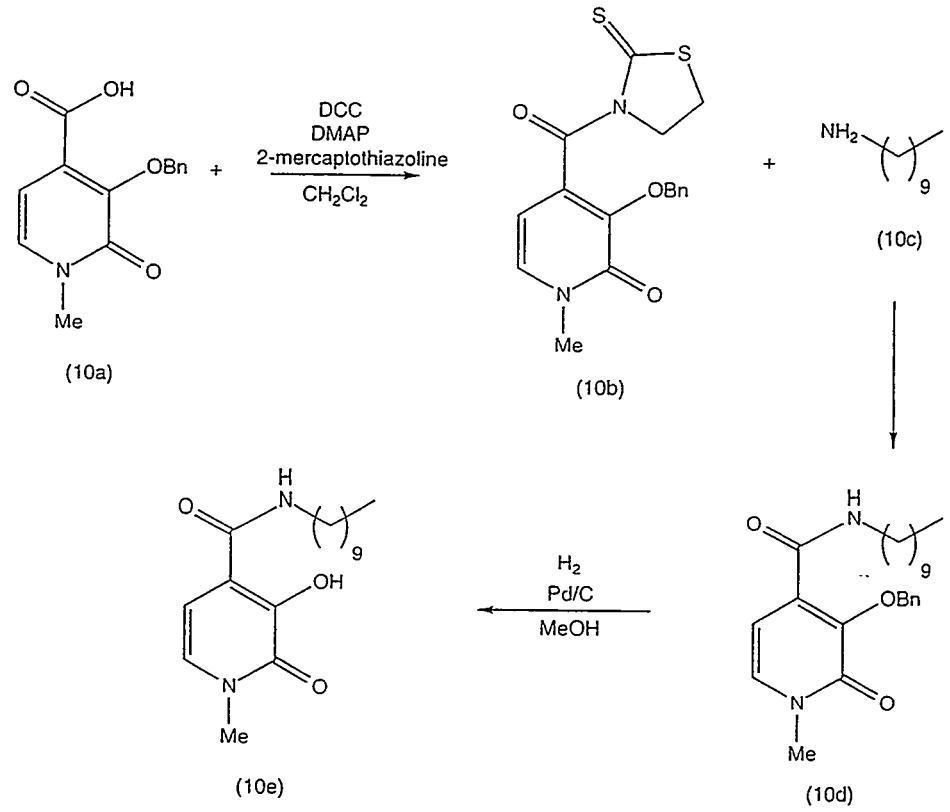

Figure 5.13: Schematic diagram of the synthetic route to 3,2-HOPO-decylamide, showing both the protected ligand (10d) and the deprotected ligand (10e).

3-hydroxy-1-methyl-2-pyridinone-4-n-decylcarboxamide (10e) (Figure 5.13).

Compound 10d was deprotected quite easily by hydrogenation. Compound 10d (0.96g, 2.41mmol) was dissolved in methanol (30ml) in a small Schlenk tube, along with 10% Pd/C catalyst (0.12g). The tube was purged three times with H_2, then allowed to react for 6h under H_2 with vigorous stirring. The catalyst was filtered with a F-grade glass frit, and four-fifths of the methanol was evaporated from the product. Ethyl acetate (30mL) was added, and after the remainder of the methanol was evaporated, white product precipitated from solution. The solution was placed in a cold-room (4°C), and later the product was filtered and washed with cold ethyl acetate. The product, compound 10e (0.72g, 2.33mmol), was dried overnight in a vacuum oven at room temperature. Yield: 97%.

^{1}H NMR (300MHz, DMSO) (Figure A.32): 0.85 (trip, 3H, terminal CH_3), 1.24 (sing, 14H, alkane chain H), 1.48 (quin, 2H, NH-CH_2-*CH_2*-CH_2), 2.504 (mult, DMSO), 3.26 (quart, 2H, NH-*CH_2*-CH_2), 3.46 (sing, 3H, HOPO-*CH_3*), 6.51 (doub, 1H, HOPO ring H), 7.19 (doub, 1H, HOPO ring H), 8.44 (trip, 1H, CO-*NH*-CH_2).

^{13}C NMR (400MHz, DMSO) (Figures A.33, A.34, A.35): low-field, 10C, 13.9, 22.1, 26.4, 28.7 (two?), 28.9, 29.0 (two), 31.3, 36.8, 39.0; high-field, 6C, 102.4, 116.9, 127.6, 148.1, 158.0, 165.6.

Elemental analysis of $C_{17}H_{28}N_2O_3$ (308.41g/mol) calc%(found%): C 66.20 (64.81), H 9.15 (9.06), N 9.09 (8.88).

3-benzyloxy-1-methyl-2-pyridinone-4-n- octadecylcarboxamide (11d) (Figure 5.14).

N-methyl-3-benzyloxy-2-pyridinone-4-carboxylic acid [117, 100] (11a) (0.90g, 3.49mmol) was dissolved with stirring in a dry 100mL single-neck round-bottom flask in dry methylene chloride (75mL) along with 2-mercaptothiazoline (0.41g, 3.49mmol) and a catalytic amount of dimethylaminopyridine (DMAP) (0.04g, 0.3mmol). Dicyclohexylcarbodiimide (DCC) (0.80g, 3.90mmol) was added and the solution slowly turned yellow. The flask was wrapped in aluminum foil (compound 11b is light-

sensitive) and allowed to stir overnight.

The solution was filtered on a M-grade glass frit to remove the dicyclohexylurea (DCU) solids; the solids were washed with dry methylene chloride, until all visible yellow was rinsed through the frit, to assure high yield. Four-fifths of the methylene chloride was evaporated from the product, and then isopropanol (40mL) was added to the flask. The activated intermediate precipitated from solution in the form of bright yellow crystals. The remainder of the methylene chloride was evaporated, and the crystals in isopropanol were placed in a cold-room (4°C). The activated intermediate, compound 11b (1.00g, 2.90mmol), was filtered on a M-grade glass frit and dried in a vacuum oven overnight at room temperature. Yield: 83%.

Compound 11b (1.00g, 2.90mmol) was dissolved in dry methylene chloride (30mL). Octadecylamine (11c) (0.78g, 2.90mmol) was added as the solid to the stirring solution, and the solution gradually lost its yellow color. The solution was covered with aluminum foil and stirred overnight; a slight yellow color after 20h was detected, so a small amount (approx. 0.05g) of the amine was added to the solution. After 1h there was no detectable color to the reaction solution. Formation of the product can be followed with silica TLC, and the product appears as a bright blue spot under UV light.

The product was purified with two basic (1M NaOH) and one acidic (1M HCl) extraction. Some solid appeared between the two liquid layers, and it contained some product, so another acidic extraction was performed on the solid. The solvent was evaporated, and a snow-white powder remained, compound 11d (1.47g, 2.88mmol). Yield: 99%.

^{1}H NMR (300MHz, $CDCl_3$) (Figures A.36, A.37): 0.87 (trip, 3H, terminal CH_3), 1.17-1.33 (mult, 32H, alkane chain H), 3.20 (quart, 2H, NH-CH_2-CH_2), 3.60 (sing, 3H, HOPO-CH_3), 5.37 (sing, 2H, O-CH_2-Bn), 6.81 (doub, 1H, HOPO ring H), 7.11 (doub, 1H, HOPO ring H), 7.26 (sing, $CDCl_3$), 7.36-7.46 (mult, 5H, Bn), 7.90 (sing, 1H, CO-NH-CH_2).

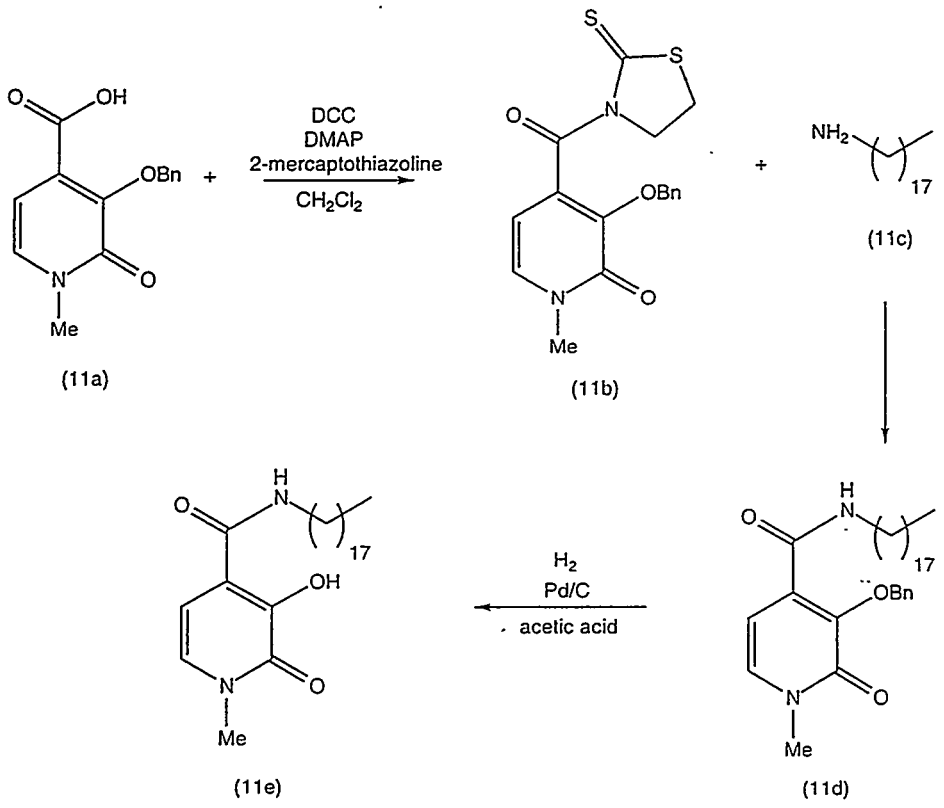

Figure 5.14: Schematic diagram of the synthetic route to 3,2-HOPO-octadecylamide, showing both the protected ligand (11d) and the deprotected ligand (11e).

3-hydroxy-1-methyl-2-pyridinone-4-n- octadecylcarboxamide (11e) (Figure 5.14).

Compound 11d was deprotected by hydrogenation. Compound 11d (1.47g, 2.88mmol), which does not dissolve in methanol, was dissolved in acetic acid (30ml) in a small Schlenk tube, along with 10% Pd/C catalyst (0.15g). The tube was purged three times with H_2, then allowed to react overnight under H_2 with vigorous stirring. The deprotected product appeared to come out of solution. The catalyst and product were filtered onto a F-grade glass frit. A number of solvents were tested for product solubility; methylene chloride dissolved the product, but not very quickly. When methylene chloride was used to filter the product from the catalyst, the methylene chloride evaporated under the reduced pressure and the glass frit was clogged. Boiling ethyl acetate was used to filter the product from the catalyst (used a 500mL F-grade glass frit, heated in an oven before use, and one quick filtration motion), and upon cooling the ethyl acetate, a beige solid precipitated from solution. The solution was placed in a cold-room (4°C), and later the product was filtered and washed with cold ethyl acetate. The product, compound 11e (0.75g, 1.78mmol), was dried overnight in a vacuum oven at room temperature. The yield for this step was lower due to many losses during the filtration. Yield: 62%.

^{1}H NMR (300MHz, $CDCl_3$) (Figures A.38, A.39): 0.85 (trip, 3H, terminal CH_3), 1.22-1.30 (mult, 30H, alkane chain H), 1.57 (quin, 2H, NH_2-CH_2-*CH_2*-CH_2), 3.41 (quart, 2H, NH-*CH_2*-CH_2), 3.61 (sing, 3H, HOPO-*CH_3*), 5.27 (sing, 1H, HOPO ring H), 6.86 (sing, 1H, HOPO ring H), 7.26 (sing, $CDCl_3$), 7.80 (trip, 1H, CO-*NH*-CH_2).

^{13}C NMR (400MHz, $CDCl_3$) (Figures A.40, A.41): low-field, 14C, 14.0, 22.6, 26.9, 29.2, 29.3, 29.4, 29.5 (two), 29.6 (five?); high-field, 6C, 106.3, 118.6, 126.7, 144.9, 159.1, 163.4.

Elemental analysis of $C_{25}H_{44}N_2O_3$ (420.63g/mol) calc%(found%): C 71.38 (68.74), H 10.54 (10.20), N 6.66 (6.34).

5.1.3 Ligand Synthesis: 1,2-HOPOs

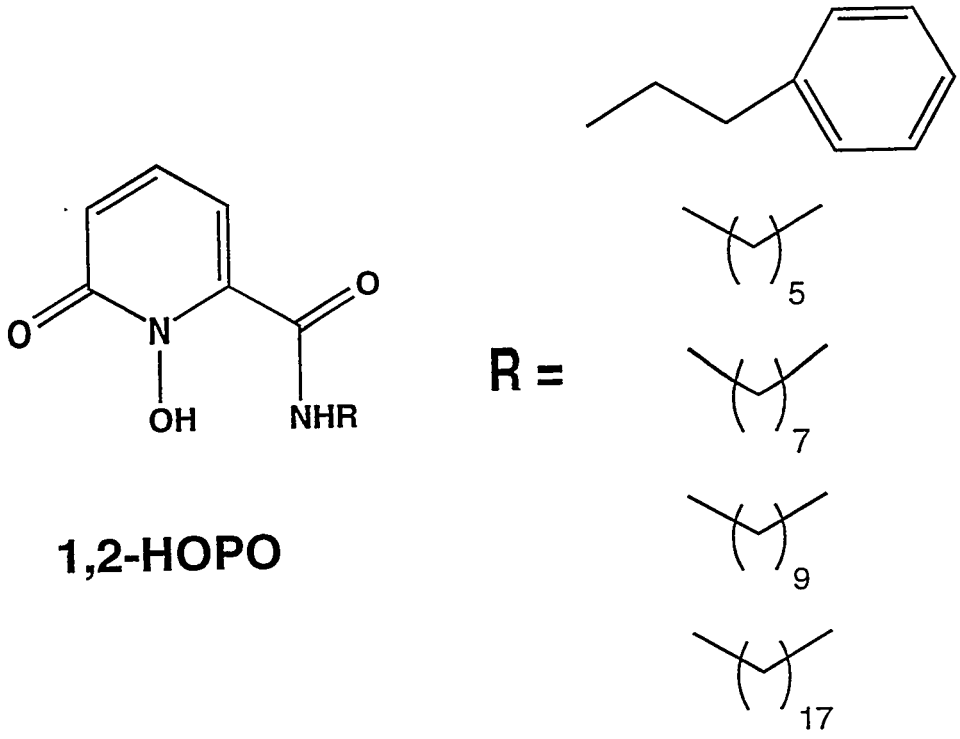

Figure 5.15: The 1,2-HOPO chelating moiety, and the side chains used to render it organophilic.

The synthesis of three 1,2-HOPO liquid/liquid extractants (Figure 5.15) was performed by Dr David White in the Raymond laboratories at the University of California, Berkeley, and described in references [118, 104]. Because these ligands were so difficult to synthesize, they were only available in small quantities for extraction studies.

5.2 Characterization

5.2.1 Spectrophotometric Titration of 3-hydroxy-2-pyridinone propylamide with Th(IV)

All titration solutions were prepared using deionized, distilled water, which was further purified using a Millipore cartridge system (resistivity 18 MΩ-cm). The water was degassed by boiling it for at least twenty minutes with argon bubbling through it. Once prepared, the water was stored under argon atmosphere to prevent dissolution of carbon dioxide. Titrant solutions were prepared from carbonate-free Baker Dilut-It concentrates. The base (0.1 M KOH) was standardized against potassium hydrogen phthalate; the acid (0.1 M HCl) was standardized against the standardized KOH solution. Phenophthalein was used as the indicator in both cases. The ionic strength of all solutions, unless otherwise indicated, was adjusted to 0.100 M, using 0.100 M KCl. The KCl (Fisher 99.99%) was used without further purification. The pH electrode (Orion Semimicro Ross combination glass pH electrode) was calibrated in concentration units by titrating 2.00 mL of standardized HCl in 50.00 mL 0.100 M KCl solution with 4.200 mL of standardized KOH. The calibration titration data were analyzed by a non-linear least-squares refinement program [119].

The thorium solution was prepared with $ThCl_4$ from Aldrich. Since this salt is hygroscopic, an ethylenediamine tetraacetic acid (EDTA) titration was performed to standardize the solution [120]. A 0.01000 M EDTA solution was used to titrate 2.00 mL of the thorium solution, with pyrocatechol violet indicator and a few drops of 6 M HCl, to the yellow endpoint. This titration was performed five times.

The ligand, 3-hydroxy-2-pyridinone propylamide (3,2-HOPO-propylamide), was synthesized and characterized in the Raymond laboratory at the University of California, Berkeley, as discussed previously (pages 96, 99). The ligand was weighed on a Cahn Model 4400 Electrobalance, and dissolved in purified water in a 10.00 mL volumetric flask. This solution was 0.006778 M in the ligand, and was used for all the titrations below. Before the titration began, UV/Vis spectra of the protonated and deprotonated ligand were collected (Figure 5.16), along with the spectra of each

of the 1:1, 2:1, 3:1, and 4:1 ligand/metal species (Figure 5.17). These spectra were used to aid in the refinement performed by REFSPEC.

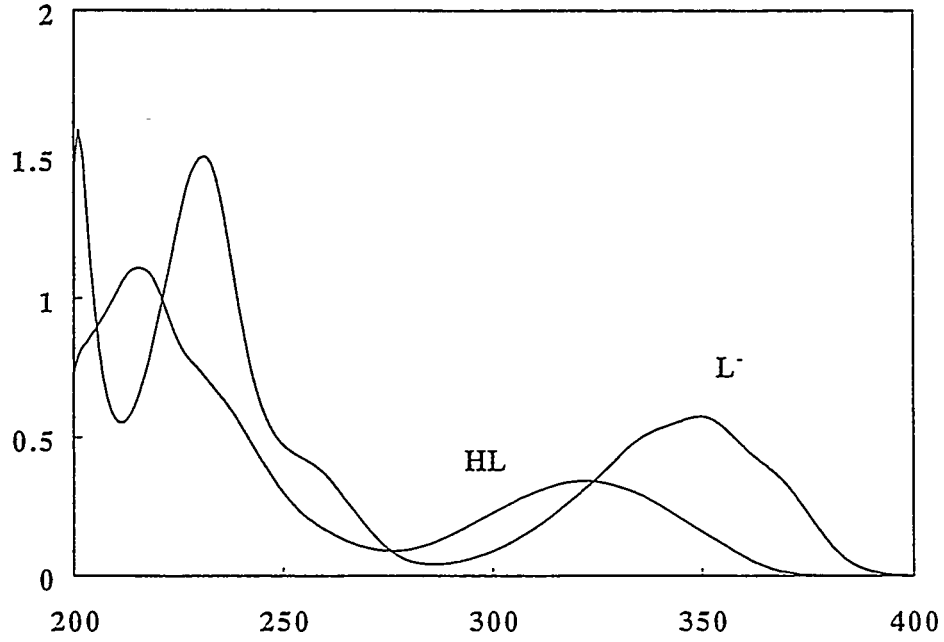

Figure 5.16: The UV/Vis spectra for both the protonated and deprotonated 3,2-HOPO-propylamide; plotted is absorbance versus wavelength (nm).

A volumetric pipette was used to measure 50.00 mL of 0.100 M KCl into a clean, dried Schlenk tube, which was kept under argon atmosphere. The solution was acidified with 2.00 mL of 0.100 M HCl, followed by the addition of 738 μL (3.387 x 10^{-6} mol) of 4.59 mmol 3,2-HOPO-propylamide and 22.4 μL (8.467 x 10^{-7} mol) of 37.8 mmol Th(IV). The total volume in the tube before titration was 52.760 mL. The titration was performed from pH = 2.3 to pH = 6.1, and not taken higher in pH because of the precipitation of thorium hydroxide beyond pH = 6.1.

The titration was repeated twice to insure reproducibility of results.

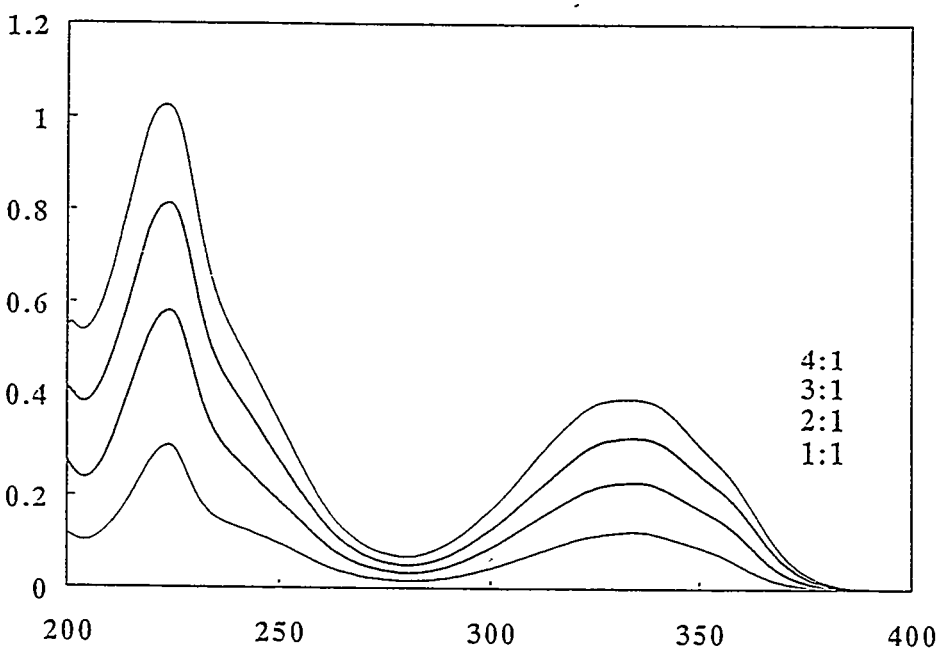

Figure 5.17: The UV/Vis spectra for the 1:1, 2:1, 3:1, and 4:1 ligand/metal species of 3,2-HOPO-propylamide with Th(IV); plotted is absorbance versus wavelength (nm).

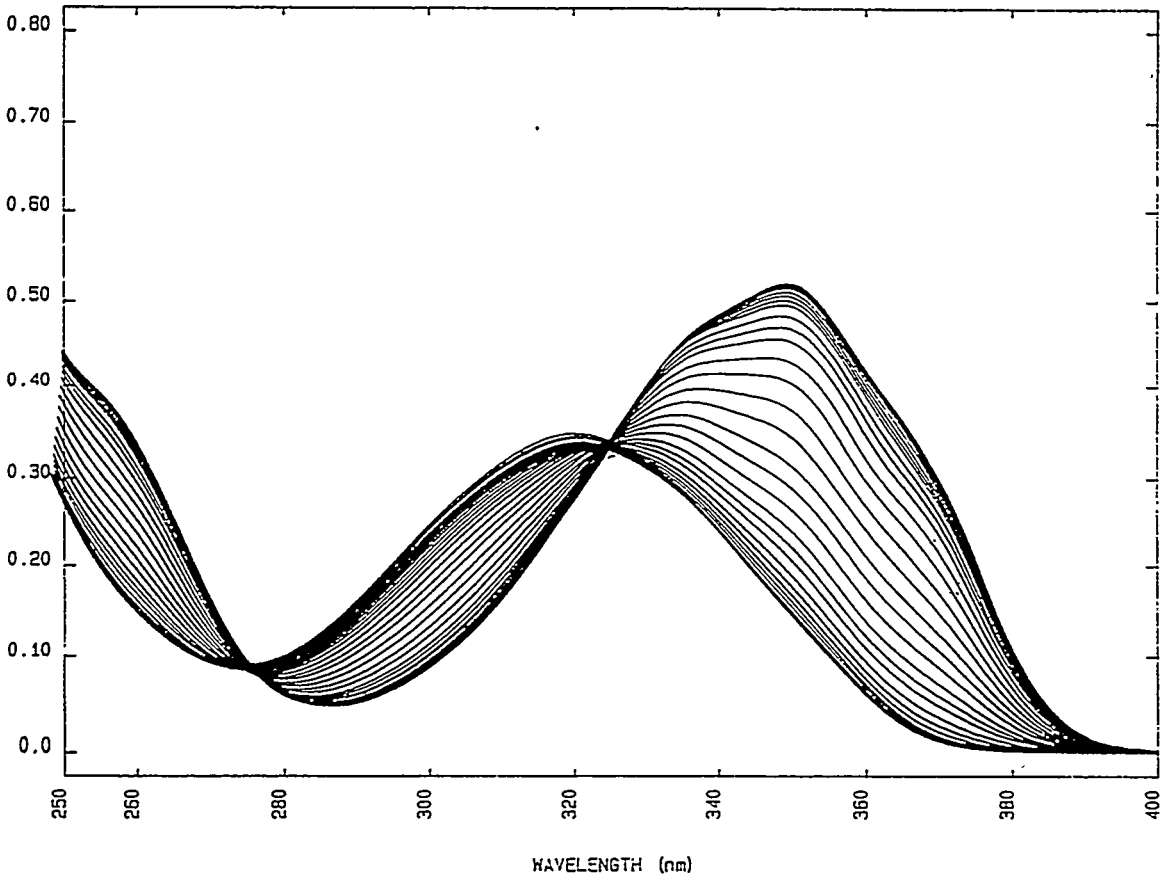

Figure 5.18: UV/Vis spectra taken during the titration of 3,2-HOPO-propylamide and Th(IV); pH ranges from 2.3 to 6.1.

5.2.2 Extraction Studies

The liquid/liquid extractions were carried out in two laboratories: iron extractions were performed in Professor Ken Raymond's laboratory at the University of California, Berkeley, and the plutonium extractions were conducted at Lawrence Livermore National Laboratory's (LLNL) Glenn T. Seaborg Institute for Transactinium Science (GTS-ITS). In each facility, the extractions were performed in an identical manner, outlined below.

The ligand to be tested was weighed in a vial, and an organic solvent was pipetted into the vial to bring the concentration of the ligand into the range of $\sim$ 2–3 mM. The ligand was dissolved, using shaking and/or heating when required, and a rough estimate of its solubility was recorded. A volume of this organic phase was then pipetted into a 1.5 mL microcentrifuge tube along with an equivalent volume of the aqueous phase to be tested. The aqueous phase contained radioactive isotopes of either ^{55}Fe or ^{242}Pu, depending upon which metal extraction was being investigated. Kinetic studies were the primary method used to determine the efficacy of a specific ligand in an organic solvent, although a small number of concentration and competition studies were performed with some of the best ligands. For the kinetic studies, five microcentrifuge tubes were prepared with the same organic and aqueous phases, and shaken with a vortex-style mixer for 1, 5, 10, 20, and 60 minutes. After mixing, each tube was centrifuged for one minute to aid in the separation of the phases. An aliquot of each phase was pipetted from the tube into a scintillation vial, mixed with a scintillation cocktail, and scintillation counted to determine the amount of the radioactive species present in each phase after extraction.

All of the organic phases had rather low concentrations ($\sim$ 2–5 mM) of the ligands, but always had concentrations in excess of the aqueous metal ($\sim$ 0.1 mM) to be extracted. Low organic phase concentrations of the ligand were used for three very practical reasons:

1. Small concentrations of the ligand were used to minimize the amount of the radioactive metal needed in the aqueous phase, thus reducing the total amount of mixed waste generated.

2. Because the ligands were sometimes difficult to synthesize, there were often very small amounts of them available for testing.

3. The solubility of some of the ligands was low.

The organic phases which were tested were chosen because of their good extraction properties, and because they are solvents which are commonly used by engineers working in nuclear fuel reprocessing or related industries. These solvents, and some of their properties, are listed in Table 5.1. None of the solvents were pre-treated in any manner.

Table 5.1: Organic solvents used in this study, along with some of their physical properties.

Property	1-octanol	MIBK †	kerosenes	dodecane
Formula	$C_8H_{18}O$	$C_6H_{12}O$	C_{10}–C_{16}	$C_{12}H_{26}$
Mol. Weight (g/mol)	130.22	100.16	varies	170.34
Boiling Point (°C)	195	118	varies	216
Density (g/ml)	0.83	0.80	0.80	0.75
Flash Point (°C)	81	55	132	132
Water solubility (%)	0.1	1.9	0.0	0.0
Toxic?	No	Yes	Yes	Yes

† — MIBK ≡ methyl isobutyl ketone.

Two different aqueous phases were used in this study, one of high ionic strength (Aqueous A), and one of low ionic strength (Aqueous B). Each aqueous phase was extracted by the various combinations of ligand and organic solvent used in this study.

The error assigned to the extraction data was from two sources: counting error and pipetting error. The counting error, usually the smaller of the two errors, was calculated using the formula

$$\sigma = \sqrt{N}, \tag{5.1}$$

where N is the total number of recorded counts (and the half-life of the radioisotope is long relative to the measurement time). The error in these data was dominated

by the pipette (volume) error, which was determined by massing multiple aliquots of each phase, and determining the average volume variation of each pipette used for each phase. The pipetting of the aqueous phase accounted for a small fraction of the pipette error, while the organic phase, because of volatility and other properties which made pipetting difficult, accounted for a much larger fraction of the error. Overall errors for some of the data are as high as $\sim$ 10%, due to multiple pipettings.

Iron Extraction Studies

Liquid/liquid extractions with radioactive ^{55}Fe were conducted in the manner outlined on page 120, above. The chemicals were all used without further purification: the nitric acid and iron(III) nitrate were from Fisher Scientific, and the sodium nitrate was from Mallinckrodt. The ligands were weighed on a Mettler Toledo AT200 balance. The pipettes were manufactured by Fisher Scientific, and were used with pipette tips from Eppendorf; the microcentrifuge cones were made by E & K Scientific Products. The phases were mixed with a Model 16715 vortex-style mixer manufactured by Thermolyne, and centrifuged in a Fisher Scientific Microcentrifuge Model 59A. The ^{55}Fe was counted in Kimble 20 mL borosillicate glass scintillation vials, with 10 mL of Fisher ScintiSafe Plus 50% scintillation cocktail, in a Mark V-5303 scintillation counter manufactured by TM-Analytic. The scintillation counter used an energy window from 2.0 keV to 7.0 keV.

The ^{55}Fe aqueous phases were prepared with deionized water, and their total composition was:

Aqueous A (high ionic strength)

- sodium nitrate ($NaNO_3$, 84.99 g/mol): 5.0001 M
- nitric acid (HNO_3, 15.8 M): 0.1000 M (pH = 1)
- iron(III) nitrate ($Fe(NO_3)_3 \cdot 9H_2O$, 404.00 g/mol): 0.1001 mM
- iron-55 chloride ($^{55}FeCl_3$, 1.0 μCi/μL on 6/92): 100 μL

Aqueous B (low ionic strength)

- sodium nitrate ($NaNO_3$, 84.99 g/mol): 0.1006 M
- nitric acid (HNO_3, 15.8 M): 0.1000 M (pH = 1)
- iron(III) nitrate ($Fe(NO_3)_3 \cdot 9H_2O$, 404.00 g/mol): 0.1001 mM
- iron-55 chloride ($^{55}FeCl_3$, 1 μCi/μL on 6/92): 100 μL

The 100 μL of $^{55}FeCl_3$ that was added to each phase did not significantly alter the Fe(III) total concentration, but was enough radioactivity to be quickly counted in the scintillation counter.

^{55}Fe is a radioactive nucleus, emitting only a very weak 6.5 keV x-ray after the rearrangement of orbital electrons that accompanies nuclear electron capture (EC). Its half-life is short ($t_{1/2}$= 2.73 years), and therefore a relatively small number of atoms will give many radioactive decays. The ^{55}Fe used in these extraction studies is from a solution that had an original activity of 1 μCi/μL on 6/92. Its current activity can be calculated using

$$A = A_0 \exp(-\lambda t), \tag{5.2}$$

where A_0 is the initial activity, λ is the decay constant, and t is the time since measurement of A_0. Solving this equation for the ^{55}Fe used in these studies gives a current activity of $A = 0.3$ μCi/μL, giving Aqueous A and B $\sim$ 30 μCi total activity.

For the iron studies, 500 μL of both organic and aqueous phase were mixed in a centrifuge cone for each extraction. A 200 μL aliquot of each phase was used for scintillation counting. If the ligand extracted 100% of the radioactive ^{55}Fe into the organic phase, this would give

$$\frac{2}{5}\left(\frac{0.5mL}{100mL} \times 30\mu Ci\right) = 0.06\mu Ci\left(\frac{2.2 \times 10^6 cpm}{1\mu Ci}\right) = 132,000 \; counts\ per\ minute$$

for scintillation counting of the organic phase. When the results of the scintillation counting were corrected for the efficiency of the counter, a 100% extraction into the organic phase gave $\sim$ 162,000 dpm, quite close to the estimated number above, given the probable error in the quoted activity of the initial 1 μCi/μL $^{55}FeCl_3$ solution.

The efficiency of the scintillation counter was measured by an external ^{133}Ba source brought underneath each vial. This radioisotope, like ^{55}Fe, decays by electron capture, and gives off a slightly more energetic x-ray. Its absolute count rate is known (certified by the manufacturer), thereby allowing the determination of the counter efficiency. On average, the efficiency was only $\sim 40\%$.

The concentrations of the ligands in the various organic solvents are listed in Table 5.2, along with their qualitative degree of solubility. If a ligand is not listed for a particular solvent, it was not soluble.

Table 5.2: The concentrations of the ligands used for the ^{55}Fe extraction studies, along with their molecular weights and qualitative degrees of solubility.

Ligand †	Mol. W. (g/mol)	Organic Solvent	Conc. (mM)	Dissolution ‡
1,2-HOPO-6	238.28	1-octanol	2.5	VF
		MIBK *	2.8	VF
		kerosene	3.1	VS
		dodecane	3.5	VS
1,2-HOPO-8	266.34	1-octanol	3.4	VF
		MIBK	2.9	VF
3,2-HOPO-6	252.31	1-octanol	3.0	VF
		MIBK	2.8	VF
3,2-HOPO-8	280.37	1-octanol	2.2	VF
		MIBK	2.2	VF
3,2-HOPO-10	308.42	1-octanol	2.2	F
		MIBK	2.3	F
3,2-HOPO-18	420.63	1-octanol	2.1	VS
3,2-HOPO-pp	286.33	1-octanol	2.1	VS
		MIBK	2.2	F
3,4-HOPO-6	266.34	1-octanol	2.5	F
		MIBK	2.7	S
3,4-HOPO-8	295.33	1-octanol	2.3	F
		MIBK	2.1	S
3,4-HOPO-10	322.44	1-octanol	2.0	F
		MIBK	2.1	VS
3,4-HOPO-18	435.57	1-octanol	1.9	VS
3,4-HOPO-pp	300.36	1-octanol	2.6	P

† — 1,2-HOPO-6 ≡ 1,2-hydroxypyridinone-hexylamide, etc.
‡ — VF ≡ very fast, F ≡ fast, S ≡ slow, VS ≡ very slow, P≡ partial.
* — MIBK ≡ methyl isobutyl ketone.

Plutonium Extraction Studies

The bulk of the extraction work was conducted at the Glenn T. Seaborg Institute for Transactinium Science (GTS- ITS), located at LLNL. GTS-ITS is an ideal laboratory setting for this study because of its unique instrumentation and equipment, both within the Institute and lab-wide, with which to handle and experiment with radioactive materials. All of the plutonium used for these experiments was handled inside a VAC Model HE-43-2 inert atmosphere (argon) glovebox operated at negative pressure.

Liquid/liquid extractions with radioactive ^{242}Pu were conducted in the manner outlined in page 120, above. The chemicals were all used without further purification: the sodium nitrate and ethylenediamine tetraacetic acid (EDTA) were from Fisher Scientific; the nitric acid, hydrochloric acid, ascorbic acid, and ferric chloride were from J.T. Baker Chemicals; the potassium iodide was from Mallinckrodt. The ligands were weighed on a Mettler Toledo AT201 balance. The pipettes were manufactured by Fisher Scientific and Eppendorf, and were used with pipette tips from Eppendorf; the microcentrifuge cones were made by Fisher Scientific. The phases were mixed with a vortex-style REAX 2000 shaker/mixer manufactured by Caframo, which was equipped with a tray to accommodate 24 microcentrifuge cones, and centrifuged in a Tomy HF-120 Capsule minicentrifuge. The ^{242}Pu was counted in Kimble 20 mL polyethylene scintillation vials, with 18 mL of Packard Hionic-Fluor scintillation cocktail, in a Tri-Carb 2700TR scintillation counter manufactured by Packard Instrument Company. The scintillation counter used an energy window from 2.3 MeV to 7.8 MeV. All UV/Vis spectra were measured with a PC Plug-in Spectrometer PC1000, and irradiated with a xenon lamp. Alpha spectrometry was accomplished with a Canberra Alpha Spectrometer, Model 7401VR.

The plutonium stock solution, which was used for all the plutonium extraction studies, was prepared from $\sim$ 200 mg of ^{242}Pu, in the form of the oxide, PuO_2. The brownish powder was obtained from Dr Ken Moody of LLNL's Isotope Science Division. It was reported as 99.84% (atomic) pure ^{242}Pu (the isotopic composition of the sample is listed in Table 5.3; for the half-lives and decay energies of all the

Table 5.3: Isotopic composition of the plutonium sample, as determined by thermal ionization mass spectrometry.

Isotope	Abundance (%)
^{238}Pu	0.0098
^{239}Pu	0.0040
^{240}Pu	0.1038
^{241}Pu	0.0468
^{242}Pu	99.8356

radioactive species mentioned in this section, see page 62), but nearly one-half of the alpha activity from the resultant solution was due to ^{241}Am (Figure 5.19). The americium in the sample is from the beta-decay of ^{241}Pu. A simple anionic column wash, described below, was performed [121] to rid the plutonium stock solution of the ^{241}Am that had grown-in since the last purification.

The solid plutonium oxide (200 mg, 0.73 mmol) was slowly dissolved in 15 mL of 10 M HCl plus one drop of concentrated HF. The solid was very slow to go into solution; shaking, and agitation with a pipette tip, were used to help the dissolution, which was complete after 3 hours. The plutonium was in the +4 oxidation state, and the solution was a red/brown color.

A large Bio-Rad quartz column was loaded with 8 mL Bio-Rad AG1x8 (200-400 mesh) anionic ion-exchange resin. The column was packed and rinsed with filtered deionized water, then preconditioned with three full-column-volumes (FCVs; equal to one-half the apparent volume, hence 4 mL) of 10 M HCl. The plutonium solution in 10 M HCl was sorbed on the column, and a brown/red band formed on the top-most portion of the resin. The column was washed with two FCVs of 10 M HCl, and collected because it contained the ^{241}Am (the separation time was 13:30 PST, 13 November 1993) (Figure 5.20). The plutonium was eluted by reduction to the +3 oxidation state using a 7:1 solution of 10 M HCl:5 M HI, warmed to 40°C to speed the redox kinetics. The elutant came off the column as bright blue Pu(III), in a fairly tight band of no more than two FCVs. Additional reductant was washed

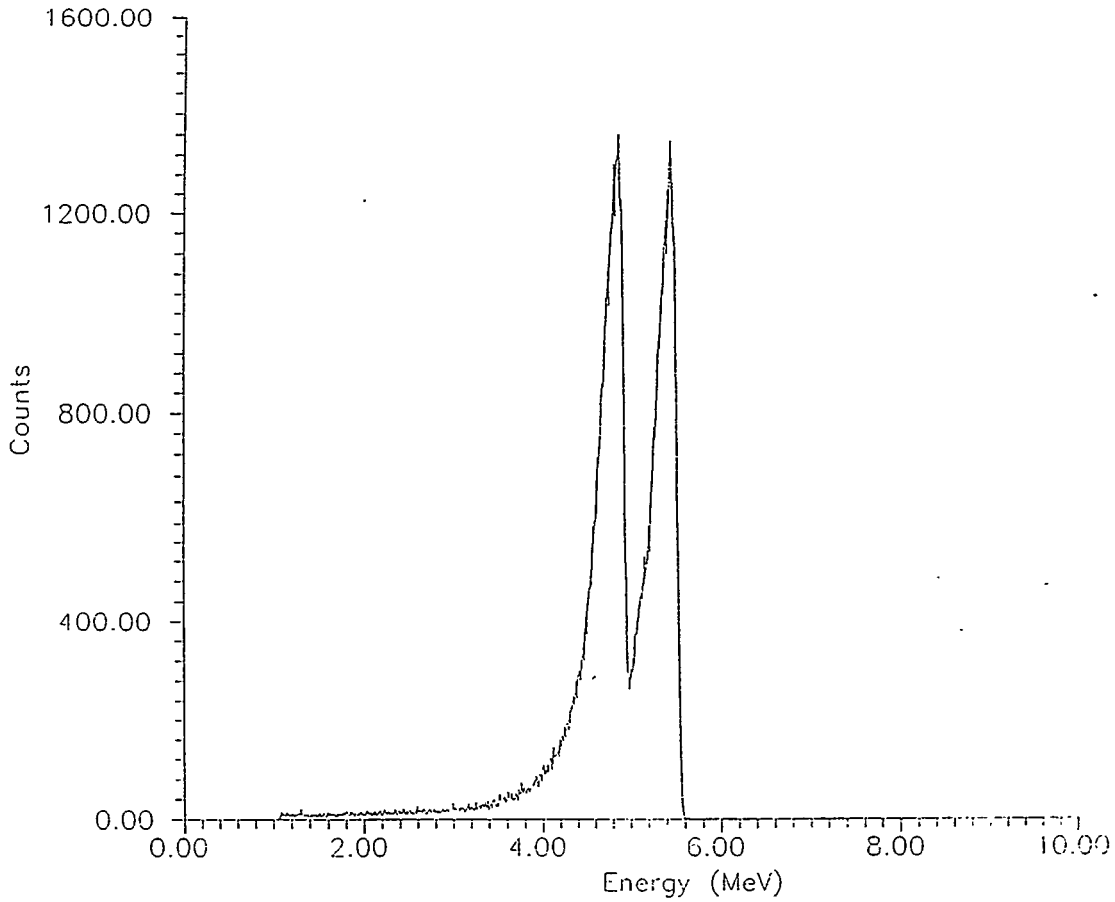

Figure 5.19: The alpha spectrum of the dissolved plutonium sample, before separation. Notice that the higher energy peak, ^{241}Am, is nearly as large as the lower energy peak, ^{242}Pu.

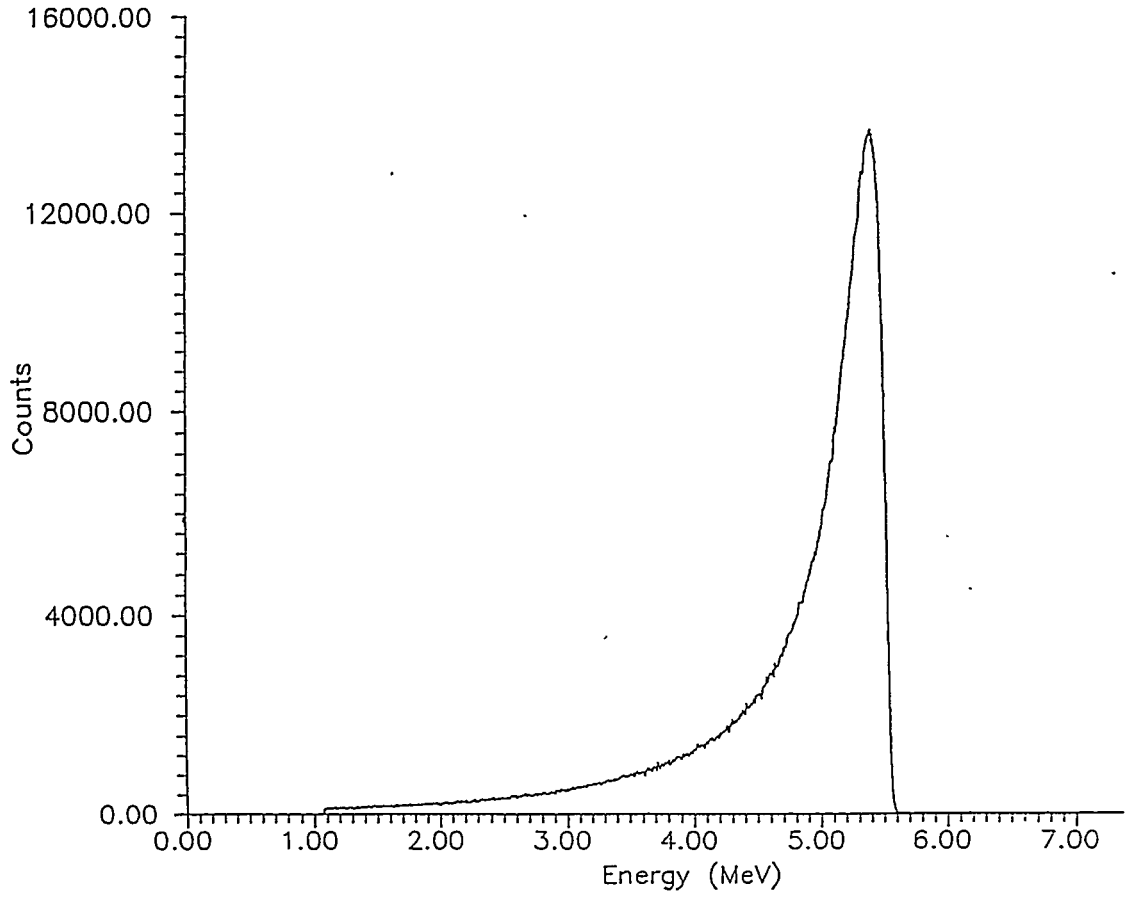

Figure 5.20: The ^{241}Am washed off the column with strong (10 M) HCl. The long tail is due to the energy loss of the alpha particles through the thick sample.

through the column to assure complete elution, then the column was rinsed with 0.5 M HCl to strip any additional radioactivity. The fractions were analyzed using alpha spectrometry (stippling and drying a 10 μL aliquot from each fraction) and UV/VIS spectrometry (Figures 5.21, 5.22).

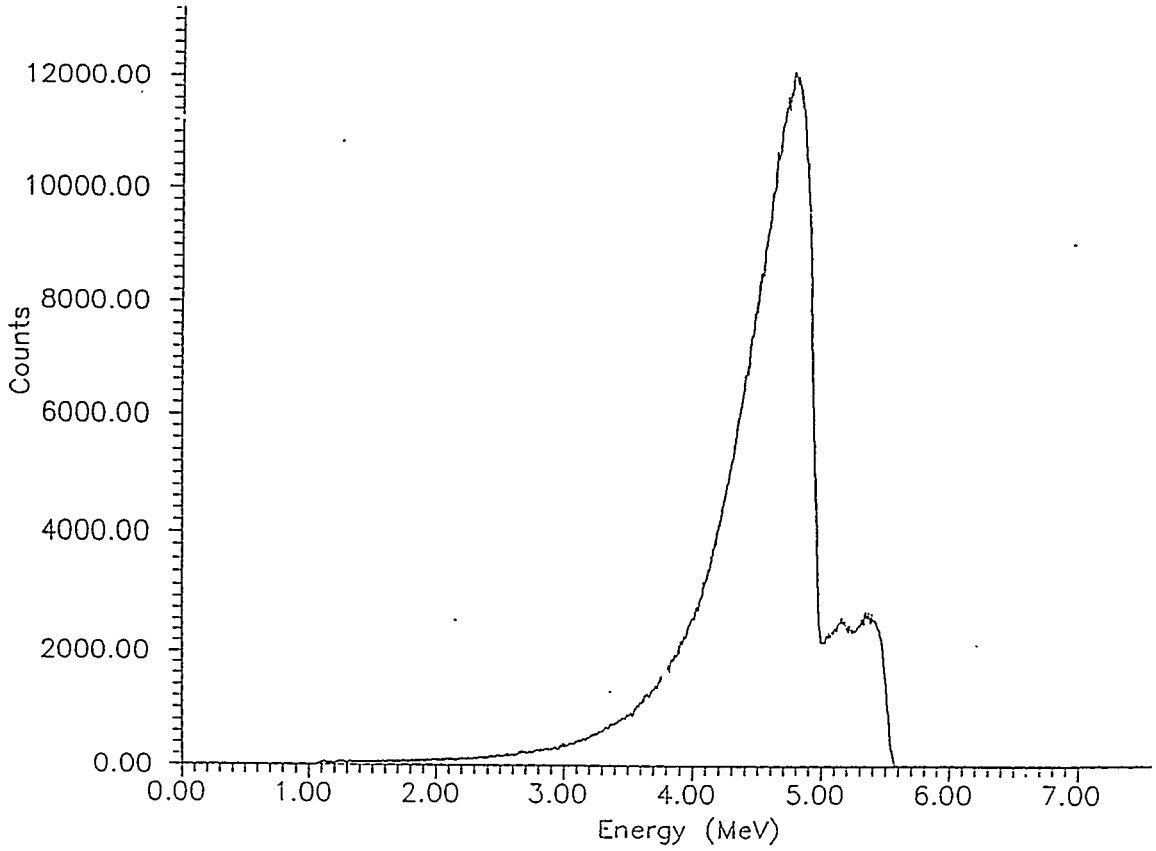

Figure 5.21: The alpha spectrum of the separated plutonium(III) isotopes: the largest peak is the 4.91 MeV ^{242}Pu, the next peak is ^{240}Pu + ^{239}Pu, and the last peak is ^{238}Pu + residual ^{241}Am. The long tailing is due to the energy loss of the alpha particles in the thick sample.

The Pu(III) solution was fumed to remove the HCl, and taken to dryness in a 50 mL single-neck round bottom flask. The remaining solid was dissolved in 8 M HNO_3, and fumed several times until all of the black solid disappeared. The nitric acid solution was a dark green color, indicating that plutonium had been oxidized to the +4 oxidation state. This solution was evaporated to dryness, leaving a black

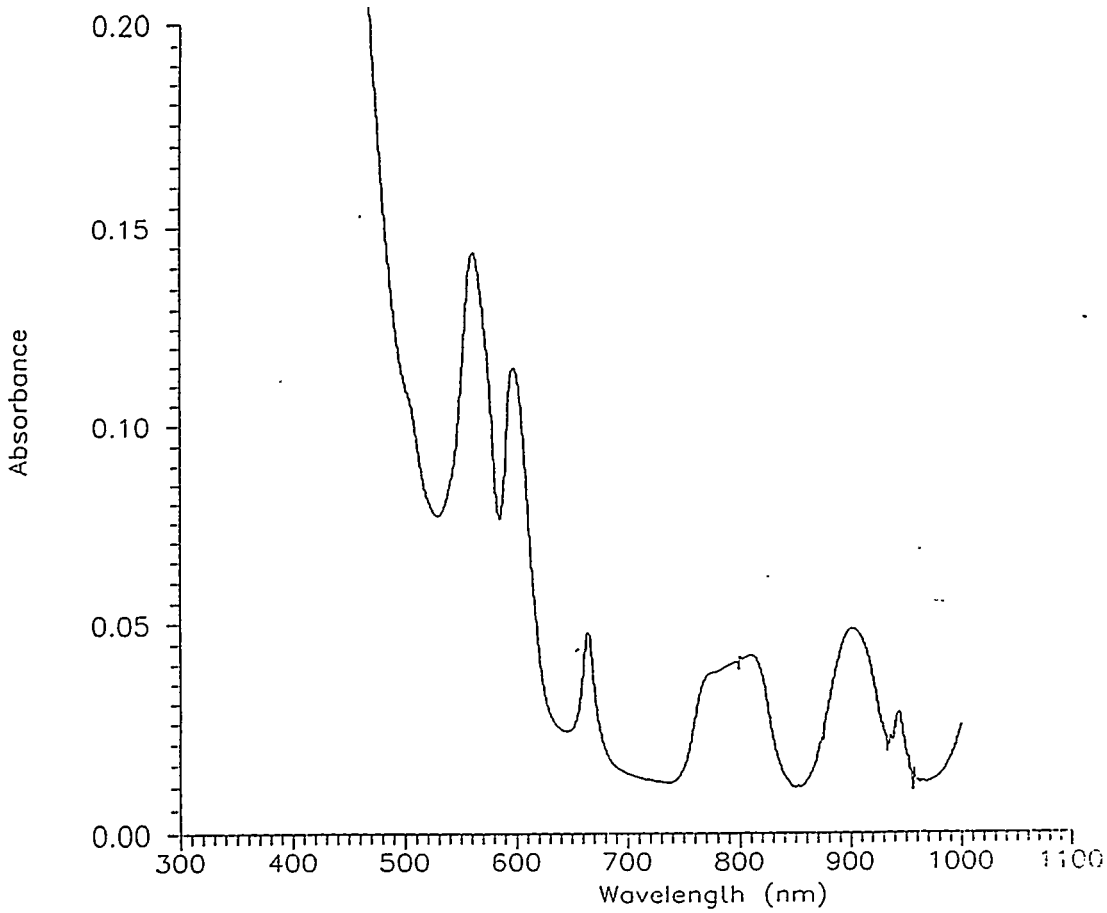

Figure 5.22: The UV/Vis spectrum of the separated plutonium(III).

crusty paste, and then dissolved in 15 mL of 2 M HCl. This solution was heated for 20 minutes, and it turned red/brown in color. UV/Vis spectroscopy of this stock solution revealed plutonium in the +4 oxidation state, and the concentration was adjusted to $\sim$ 0.10 M.

The ^{242}Pu aqueous solutions were prepared with distilled, deionized water, and their total composition was:

Aqueous A (high ionic strength)

- sodium nitrate ($NaNO_3$, 84.99 g/mol): 5.0007 M
- nitric acid (HNO_3, 15.8 M): 1.000 M (pH = 0)
- plutonium-242 chloride ($^{242}PuCl_4$, 0.10 M): 0.10 mM

Aqueous B (low ionic strength)

- sodium nitrate ($NaNO_3$, 84.99 g/mol): 0.1029 M
- nitric acid (HNO_3, 15.8 M): 1.000 M (pH = 0)
- plutonium-242 chloride ($^{242}PuCl_4$, 0.10 M): 0.10 mM

The amount of $^{242}PuCl_4$ in 2 M HCl that was added to each phase (30 μL) did not significantly alter the pH of the final solution, which was targeted for pH = 0.

^{242}Pu is a radioactive nucleus, and its half-life is long (see page 62) relative to most isotopes of plutonium. Thus, it has a relatively low specific activity compared to other plutonium isotopes and is easier to handle safely. Its current activity can be calculated using

$$A = \lambda N, \tag{5.3}$$

where A is the activity, λ is the decay constant, and N is the number of radioactive atoms. Solving this equation for the ^{242}Pu used in these studies yields a current activity of $A = 211$ dpm/μL, giving Aqueous A and B greater than $\sim 6.3 \times 10^6$ dpm total activity.

For the plutonium studies, 200 μL of both organic and aqueous phase were mixed in a centrifuge cone for each extraction. A 100 μL aliquot of each phase was

used for scintillation counting. Extraction of 100% of the radioactive ^{242}Pu into the organic phase gives:

$$\frac{1}{2}(\frac{0.2mL}{30mL} \times 6.3 \times 10^6 cpm) = 2.1 \times 10^4 \textit{ counts per minute}$$

for scintillation counting of the organic phase. The results of the scintillation counting gave $\sim$ 28,000 dpm for $\sim$ 100% extraction into the organic phase, quite close to the estimated number above; however, it is apparent that the plutonium stock solution used was slightly more concentrated than indicated.

The scintillation cocktail used in the ^{242}Pu experiments (Packard's Hionic-Fluor) was made for use with high ionic strength samples, so it proved ideal for these studies. There was no efficiency correction in these experiments, because of the nature of the radioactivity (alpha activity), the quality of the cocktail, and the quality of the scintillation counter; the relative amount of quenching in each sample did not change. There were problems with the stability of the aqueous phase, however. An initial Aqueous A and B were prepared with the same composition as the iron aqueous phases; at that acid concentration (0.1 M, pH = 1) the plutonium activity began to precipitate out of the high ionic strength (Aqueous A) solution (see Figure 5.23). The formation of plutonium polymer has been witnessed in other studies, when the acid concentration was below 0.5 M [122] or the nitrate anion concentration was above 3 M [123]. Therefore, the aqueous phases used for these plutonium extraction studies were maintained at pH = 0 (1.0 M acid) and used quickly (within 48 hours) in order to avoid plutonium polymerization. Figure 5.24 illustrates the concentrations of various Pu(IV) hydrolysis species as a function of pH [124], and shows Fe(III) hydrolysis species for reference. The activity of each aqueous phase was monitored during the extraction procedure to insure that no polymerization was taking place.

Because the plutonium stock solution was last separated from its decay products approximately three years ago, there will be some alpha activity that is not due to plutonium. ^{241}Am, from the beta-decay of ^{241}Pu which is present in a small percentage in the plutonium solution, is the main source of non-plutonium alpha decays. Solving Equation 5.2 to figure how much americium is present and Equation 5.3 to determine its activity yields 1157 $\pm$ 34 dpm, or $\sim$ 5%. If the synthesized ligands are

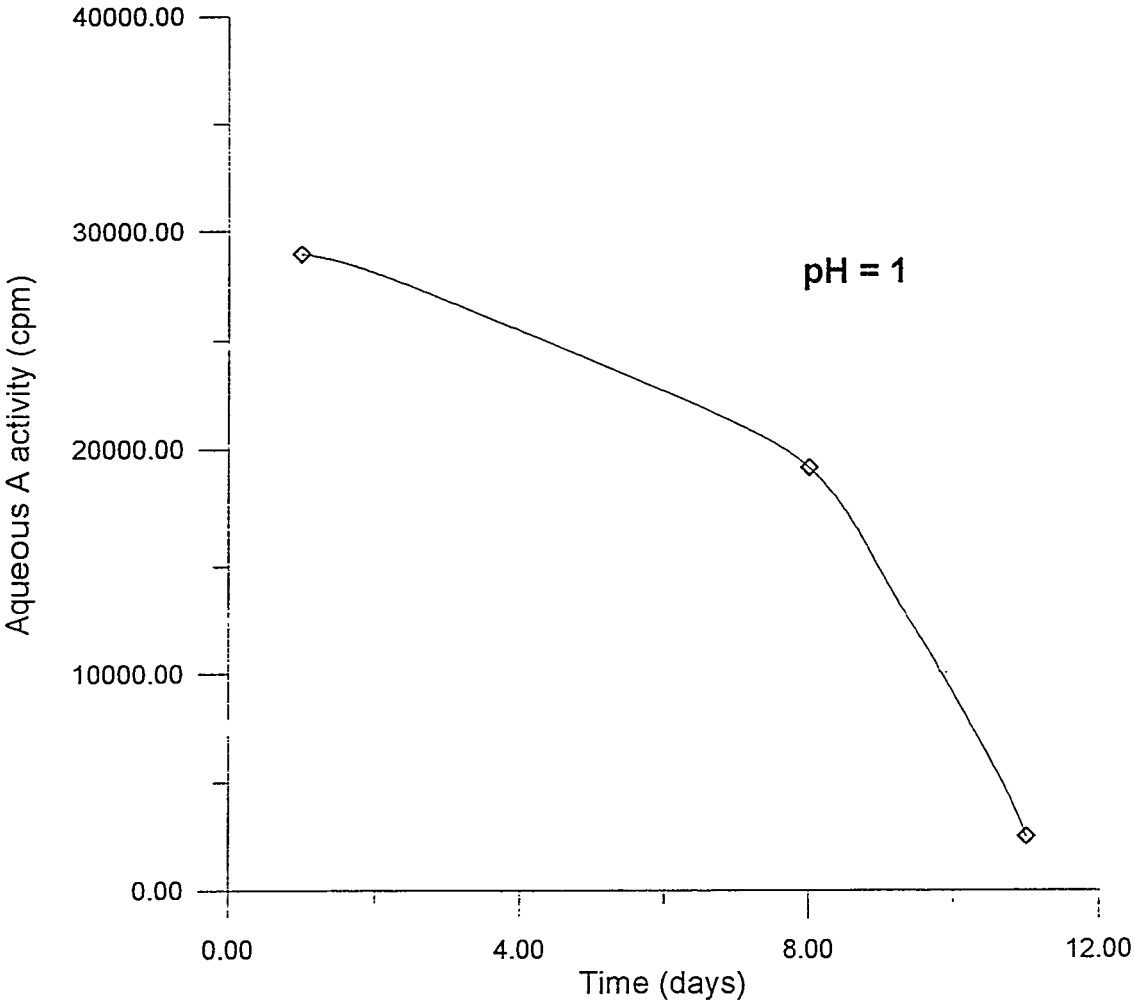

Figure 5.23: Activity of Aqueous A (high ionic strength) as a function of time, with pH = 1; at this pH, the activity precipitates out of solution as plutonium polymer at a fast rate.

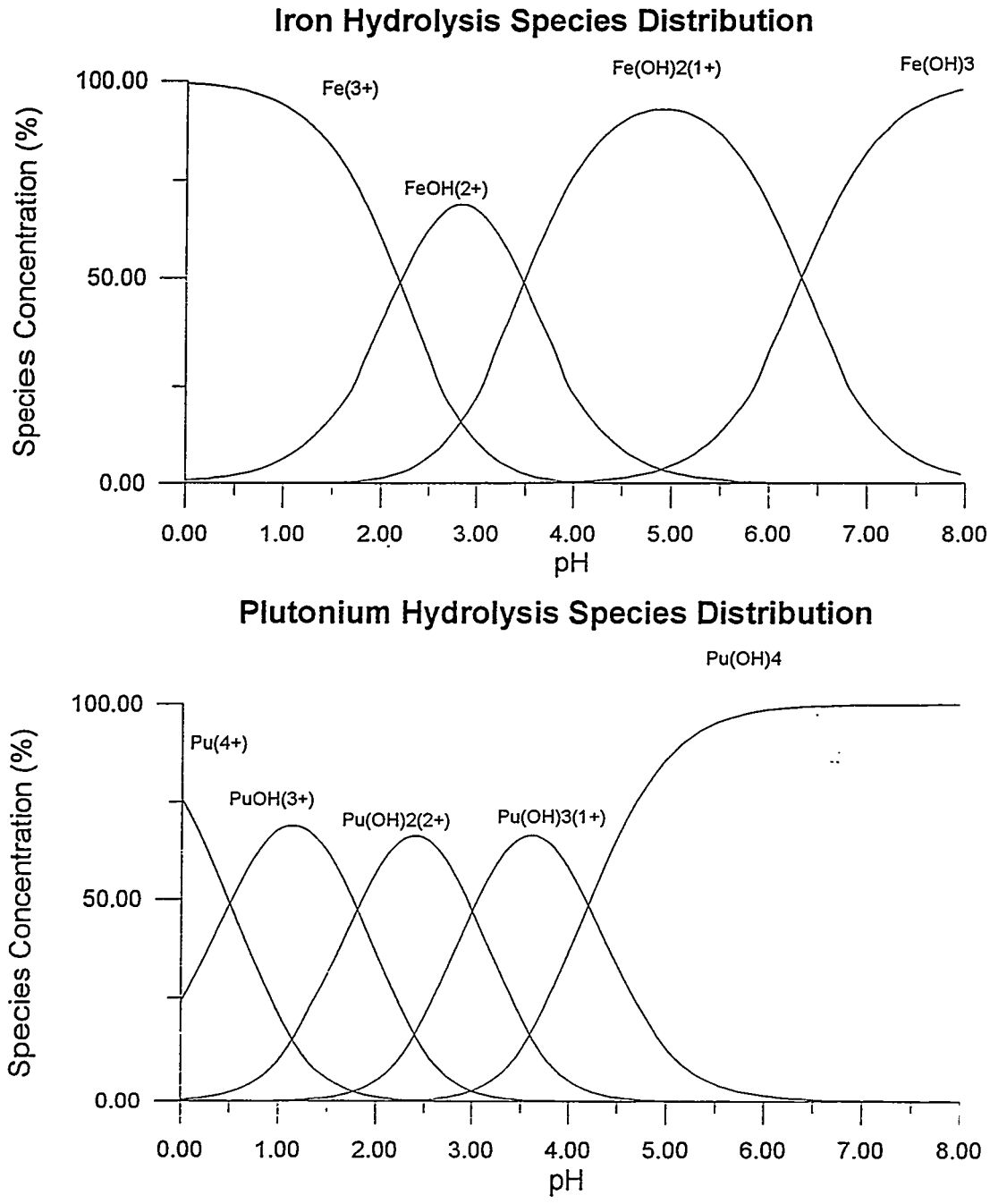

Figure 5.24: Fe(III) and Pu(IV) species distribution calculations, plotting species concentration versus pH. At pH = 1, the concentration of free Pu(IV) is only about 15%; at pH = 0, it increases to about 75%. These calculations were performed for low (10^{-4}M) metal concentrations, like those used in the experiments.

indeed selective for An(IV) cations, then no extraction of the ^{241}Am(III) should be seen. This supposition has been experimentally verified in two ways:

1. The extraction samples have been gamma counted by the Isotope Science Division's Environmental Group at LLNL, to look for the 59.5 keV gamma ray from ^{241}Am. The analysis shows no ^{241}Am above background in the organic samples (after extraction), and the small amount expected in the aqueous samples (see Figure 5.25).

2. The scintillation spectra (Figure 5.26) of the organic and aqueous phases (after extraction) show a peak in the aqueous phase that corresponds to the 5.486 MeV alpha particle from ^{241}Am, proving that $^{241}Am^{3+}$ does not extract. This peak integrates to 1278 $\pm$ 114 cpm, on average, and is consistent with the predicted 1157 $\pm$ 34 dpm figured above.

In the analysis of these extraction data, the experimentally obtained average of 1278 $\pm$ 114 cpm due to ^{241}Am alpha decay was subtracted from all the post-extraction aqueous phases.

The distribution of the uncomplexed ligands was measured in order to estimate their degree of organophilicity. In a microcentrifuge cone, 500 μL of an organic phase with the ligand to be tested was shaken with an equal volume of distilled, deionized water. The use of UV/Vis spectrometry to measure the leaching of the ligand into the aqueous phase required the use of deionized water, as opposed to a salted aqueous phase, because of interference in the spectra. After shaking for 20 minutes, the cones were centrifuged to aid the separation of the layers, and 200 μL aliquots of each phase were added to a cuvette that contained 1 mL of the associated pure phase. The cuvettes were then examined by UV/Vis spectrometry.

The concentrations of the ligands in the various organic solvents are listed in Table 5.4, along with their qualitative degrees of solubility.

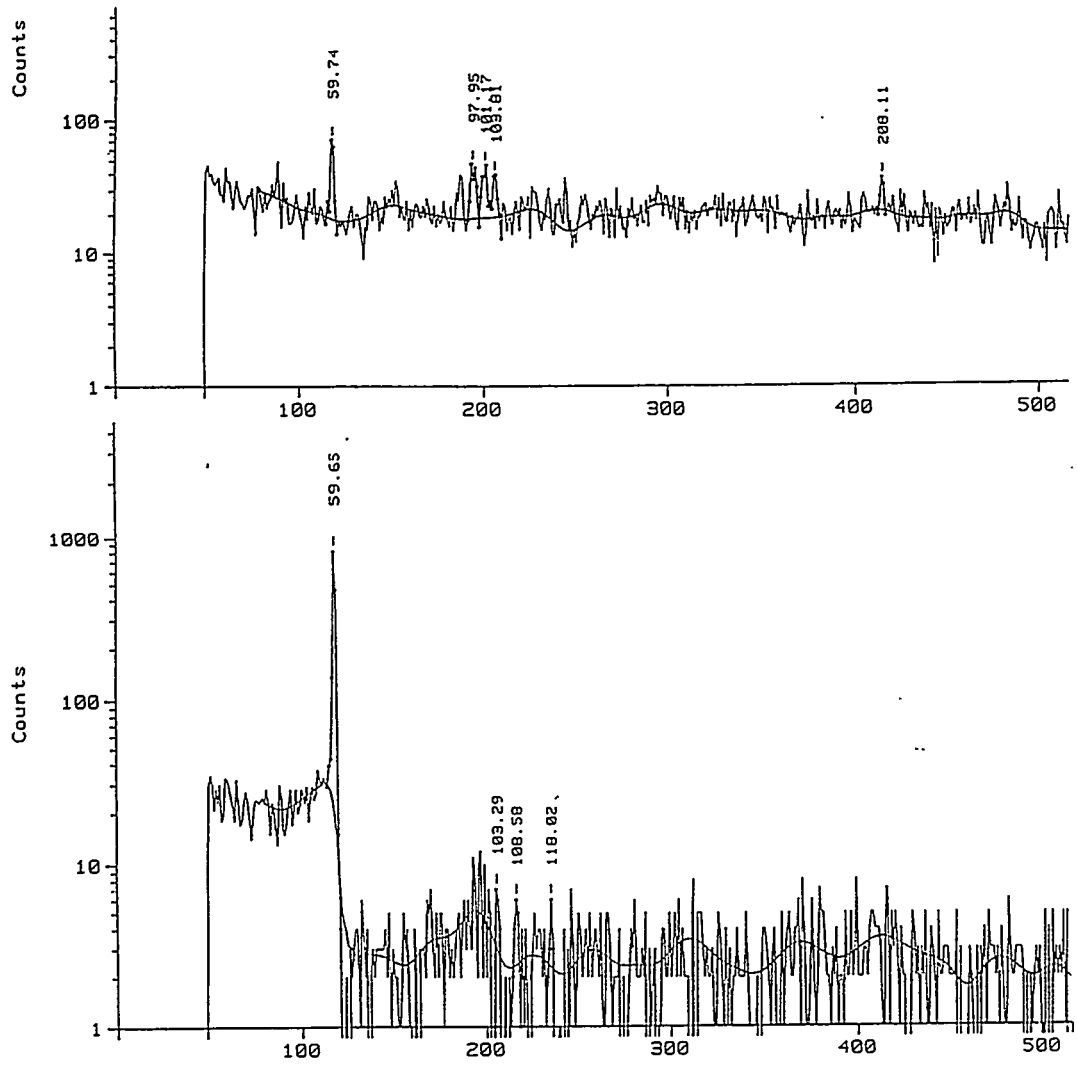

Figure 5.25: Gamma spectra of the organic phase (upper) and the aqueous phase (lower), after extraction. Notice the 59.5 keV ^{241}Am peak in the aqueous spectrum, but only a very small peak above background ($\sim$ 8% of the aqueous phase peak) in the organic spectrum; this indicates no extraction of americium by the ligands into the organic phase. The y-axis is scaled logarithmically.

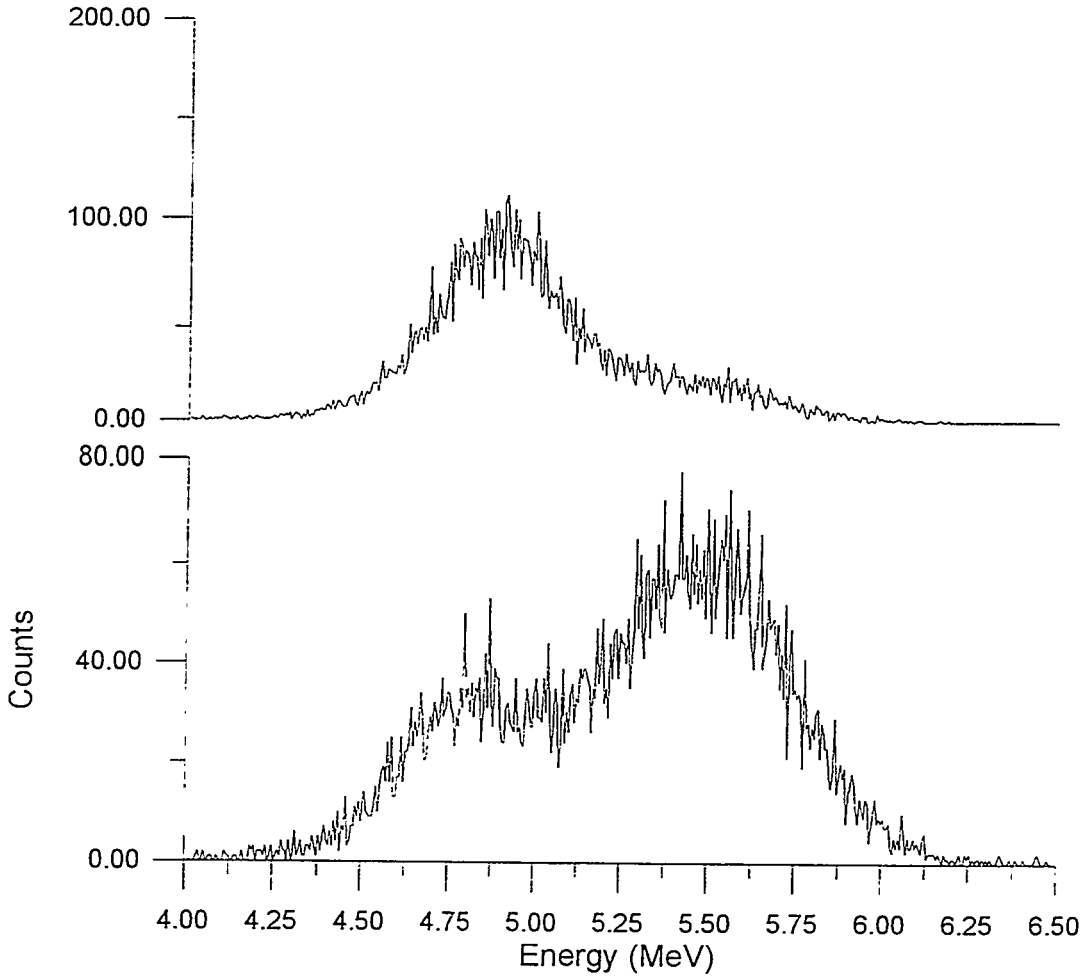

Figure 5.26: Scintillation spectra of the organic phase (upper, 21 sec counting time) and the aqueous phase (lower, 5.7 min counting time), after extraction. The organic phase spectrum is all ^{242}Pu, while the aqueous phase shows a small amount of ^{242}Pu and the presence of a large relative amount of ^{241}Am.

Table 5.4: The concentrations of the ligands used for the ^{242}Pu extraction studies, along with their molecular weights and qualitative degrees of solubility.

Ligand †	Mol. W. (g/mol)	Organic Solvent	Conc. (mM)	Dissolution ‡
1,2-HOPO-6	238.28	1-octanol	2.73	VF
		MIBK *	4.48	VF
		kerosene	4.82	VS
		dodecane	4.95	VS
1,2-HOPO-8	266.34	1-octanol	3.96	VF
		MIBK	4.99	VF
		kerosene	5.56	VS
		dodecane	5.29	VS
3,2-HOPO-6	252.31	1-octanol	5.33	VF
		MIBK	3.77	VF
3,2-HOPO-8	280.37	1-octanol	3.47	VF
		MIBK	3.80	VF
3,2-HOPO-10	308.42	1-octanol	2.86	F
		MIBK	3.31	F
3,2-HOPO-18	420.63	1-octanol	2.83	VS
3,2-HOPO-pp	286.33	1-octanol	3.05	VS
		MIBK	3.63	F
3,4-HOPO-6	266.34	1-octanol	2.65	F
		MIBK	3.90	S
3,4-HOPO-8	295.33	1-octanol	2.90	F
		MIBK	3.56	S
3,4-HOPO-10	322.44	1-octanol	3.20	F
		MIBK	3.85	VS
3,4-HOPO-18	435.57	1-octanol	2.17	VS
3,4-HOPO-pp	300.36	1-octanol	4.14	P

† — 1,2-HOPO-6 ≡ 1,2-hydroxypyridinone-hexylamide, etc.
‡ — VF ≡ very fast, F ≡ fast, S ≡ slow, VS ≡ very slow, P ≡ partial.
* — MIBK ≡ methyl isobutyl ketone.

Other Extraction Studies

The ligand/organic extraction system that performed the best in the initial extraction studies was used to perform a variety of other interesting extraction experiments:

Concentration Study Extractions were performed with the ligand-to-metal (L:M) ratio adjusted to 1.0:1, 3.1:1, 6.2:1, 15.5:1, and 31:1 (this last ratio had the standard 3.1 mM ligand concentration).

Fe(III) Competition Study Extractions were performed with the Fe(III)-to-Pu(IV) ratio adjusted to 109:1 and 1090:1, to test ligand extraction in the presence of an interfering metal.

EDTA Competition Study The ability of the ligand to extract Pu(IV) away from EDTA in the aqueous phase was tested with an EDTA-to-HOPO ratio of 2.7:1.

Stripping Three different methods of removing plutonium from the HOPO ligands were investigated:

1. Nitric acid stripping, with 7–16 M HNO_3.
2. Reduction to Pu(III), with 0.1060 M KI in 0.4000 M HCl.
3. Reduction to Pu(III), with 0.0121 M ascorbic acid in 0.5000 M HNO_3.

Chapter 6

Analysis and Discussion

6.1 Synthesis

The syntheses of the 3,2-HOPOs proved to be somewhat easier than the syntheses of the 3,4-HOPOs. Because the thiazolide intermediate can be isolated and more easily purified in the 3,2-HOPO synthesis, the yields tend to be higher and the elemental analyses tend to be closer to pure.

Nearly all of the elemental analysis results for the 3,4-HOPOs revealed some impurity in the final product. However, all of the NMR spectra for these materials looked quite pure (see Appendix A). This apparent contradiction can be explained two ways:

1. In the synthesis of the 3,4-HOPOs, it was very difficult to separate the protected amide product from the starting amine; in the synthesis of the 3,2-HOPOs, this was not a problem, because the protected amide precipitated out of solution, leaving any unreacted amine in solution. The similar chemical environments of the amide protons and the amine protons would substantially mask the amine impurity in the NMR spectra.

2. The final purification steps for the 3,4-HOPOs (acidic and basic extraction) involve high concentrations of salts, and the salts could be carried through to the final product with any water left in the product. Salts would significantly

alter the elemental analysis results, but would not alter the NMR results (no hydrogen).

Depending upon the degree of successful purification of the final product, either one of these reasons could explain the elemental analysis results for the 3,4-HOPOs. In the case of 3,4-HOPO-decylamide, accurate elemental analysis results were obtained by triturating (grinding in water) the sample; however, many of the other 3,4-HOPOs were too water-soluble for this technique to be used effectively. If the 3,4-HOPOs need to be prepared for future studies, then their syntheses should be conducted with greater attention given to the final purification steps.

For the 3,2-HOPOs, the elemental analysis results were all much more accurate than for the 3,4-HOPOs. Again, all of the proton NMRs looked as they should; additionally, all of the ^{13}C NMRs looked pure (Appendix A).

The 3,2-HOPOs appear to be a great deal more organophilic than the 3,4-HOPOs, and this fact can be rationalized by looking at their structures. The 3,4-HOPO moiety (see Figure 5.3) has a much more distended structure, with the binding oxygens arranged more para- to the organophilic alkane side chain; the 3,2-HOPO moiety (see Figure 5.9) has a much less easily defined dipole, with the binding oxygens placed more ortho- to the organophilic alkane side chain. This greater organophilicty directly translates into a more efficient liquid/liquid extractant.

The 3,2-HOPO-propylamide ligand was synthesized in order to measure the formation constant of the 3,2-HOPO/Th(IV) system. Its elemental analysis indicated it was the most pure of all the ligands, which aided in the accurate determination of its formation constant with Th(IV).

6.2 Characterization

6.2.1 Spectrophotometric Titration of 3-hydroxy-2-pyridinone propylamide with Th(IV)

In a standard potentiometric titration, the amount of base it takes to effect a measured change in pH ($-\log [H^+]$) is used to calculate molecular proton dissociation constant(s), or pK_a(s). In spectrophotometric work, pK_a is replaced by $\log \beta$, which is a more general descriptor of an equilibrium constant (see reference [125]). The β notation has three main distinctions from K_a notation:

1. β notation includes a subscript to indicate the number of metals, ligands, and protons on the formed species, in the form of β_{mlh}. The formation constant for a fully deprotonated 3:1 ligand/metal species would be given by $\log \beta_{130}$.

2. Whereas pK_a notation is for a dissociative reaction (*i.e.*, acid dissociation), β notation reverses that reaction to show formation.

3. β notation is additive (*i.e.*, $\log \beta_{130} = \log \beta_{110} + \log \beta_{120}$).

In a simple system of molecules and protons, only a burette, a pH electrode, and a pH meter are required to perform accurate measurements. However, when measuring the thermodynamic formation constants between metals and ligands, the system becomes more complex with the addition of another "player" in solution: besides molecules and protons, there is now a metal ion. This addition requires the measurement of another aspect of the system, so as to provide the needed concentration values to constrain the mathematical equations that determine the formation constants. The additional measurement used in a spectrophotometric titration is the UV/Vis spectrum of the solution after each addition of base.

A spectrophotometric titration proceeds much like a potentiometric titration – some base is added and the pH is measured; and in the case of a spectrophotometric titration, a UV/Vis spectrum is taken. In order for the spectrum to be meaningful, the ligand and the metal/ligand complexes must absorb light in the UV/Vis

range of wavelengths. These spectra, at stepped pHs, are then used to determine which species are in solution at each pH, and their concentrations, via Beer's Law:

$$A = \varepsilon bc, \tag{6.1}$$

where ε is the molar absorptivity (extinction coefficient), b is the pathlength, and c is the concentration. The method used to determine which species are in solution, and their concentrations, involves solving a large number of nested equilibrium and mass-balance equations. The most efficient and painless means of solving all these equations is computer-based, using the code REFSPEC [126]. (A good primer for understanding all the equilibrium and mass-balance equations, and how a computer code goes about solving them for useful thermodynamic data, is found in reference [125].)

REFSPEC is a program which uses the extinction coefficients and concentrations of all the species in solution to calculate a hypothetical absorbance spectrum. The code then modifies these variables, in an iterative fashion, to achieve the best least-squares fit between the calculated absorbance spectrum and the experimental absorbance spectrum. The program can then calculate the formation constants of the metal/ligand species because *it is the formation constant for each species that determines the concentration of that species in solution.*

The user supplies REFSPEC with an input file which contains:

1. A listing of all the species in solution (including protonated and deprotonated ligand, all reasonable metal/ligand species, and all metal hydrolysis species).

2. An initial "ball-park" estimate of the formation constants for each species of interest.

3. Instructions as to which numerical values to vary.

4. Known extinction coefficients (*i.e.*, for the protonated and deprotonated ligand) for the program to use as constraining constants; this helps REFSPEC fit more quickly and accurately.

Running on a 33 MHz 486 processor, REFSPEC can refine the data into thermodynamic formation constants in approximately thirty seconds.

Many different species were included in different trial fits with REFSPEC for this titration, ranging from simple 4:1 and 3:1 ligand/metal species, to mixed ligand/hydroxide species (see Figures 6.1, 6.2, 6.3). The addition of the mixed species did not affect the formation constant numbers to any notable extent, but they did add some realism to the picture of what was most likely happening in solution, as well as alter the extinction coefficients to more believable values.

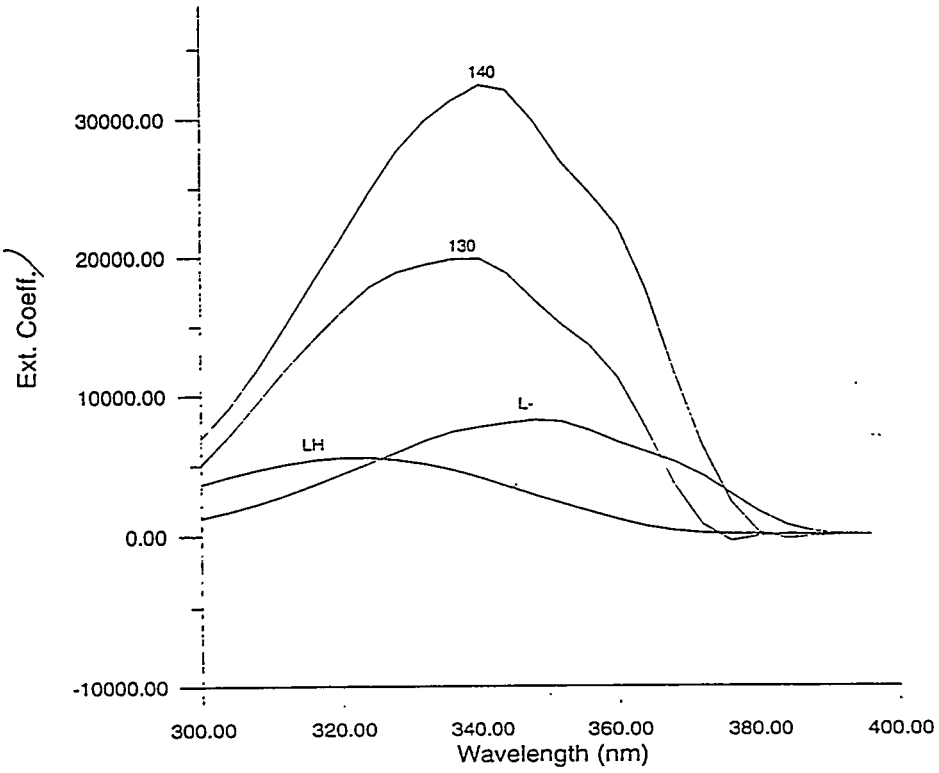

Figure 6.1: Calculated absorption spectra by REFSPEC; extinction coefficient axis is equivalent to absorption.

As determined by REFSPEC, the 4:1 ligand/metal complex for 3,2-HOPO-propylamide and Th(IV) has a formation constant ($\log \beta_{140}$) of 38.3 $\pm$ 0.3; the 3:1 complex has a formation constant ($\log \beta_{130}$) of 32.0 $\pm$ 0.3. These formation constants compare favorably with the formation constants measured for other hydroxypyridin-

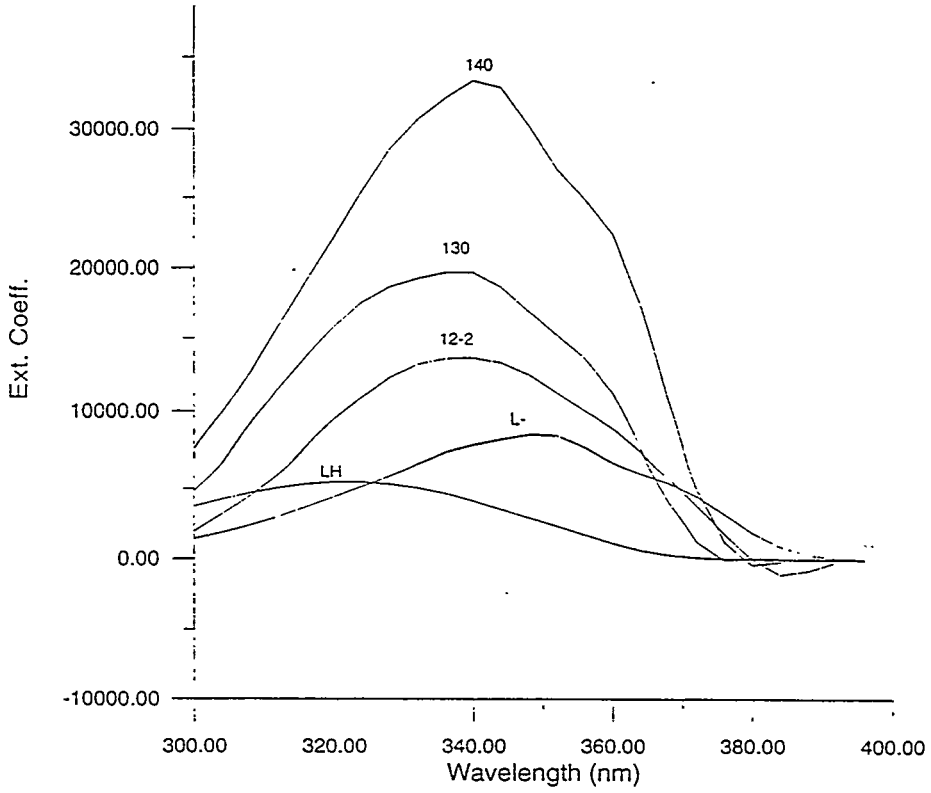

Figure 6.2: Calculated absorption spectra by REFSPEC, including some mixed ligand/hydroxide species; extinction coefficient axis is equivalent to absorption.

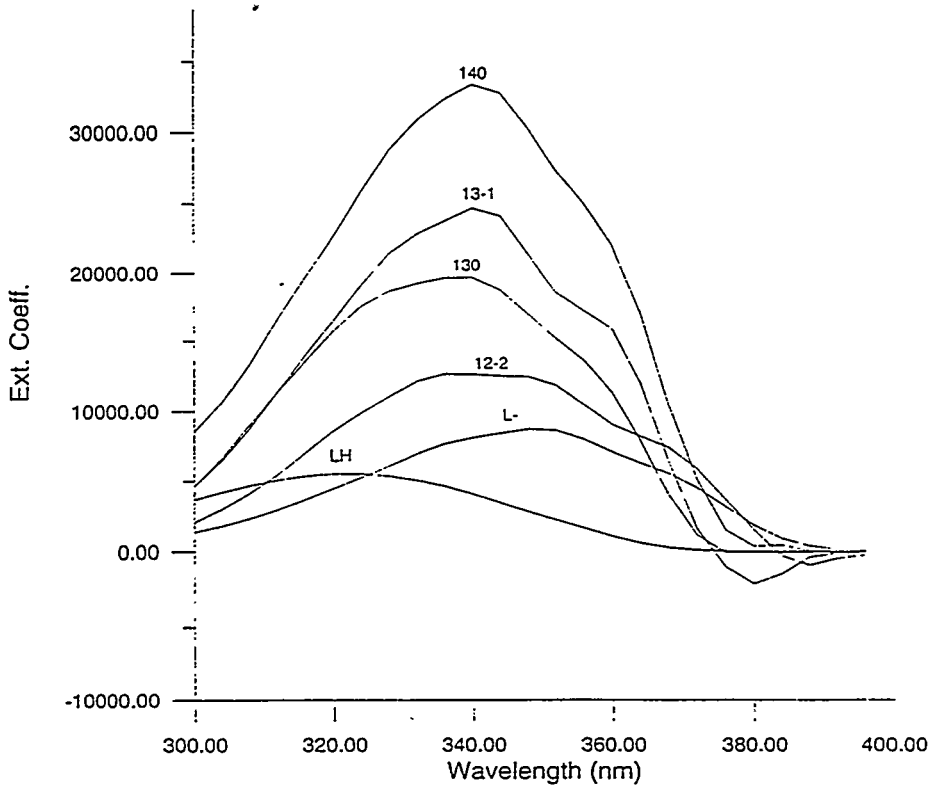

Figure 6.3: Calculated absorption spectra by REFSPEC, including some other mixed ligand/hydroxide species; extinction coefficient axis is equivalent to absorption.

Table 6.1: Formation constants measured in this study for Th(IV) with 3,2-HOPO-propylamide and the other HOPOs.

$\log\beta$	**3,4-HOPO**	**3,2-HOPO**	**1,2-HOPO**
140	41.8±0.5	38.3±0.3	36.0±0.3
130	35.8±0.2	32.0±0.3	NM †

† — NM ≡ not measured

ones used by this group (see Table 6.1) [105].

Since 3,4-HOPO is the most basic of the HOPO ligands listed above, it is expected to have the largest formation constant with a Lewis-acidic metal ion, as it does; 3,2-HOPO and 1,2-HOPO follow in that order in basicity, and have correspondingly weaker formation constants as compared to 3,4-HOPO. Additionally, going from 1,2-HOPO to 3,2-HOPO to 3,4-HOPO, as the oxy-chelating groups on the HOPO ring move away from the ring nitrogen, the formation constant of that HOPO increases; this is caused by the resonance structures of the deprotonated HOPOs, which show a zwitterionic positive charge on the ring nitrogen (N^+). As the nitrogen, and hence the positive charge, move around the ring and away from the position of metal coordination, the ligand becomes more stable when bound to a metal [127]. It must be borne in mind, however, that while 3,4-HOPO is the strongest of the HOPOs at high pH, this is not necessarily the case at lower pHs. The proper HOPO must be chosen to complex a metal ion *depending upon the pH of the solution.* This consideration is very important for the remediation work that is discussed in this study, for the pH of the solution to be remediated is a variable, depending on the waste stream (see page 77).

6.2.2 Extraction Studies

CINDERELLA could not go to the ball unless she carried out her stepmother's demand that she should separate an intimate mixture of lentils and ashes. Her friends, the turtle doves and tame pigeons, came in response to her urgent request to pick out

"the good lentils into the pot
the rest into your crop"

The birds finished the job in one hour with an efficiency of 100%.

Adapted from "Aschenputtel"
by the Brothers Grimm [128]

The extractions discussed in the next sections were performed with two main organic phase solvents – 1-octanol and methyl isobutyl ketone (MIBK). Kerosene and dodecane were used as solvents for a few of the extractions, but most of the ligands did not show adequate solubility in these solvents. Additionally, methylene chloride (CH_2Cl_2) and chloroform ($CHCl_3$) were used in some initial extraction experiments, but were abandoned because of volatility problems and difficulty with pipetting. It is unlikely that these last two solvents would ever be candidates in a large-scale industrial extraction process.

The expression used to calculate the percent extraction,

$$\%Ext = [A_{org}/A_{org+aq}] \times 100, \tag{6.2}$$

where A_{org} is the activity of the organic phase and A_{org+aq} is the total activity, uses the experimentally determined total activity, instead of the theoretical total activity. Therefore, small fluctuations in the total activity for each individual extraction, which might come from pipetting and other sources, could be accounted for within each extraction.

From the percent extraction, two other interesting extraction parameters, the distribution ratio (D) and the decontamination factor ($D.F.$), were calculated. The distribution ratio for these extractions was calculated using the expression

$$D = A_{org}/A_{aq}, \tag{6.3}$$

where A_{org} is the activity in the organic phase and A_{aq} is the activity in the aqueous phase. Obviously, the larger the value of the distribution ratio, the better the ability of the extractant to remove metal from the aqueous phase into the organic phase. The other quantity, the decontamination factor, is calculated using the expression

$$D.F. = A_{org+aq}/A_{aq}, \tag{6.4}$$

where A_{org+aq} is the total activity and A_{aq} is the activity of the aqueous phase. This quantity is called the decontamination factor because a large value indicates a high degree of decontamination effected by the extraction. For extractions greater than $\sim 97\%$, $D.F. \approx D$, because $A_{aq} \approx A_{org+aq}$. The bulk of the data from the Fe(III) and Pu(IV) extractions is contained in Appendix B.

Uncomplexed Ligand Distributions

Since the hydroxypyridinone (HOPO) ligands studied here had never been used as liquid/liquid extractants before, it was useful to first characterize the ligands by measuring their distribution between the organic and aqueous phases, free of all metals. Because the spectrophotometric titration results listed in Table 6.1 above were measured in water, it is obvious that all of the HOPOs that have propyl- (three-carbon) side chains are water soluble. The five ligands used in this study had side chains ranging in length from hexyl- (six-carbon) to octadecyl- (eighteen-carbon), and included one with an aromatic phenylpropyl side chain.

Because the two principal organic solvents used, methyl isobutyl ketone (MIBK) and 1-octanol, both have a small solubility in water, a blank extraction was performed with each pure organic phase and a straight deionized water phase (kerosene and dodecane were also measured, but each has an insignificant solubility in water). Results for these blank extractions are shown in Figure 6.4. The aqueous phase of the blank 1-octanol extraction was void of any dissolved 1-octanol; any minuscule amount of 1-octanol in this phase was below the limit of UV/Vis detection. For MIBK, though, there was a relatively large absorbance in the aqueous phase at $\lambda_{max} = 267$ nm. This is due to the 1.9% (w/w) solubility of MIBK in water. The absorbance peak of $\sim$ 0.75 AU gives a calculated molar absorptivity (ε) of $\sim$ 23

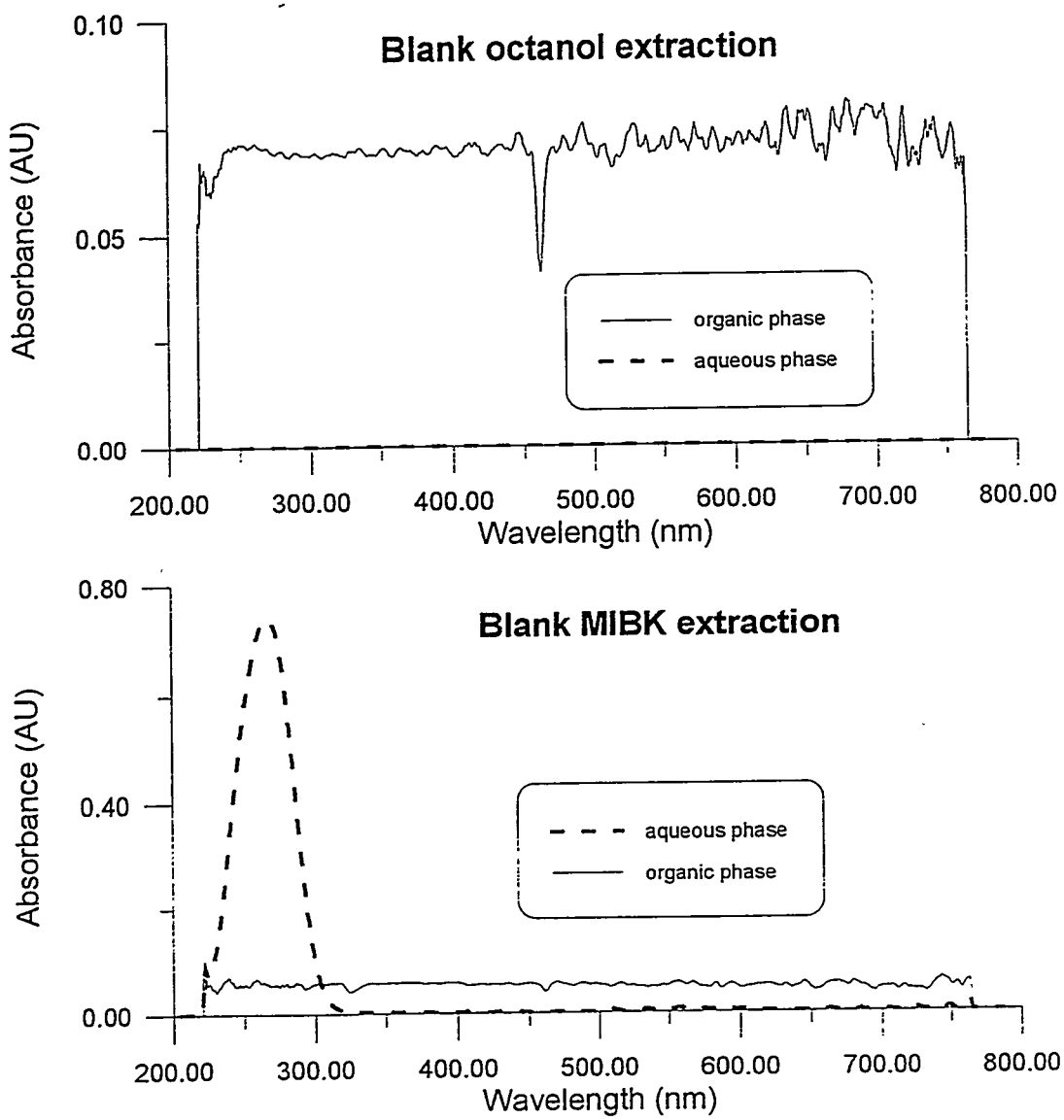

Figure 6.4: Blank 1-octanol (upper) and MIBK (lower) extractions. There is no 1-octanol in the aqueous phase to the limit of UV/Vis detection; however, MIBK appears in the aqueous phase with an intensity of ~ 0.75 AU at $\lambda_{max} = 267$ nm.

mol^{-1} cm^{-1}. This absorbance peak appeared at roughly the same intensity in all the other uncomplexed ligand distributions for MIBK shown in this section.

Table 6.2 lists the λ_{max}, intensity, measured ε, and qualitative percentage of ligand in the aqueous phase, for each uncomplexed ligand distribution measured. The percentage of ligand in the aqueous phase was very difficult to measure, because it required accurate knowledge of the molar absorptivity in both the aqueous and organic phases. The qualitative number presented in this section is simply an estimate reflecting the height of the ligand peak in the aqueous and organic phases. Since the aqueous molar absorptivity is almost certainly larger than the organic molar absorptivity ($\varepsilon_{aq} > \varepsilon_{org}$), the actual ligand percentage in the aqueous phase was probably lower than that given in this section.

The figures in this section graphically represent selected data found in the table:

Figure 6.5 Uncomplexed ligand distribution for 1,2-HOPO-hexylamide in 1-octanol and MIBK.

Figure 6.6 Uncomplexed ligand distribution for 3,2-HOPO-hexylamide in 1-octanol and MIBK.

Figure 6.7 Uncomplexed ligand distribution for 3,4-HOPO-hexylamide in 1-octanol and MIBK.

Figure 6.8 Uncomplexed ligand distribution for 3,4-HOPO-phenylpropylamide in 1-octanol.

These figures show that for all of the HOPO-hexylamides in both organic solvents (except the 3,2-HOPO-hexylamide in 1-octanol) some uncomplexed ligand was detected in the aqueous phase. For the 3,2-HOPOs and the 1,2-HOPOs the aqueous percentage was quite small, always $\leq 5\%$; but for the 3,4-HOPOs, the percentage was very large, amounting to as much as $\sim 100\%$ in the case of 3,4-HOPO-hexylamide in MIBK (Figure 6.7). The 3,4-HOPO-phenylpropylamide (Figure 6.8) also appears in the aqueous phase in a large percentage, roughly $\sim 40\%$.

Table 6.2: Data from the UV/Vis spectra of the uncomplexed ligand distribution between the aqueous and organic phases. The spectral data presented are from the ligand in the organic phase; the qualitative percentage is measured in the aqueous phase.

Ligand	Organic solvent	λ_{max} (nm)	Abs. (AU)	ε_{org} (mol^{-1} cm^{-1})	Estimated Ligand (aq.) (%)
1,2-HOPO-6 †	1-octanol	316	0.49	1134	≤ 5
	MIBK	333	1.44	2030	≤ 5
1,2-HOPO-8	1-octanol	317	1.94	2939	0
	MIBK	334	1.50	1804	0
3,2-HOPO-6	1-octanol	322	1.44	1621	0
	MIBK	335	1.61	2642	≤ 3
3,2-HOPO-8	1-octanol	323	1.54	2663	0
	MIBK	333	1.32	2084	0
3,2-HOPO-10	1-octanol	325	0.29	608	0
	MIBK	334	1.50	2719	0
3,2-HOPO-18	1-octanol	242	0.13	276	0
3,2-HOPO-pp	1-octanol	325	0.45	885	0
	MIBK	332	1.27	2099	0
3,4-HOPO-6	1-octanol	281	0.50	2256	≤ 50
	MIBK	—	—	—	≤ 100
3,4-HOPO-8	1-octanol	282	0.54	1117	0
	MIBK	NM ‡	NM	NM	NM
3,4-HOPO-10	1-octanol	282	0.72	1350	0
	MIBK	NM	NM	NM	NM
3,4-HOPO-18	1-octanol	282	0.54	1493	0
3,4-HOPO-pp	1-octanol	282	1.16	1681	≤ 40

† — 1,2-HOPO-6 ≡ 1,2-hydroxypyridinone-hexylamide, etc.

‡ — NM ≡ not measured

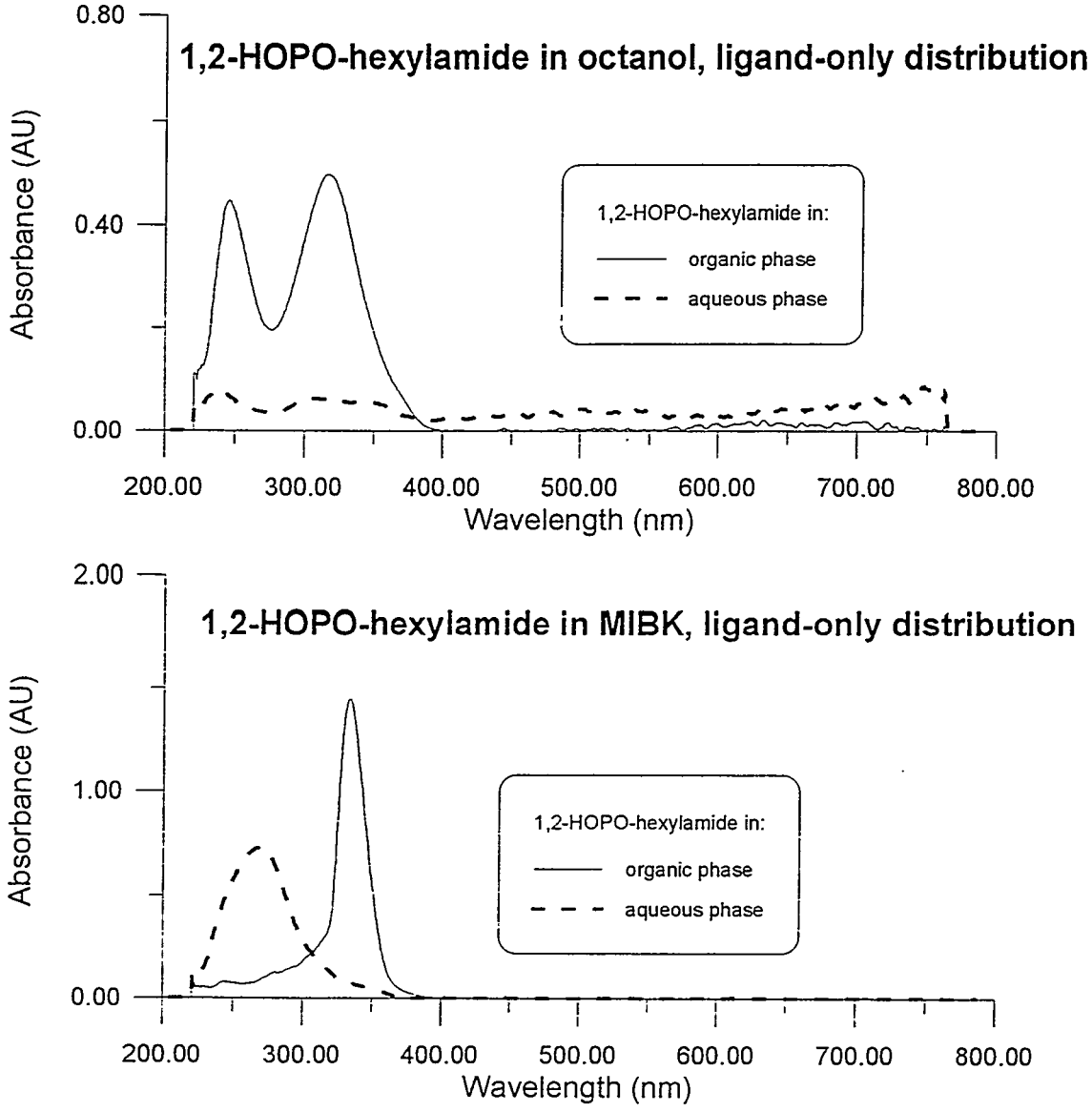

Figure 6.5: Uncomplexed ligand distribution for 1,2-HOPO-hexylamide in 1-octanol (upper) and MIBK (lower). For the 1-octanol plot, the ligand appears in the aqueous phase with an intensity of $\sim$ 0.05 AU above background; for the MIBK plot, the ligand appears in the aqueous phase as a very small shoulder on the much larger MIBK peak.

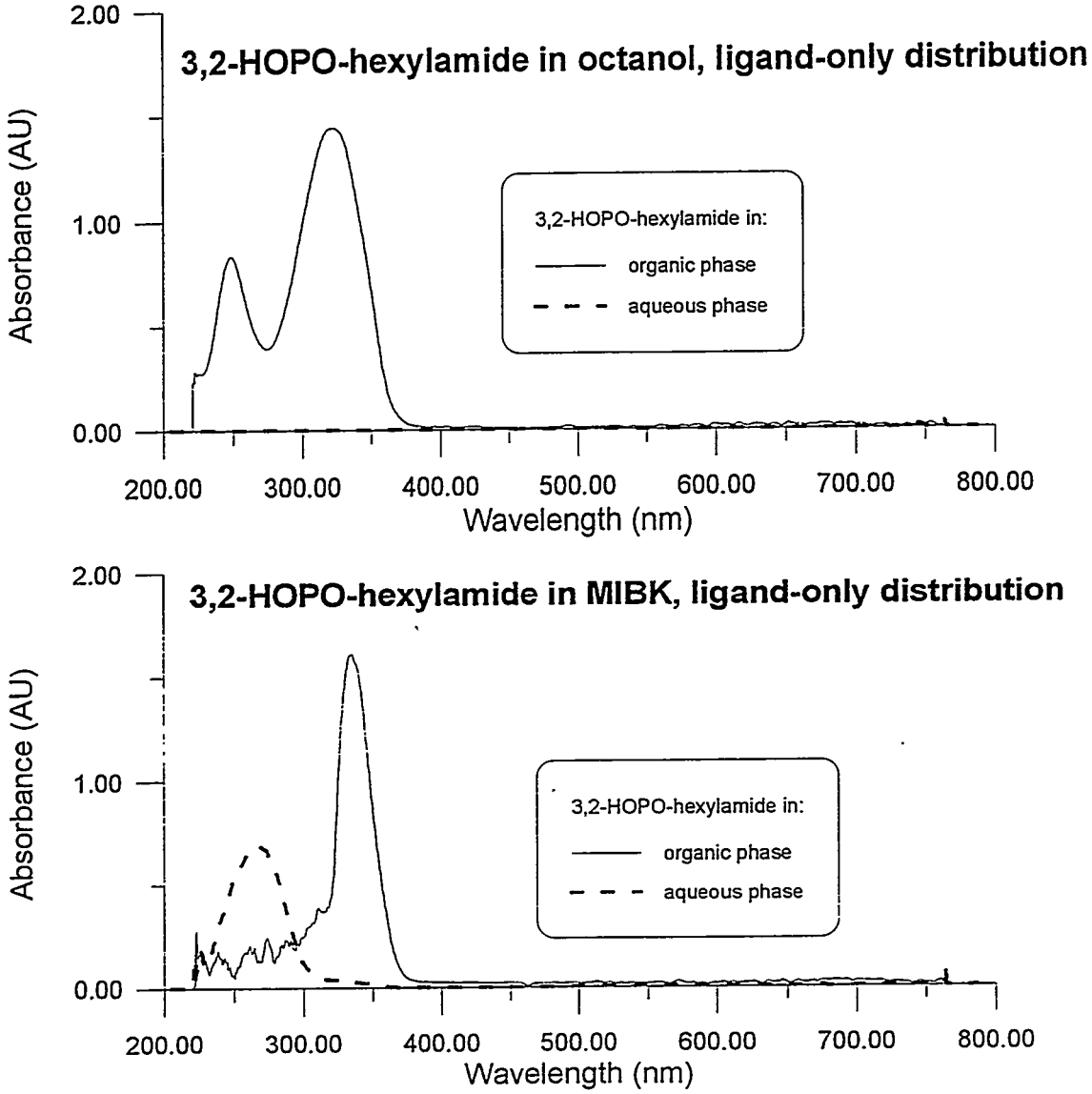

Figure 6.6: Uncomplexed ligand distribution for 3,2-HOPO-hexylamide in 1-octanol (upper) and MIBK (lower). For the 1-octanol plot, the ligand does not distribute into the aqueous phase; for the MIBK plot, the ligand appears in the aqueous phase as a very small shoulder on the much larger MIBK peak.

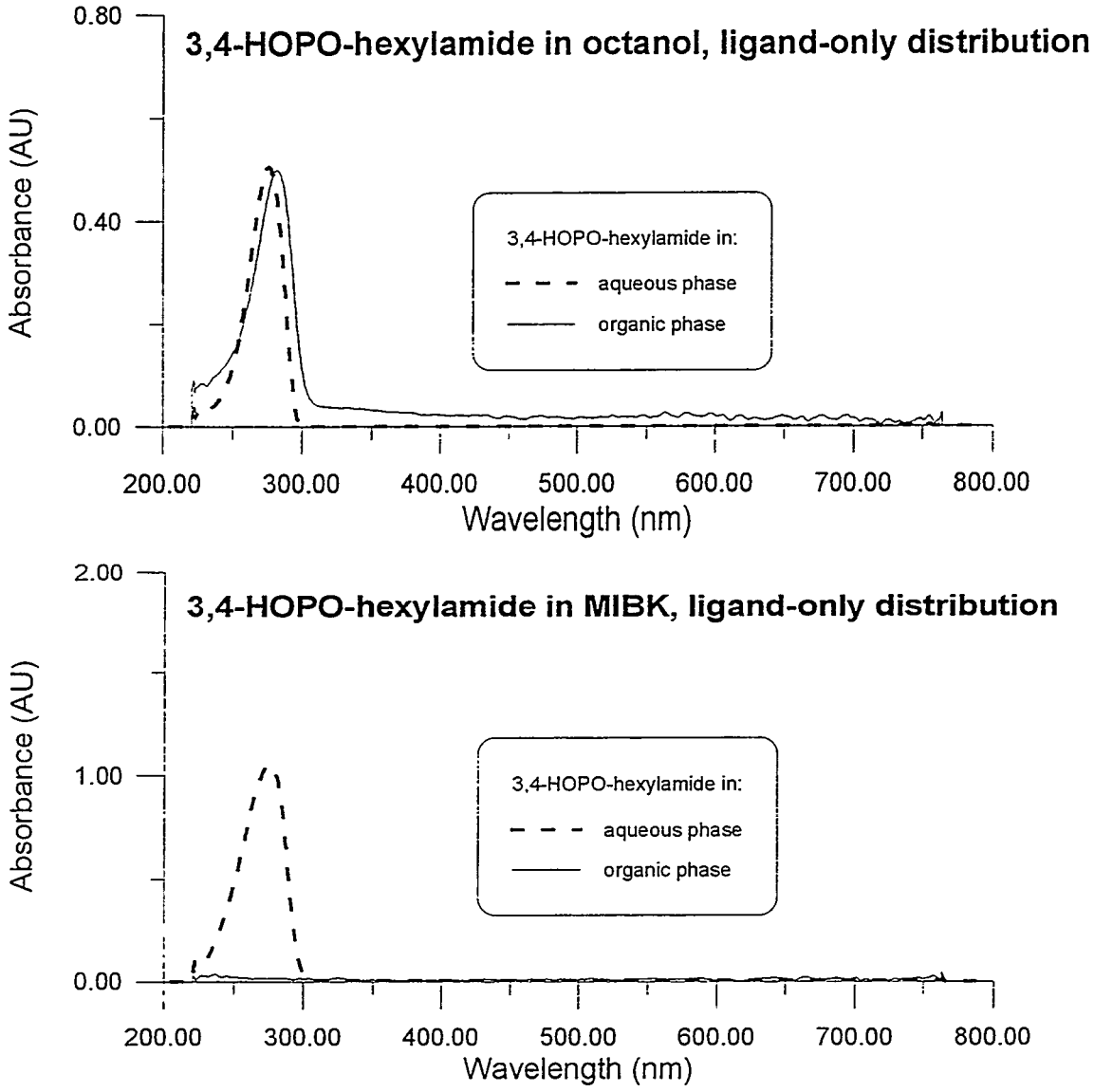

Figure 6.7: Uncomplexed ligand distribution for 3,4-HOPO-hexylamide in 1-octanol (upper) and MIBK (lower). For the 1-octanol plot, the ligand appears in the aqueous phase with a large intensity of $\sim$ 0.50 AU; for the MIBK plot, there is no ligand in the organic phase.

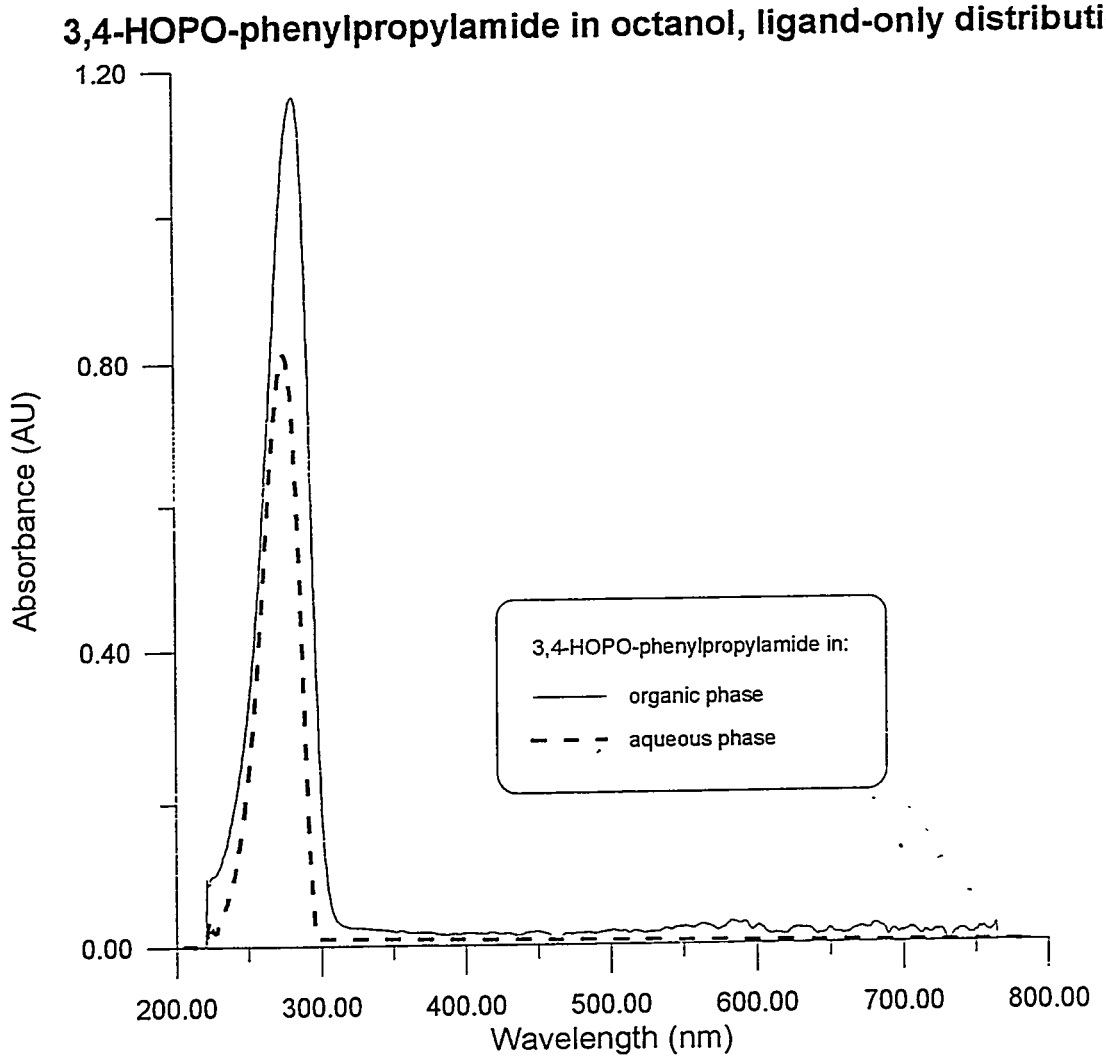

Figure 6.8: Uncomplexed ligand distribution for 3,4-HOPO-phenylpropylamide in 1-octanol; the ligand appears in the aqueous phase with a large intensity of $\sim$ 0.80 AU.

The uncomplexed ligand distribution study showed no detectable partitioning into the aqueous phase for thirteen of the eighteen ligand/organic phase pairings; this verifies the organophilic character of the modified HOPO extractants. All the ligands that showed any degree of hydrophilicity were confined to the shortest chain representatives, the hexylamides and one phenylpropylamide. When these bidentate ligands are arranged around a metal, with polar chelate groups pointing inward and non-polar alkane side chains pointing outward, their organophilicity will increase.

Iron Extraction Studies

The iron extraction studies were undertaken for two reasons:

1. As discussed earlier (page 68), the similarities between Fe(III) and Pu(IV) initially motivated this study. Extractions with Fe(III) should give a good indication of the strength of these ligands as extractants for Pu(IV). Additionally, Fe(III) will be one of the chief interfering metals in any of the waste streams that these ligands might be used to remediate; a good measure of how the ligands extract Fe(III) will provide information concerning the selectivity of the ligands.

2. Very practically, extractions with ^{55}Fe provide good practice in the method of liquid/liquid extraction, so that when extractions with ^{242}Pu are conducted, they will proceed smoothly, with a minimum number of technical surprises.

As a check on the accuracy of the extraction experiments, the quench-corrected counts per minute (cpm) from both the aqueous and organic phase were added together (called the "total activity") and compared with the expected number of disintegrations per minute (dpm) for each extraction. Figure 6.9 plots the course of this number (percentage of total Fe(III)) over the many iron extractions performed. For the first two-thirds of the extractions, the total activity remained fairly constant with an average of $\sim$ 95% of that expected. For the last one-third of the extractions, however, the total activity falls off to $\sim$ 90%, on average; during these last extractions, a different set of pipettes were used, thus giving a slightly different volume delivery and altering the total activity measured.

Figure 6.10 shows the percent extraction versus time for all of the octylamides of the three HOPOs. The extraction pattern that is shown in this first plot is one that is followed for the rest of the Fe(III) extractions: *at pH = 1, the ability of each HOPO to extract Fe(III) is directly related to its* $\log K_a$. Figure 6.11 shows the protonated and deprotonated forms of the chelate groups, and the associated protonation constants ($\log K_a$s) for each of the three HOPOs, with catechol included for reference. Catechol is the most basic of the chelating groups, with $\log K_{a1} = 13.0$,

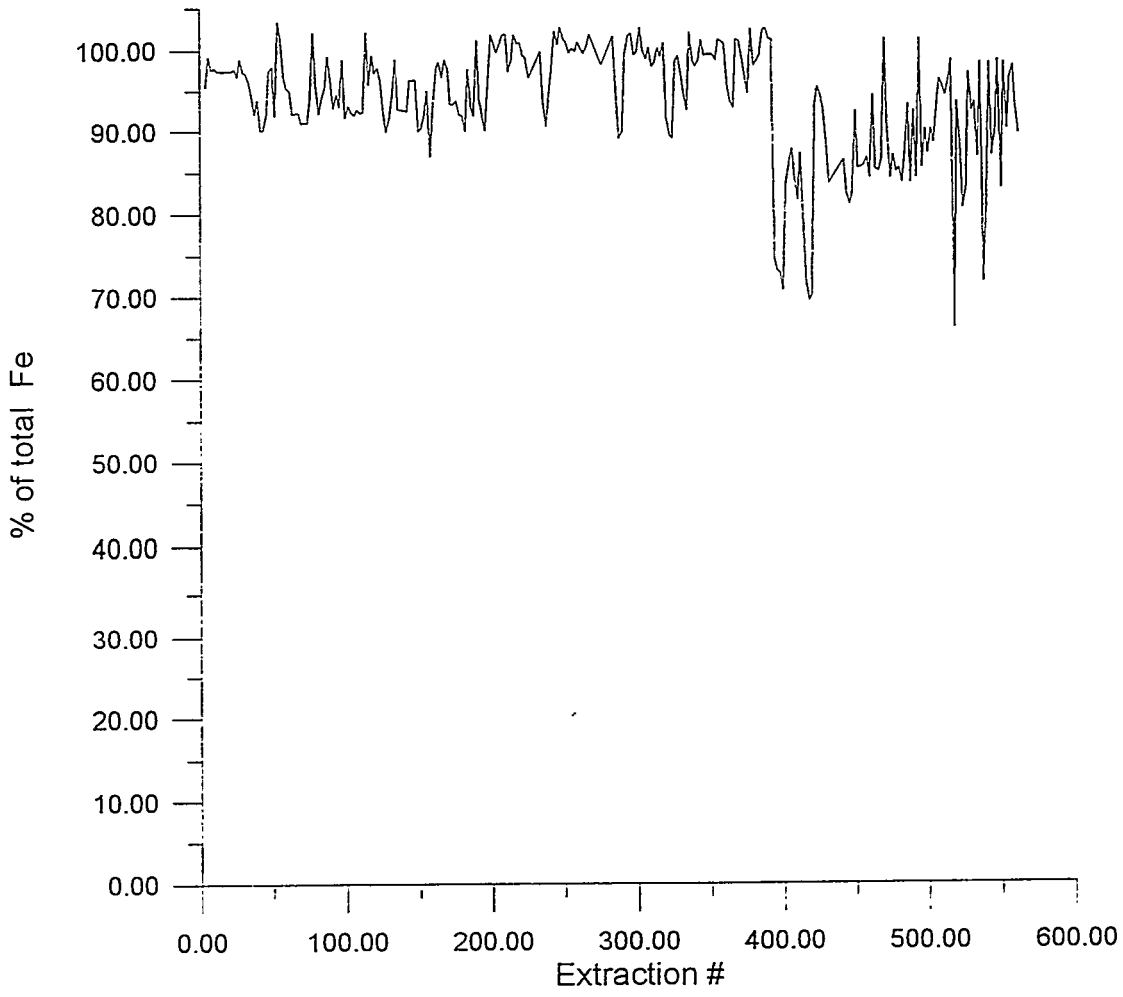

Figure 6.9: Percent total Fe(III), measured by summing the activities in the aqueous and organic phases, versus the extraction number.

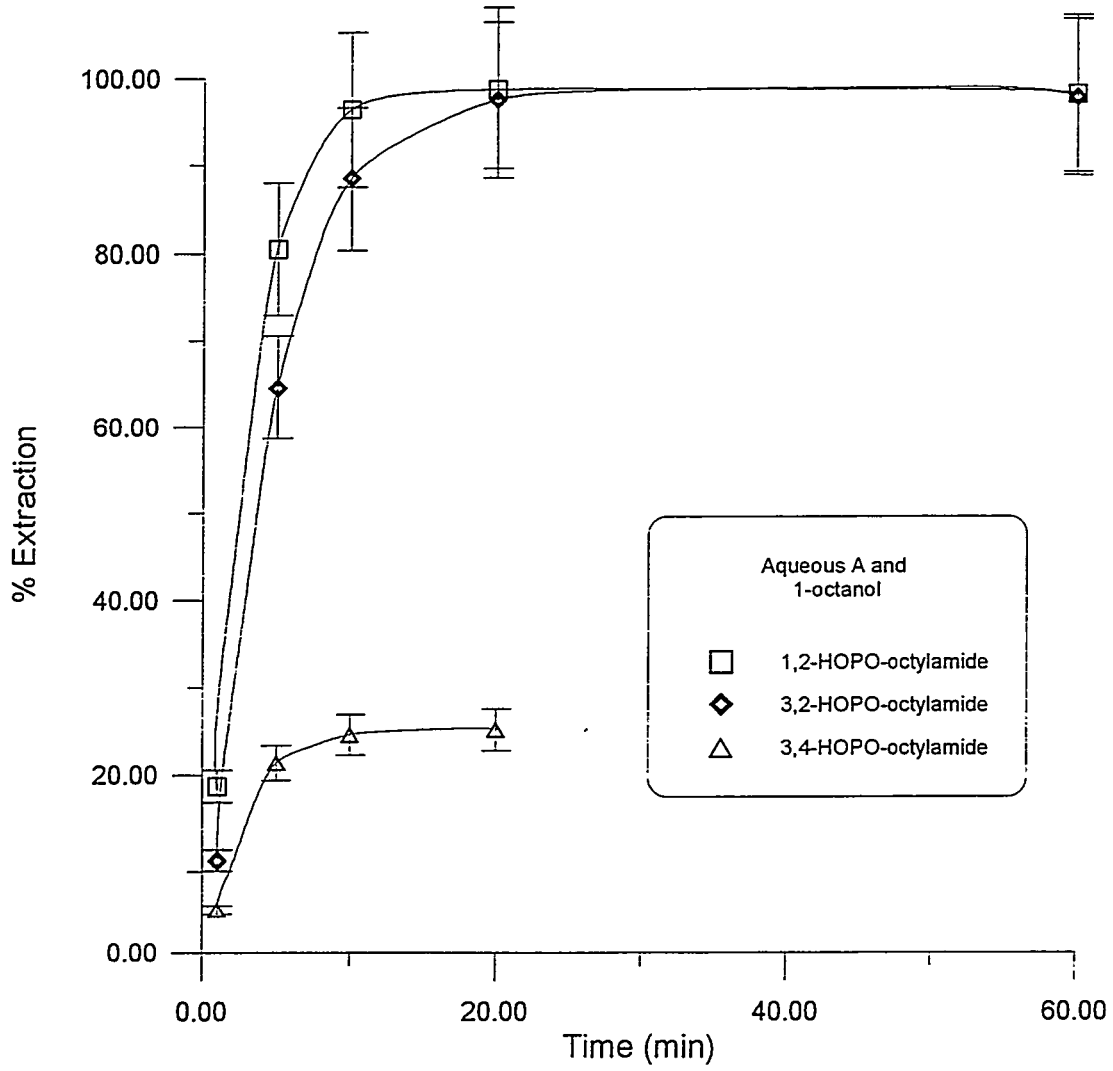

Figure 6.10: Percent extraction versus time for the octylamides of the three HOPOs — the 3,4-HOPO-octylamide extraction reached a plateau by 20 min.

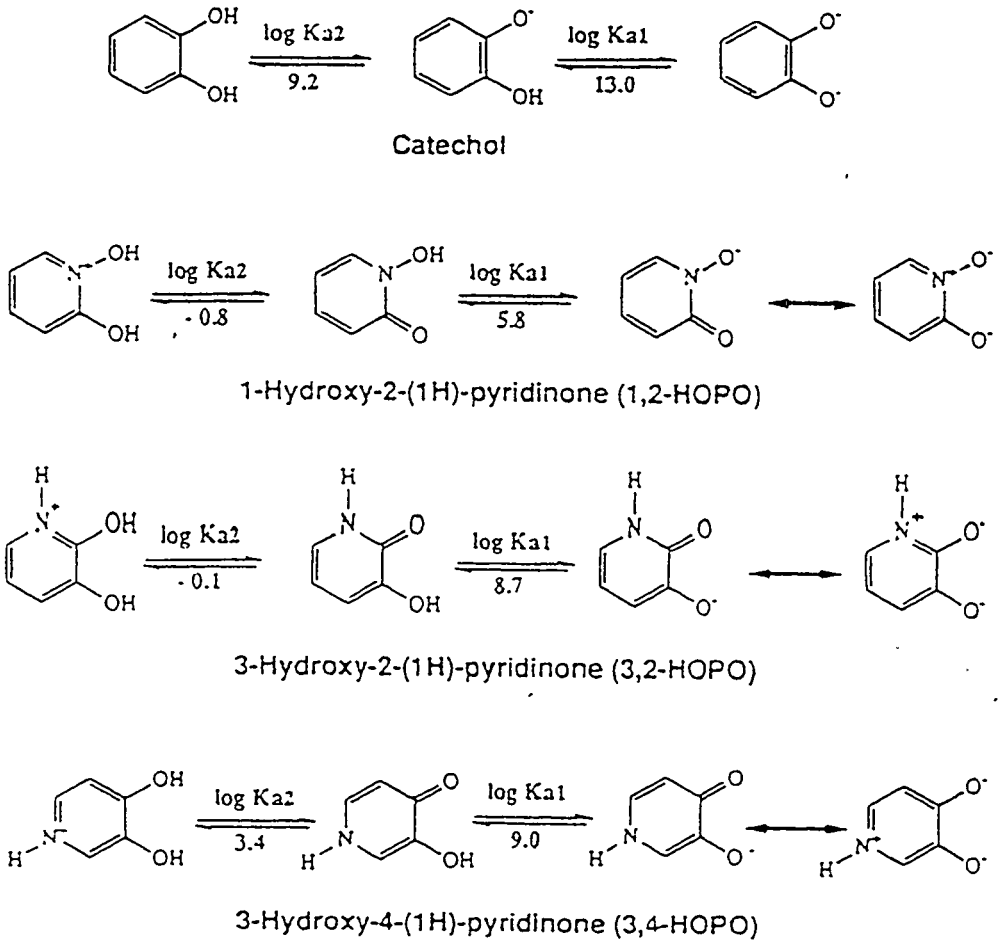

Figure 6.11: $\log K_a$ values for the protonated and deprotonated forms of the hydroxypyridinones (HOPOs), and catechol.

followed by 3,4-HOPO with log $K_{a1} = 9.0$, 3,2-HOPO with log $K_{a1} = 8.7$, and finally, the most acidic of the ligands, 1,2-HOPO, with log $K_{a1} = 5.8$. The log K_a simply tells at what pH the ligand will be deprotonated (i.e., 1,2-HOPO will be deprotonated at pH = 5.8). This means that under the acidic conditions (pH = 1) used to test these ligands, 1,2-HOPO is the ligand best suited to shed its proton on the hydroxy group and bind a Lewis acidic metal (like Fe(III) or Pu(IV)); then follow 3,2-HOPO and 3,4-HOPO, in that order. Figure 6.10 shows that, indeed, 1,2-HOPO-octylamide displayed the fastest extraction kinetics of all the HOPO-octylamides, and the highest percent extraction. But 3,2-HOPO-octylamide also had a very high extraction (and slightly slower kinetics), given the fact that its log K_{a1} is so much higher than that of 1,2-HOPO. 3,4-HOPO-octylamide had a very low percent extraction, $\sim$ 20%, due to its high log K_{a1}, and possibly solubility problems (see page 142).

Figure 6.12 displays another general trend seen in all the Fe(III) extractions: *extraction from the higher ionic strength aqueous phase was favored, in most cases dramatically, over extraction from the lower ionic strength aqueous phase.* In this figure, 1,2-HOPO-octylamide was used to extract Fe(III) into 1-octanol. While the final percent extraction, at 60 minutes, was roughly the same for Aqueous A and B, the kinetics of extraction were much slower for Aqueous B. For the other HOPO chelate groups, as will be seen in later figures, the percent extraction from Aqueous B was also drastically lower than that from Aqueous A.

The last general trend seen in the Fe(III) extractions is shown in Figure 6.13: *extraction of Fe(III) into 1-octanol was faster, and often higher, than extraction into MIBK.* This plot shows extraction by 3,2-HOPO-octylamide from Aqueous A into 1-octanol and MIBK. Extraction into 1-octanol reaches its maximum percent after $\sim$ 15–20 minutes; it takes MIBK a full 60 minutes of contact time to reach the same level of extraction.

The remainder of figures displayed in this section give the extraction behavior of all the HOPOs in the organic phases 1-octanol and MIBK, for extraction of Fe(III) from Aqueous A (high ionic strength aqueous phase):

Figure 6.14 all 1,2-HOPOs.

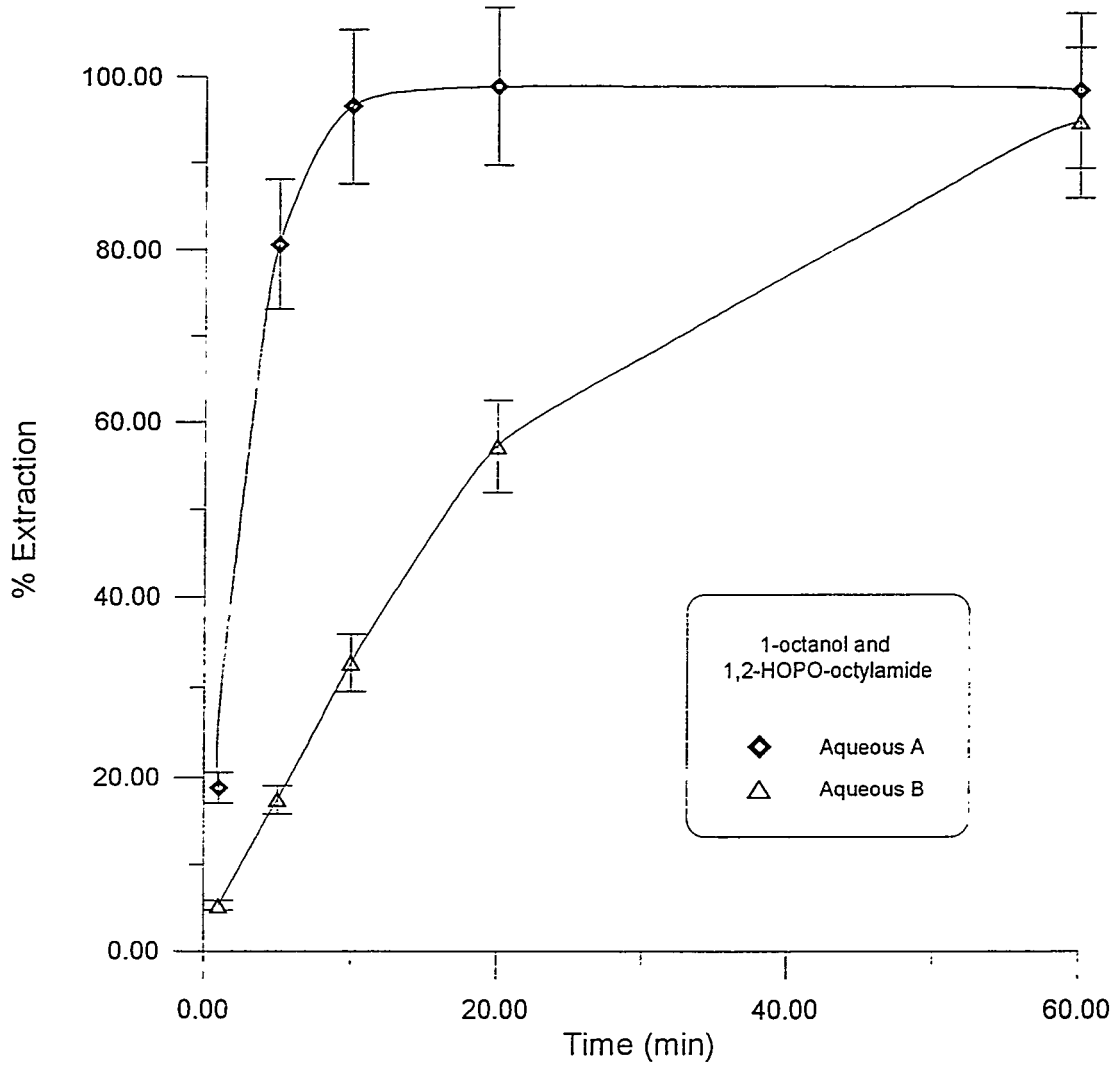

Figure 6.12: A comparison of the percent extraction by the same ligand from Aqueous A (high ionic strength) and Aqueous B (low ionic strength).

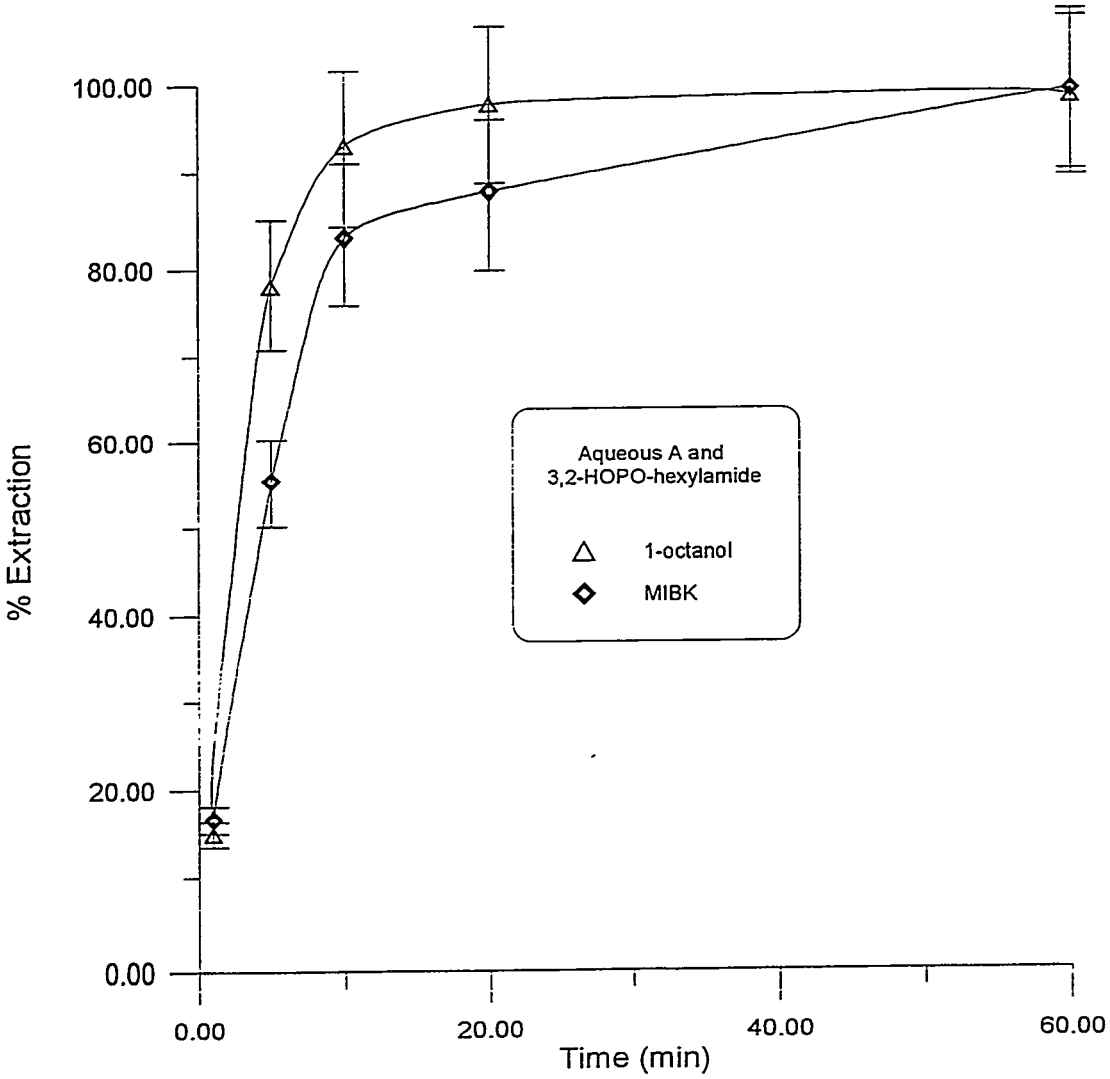

Figure 6.13: A comparison of the percent extraction by the same ligand from Aqueous A into two different organic phases, 1-octanol and MIBK.

Figure 6.15 all 3,2-HOPOs.

Figure 6.16 all 3,4-HOPOs.

The 1,2-HOPOs, as discussed earlier, were the ligands best suited to perform these extractions. For both organic phases, they extracted a very high percentage of the Fe(III) (> 99%) with rapid kinetics (~ 10 minutes). Additionally, these ligands were very easily dissolved in both 1-octanol and MIBK, and even dissolved (albeit slowly) in kerosene and dodecane. Their ability to extract Fe(III) in these last two organic phases was very good, but no better than into the first two organic phases.

The 3,2-HOPOs behaved quite differently from the 1,2-HOPOs. In 1-octanol, all the 3,2-HOPO ligands extracted Fe(III) very well, extracting 90-100% in 20 minutes, and 98+% after 60 minutes of contact time. Ordering the 3,2-HOPO extractants by extraction kinetics (fastest to slowest) shows an interesting dependence on the side chain length:

1. 3,2-HOPO-hexylamide
2. 3,2-HOPO-octadecylamide
3. 3,2-HOPO-octylamide
4. 3,2-HOPO-decylamide
5. 3,2-HOPO-phenylpropylamide

The eighteen carbon side chain extractant and the six carbon side chain extractant were the two fastest extractants of the 3,2-HOPOs in 1-octanol; this is an interesting result because the ligands are so different from one another. The hexylamide is the least organophilic of the set, perhaps giving it the most mobility across the phase interface. The octadecylamide is the most organophilic of the set, possibly being the most easily dissolved of the extractants in the organic phase. For the hexylamide and octadecylamide to both extract the fastest gives an indication that phase cross-over and organic solubility are very important factors affecting extraction rate (see page 73).

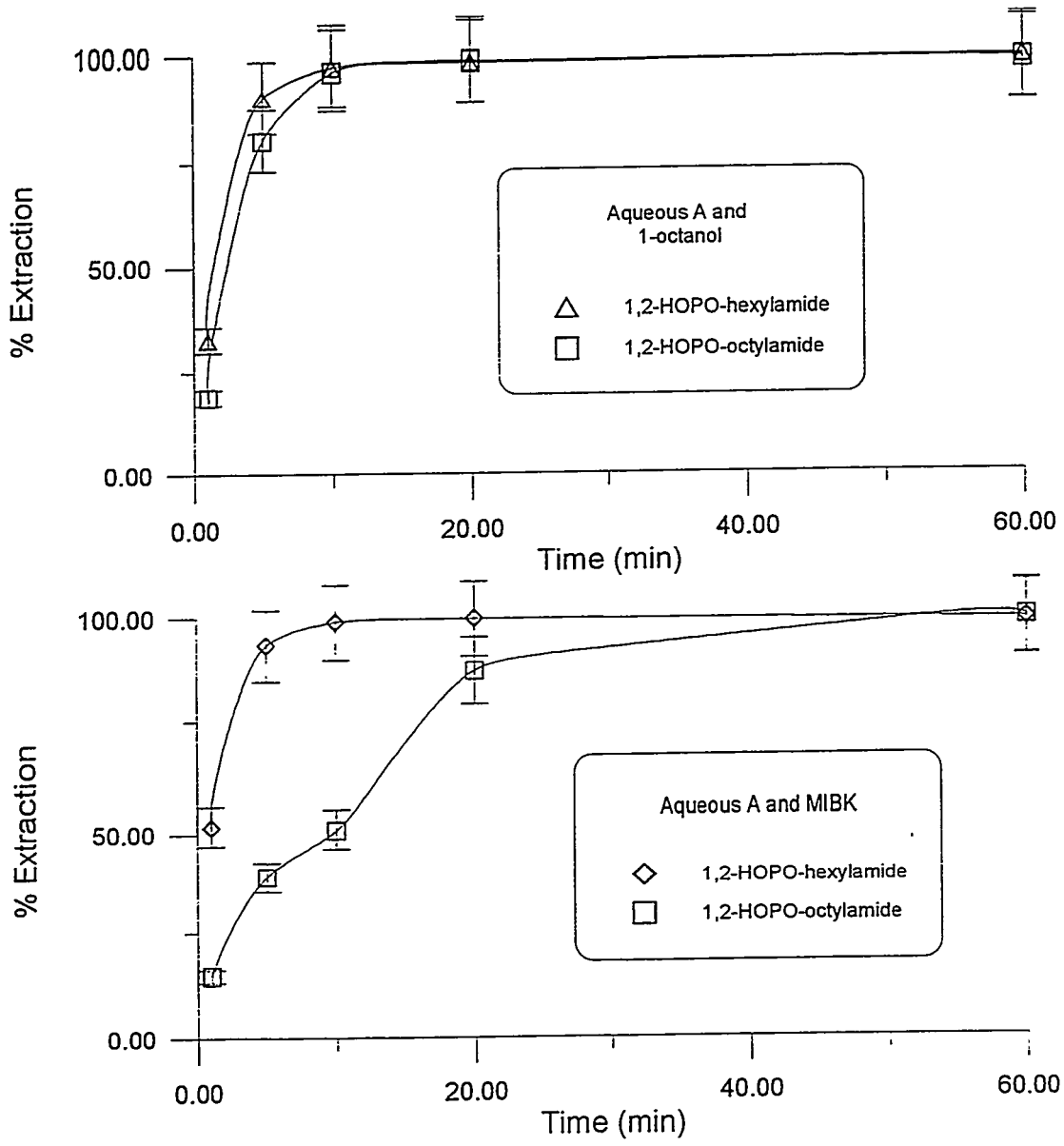

Figure 6.14: A comparison of the percent extraction of Fe(III) by the 1,2-HOPOs from Aqueous A into 1-octanol (upper) and MIBK (lower).

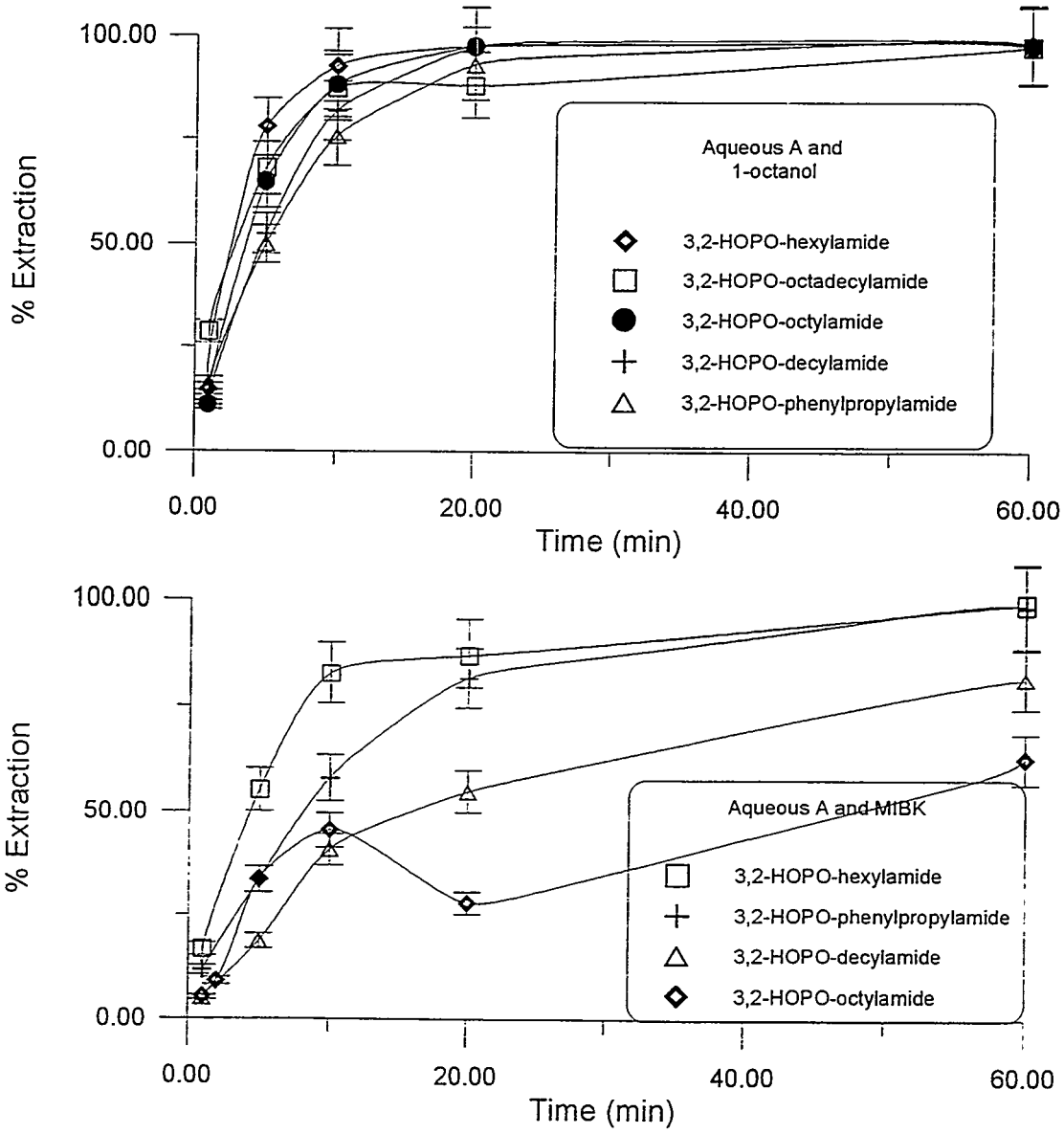

Figure 6.15: A comparison of the percent extraction of Fe(III) by the 3,2-HOPOs from Aqueous A into 1-octanol (upper) and MIBK (lower).

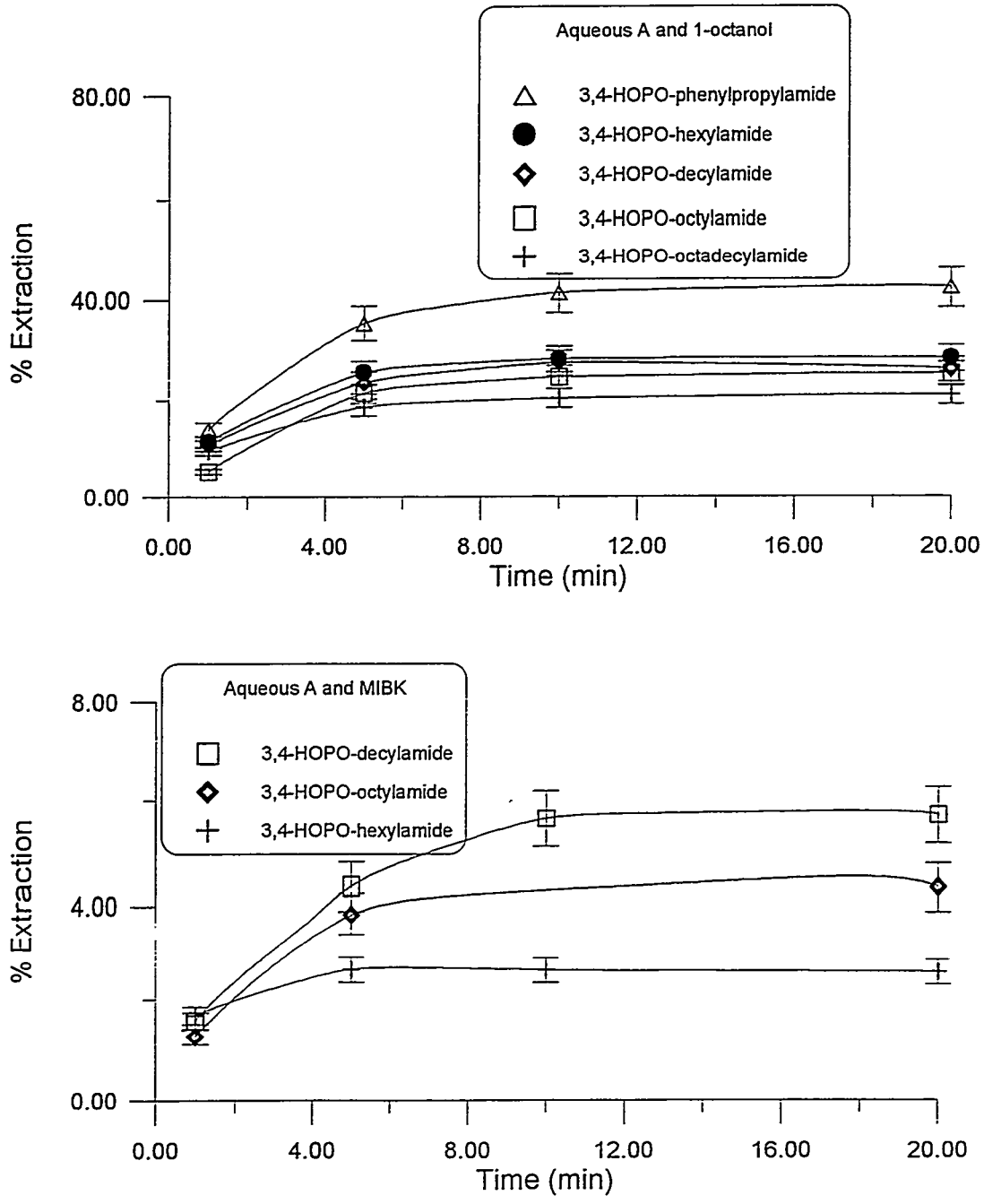

Figure 6.16: A comparison of the percent extraction of Fe(III) by the 3,4-HOPOs from Aqueous A into 1-octanol (upper) and MIBK (lower); notice the low percent extraction in both cases.

For the 3,2-HOPOs in MIBK, the picture was a little more confusing. While the hexylamide was still the best extractant, overall extraction percentages were lower and the kinetics were slower. The phenylpropylamide was the second best extractant (in 1-octanol it was the slowest), and 3,2-HOPO-octadecylamide was not soluble in MIBK. This indicates the very different solvating nature of MIBK relative to that of 1-octanol. Overall, MIBK performs worse as an organic phase than 1-octanol for these extractants and Fe(III).

For the 3,4-HOPOs, extraction into 1-octanol was very poor ($\sim$ 20–40% at 20 minutes), and poorer still ($\sim$ 2–6% at 20 minutes) into MIBK.

None of the results of extraction of Fe(III) from Aqueous B (lower ionic strength) are shown in graphical form (with the exception of Figure 6.12, which compares Aqueous A and B), because extraction was generally rather poor into this phase. The exception was the 1,2-HOPOs, for which extraction was excellent under all conditions tested. Extraction from Aqueous B into 1-octanol was poor for all the 3,2-HOPOs and 3,4-HOPOs. Interestingly, extraction into MIBK from Aqueous B was rather good ($\sim$ 90–100%) for 3,2-HOPO-hexylamide and 3,2-HOPO-phenylpropylamide. This indicates that these ligands and organic phases have individual characteristics which suit different waste streams. As discussed in the introductory chapter (Section 4.3), this is a very important characteristic for these extractions, because the exact nature of the final waste stream to be remediated is not currently known.

Values in the range of $\sim$ 200 are typically very good decontamination factors (D.F.) for a multi-stage extraction process [106]. For these studies, in which only a simple single-stage extraction was used, decontamination factors as high as $\sim$ 160 were achieved. All of the calculated extraction parameters for the Fe(III) extractions are listed in Appendix B.

From these Fe(III) extraction data, the top ligand/organic extraction systems, in order, are:

1. 1,2-HOPO-hexylamide in 1-octanol

2. 1,2-HOPO-hexylamide in MIBK

3. 1,2-HOPO-octylamide in 1-octanol

4. 1,2-HOPO-octylamide in MIBK

5. 3,2-HOPO-hexylamide in 1-octanol

Plutonium Extraction Studies

Just as in the Fe(III) experiments, the quench-corrected counts per minute (cpm) from both the aqueous and organic phase were added together (called the "total activity") and compared with the expected number of disintegrations per minute (dpm) for each extraction. Figure 6.17 plots the course of this number (percentage of total Pu(IV)) over the many plutonium extractions performed. For the first two-thirds of the extractions, the total activity remained fairly constant and roughly between 90–100% of that expected. For the last one-third of the extractions, however, the total activity falls off drastically to between 10–90%; these last extractions were the ones involving kerosene and dodecane as organic phases. By visual inspection of the centrifuge cone, these extractions appeared to separate incompletely, or not at all. Some of these extractions formed an apparent third hazy liquid layer at the phase interface, which has been witnessed previously for kerosene in the PUREX process [79], and also by Mills, *et al.* [129]. Since dissolution of the extractants in kerosene and dodecane was extremely slow anyway, these organic solvents were not used in any further extraction experiments.

Just as was the case for the extractions of Fe(III) at pH = 1, the extraction pattern that is shown in Figure 6.18 is one that is followed for the rest of the Pu(IV) extractions: *at pH = 0, the ability of each HOPO to extract Pu(IV) is directly related to its* $\log K_a$. Figure 6.11, page 162, shows the protonated and deprotonated forms of the chelate groups, and the associated protonation constants ($\log K_a$s) for each of the three HOPOs, with catechol included for reference. Catechol is the most basic of the chelating groups, with $\log K_{a1} = 13.0$, followed by 3,4-HOPO with $\log K_{a1} = 9.0$, 3,2-HOPO with $\log K_{a1} = 8.7$, and finally, the most acidic of the ligands, 1,2-HOPO, with $\log K_{a1} = 5.8$. The $\log K_a$ simply tells at what pH the ligand will be deprotonated (i.e., 1,2-HOPO will be deprotonated at pH = 5.8). This means that under the acidic conditions (pH = 0) used to test these ligands, 1,2-HOPO is the ligand best suited to shed its proton on the hydroxy group and bind a Lewis acidic metal (like Pu(IV)); then follow 3,2-HOPO and 3,4-HOPO, in that order. Figure 6.18 shows that, indeed, 1,2-HOPO-hexylamide displayed the highest percent extraction

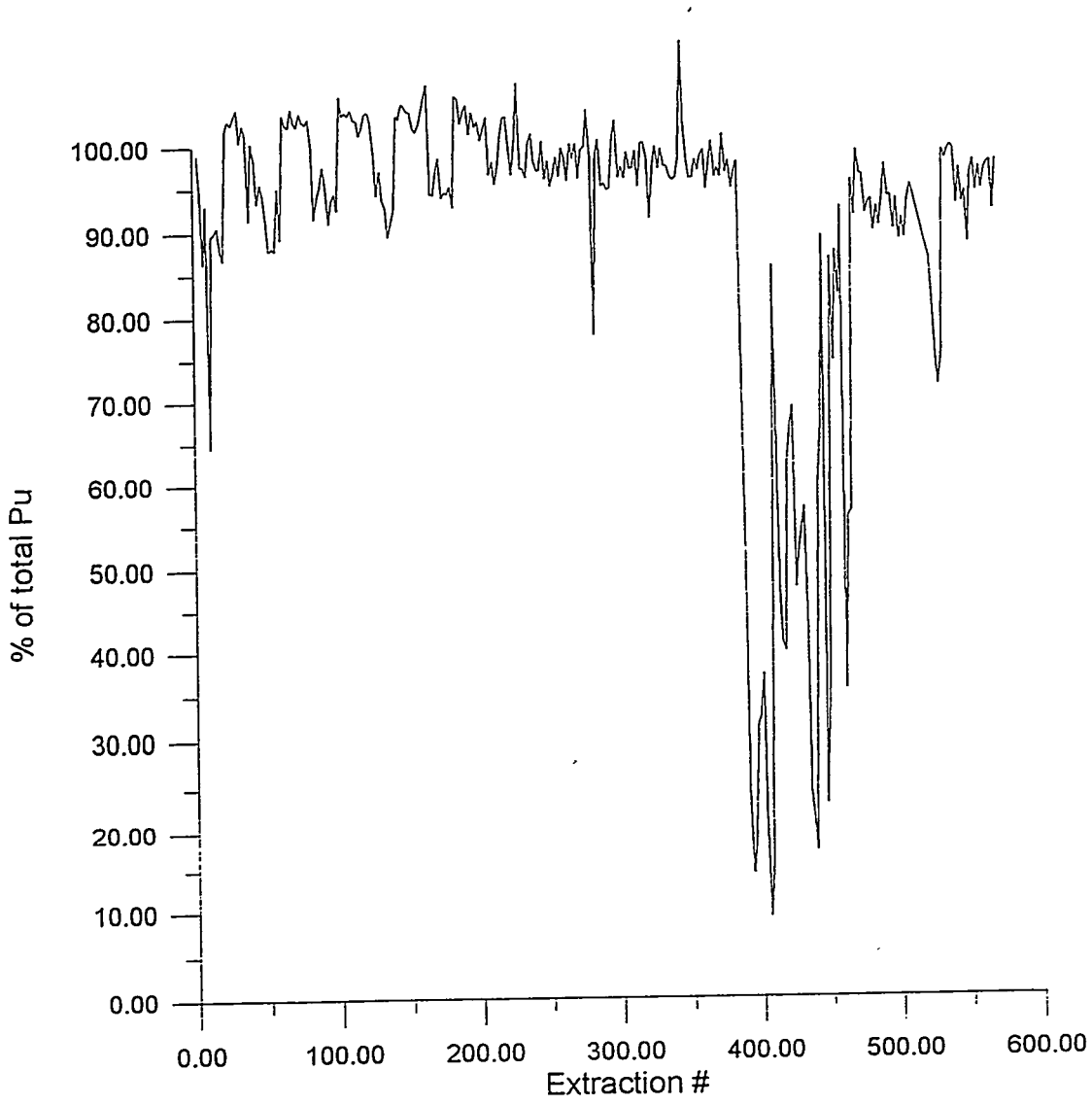

Figure 6.17: Percent total Pu(IV), measured by summing the activities in the aqueous and organic phases, versus the extraction number.

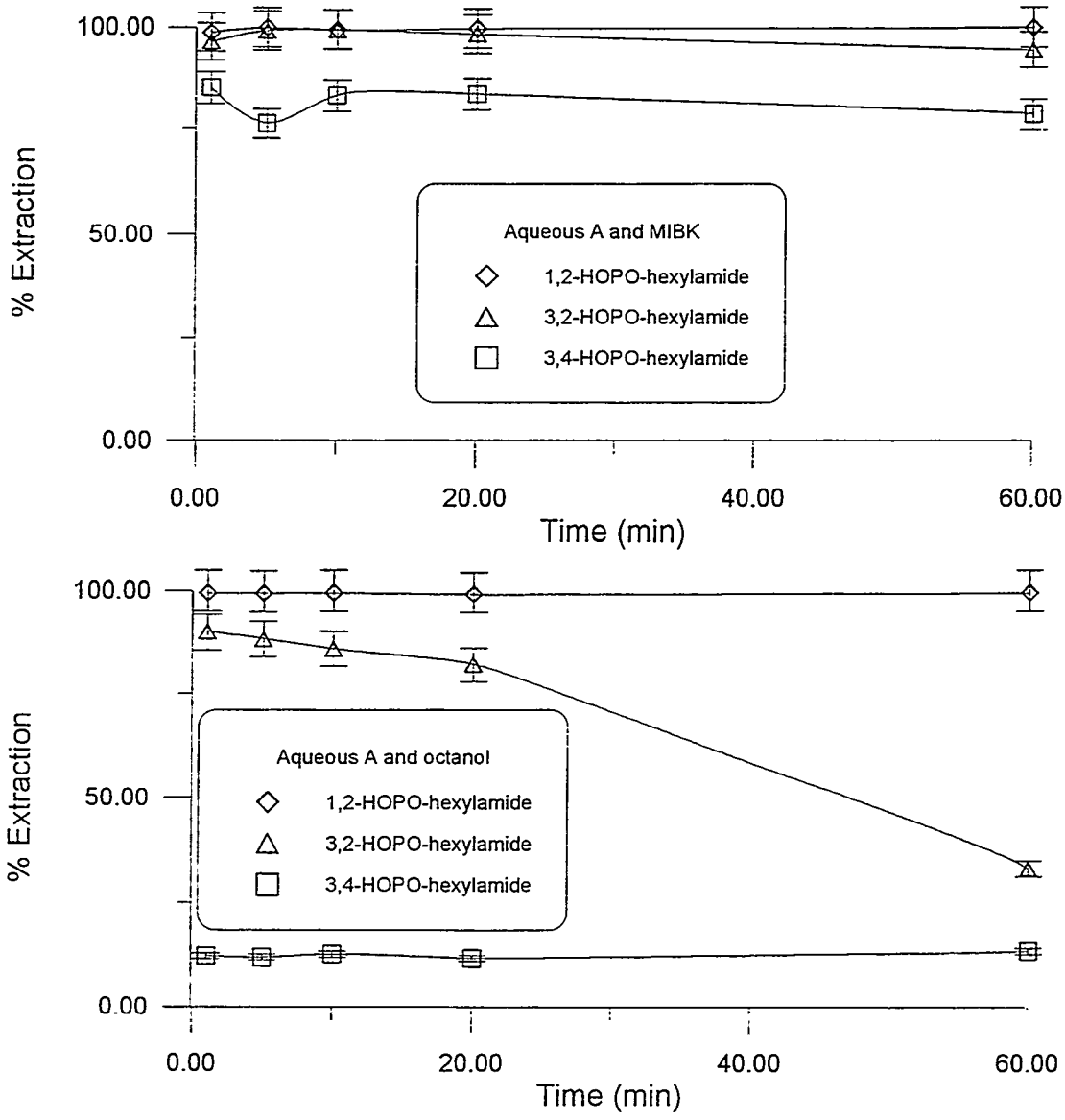

Figure 6.18: The upper plot displays the percent Pu(IV) extraction from Aqueous A versus time for the hexylamides of each of the HOPOs in MIBK; the lower plot is the same as the upper plot, but with 1-octanol as the organic solvent.

of all the HOPO-hexylamides. But 3,2-HOPO-hexylamide also showed a very high extraction, given the fact that its $\log K_{a1}$ is so much higher than that of 1,2-HOPO. Interestingly, 3,4-HOPO-hexylamide performed a very poor extraction in 1-octanol, $\sim 15\%$, but a very respectable extraction in MIBK, $\sim 80\%$. This is interesting because it is very different from the Fe(III) results, in which the 3,4-HOPO extractants never gave appreciable levels of metal extraction. Because the 3,4-HOPO moiety has such a high $\log K_{a1}$, and possibly solubility problems, these large extraction values were not expected.

The correlation between the first $\log K_a$ and the extraction ability of a HOPO chelate group is an obvious one, no matter which metal is being extracted. But that is where the similarities between the Fe(III) and Pu(IV) extractions end. It will be shown in this section that:

- In most cases, extraction into methyl isobutyl ketone (MIBK) was greater than into 1-octanol; this is the exact opposite of what was seen in the Fe(III) extractions.

- Aqueous A remained easier to extract from than Aqueous B, but in most cases the difference between extraction from the two was very small, and in some cases there was no difference in extraction.

- The kinetics for extraction of Pu(IV) were extremely fast, with full extraction accomplished for most systems by one minute.

- Strangely, for a few extractions, especially those with the 3,2-HOPO chelate group, longer contact time led to a *decrease* in the percent Pu(IV) extracted.

Fiure 6.19 plots the percent Pu(IV) extracted from Aqueous A versus time for the HOPO-hexylamides in the two organic solvents tested, 1-octanol and MIBK. 1,2-HOPO-hexylamide (upper) showed instantaneous extraction of $> 99\%$ of the Pu(IV) into each organic phase. As in the Fe(III) extractions, the 1,2-HOPO chelate group extracted very well under all the extraction conditions that were tested. 3,2-HOPO-hexylamide also extracted very well, although it does not appear to be as

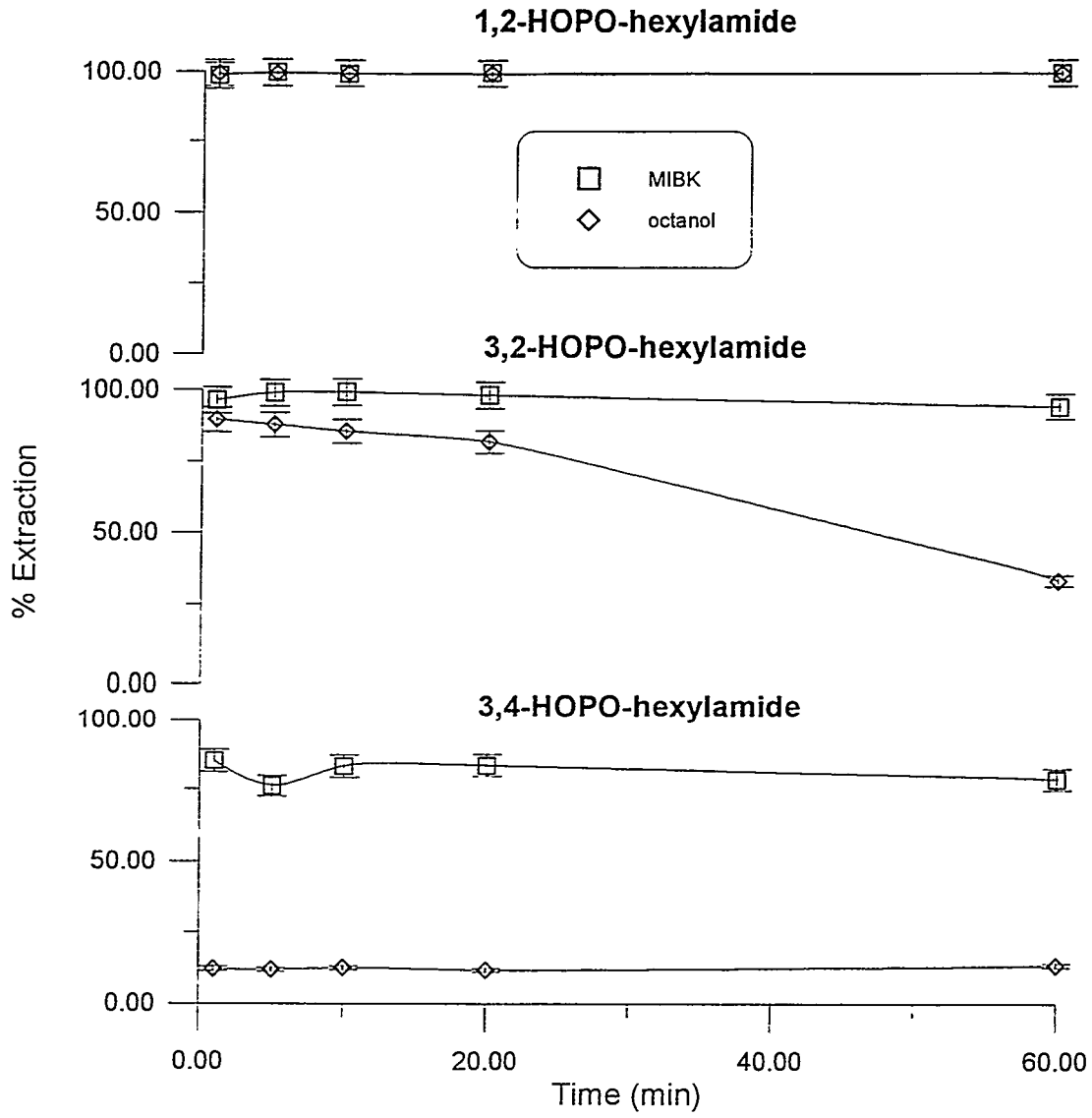

Figure 6.19: A comparison of the percent extraction of Pu(IV) by the HOPO-hexylamides from Aqueous A, into two different organic solvents, 1-octanol and MIBK. The upper plot is of 1,2-HOPO-hexylamide, the middle of 3,2-HOPO-hexylamide, and the lower of 3,4-HOPO-hexylamide.

versatile as 1,2- HOPO-hexylamide; the 3,2-HOPO extracted > 99% of the Pu(IV) into MIBK, but showed rather interesting kinetics for extraction into 1-octanol. While the initial (1-20 minutes) extraction of Pu(IV) into 1-octanol was very high ($\sim$ 90%), after 20 minutes of contact time the percent extracted began to decrease, and eventually reached $\sim$ 30% at 60 minutes. (This was not simply a case of random error, but instead was a pattern for many of the 3,2-HOPO extractions, and will be shown below). The result for 3,4-HOPO-hexylamide was also interesting — in MIBK, it extracted Pu(IV) with $\sim$ 80% efficiency, and showed the same rapid kinetics as all of the Pu(IV) extractions. In 1-octanol, 3,4-HOPO-hexylamide performed in the same manner as it did for the Fe(III) extractions, with only $\sim$ 15% extraction.

There could be any number of reasons why the two solvents used in these extractions give such different Fe(III) and Pu(IV) extractions. The easiest explanation is that the Fe(III)/ligand complex is different from the Pu(IV)/ligand complex. Fe(III) forms hexadentate complexes, while Pu(IV) forms octadentate complexes, and this difference will certainly change the steric arrangement of the final metal complex. Perhaps either Fe(III) or Pu(IV) is too small to achieve a fully saturated coordination sphere with these bulky extractants, so the species that extracts is a mixture of the extractants and other anions from the aqueous phase, such as NO_3^-. There are many complex variables in this extraction scheme that make an explanation very difficult; this topic is discussed below in more detail (page 186).

The next six figures displayed in this section give the extraction behavior of all the HOPOs in the organic phases 1-octanol and MIBK, extracting Pu(IV) from Aqueous A and B:

Figure 6.20 1,2-HOPOs in MIBK.

Figure 6.21 3,2-HOPOs in MIBK.

Figure 6.22 3,4-HOPOs in MIBK.

Figure 6.23 1,2-HOPOs in 1-octanol.

Figure 6.24 3,2-HOPOs in 1-octanol.

Figure 6.25 3,4-HOPOs in 1-octanol.

Figures 6.20, 6.21, and 6.22 show the extraction of Pu(IV) into MIBK by all the HOPOs. The most notable feature of all these plots is how well all the extractants, with the exception of the 3,4- HOPOs for Aqueous B, eliminated Pu(IV) from the aqueous phase. The 1,2-HOPOs all exhibited > 99% extraction from both aqueous phases. The 3,2-HOPOs extracted with 95+% efficiency from Aqueous A, and 90+% efficiency from Aqueous B. As mentioned previously, the 3,4-HOPOs extracted rather well from Aqueous A, removing $\sim$ 75–85%; however, they showed their weakness versus Aqueous B, removing only $\sim$ 10–25%.

Figures 6.23, 6.24, and 6.25 show the extraction of Pu(IV) into 1-octanol by all the HOPOs. Extraction into 1-octanol is a little lower than for MIBK, but the majority of the extraction numbers are still rather high. As usual, the 1,2-HOPOs transferred Pu(IV) very well from both aqueous phases into 1-octanol (> 99% extraction, very rapid kinetics). All the 3,2-HOPOs were able to extract with 80+% efficiency within the first five minutes, but then they all exhibited the anomalous decrease in percent extraction over the course of sixty minutes. It is possible that this effect could be due to radiolysis, but it seems unlikely that radiolysis would only affect the 3,2-HOPO moiety alone. A more likely explanation is that the increase in acidity to pH = 0 for these Pu(IV) extractions had more of an affect on the 3,2-HOPOs than the other HOPOs. The anomalous decrease was more pronounced for extraction from Aqueous A (extraction by 3,2-HOPO-hexylamide decreased from $\sim$ 90% at one minute to < 30% by sixty minutes), and extraction into 1-octanol, indicating a dependence on ionic strength and organic solvent. Extraction by the 3,4-HOPOs was rather poor for both aqueous phases, with all extracting $\sim$ 15% for Aqueous A and < 5% for Aqueous B.

Figure 6.26 displays the extraction data in a slightly different way. All of the previous extraction plots showed percent extraction versus contact time; this figure represents a third axis in those plots, the extractant side chain length axis, which in three dimensions would point directly out-of-the-page on all the previous extraction plots. This figure views all the previous kinetic curves from the side, and reveals

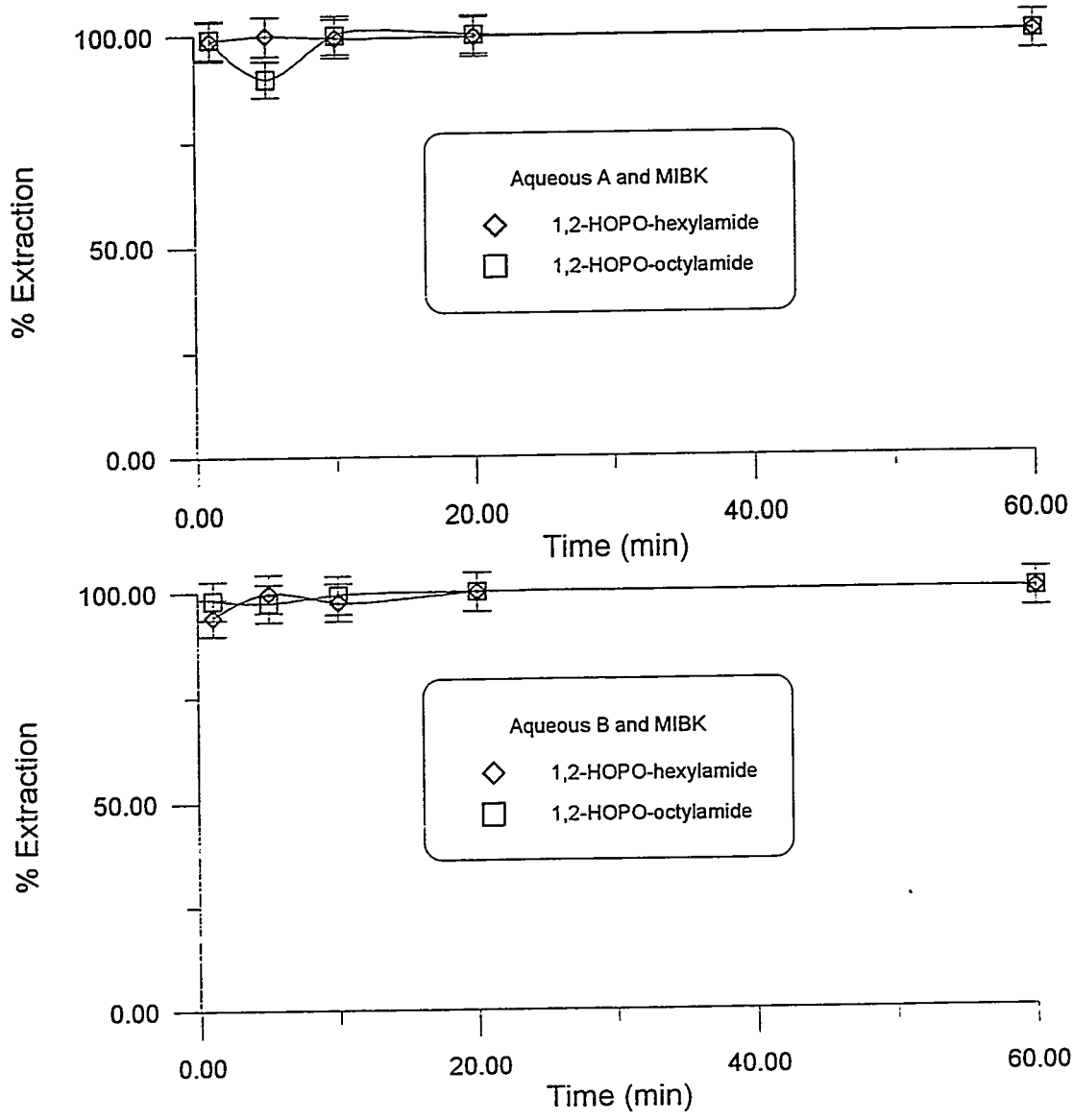

Figure 6.20: A comparison of percent extraction of Pu(IV) by the 1,2-HOPO extractants into MIBK. The upper plot is Aqueous A and the lower plot is Aqueous B.

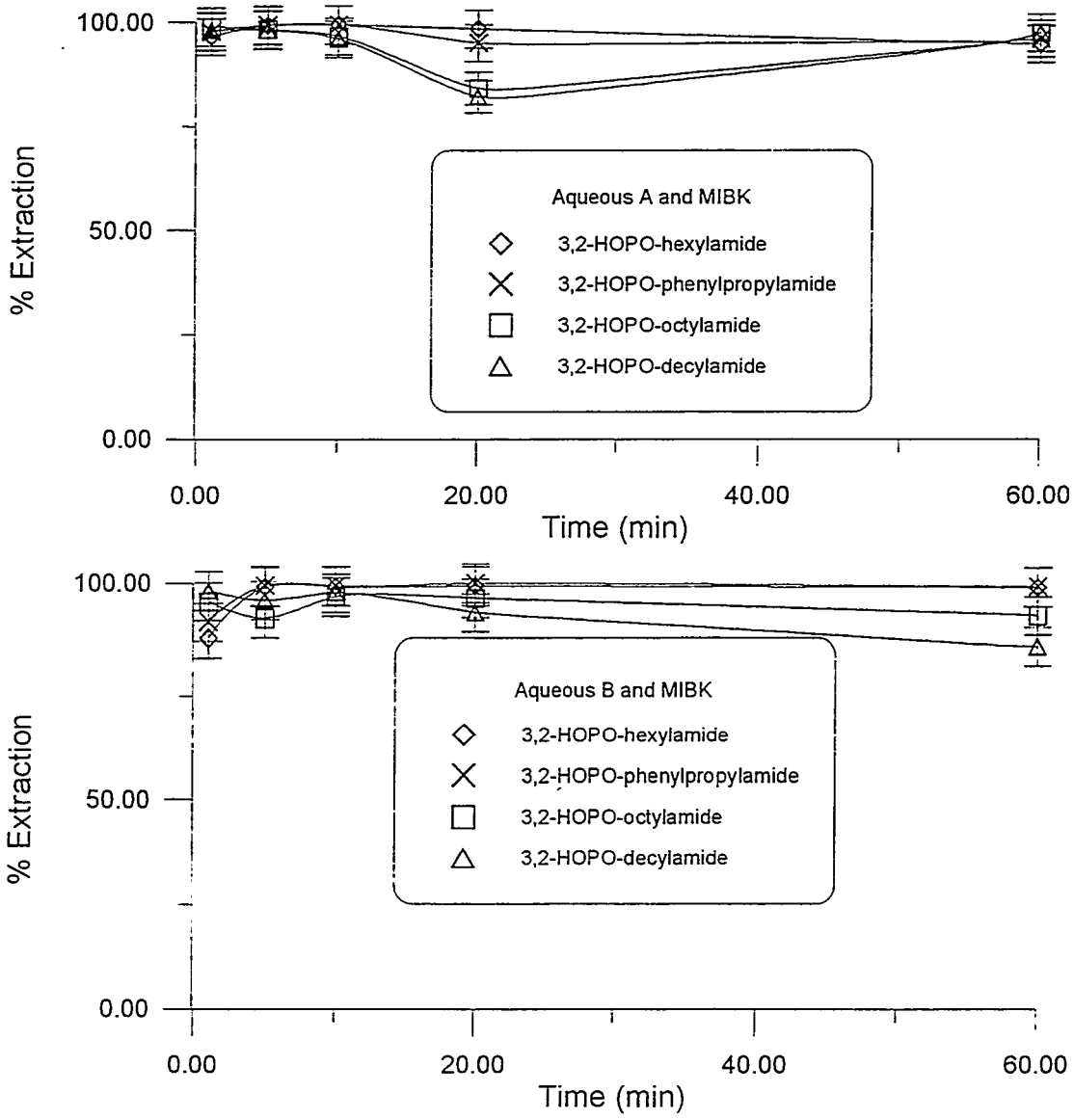

Figure 6.21: A comparison of percent extraction of Pu(IV) by the 3,2-HOPO extractants into MIBK. The upper plot is Aqueous A and the lower plot is Aqueous B.

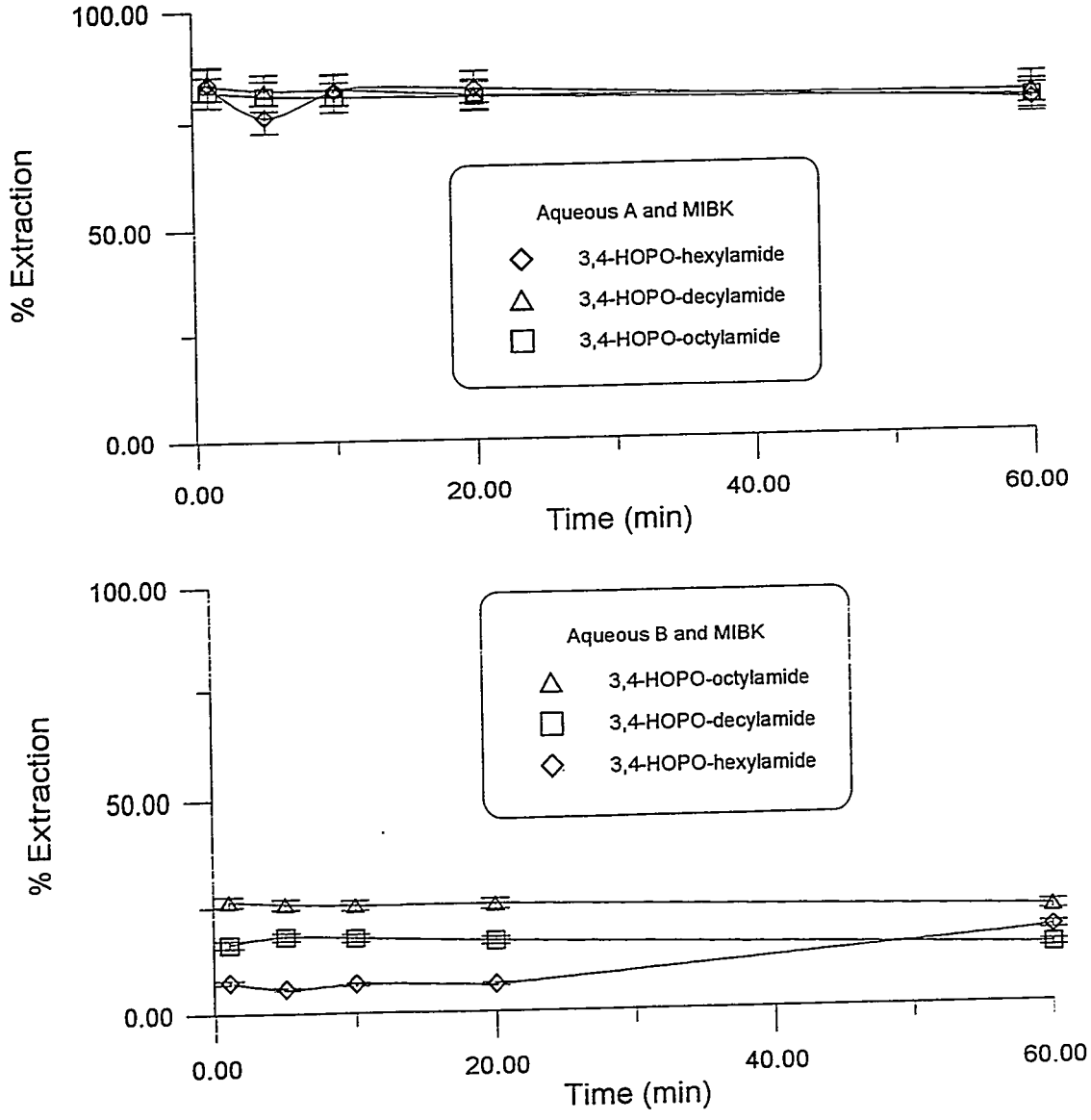

Figure 6.22: A comparison of percent extraction of Pu(IV) by the 3,4-HOPO extractants into MIBK. The upper plot is Aqueous A and the lower plot is Aqueous B.

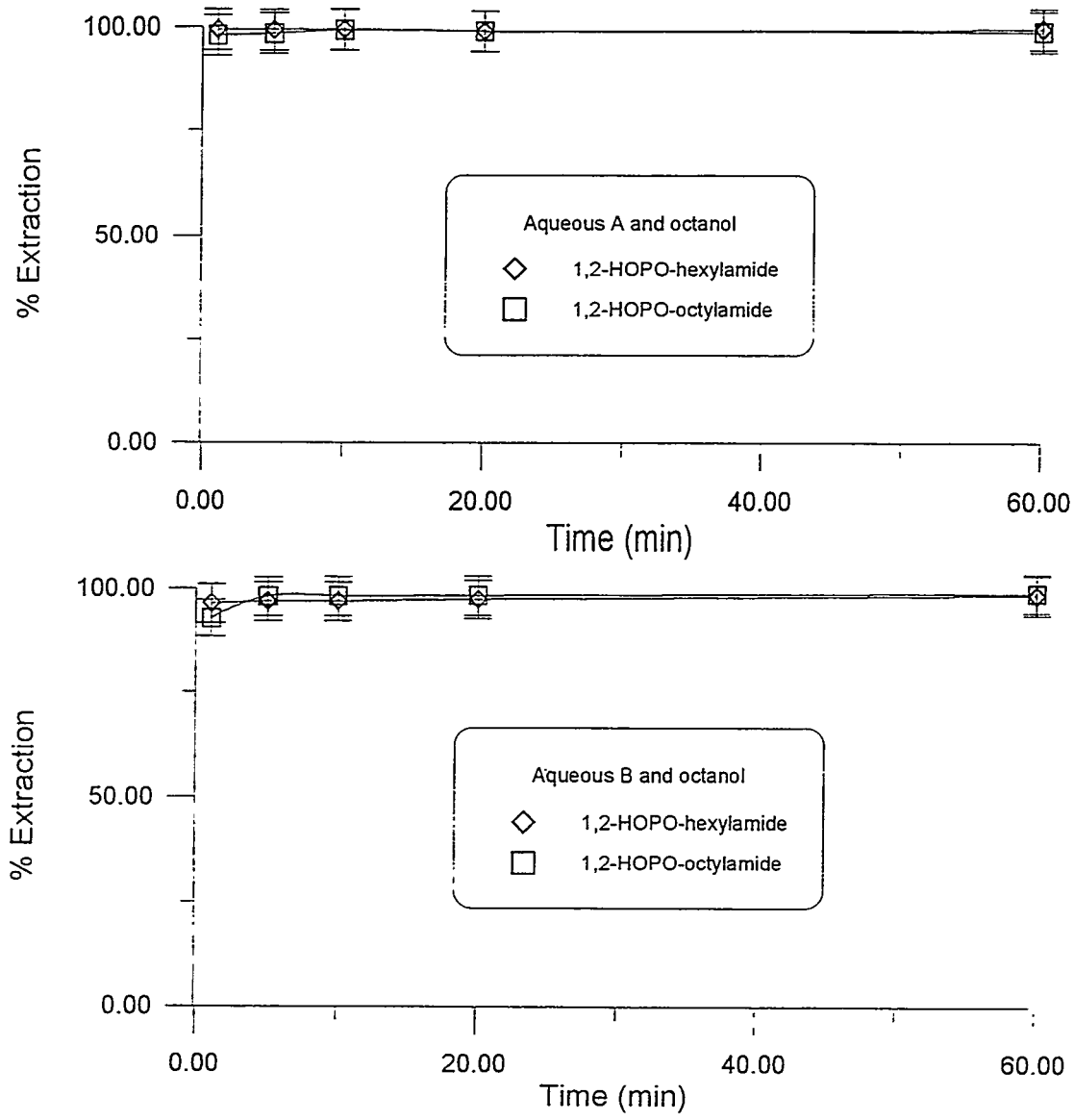

Figure 6.23: A comparison of percent extraction of Pu(IV) by the 1,2-HOPO extractants into 1-octanol. The upper plot is Aqueous A and the lower plot is Aqueous B.

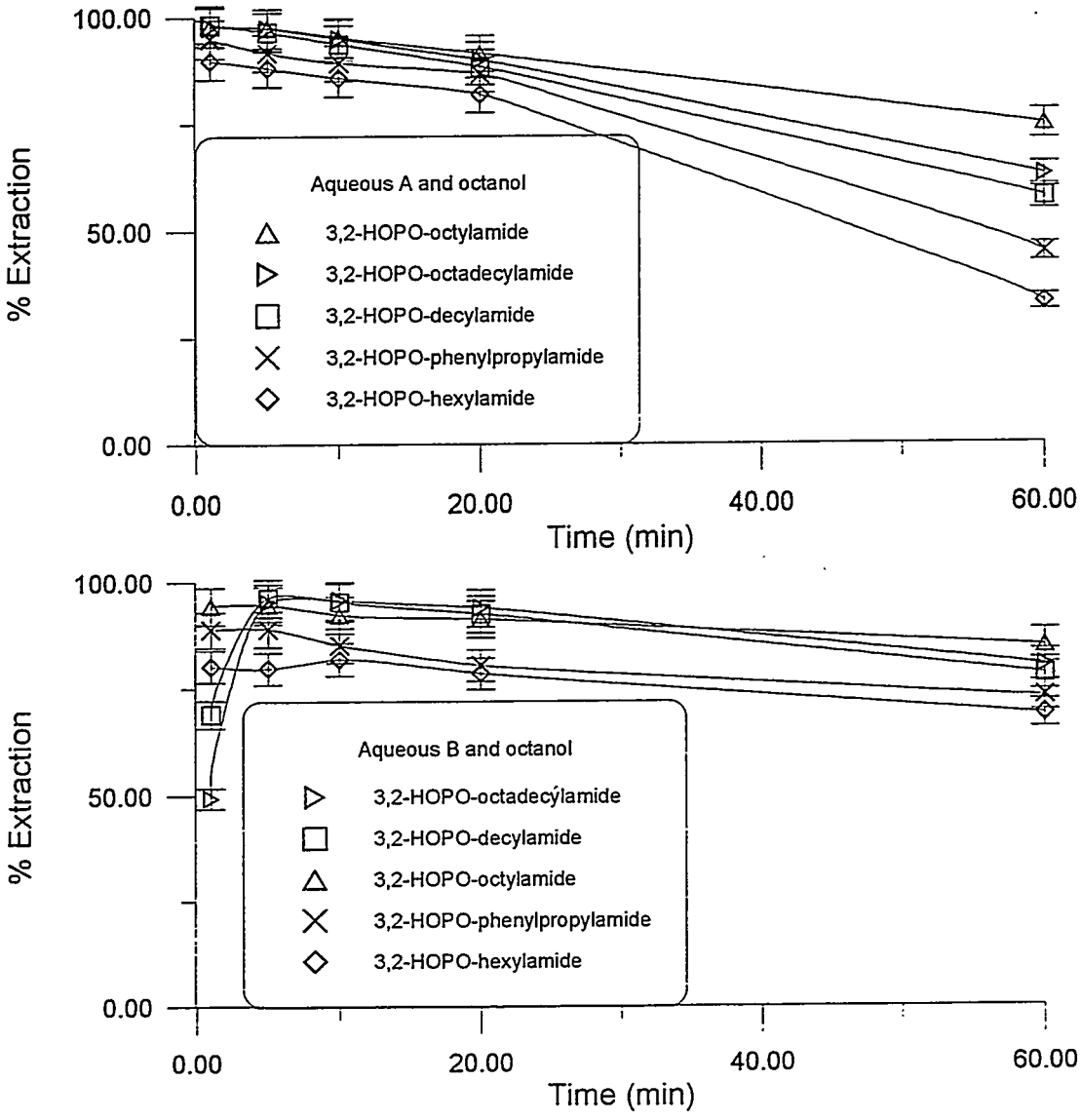

Figure 6.24: A comparison of percent extraction of Pu(IV) by the 3,2-HOPO extractants into 1-octanol. The upper plot is Aqueous A and the lower plot is Aqueous B.

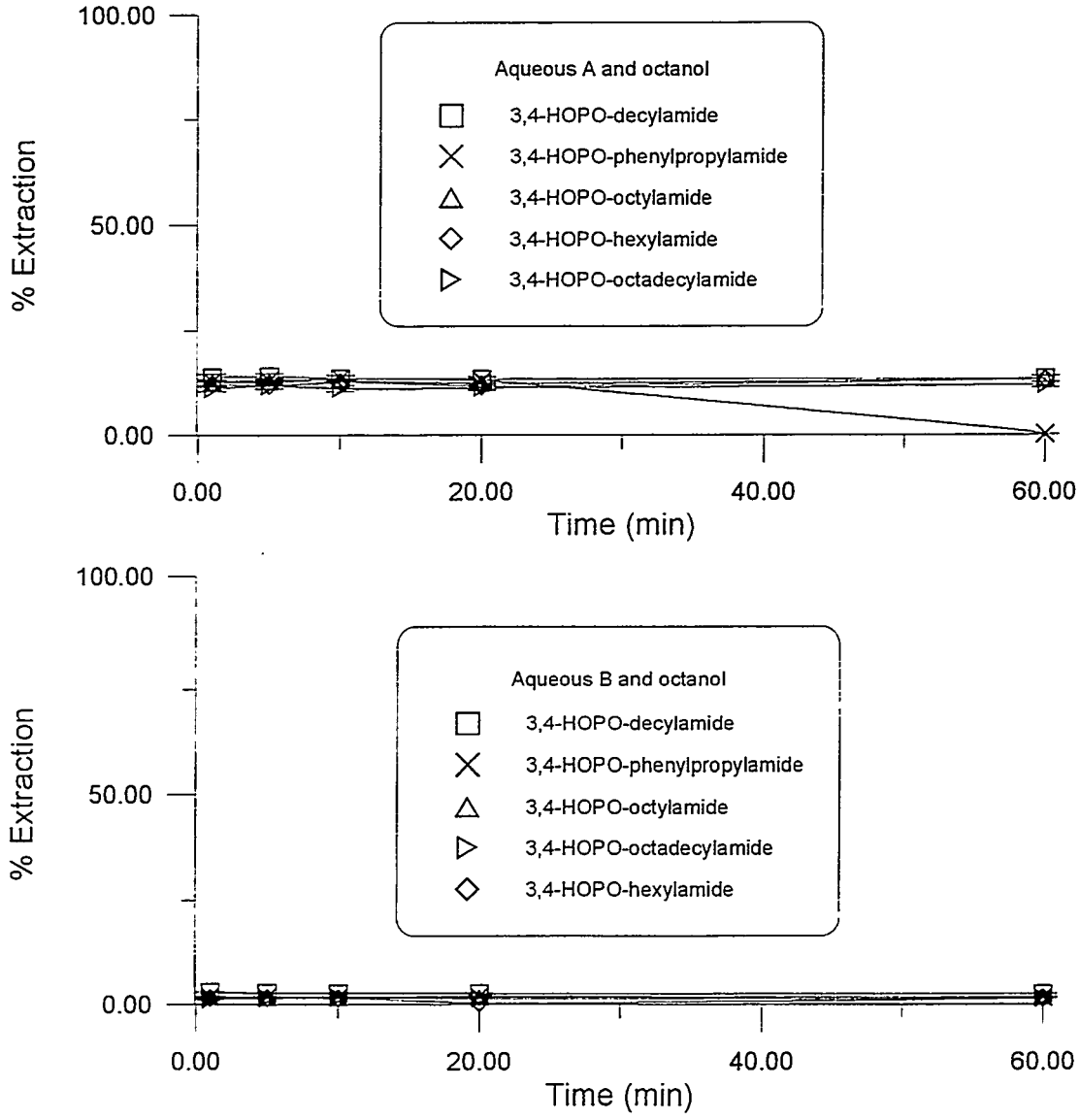

Figure 6.25: A comparison of percent extraction of Pu(IV) by the 3,4-HOPO extractants into 1-octanol. The upper plot is Aqueous A and the lower plot is Aqueous B.

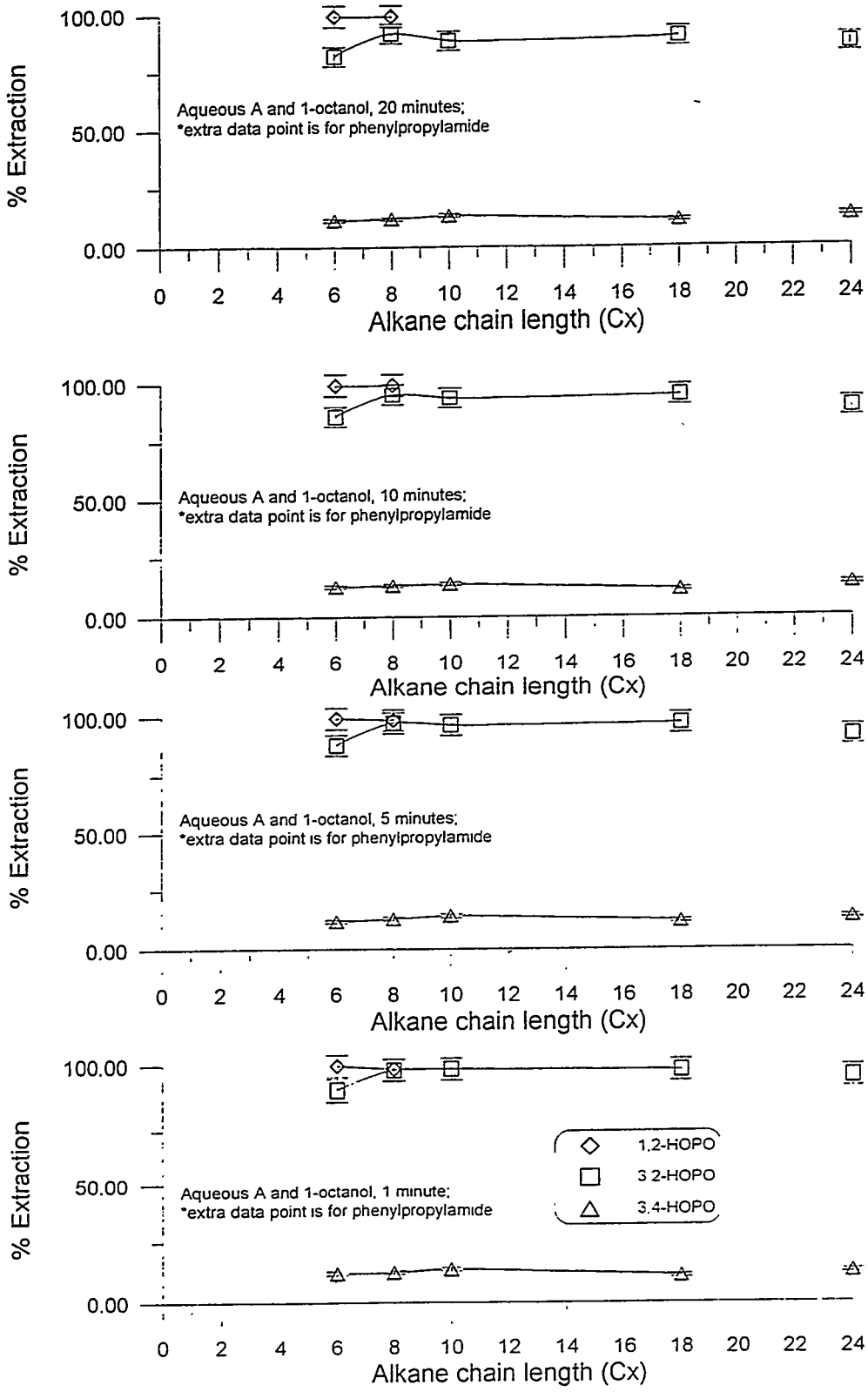

Figure 6.26: A comparison of Pu(IV) extraction by all the HOPOs from Aqueous A into 1-octanol; percent extraction is plotted versus the side chain length (number of carbons) of the extractant. The top plot is at a contact time of 20 minutes, the second, 10 minutes, the third, 5 minutes, and the bottom, 1 minute.

how the percent extraction depends on the extractant side chain length. For the Pu(IV) extraction data, this figure reveals very little side chain length dependence. Counting the plots in this figure from the bottom, they display percent extraction at one minute, five minutes, ten minutes, and twenty minutes. What is interesting in this figure is that, from plot to plot, there is very little change in the percent extraction for a given HOPO moiety; that is, *the percent Pu(IV) extraction showed very little dependence on carbon side chain length.* Far more important to extraction efficiency is the HOPO moiety itself. It should be noted that for the 3,2-HOPOs, the hexylamide gave the lowest percent extraction, and the octylamide the highest percent extraction.

Of all the differences between the Pu(IV) and Fe(III) extractions, perhaps the most striking was in the extraction kinetics. Figure 6.27 illustrates this difference by comparing the kinetics of extraction for both Pu(IV) and Fe(III) from Aqueous A into 1-octanol. For Pu(IV), transfer into the organic phase was instantaneous — $> 99\%$ complete after one minute of contact time. For Fe(III), the extraction process was much slower, being $> 99\%$ complete only after $\sim$ 15–20 minutes contact time. Why was there such a large kinetic difference for two metals that are so similar, and extracted under nearly identical conditions?

To begin to answer this question, it must first be realized that, while these two metals are very similar, they are not exactly the same (see page 68 for the discussion of the similarities between Fe(III) and Pu(IV)). Fe(III) has an ionic radius of 0.65 Å, while the ionic radius of Pu(IV) is much larger (as would be expected for an actinide), measuring 0.96 Å. As Figure 4.1 illustrated, the charge-to-ionic radius ratios of these two metals are similar, but Pu(IV) has a slightly larger ratio of 4.6, while Fe(III) has a ratio of 4.2. Pu(IV), due to its larger size and additional unit charge, prefers to be eight-coordinate, while Fe(III) prefers six-coordinate. Since these extraction experiments were conducted with radioactive isotopes of the metals, there is an additional difference between the two metals in their types of radioactivity — Fe(III) emits a very soft x-ray with an energy of 6.5 keV, while Pu(IV) gives off a much more energetic alpha particle with 4.90 MeV. Finally, each metal exhibits a very different pH-dependent species distribution.

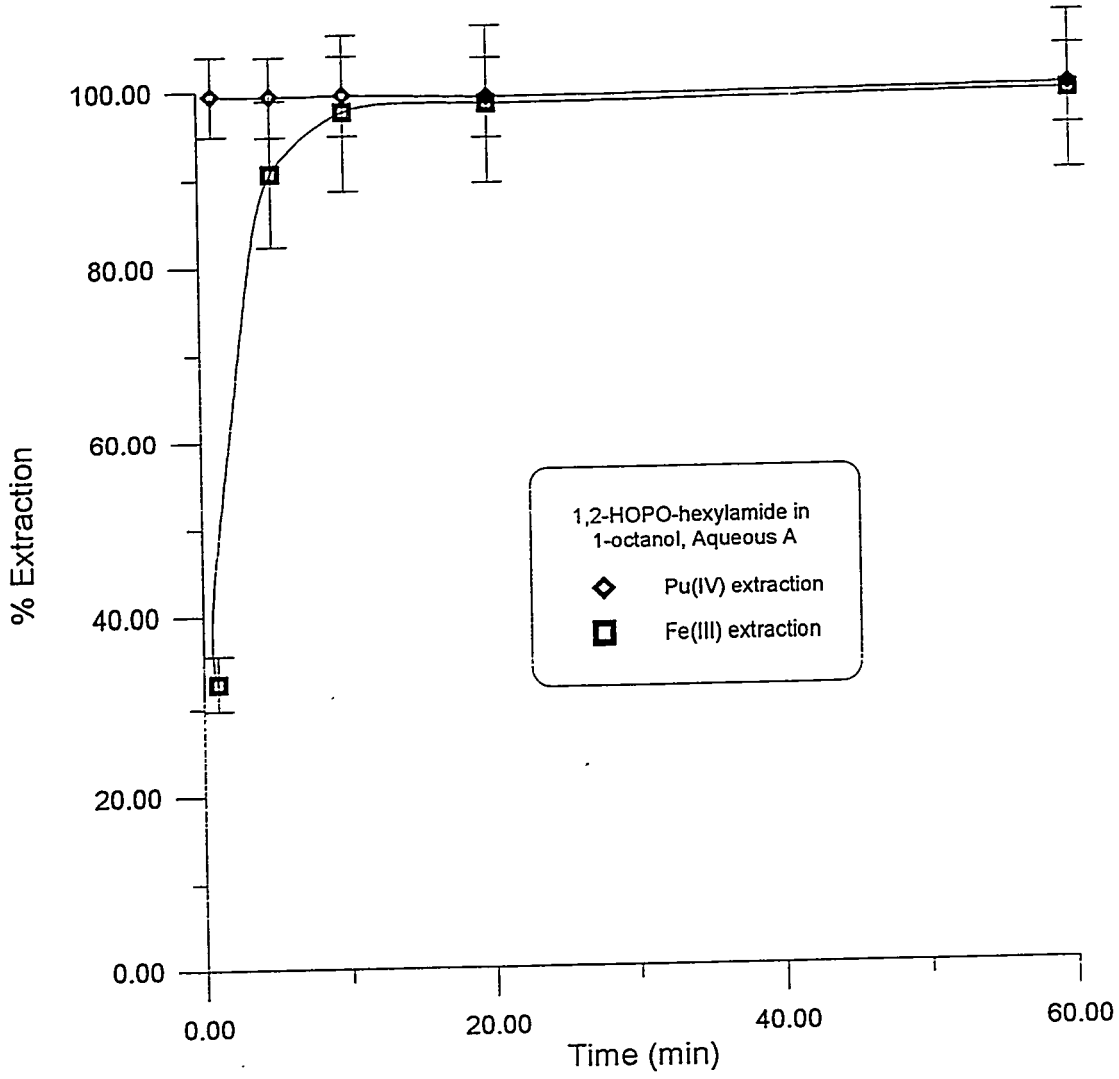

Figure 6.27: A comparison of percent extraction of Pu(IV) (diamonds) and Fe(III) (squares) from Aqueous A into 1-octanol. The extraction kinetics are much faster for Pu(IV).

While the reaction conditions used for the Pu(IV) and Fe(III) extractions were nearly identical, they, too, were not exactly the same. Each metal has a very different pH-dependent species distribution, and the two extraction experiments used two different pHs — the Fe(III) extractions were at pH = 1, and the Pu(IV) extractions were at pH = 0. Figure 5.24 (page 135) shows Fe(III) and Pu(IV) species concentrations from pH = 0–12. For Pu(IV) at pH = 0, there is $\sim$ 75% free Pu^{4+} and $\sim$ 25% $PuOH^{3+}$; for Fe(III) at pH = 1, there is $\sim$ 90% free Fe^{3+} and $\sim$ 10% $FeOH^{2+}$. It is very difficult to translate these numbers directly into an explanation of the different kinetic behavior of the two metals, but the different concentrations of free metal in each case could possibly account for part of the kinetic difference.

Given that there are these differences between the species in solution for the Fe(III) and Pu(IV) extractions, perhaps there is a *slightly different metal chelate complex being extracted in each case.* It has been seen previously [127] that while octadentate complexes of Pu(IV) are more thermodynamically stable, at physiological pH (pH $\approx$ 7.4) the large $\log K_{a1}$ of the fourth added ligand (catechol or HOPO) kinetically prevents the Pu(IV) complex from fully saturating its coordination sphere. In other words, in the competition for the oxo-chelating groups of the fourth bidentate ligand, the proton (H^+) beats out Pu(IV), because Pu(IV) has so little of its "hard" Lewis acid character remaining. Considering that these extraction experiments were conducted at pHs much lower than physiological pH, it is certainly not unbelievable that something other than an ML_4 complex is being extracted into the organic phase. The ionic strength of these solutions is high enough (with 5 M or 0.1 M NO_3^-) to neutralize any charge on a partial metal/ligand species, in order for it to more easily pass into the organic phase.

How does this translate into faster extraction kinetics for Pu(IV)? One possible explanation concerns the 25% concentration of $PuOH^{3+}$ at pH = 0. If the already-coordinated OH^- aids in the charge neutralization of a partial metal/ligand complex, then kinetics into the organic phase should be faster. Another explanation might be that optimal solubility in each of the organic phases requires at least three organophilic groups coordinated to the extracted metal. In the case of Pu(IV), this means the extracted species would be an ML_3^+ complex with an associated anion; for

Fe(III), it would mean the extracted species had to be fully saturated (ML_3) in order for optimum solubility. This would translate into slower kinetics for the formation of an organophilic Fe(III) species if the ML_3 complex were sterically hindered.

This last point about a fully saturated metal leads into a discussion concerning the steric arrangement of the extracted metal/ligand species. Figures 6.28, 6.29, and 6.30 show CAChe-generated pictures of the arrangement of 1,2-HOPO-hexylamide, 3,2-HOPO-hexylamide, and 3,4-HOPO-hexylamide, respectively, around Pu(IV). The larger ionic radius of Pu(IV) (0.96 Å) translates directly into more "space" around the coordination sphere of plutonium. Using the ionic radii of these two metals, their surface areas can be calculated. Pu(IV) has *over two-times as much surface area* as Fe(III), while in order to saturate its coordination sphere, Pu(IV) only needs to coordinate one additional bidentate group. Since the bidentate groups used in these extractions are very large, bulky, organophilic-type extractants, with floppy alkane side chains, steric hindrance could play a large role in determining the degree of metal coordination. The increased surface area of Pu(IV) translates directly into increased "bite angle" for any bidentate groups coordinating to Pu(IV).

Values in the range of ~ 200 are typically very good decontamination factors (D.F.) for a multi-stage extraction process [106]. For these studies, in which only a simple single-stage extraction was used, decontamination factors as high as ~ 7500 were achieved. All of the calculated extraction parameters for the Pu(IV) extractions are listed in Appendix B.

From these Pu(IV) extraction data, the top ligand/organic extraction systems, in order, are:

1. 1,2-HOPO-hexylamide in 1-octanol
2. 1,2-HOPO-hexylamide in MIBK
3. 1,2-HOPO-octylamide in 1-octanol
4. 1,2-HOPO-octylamide in MIBK
5. 3,2-HOPO-octylamide in MIBK

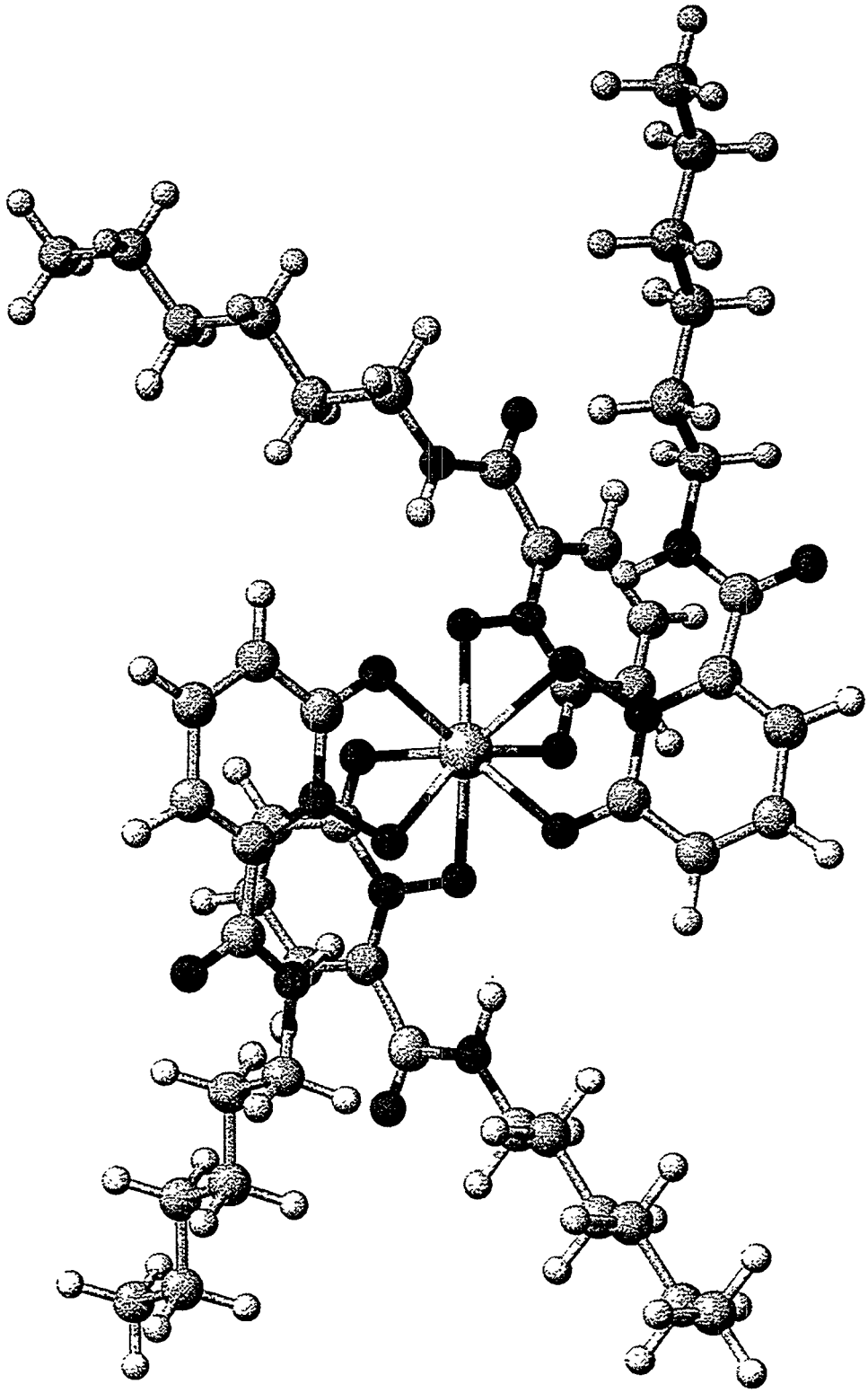

Figure 6.28: CAChe-generated picture of the arrangement of four 1,2-HOPO-hexylamide extractants around Pu(IV). CAChe performed a simple energy minimization algorithm, and the H-bonding of the amide proton to the ortho-hydroxyl oxygen is shown for all four extractants.

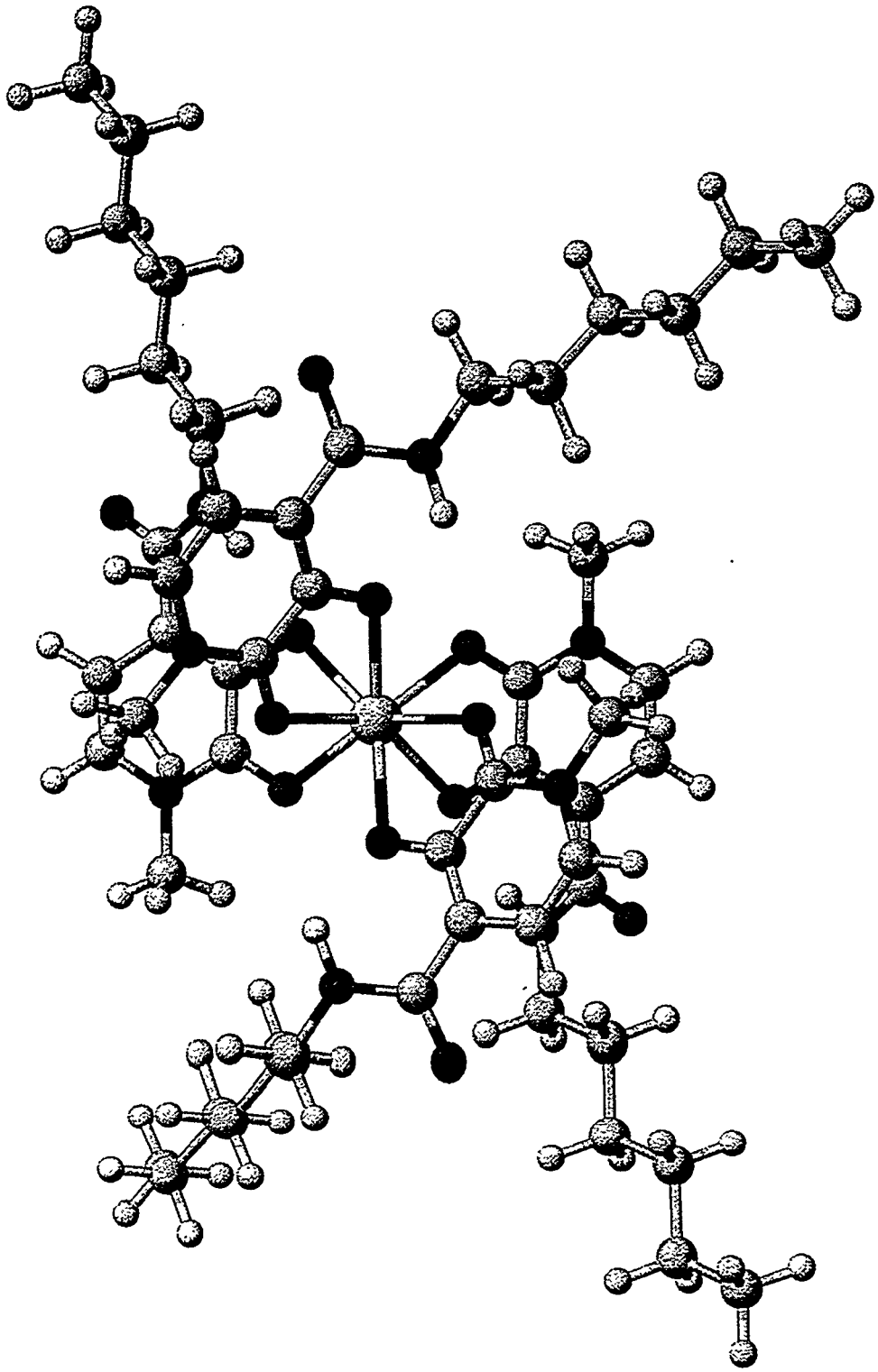

Figure 6.29: CAChe-generated picture of the arrangement of four 3,2-HOPO-hexylamide extractants around Pu(IV). CAChe performed a simple energy minimization algorithm, and the H-bonding of the amide proton to the ortho-hydroxyl oxygen is shown for all four extractants.

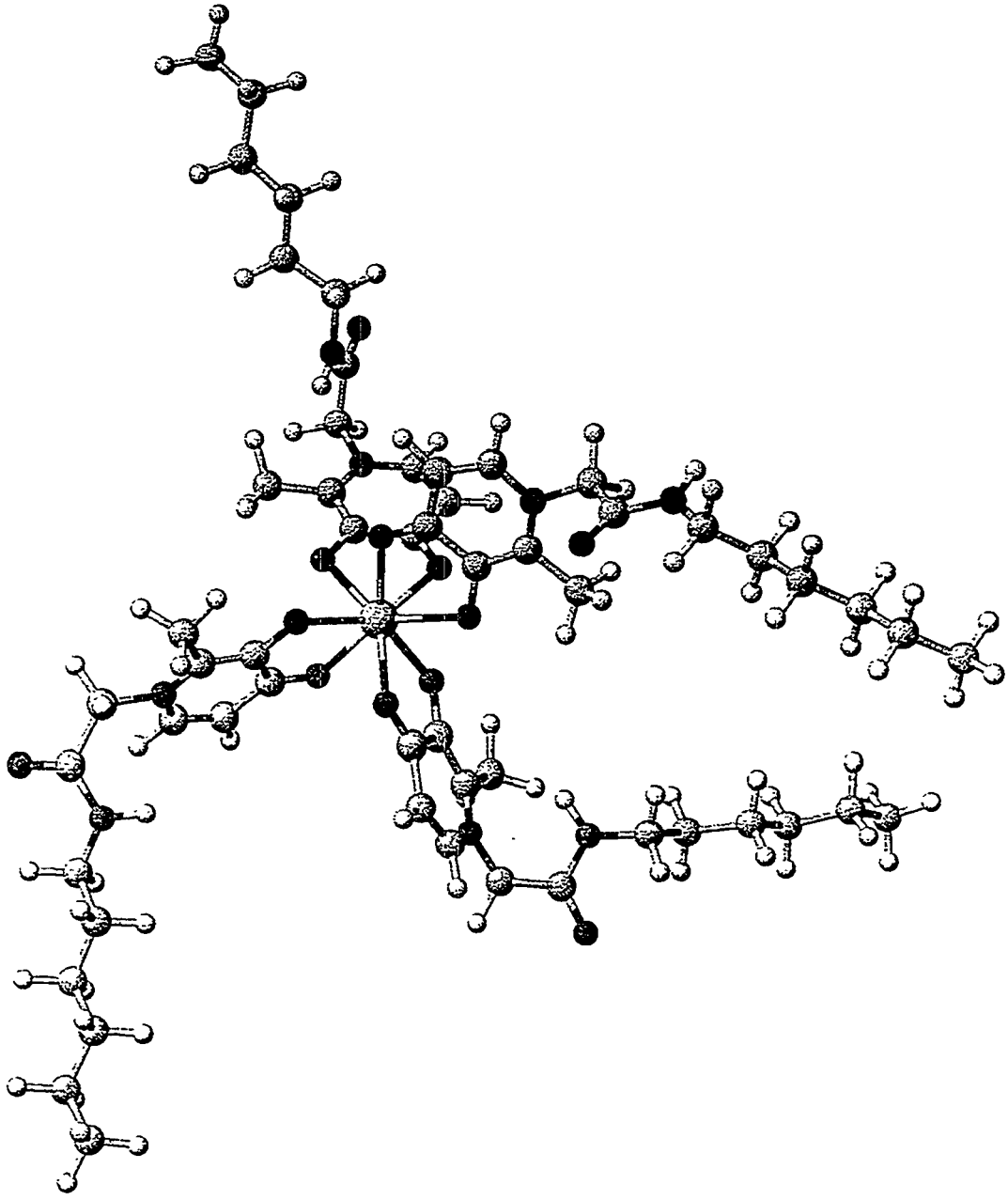

Figure 6.30: CACHe-generated picture of the arrangement of four 3,4-HOPO-hexylamide extractants around Pu(IV). CACHe performed a simple energy minimization algorithm; notice that there is no H-bonding of the amide proton to the hydroxyl oxygen, because the oxygen is no longer in the ortho- position.

This is the same order that was seen in the Fe(III) extractions, with the exception of the exchange of 3,2-HOPO-hexylamide in 1-octanol for 3,2-HOPO-octylamide in MIBK.

Other Extraction Studies

Other extraction studies were done with one of the best ligand/organic extraction systems from the previous section, 1,2-HOPO-octylamide in MIBK:

Fe(III) Competition Study Extractions were performed with the Fe(III)-to-Pu(IV) ratio adjusted to 109:1 and 1090:1, to test ligand extraction in the presence of an interfering metal.

EDTA Competition Study The ability of the ligand to extract Pu(IV) away from EDTA in the aqueous phase was tested with an EDTA-to-HOPO ratio of 2.7:1.

Concentration Study Extractions were performed with the ligand-to-metal (L:M) ratio adjusted to 1.0:1, 3.1:1, 6.2:1, 15.5:1, and 31:1 (this last ratio had the standard 3.1 mM ligand concentration).

Stripping Three different methods of removing plutonium from the HOPO ligands were investigated:

1. Nitric acid stripping, with 7–16 M HNO_3.
2. Reduction to Pu(III), with 0.1060 M KI in 0.4000 M HCl.
3. Reduction to Pu(III), with 0.0121 M ascorbic acid in 0.5000 M HNO_3.

In the eventual real waste stream encountered by these extractants, whether it be waste from the Hanford Site, Oak Ridge National Laboratory Site, or some other source, there will likely be many interfering metals in the waste that could make it difficult for these extractants to efficiently and effectively remediate the waste. In order to test the selectivity of these extractants, they were used to extract Pu(IV) from two aqueous phases that had $\sim$ 100 times and $\sim$ 1000 times more Fe(III) than Pu(IV). Fe(III) is likely to be the most competitive of all possible interfering metals, because of its similarity to Pu(IV), and because of its abundance in most nuclear fuel reprocessing wastes [81]. Figure 6.31 shows how 1,2-HOPO-octylamide in MIBK performed with such large Fe(III) concentrations in Aqueous A. Regardless of the excess of Fe(III), 1,2-HOPO-octylamide, which is present in the standard 30-fold

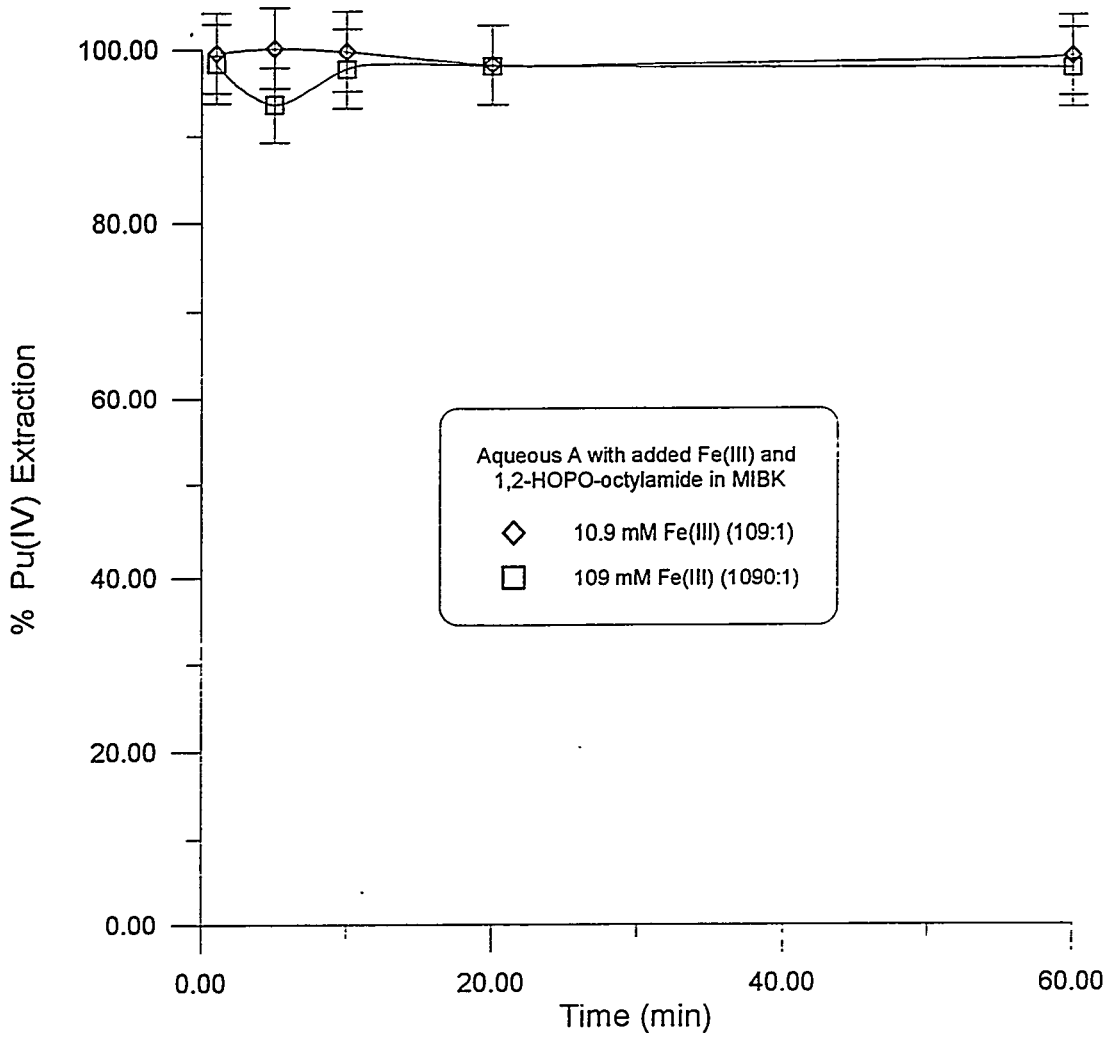

Figure 6.31: Extraction of Pu(IV) by 1,2-HOPO-octylamide in MIBK, from two Aqueous A solutions loaded with 10.9 mM ($\sim$ 100-fold excess) Fe(III), and 109 mM ($\sim$ 1000-fold excess) Fe(III).

excess to Pu(IV), extracts as though there is no interfering metal in solution. In other words, *in as much as a 1000-fold excess of Fe(III), 1,2-HOPO-octylamide is* $> 99\%$ *selective for Pu(IV).* This is a testimony to the strength and selectivity of the HOPO ligands in general, and confirms the results of the previous extraction experiments that indicated that extraction of Pu(IV) was greater and faster than extraction of Fe(III).

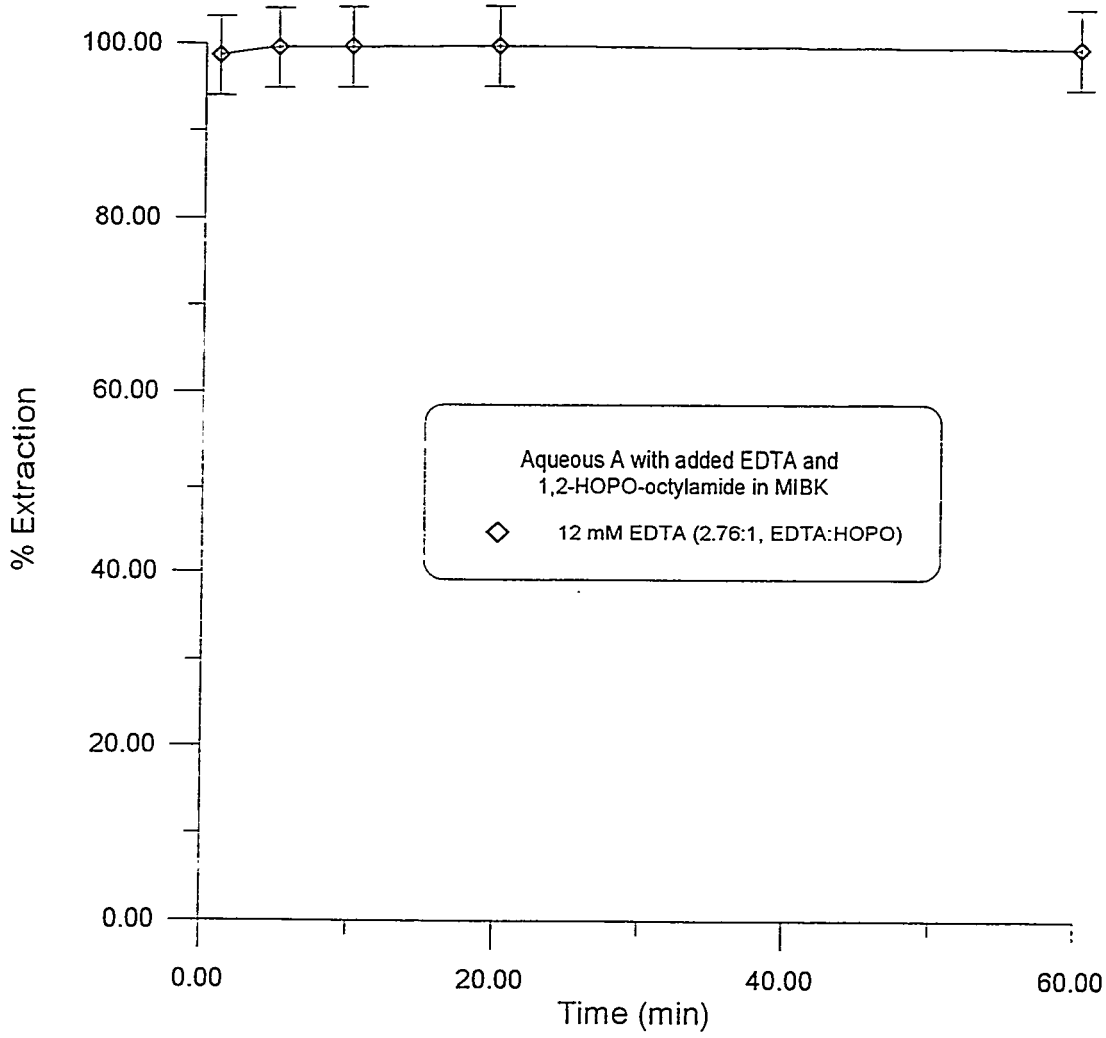

Figure 6.32: Extraction of Pu(IV) by 1,2-HOPO-octylamide in MIBK, from Aqueous A loaded with 12 mM ($\sim$ 3-fold excess relative to HOPO) EDTA.

Figure 6.32 illustrates another competitive extraction, in which 1,2-HOPO-octylamide competes with EDTA for chelation of Pu(IV). Just as was the case with Fe(III), EDTA is likely to be present in relatively high concentrations in waste streams that are to be treated with these HOPO extractants [81]. In this extraction experiment, EDTA was dissolved in Aqueous A in $\sim$ 3-fold excess to 1,2-HOPO-octylamide in the organic phase. Again, as in the Fe(III) competition extraction, 1,2-HOPO-octylamide extracts Pu(IV) with $>$ 99% efficiency, as though there is no EDTA in the aqueous phase. All the HOPOs have much larger formation constants with Pu(IV) than does EDTA; additionally, at the low pH of Aqueous A, EDTA is probably not able to deprotonate to a significant enough extent to bind Pu(IV) strongly.

Figure 6.33 shows the dependence of the percent Pu(IV) extraction on the ligand-to-metal ratio. The data points in the plot are for L:M ratios of $\sim$ 1:1, 3:1, 6:1, 15:1, and 30:1. At first glance, this plot looks odd, because at a ligand-to-metal ratio of 1:1, 1,2-HOPO-octylamide was able to extract $\sim$ 90% of Pu(IV) from Aqueous A. This finding supports the hypothesis advanced above (see page 188) that there may be another or many other extractable metal/ligand species rather than simply the theoretical ML_4. These concentration-dependent extractions were allowed 30 minutes of contact time, which is likely to be sufficient time to allow even a kinetically-hindered species to form and extract. For all the L:M ratios above 1:1 in the plot, there was $>$ 99% extraction.

The results shown in Figure 6.34, and those taken from the stripping experiments which attempted to reduce Pu(IV) to Pu(III), illustrate one of the negative aspects of the HOPO extractants — *the extracted HOPO complexes were so strong that stripping plutonium from the organic phase was very difficult.* The figure shows that there was effectively no stripping of Pu(IV) from MIBK with HNO_3 concentrations below 13 M; at 13 M, $\sim$ 4% of the Pu(IV) was stripped away from 1,2-HOPO-octylamide, while at concentrated (15.8 M) HNO_3, $\sim$ 40% was stripped. Because concentrated nitric acid is such a strong oxidizer, and organics represent a fuel, it is unlikely that HNO_3 stripping would be a very feasible means of removing the Pu(IV) from the organic phase in any large-scale industrial separation process.

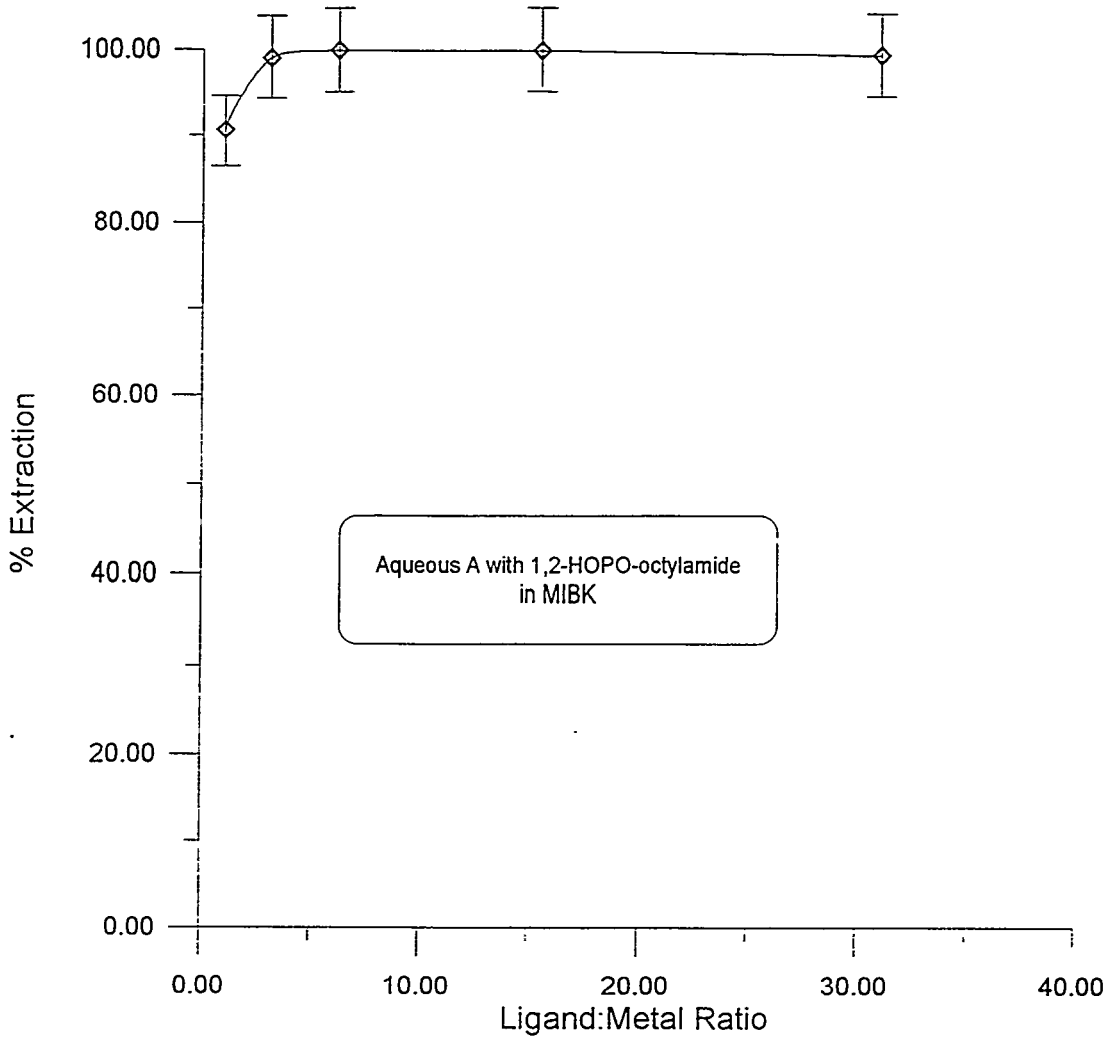

Figure 6.33: Extraction of Pu(IV) from Aqueous A versus the ligand-to-metal (L:M) ratio, for 1,2-HOPO-octylamide in MIBK.

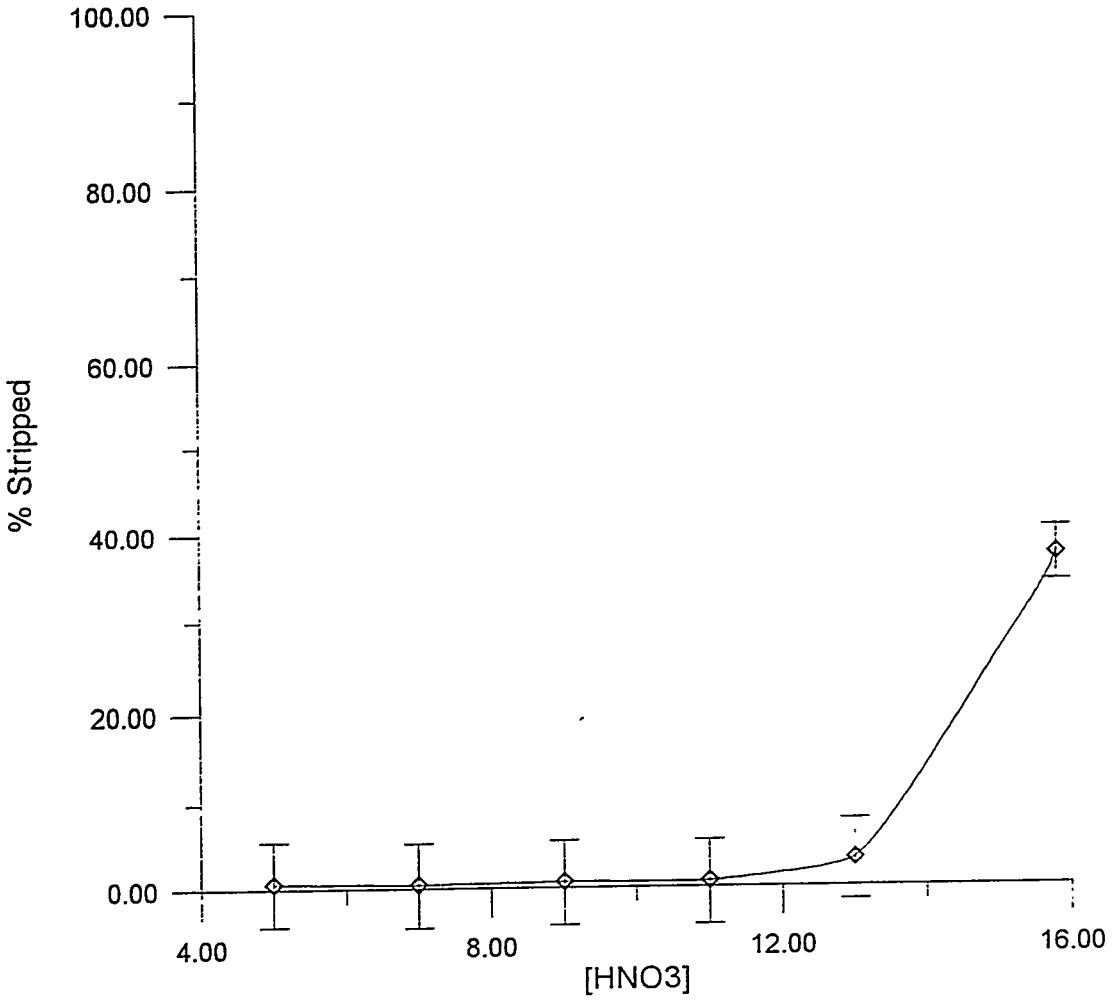

Figure 6.34: Amount of Pu(IV) stripped from the organic phase (MIBK) versus the concentration of HNO_3 used to strip it. Notice that there was effectively no stripping until the HNO_3 concentration was above 13 M.

Two other methods, both involving the reduction of Pu(IV) to Pu(III) in hopes of breaking apart the metal/ligand complex, were attempted. The first method used potassium iodide (KI) in HCl to reduce the Pu(IV), and the second used ascorbic acid in HNO_3; both methods failed. Their failure can be rationalized in two ways:

1. The HOPOs bind Pu(IV) in such a thermodynamically strong complex that the reducing agents are not strong enough to effect the reduction (this has been seen previously with the TRUEX process; see Horowitz, *et al.* [107]). Using the estimated formation constants for the Pu(IV)/HOPO and Pu(III)/HOPO complexes, along with the electrochemical potential needed to reduce Pu(IV) to Pu(III), the required potential to reduce the Pu(IV)/HOPO complex to the Pu(III)/HOPO complex is around -0.2 V; iodine and ascorbic acid are not strong enough reducing agents.

2. The metal/ligand complex, with its chelate groups pointed in toward the metal, is much more organophilic than just the extractant alone. This may remove all solubility of the metal chelate complex in the aqueous phase, thereby eliminating any contact time with the reducing agents in the aqueous phase.

Either better methods for stripping the plutonium from the organic phase need to be found, or perhaps some of the less-strong HOPOs need to be tested in competitive extractions and stripping experiments. The lesser HOPO extractants may show the same strength and selectivity for Pu(IV) over the interfering species, but may allow for a more facile stripping of the extracted plutonium from the organic phase.

The results of these competition extractions, with the exception of the stripping experiments, bode well for the use of these HOPO extractants in future waste remediation schemes. With some fine-tuning of the parameters used in these extraction experiments, a whole new generation of strong, highly selective actinide(IV) chelators can be envisioned for use in liquid/liquid extraction waste remediation schemes.

6.3 Conclusions

Eleven different liquid/liquid extractants were synthesized based upon the chelating moieties 3,2-HOPO and 3,4-HOPO; additionally, two liquid/liquid extractants based upon the 1,2-HOPO chelating moiety were obtained for extraction studies. The extractants were rendered organophilic by the attachment of long alkane side chains of varying length to the chelating moiety. Synthesis of the 3,2-HOPOs was achieved with greater ease, higher yield, and greater purity than synthesis of the 3,4-HOPOs.

A spectrophotometric titration of 3,2-HOPO-propylamide with Th(IV) gave a formation constant of $\log \beta_{140} = 38.3 \pm 0.3$. This formation constant compares favorably with the other measured formation constants for the chelate groups 1,2-HOPO and 3,4-HOPO.

Measurements of the fraction of uncomplexed ligand in the aqueous phase showed that the majority of the extractants remained in the organic phase, and only three extractant/organic phase pairs showed significant ligand solubility in the aqueous phase.

The Fe(III) extractions indicated three general trends: first, the 1,2-HOPO extractants performed the best, followed closely by the 3,2-HOPOs, with the 3,4-HOPOs extracting very poorly; second, extraction from the higher ionic strength aqueous phase was favored over extraction from the lower ionic strength aqueous phase; third, extraction into the organic phase when 1-octanol was the solvent was much greater and proceeded more rapidly than when methyl isobutyl ketone (MIBK) was the solvent. For all conditions, however, the 1,2-HOPO extractants performed very well, extracting $> 99\%$.

The Pu(IV) extractions, quite surprisingly, yielded results that were very different from the Fe(III) extractions. The first trend remained the same: the 1,2-HOPOs were the best extractants, followed closely by the 3,2-HOPOs, followed by the 3,4-HOPOs; but in these Pu(IV) extractions the 3,4-HOPOs performed much better than in the Fe(III) extractions. There was a reversal in the organic solvent ordering, with MIBK, in general, performing better as the organic phase than 1-

octanol. The difference in extraction between the high ionic strength aqueous phase and the low ionic strength aqueous phase was less, but the high ionic strength phase still showed higher extraction. As with the Fe(III) extractions, the 1,2-HOPOs performed extremely well under all conditions tested, extracting > 99% of the Pu(IV). The kinetics for the Pu(IV) extractions were much faster than for the Fe(III) extractions. The percent extraction showed no significant dependence on the length of the organophilic side chain.

Since the 1,2-HOPOs performed so well in both metal extractions, 1,2-HOPO-octylamide in MIBK was chosen to test some additional extraction properties. This extractant was able to remove 95–100% of the Pu(IV) in competition studies with 100:1 Fe(III) (D.F. = 325), 1000:1 Fe(III) (D.F. = 60), and 3:1 EDTA (D.F. = 490). Concentration studies with this extractant support the hypothesis that a species other than ML_4 can be extracted into the organic phase. 1,2-HOPO-octylamide is such a strong complex that the Pu(IV) could not be stripped away from it by an aqueous phase reducing agent; only $\sim$ 40 % could be stripped by concentrated (15.8 M) nitric acid.

6.4 Future Work

The results of this study are rather encouraging. The 1,2-HOPO chelating group proved to be the best extractant for Pu(IV) and Fe(III), but only the hexylamide and octylamide extractants of this moiety were synthesized. It might be interesting to test the 1,2-HOPO decylamide and octadecylamide extractants, if their synthesis can be accomplished; however, since the extraction by other chelating groups showed very little side chain dependence, other investigations should be given priority. The two most important avenues of investigation that are crucial to the advancement of this project to the remediation stage are:

1. Finding efficient ways to strip the Pu(IV) from ligand complex in the organic phase. Perhaps stronger reducing agents are needed, or longer contact times, or an increase in the temperature of the extraction; perhaps all of these are required to strip Pu(IV) from the organic phase.

2. Studying the extraction properties with a real waste solution. Because of the complex nature of real waste, the true efficacy of these ligands can not be known until they are used to remediate real waste. This may be the most difficult and time-consuming step in the project; both politics and paperwork, a deadly combination, are involved.

If the project proceeds to the point of application to a real waste remediation scenario, then the optimization of ligand synthesis needs to be addressed.

To further the basic understanding of how this new class of extractants works, it would be very interesting to design some experiments that probed the nature of the extracted species. How many different extractable species are there? Which is the most desirable for optimal extraction? Various analytical techniques, such as UV/Vis, NMR (proton and carbon, and perhaps iron), and X-ray Absorption Fine Structure (XAFS), could be used to help elucidate these finer points.

Appendix A

Ligand Synthesis NMR Spectra

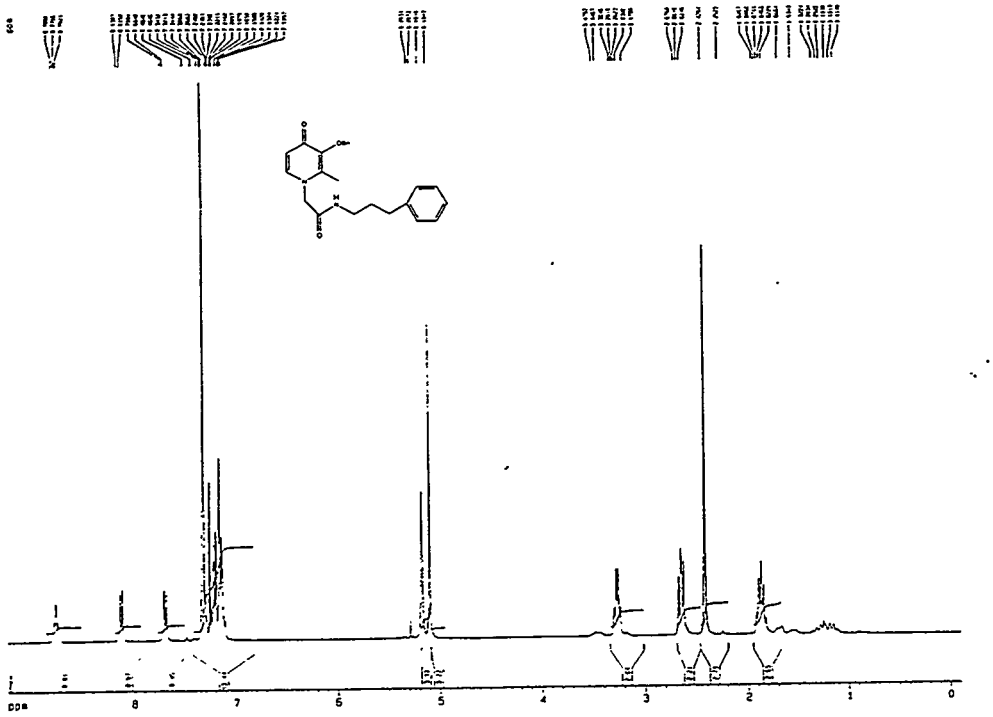

Figure A.1: The ^{1}H NMR of 3,4-HOPO-phenylpropylamide, protected; the conditions used for this NMR and the peak assignments are listed on page 82.

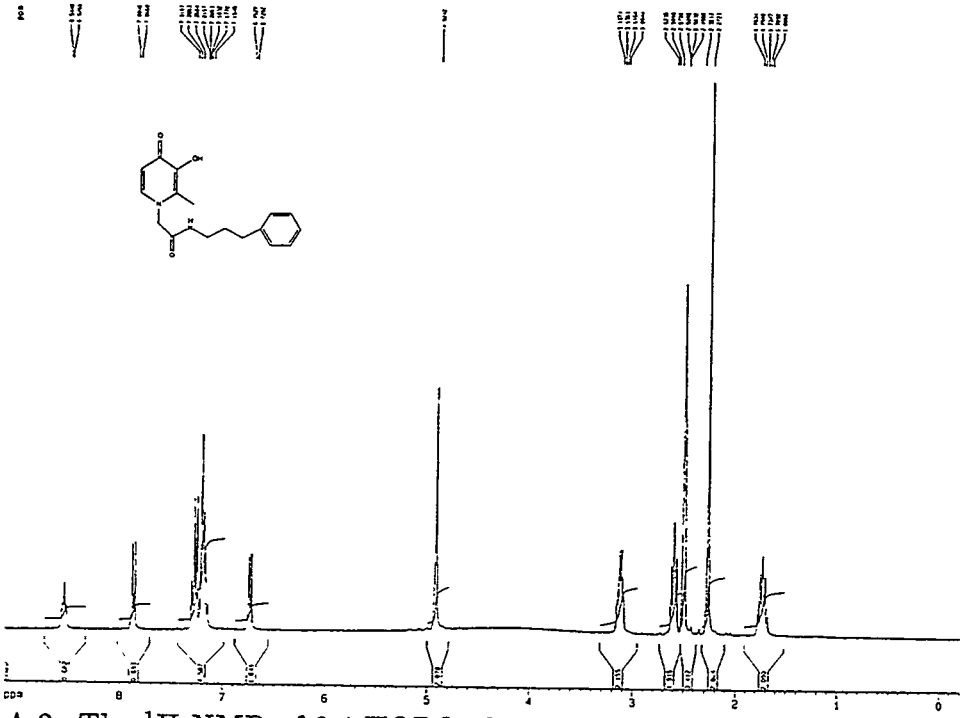

Figure A.2: The ^{1}H NMR of 3,4-HOPO-phenylpropylamide, deprotected; the conditions used for this NMR and the peak assignments are listed on page 84.

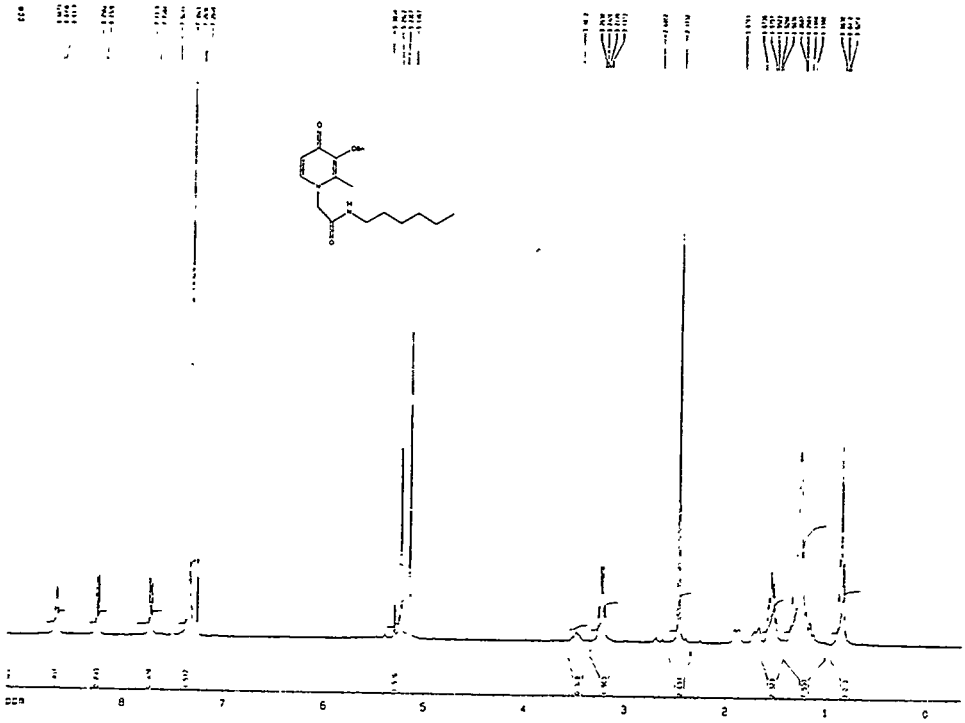

Figure A.3: The ^{1}H NMR of 3,4-HOPO-hexylamide, protected; the conditions used for this NMR and the peak assignments are listed on page 85.

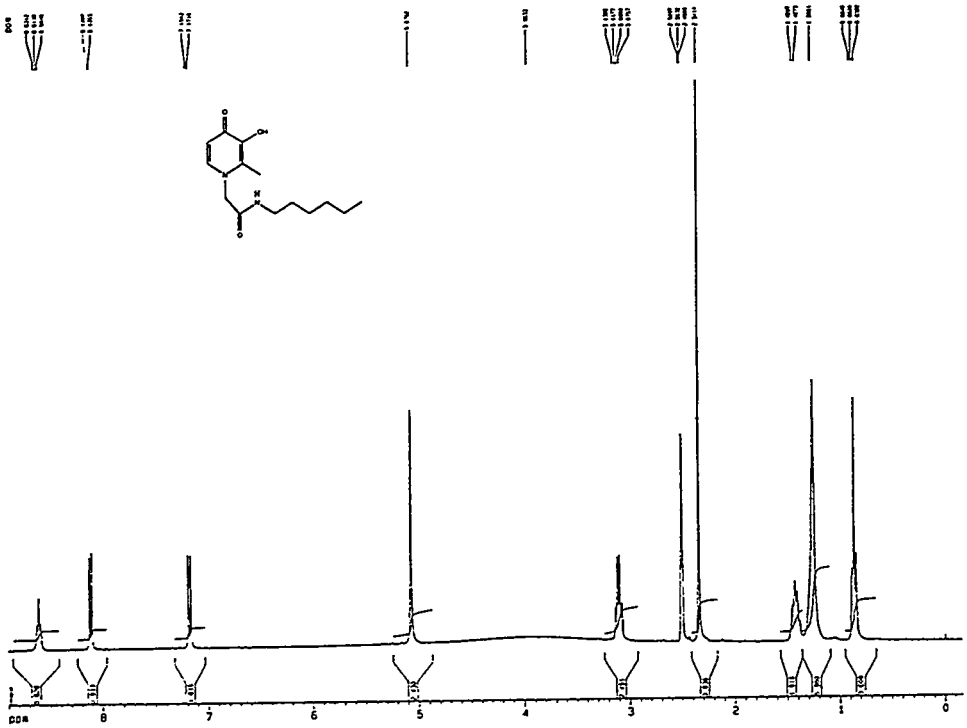

Figure A.4: The ^{1}H NMR of 3,4-HOPO-hexylamide, deprotected; the conditions used for this NMR and the peak assignments are listed on page 87.

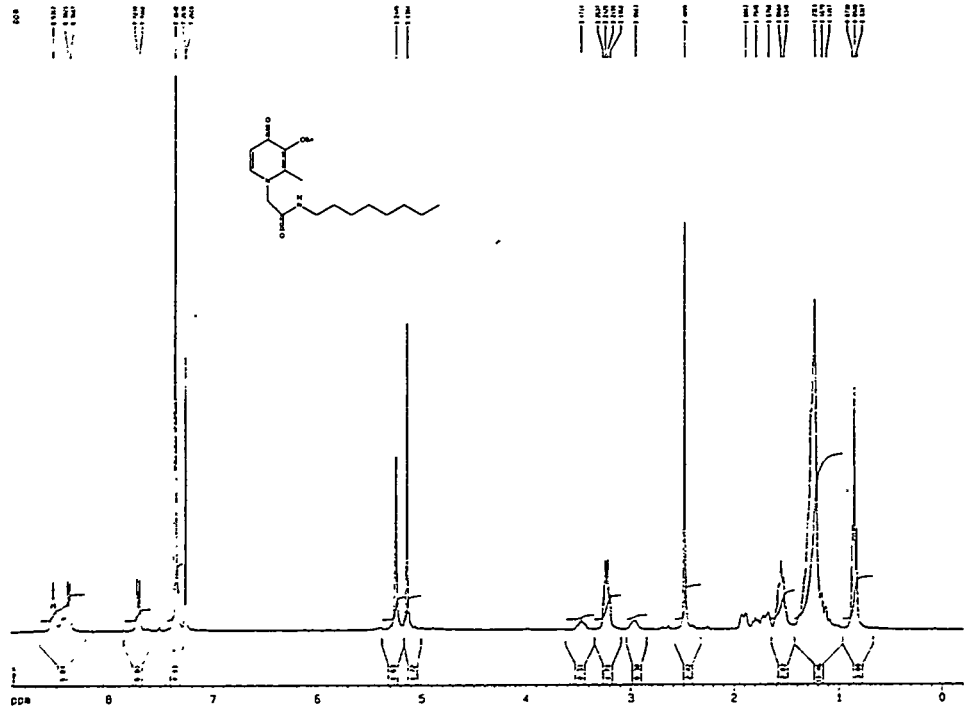

Figure A.5: The ^{1}H NMR of 3,4-HOPO-octylamide, protected; the conditions used for this NMR and the peak assignments are listed on page 88.

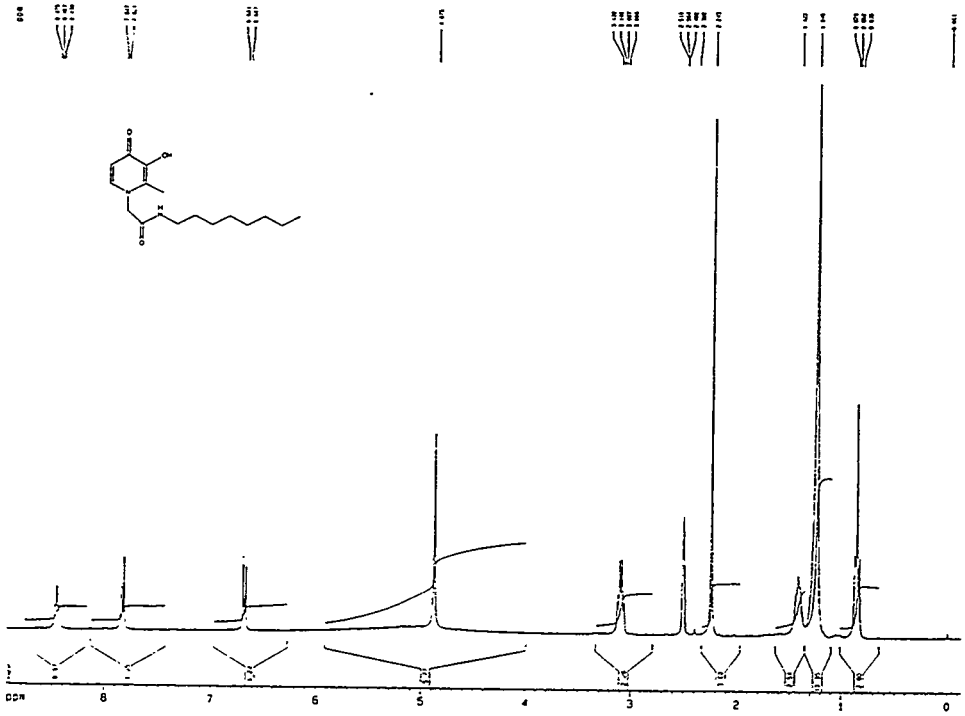

Figure A.6: The ^{1}H NMR of 3,4-HOPO-octylamide, deprotected; the conditions used for this NMR and the peak assignments are listed on page 89.

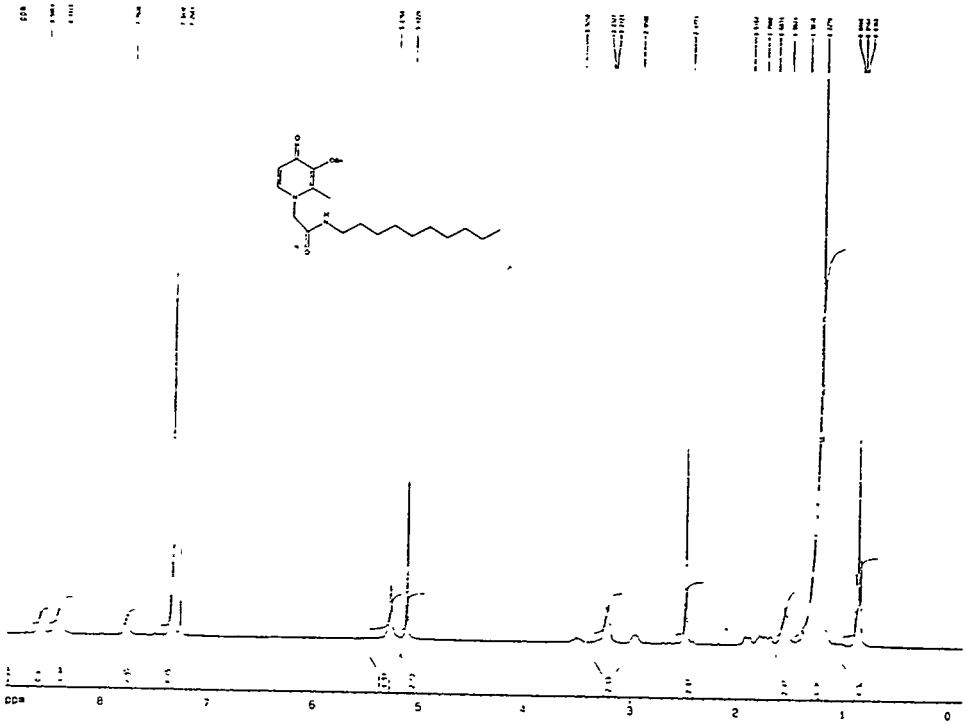

Figure A.7: The ^{1}H NMR of 3,4-HOPO-decylamide, protected; the conditions used for this NMR and the peak assignments are listed on page 90.

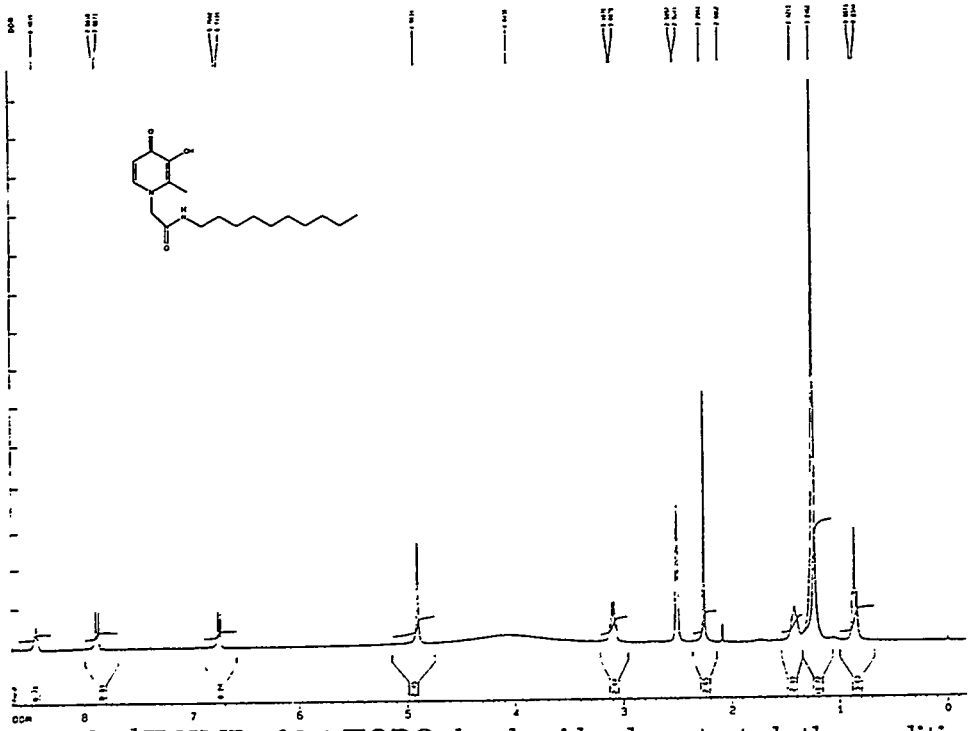

Figure A.8: The ^{1}H NMR of 3,4-HOPO-decylamide, deprotected; the conditions used for this NMR and the peak assignments are listed on page 92.

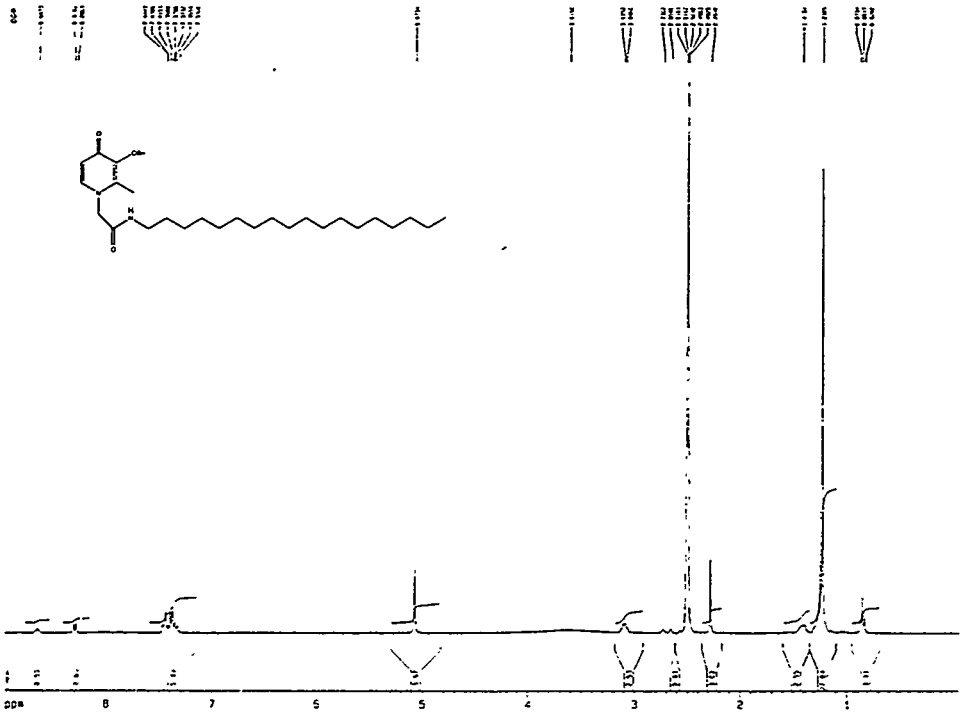

Figure A.9: The ^{1}H NMR of 3,4-HOPO-octadecylamide, protected; the conditions used for this NMR and the peak assignments are listed on page 93.

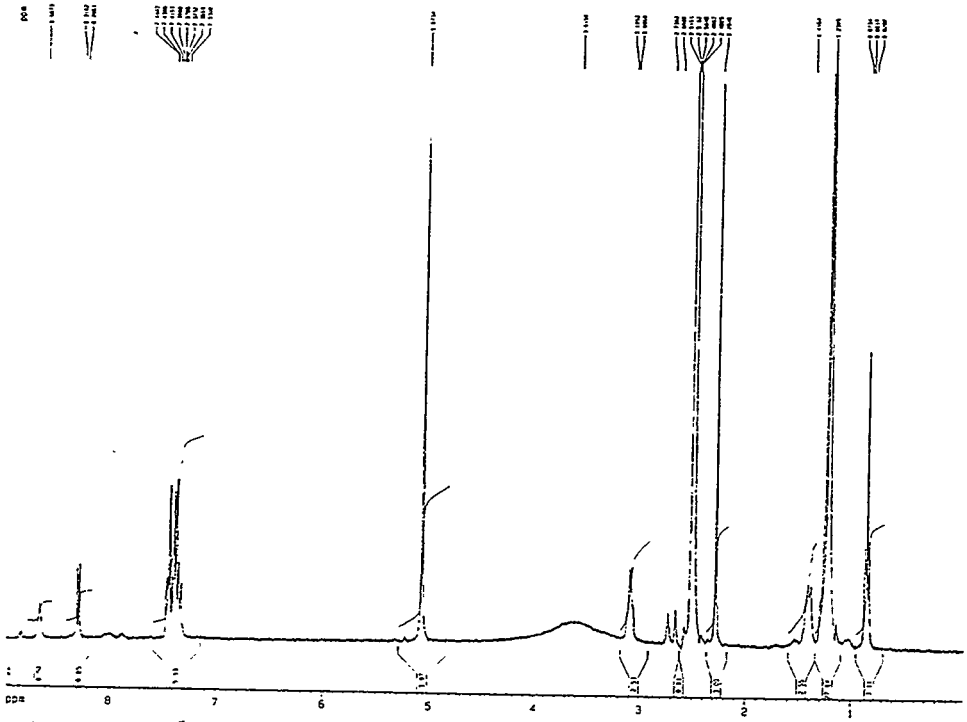

Figure A.10: The ^{1}H NMR of 3,4-HOPO-octadecylamide, protected; the conditions used for this NMR and the peak assignments are listed on page 93.

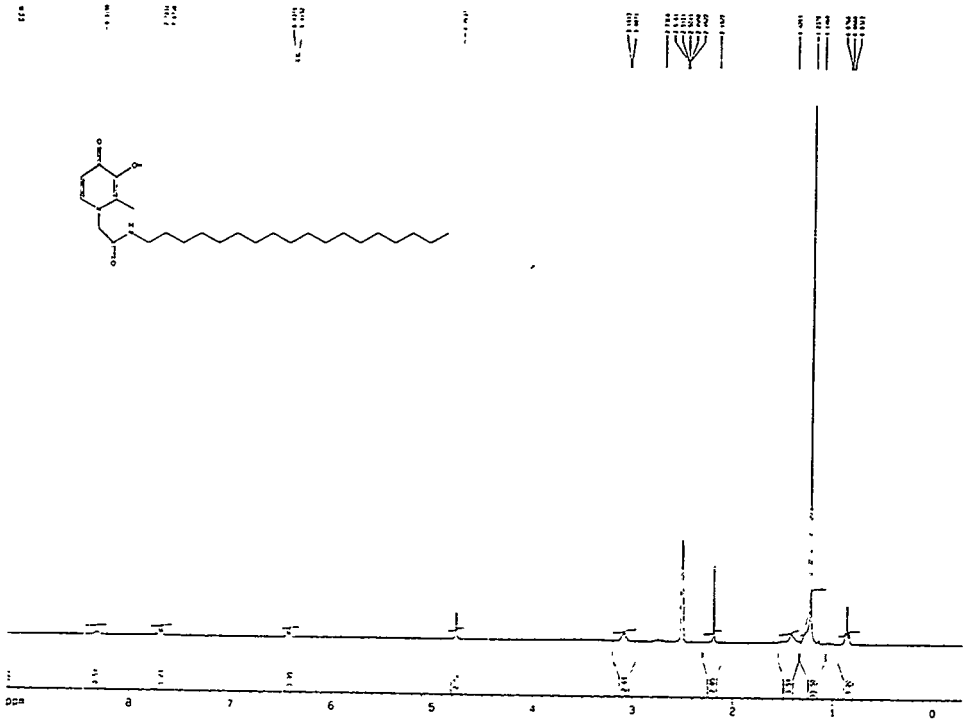

Figure A.11: The ^{1}H NMR of 3,4-HOPO-octadecylamide, deprotected; the conditions used for this NMR and the peak assignments are listed on page 93.

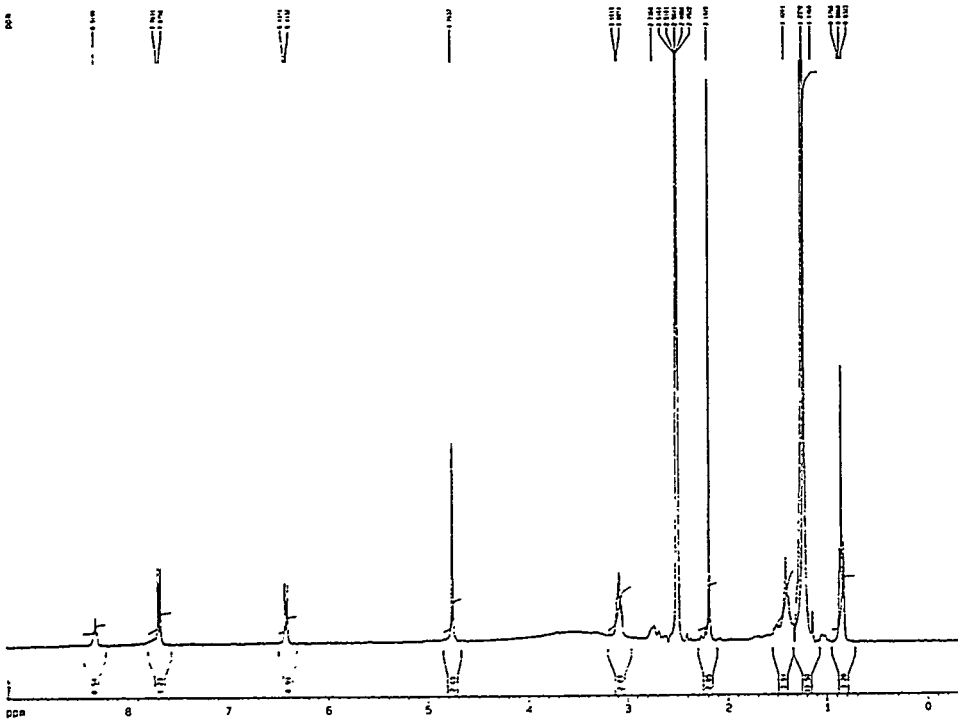

Figure A.12: The ^{1}H NMR of 3,4-HOPO-octadecylamide, deprotected; the conditions used for this NMR and the peak assignments are listed on page 93.

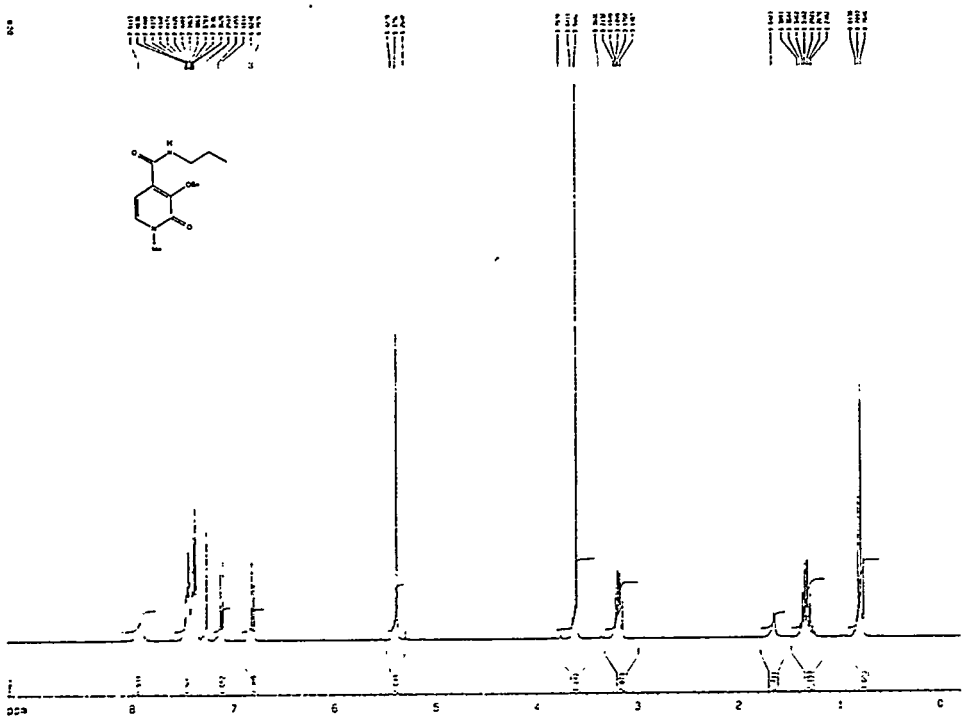

Figure A.13: The ^{1}H NMR of 3,2-HOPO-propylamide, protected; the conditions used for this NMR and the peak assignments are listed on page 97.

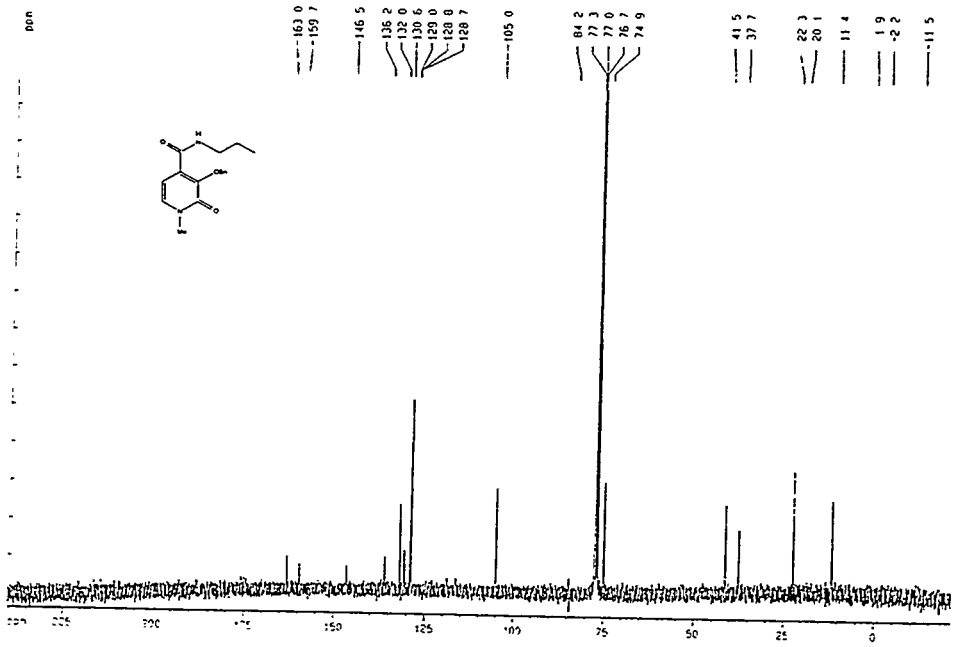

Figure A.14: The ^{13}C NMR of 3,2-HOPO-propylamide, protected; the conditions used for this NMR and the peak assignments are listed on page 97.

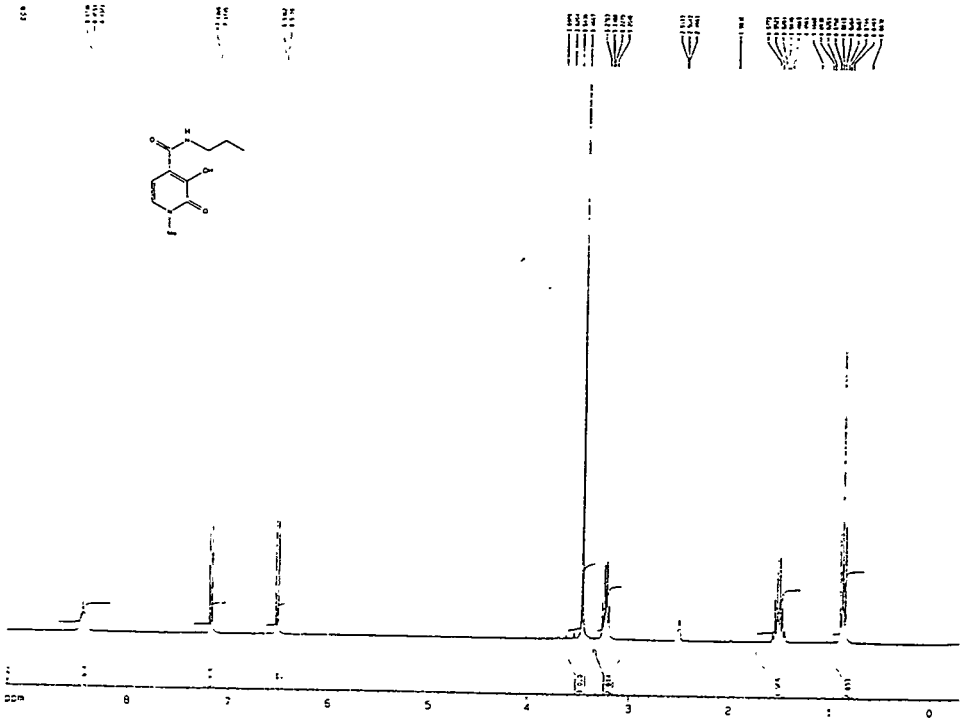

Figure A.15: The ^{1}H NMR of 3,2-HOPO-propylamide, deprotected; the conditions used for this NMR and the peak assignments are listed on page 99.

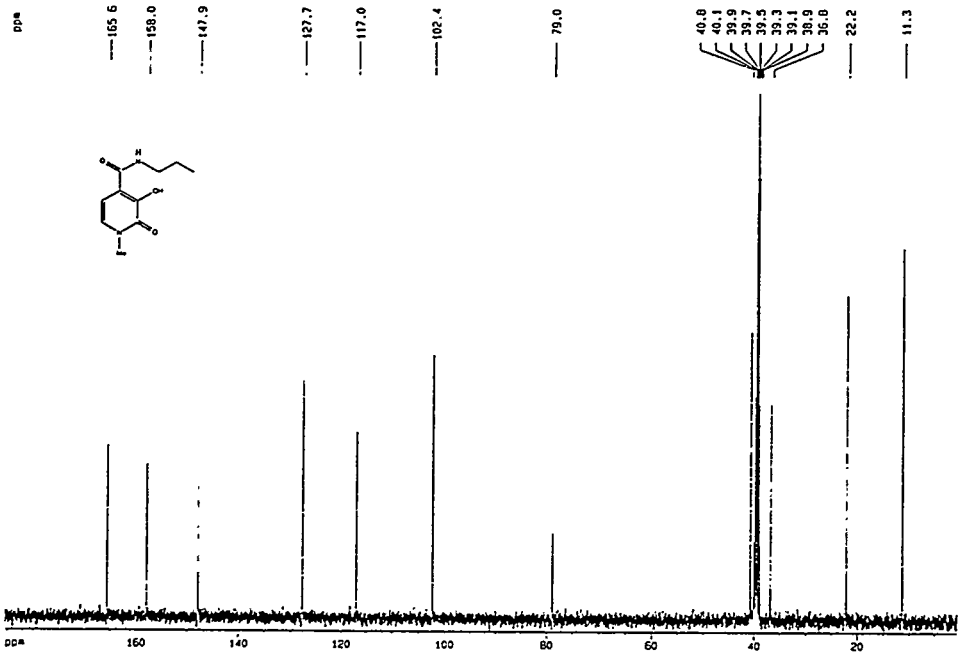

Figure A.16: The ^{13}C NMR of 3,2-HOPO-propylamide, deprotected; the conditions used for this NMR and the peak assignments are listed on page 99.

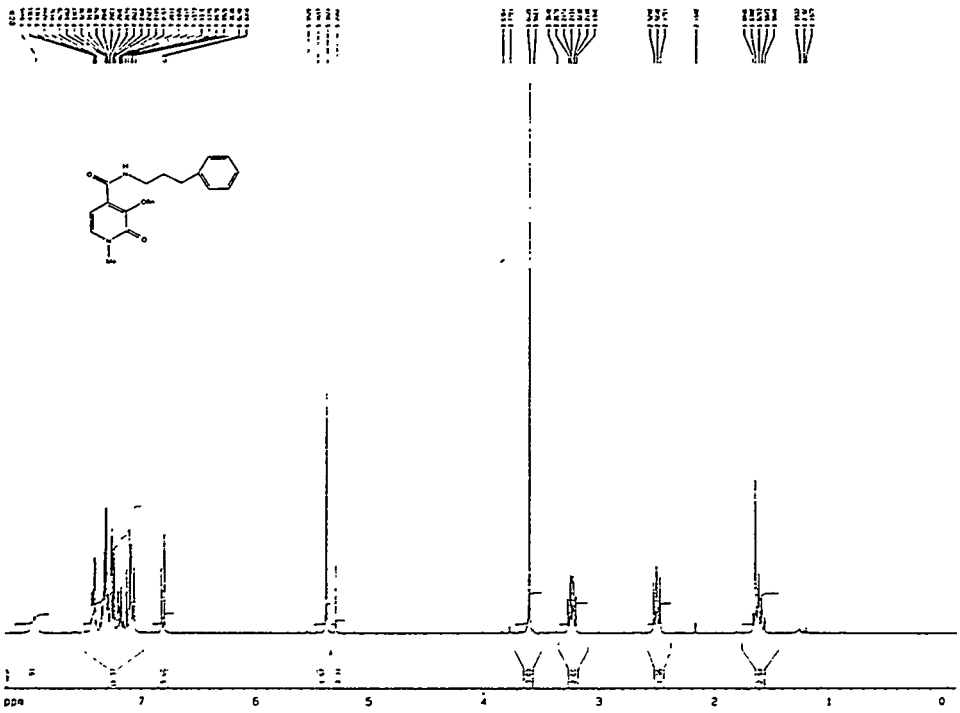

Figure A.17: The ^{1}H NMR of 3,2-HOPO-phenylpropylamide, protected; the conditions used for this NMR and the peak assignments are listed on page 100.

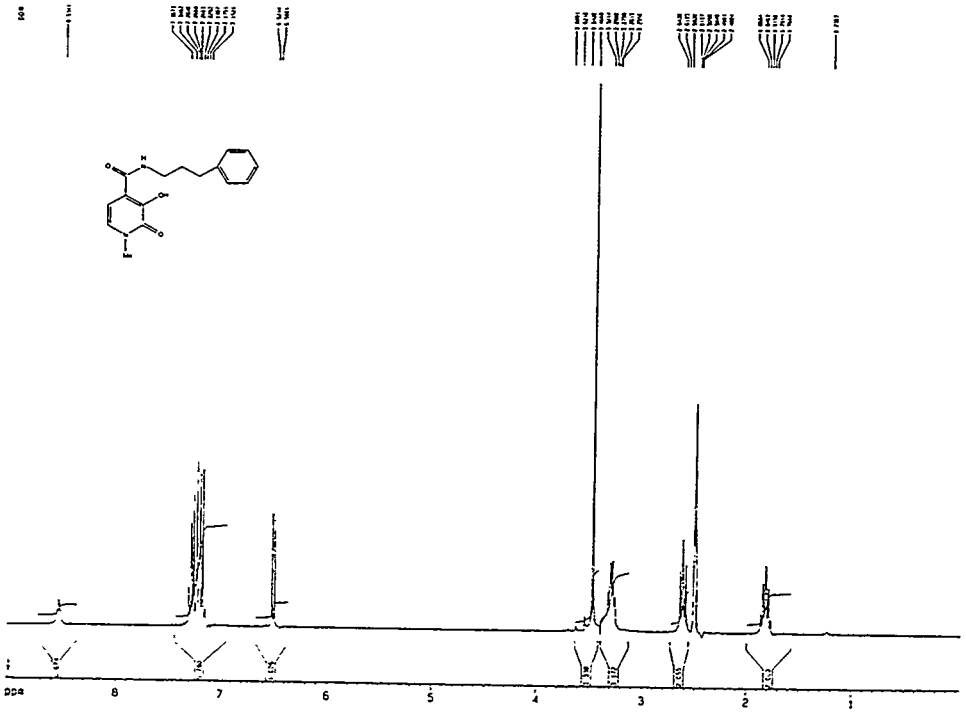

Figure A.18: The ^{1}H NMR of 3,2-HOPO-phenylpropylamide, deprotected; the conditions used for this NMR and the peak assignments are listed on page 102.

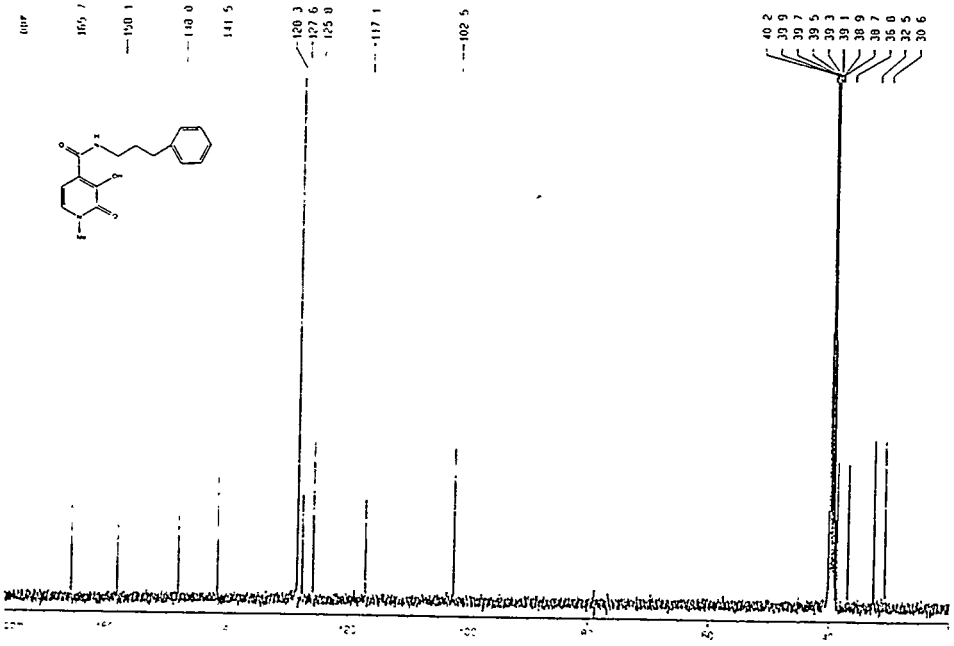

Figure A.19: The ^{13}C NMR of 3,2-HOPO-phenylpropylamide, deprotected; the conditions used for this NMR and the peak assignments are listed on page 102.

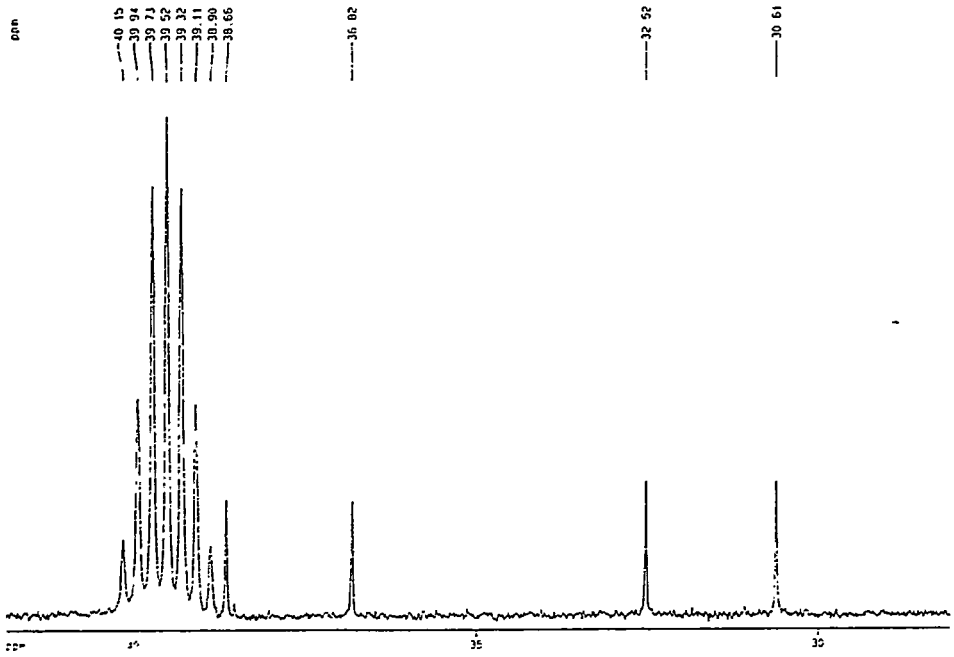

Figure A.20: The ^{13}C NMR of 3,2-HOPO-phenylpropylamide, deprotected; the conditions used for this NMR and the peak assignments are listed on page 102.

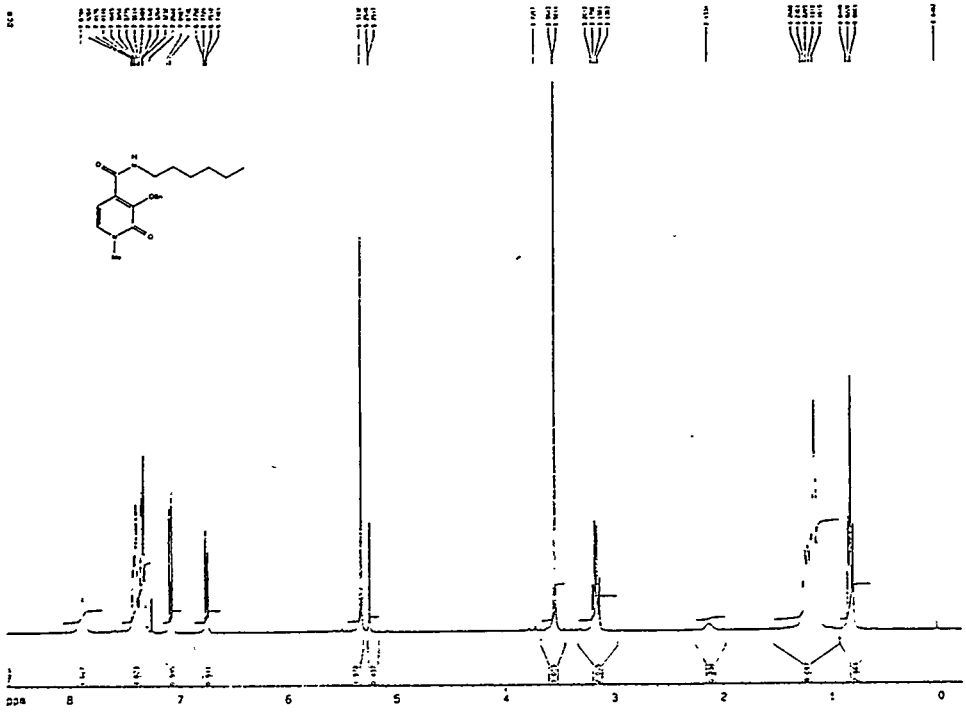

Figure A.21: The ^{1}H NMR of 3,2-HOPO-hexylamide, protected; the conditions used for this NMR and the peak assignments are listed on page 103.

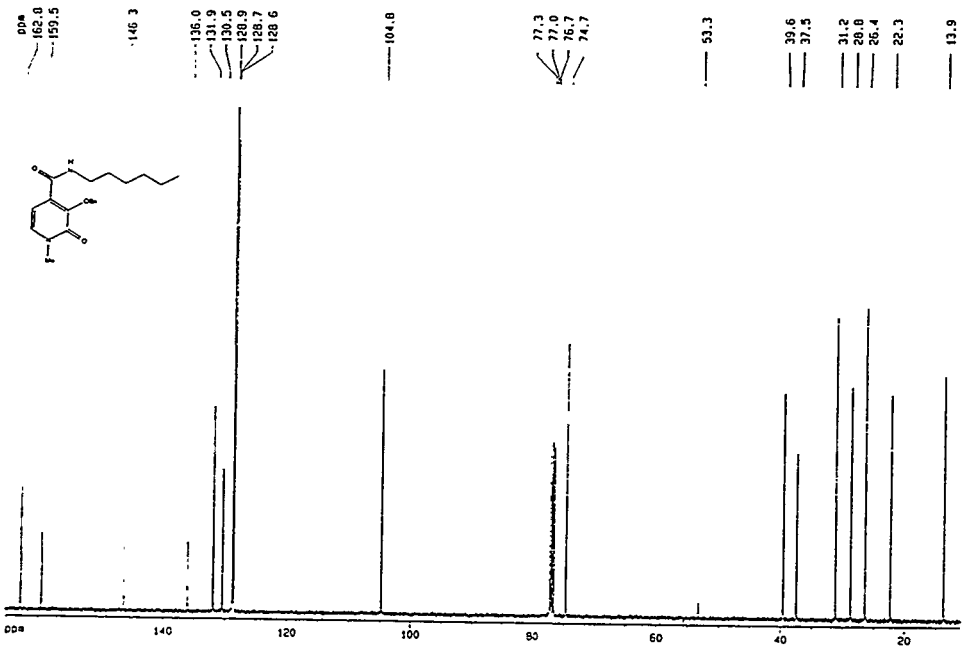

Figure A.22: The ^{13}C NMR of 3,2-HOPO-hexylamide, protected; the conditions used for this NMR and the peak assignments are listed on page 103.

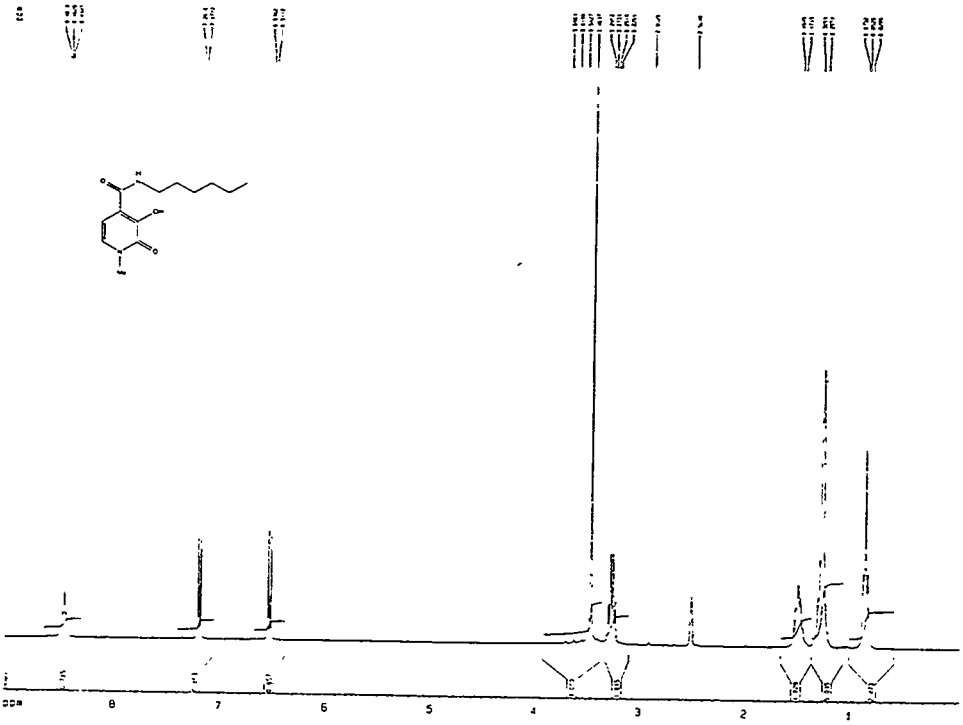

Figure A.23: The ^{1}H NMR of 3,2-HOPO-hexylamide, deprotected; the conditions used for this NMR and the peak assignments are listed on page 105.

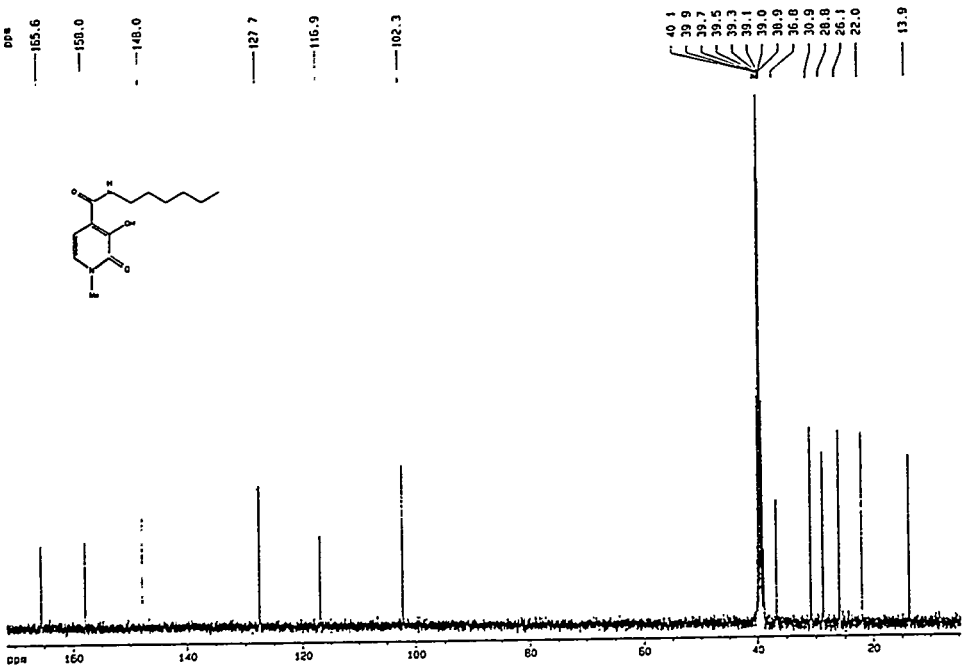

Figure A.24: The ^{13}C NMR of 3,2-HOPO-hexylamide, deprotected; the conditions used for this NMR and the peak assignments are listed on page 105.

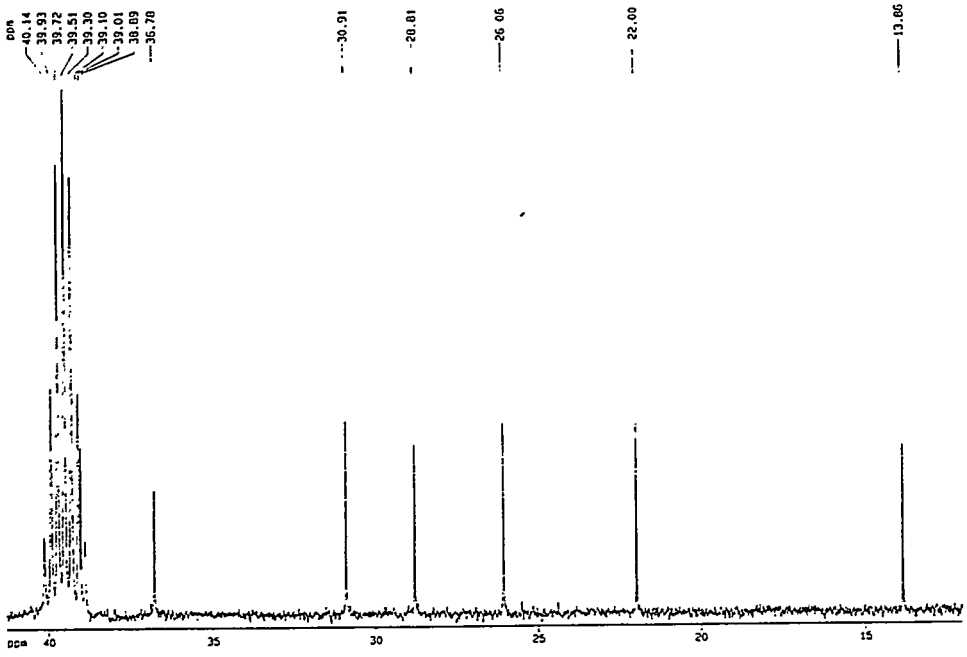

Figure A.25: The ^{13}C NMR of 3,2-HOPO-hexylamide, protected; the conditions used for this NMR and the peak assignments are listed on page 105.

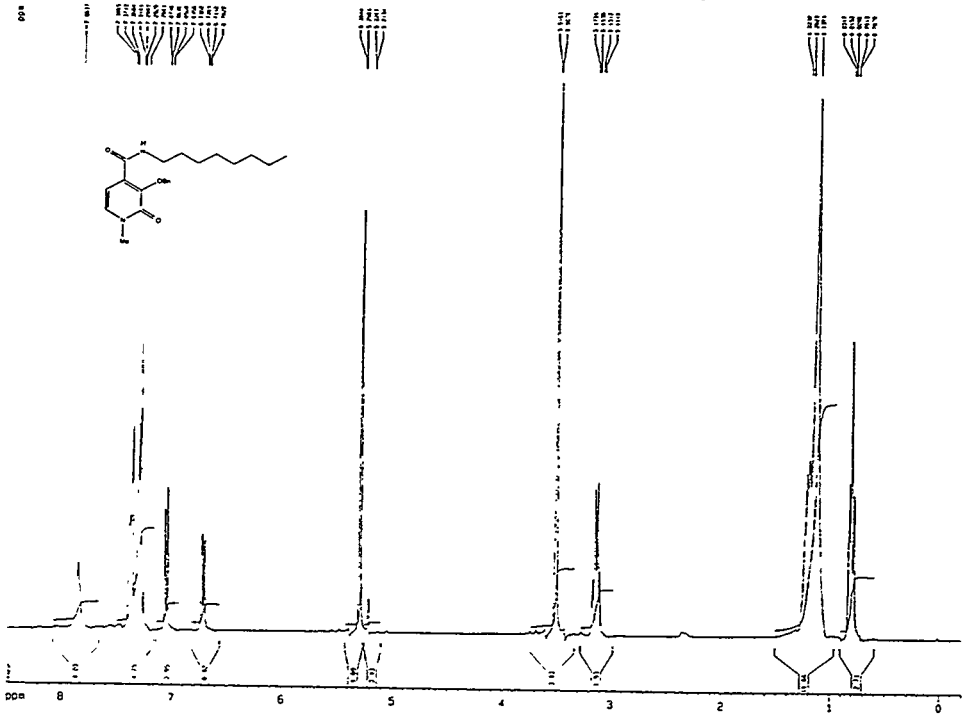

Figure A.26: The ^{1}H NMR of 3,2-HOPO-octylamide, protected; the conditions used for this NMR and the peak assignments are listed on page 106.

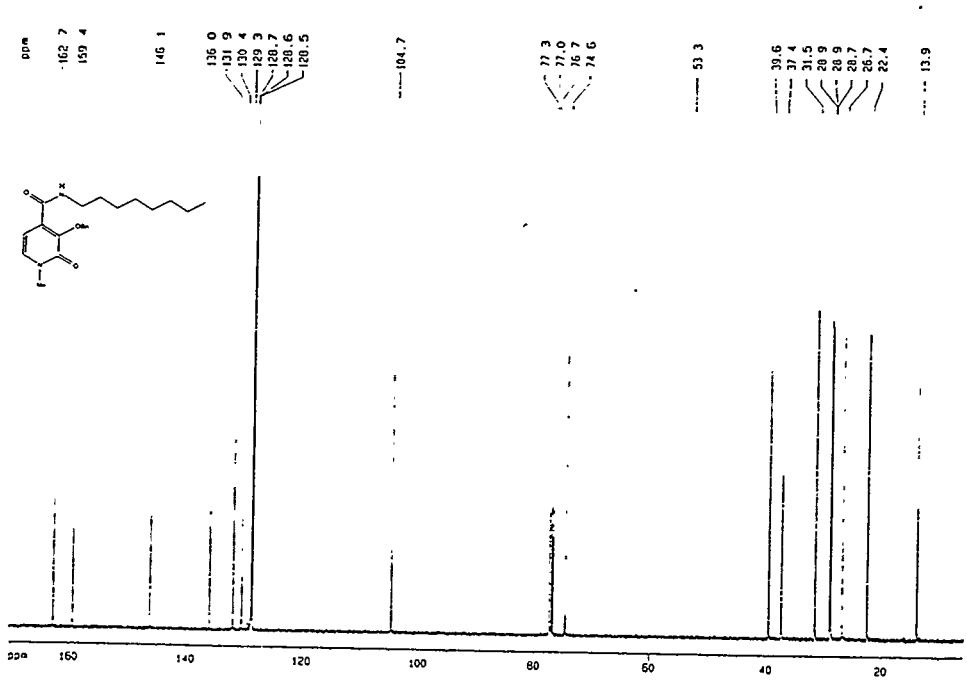

Figure A.27: The ^{13}C NMR of 3,2-HOPO-octylamide, protected; the conditions used for this NMR and the peak assignments are listed on page 106.

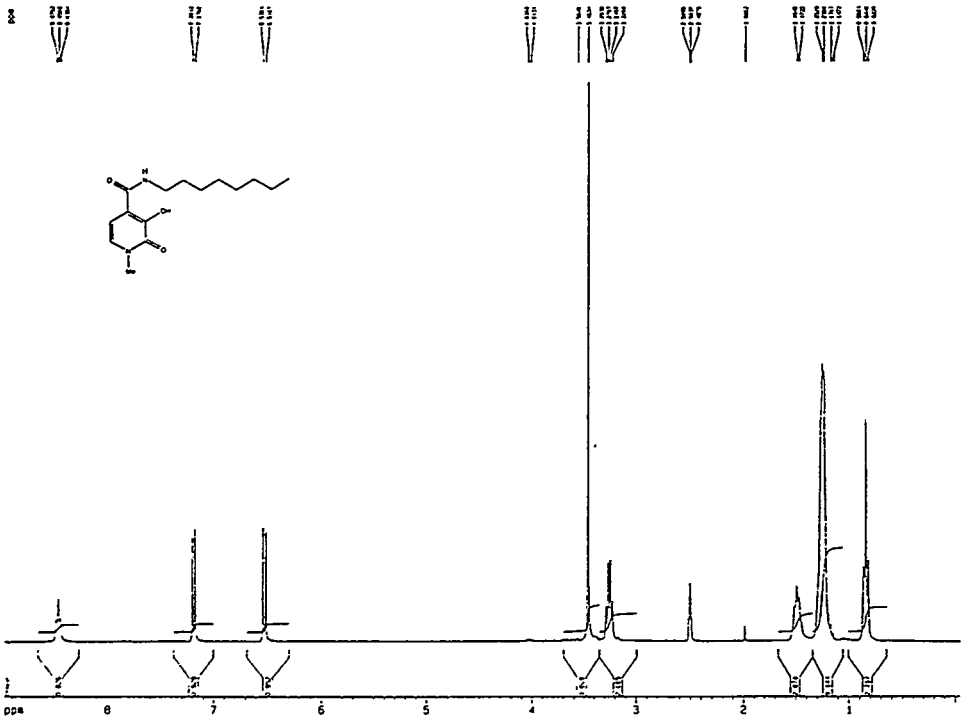

Figure A.28: The ^{1}H NMR of 3,2-HOPO-octylamide, deprotected; the conditions used for this NMR and the peak assignments are listed on page 108.

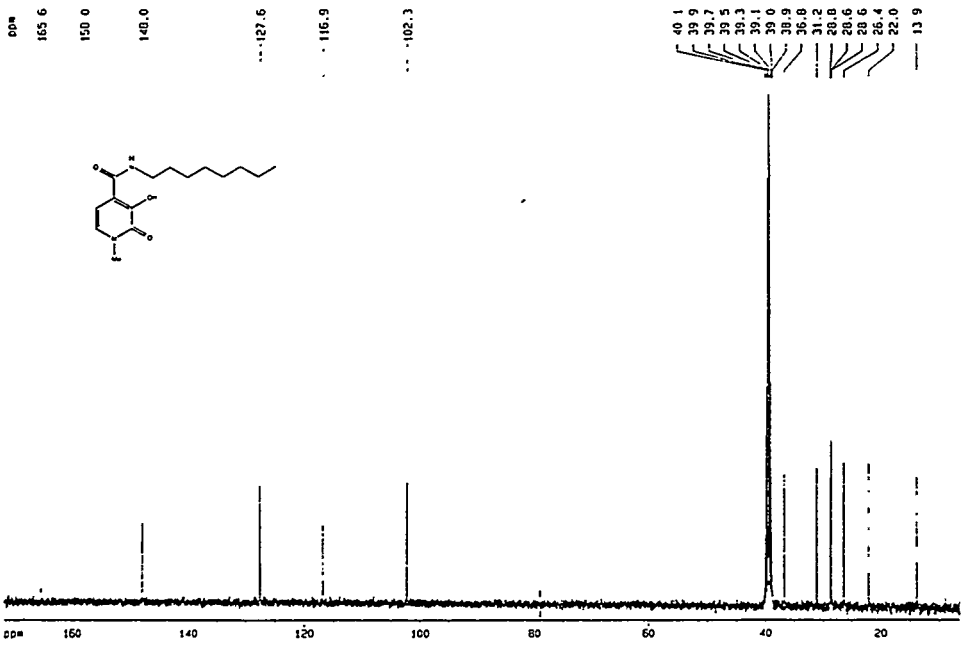

Figure A.29: The ^{13}C NMR of 3,2-HOPO-octylamide, deprotected; the conditions used for this NMR and the peak assignments are listed on page 108.

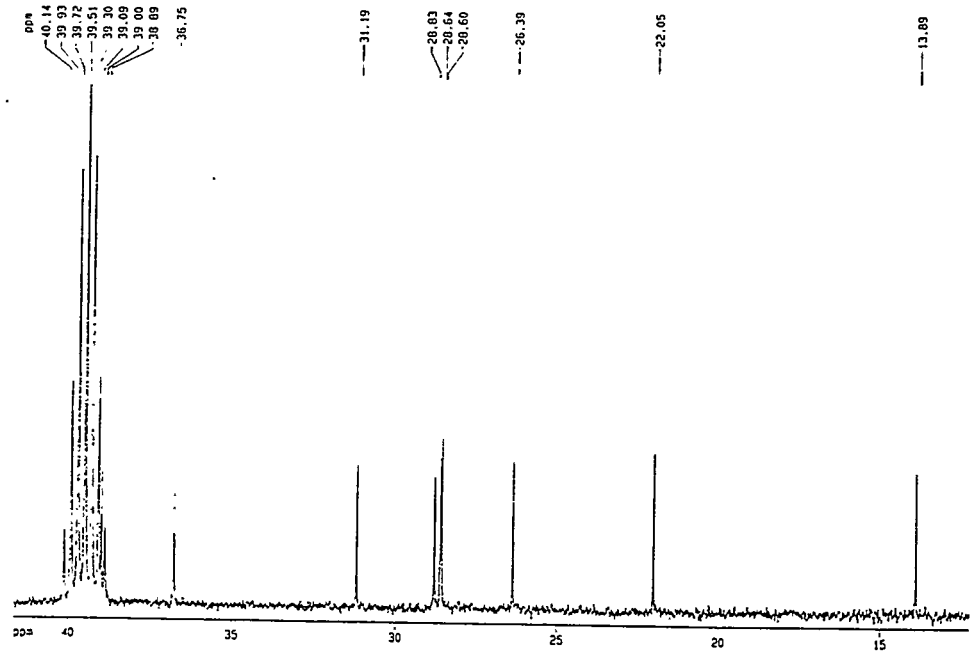

Figure A.30: The ^{13}C NMR of 3,2-HOPO-octylamide, protected; the conditions used for this NMR and the peak assignments are listed on page 108.

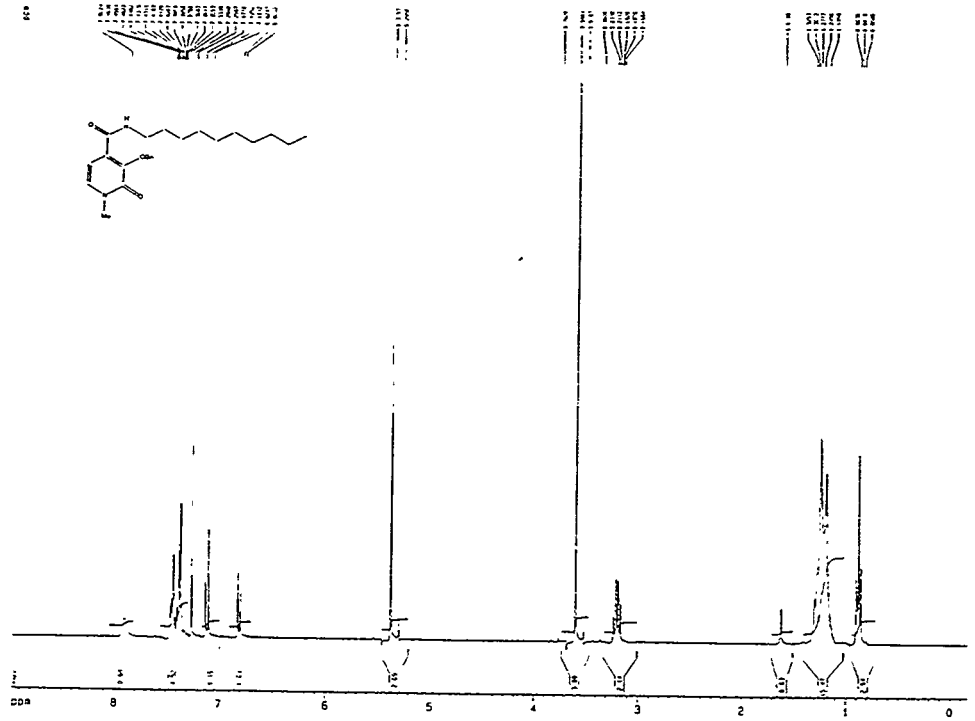

Figure A.31: The ^{1}H NMR of 3,2-HOPO-decylamide, protected; the conditions used for this NMR and the peak assignments are listed on page 109.

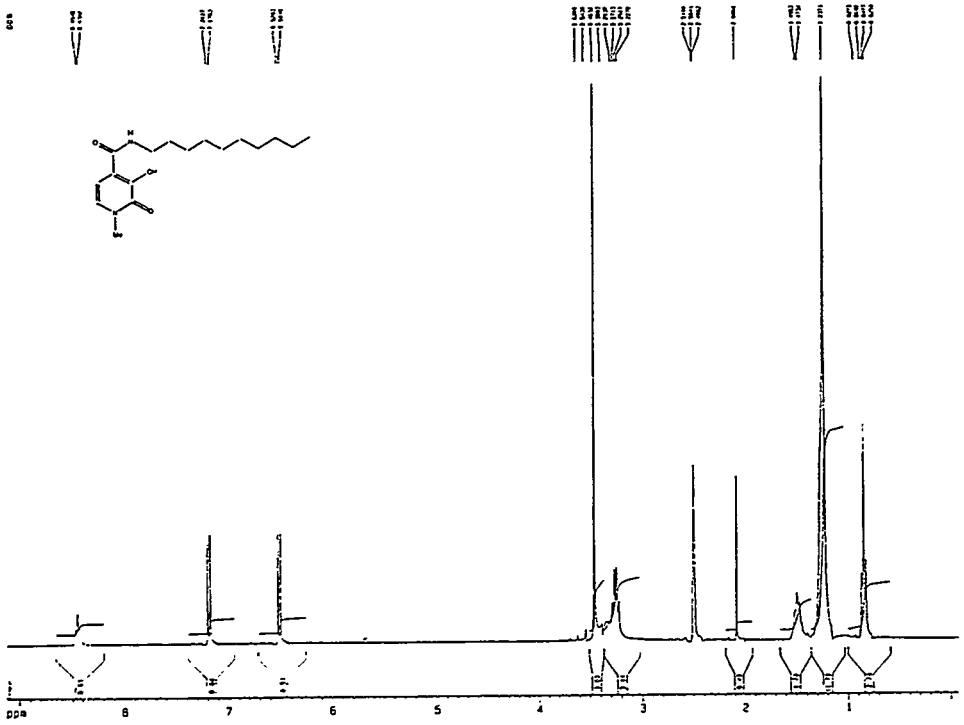

Figure A.32: The ^{1}H NMR of 3,2-HOPO-decylamide, deprotected; the conditions used for this NMR and the peak assignments are listed on page 111.

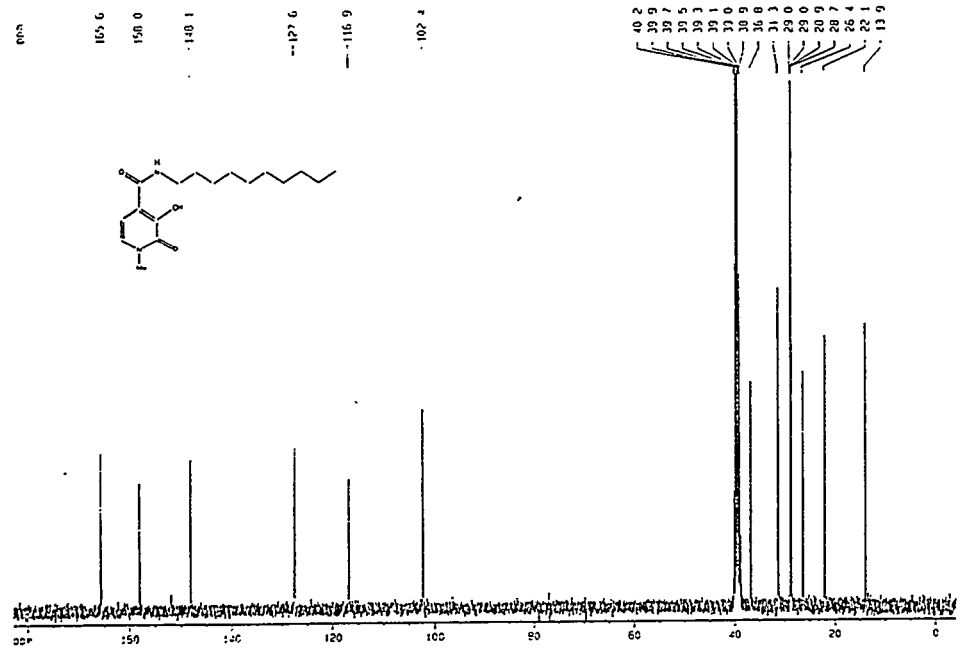

Figure A.33: The ^{13}C NMR of 3,2-HOPO-decylamide, deprotected; the conditions used for this NMR and the peak assignments are listed on page 111.

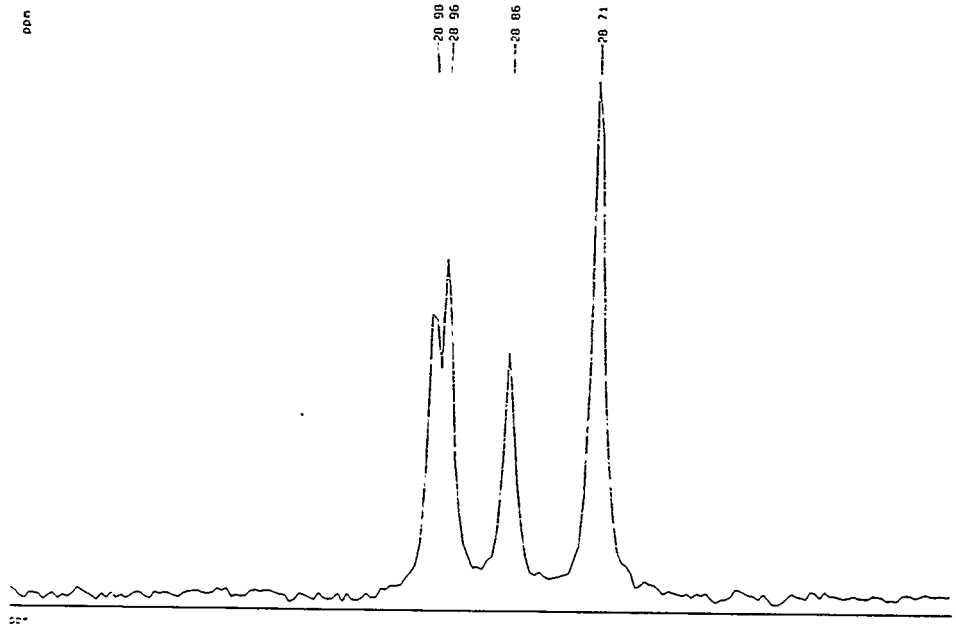

Figure A.34: The ^{13}C NMR of 3,2-HOPO-decylamide, deprotected; the conditions used for this NMR and the peak assignments are listed on page 111.

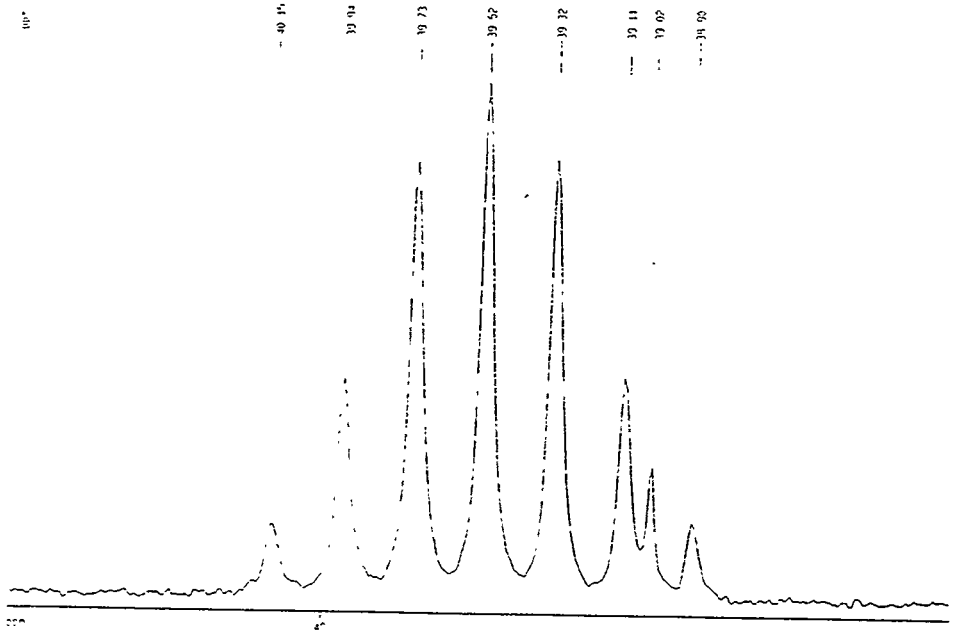

Figure A.35: The ^{13}C NMR of 3,2-HOPO-decylamide, deprotected; the conditions used for this NMR and the peak assignments are listed on page 111.

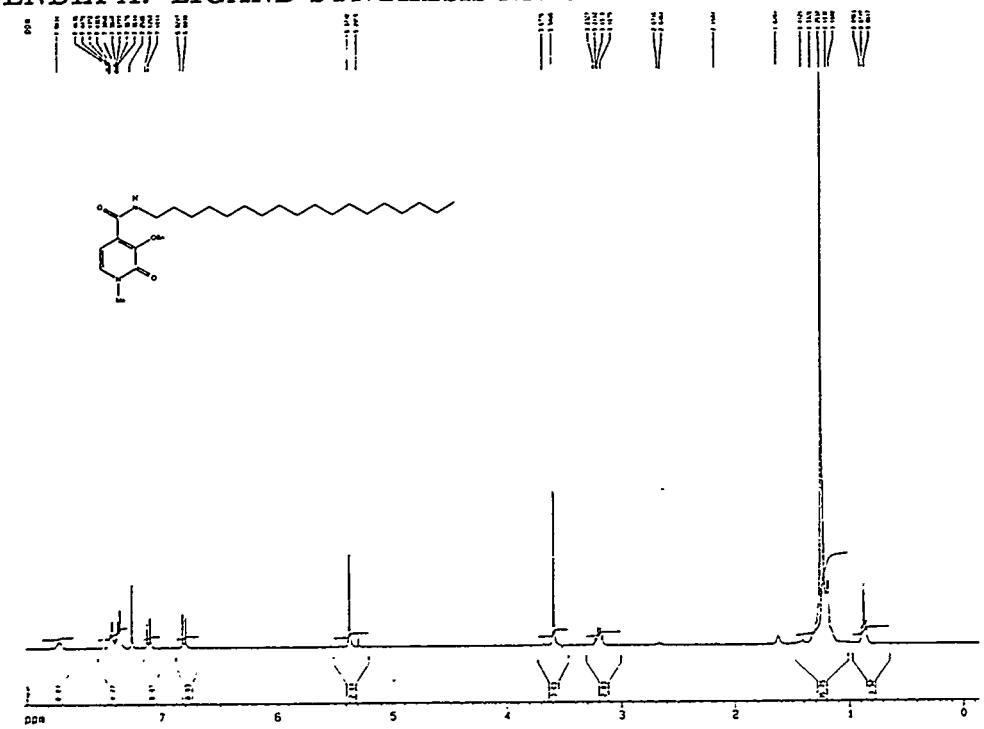

Figure A.36: The ^{1}H NMR of 3,2-HOPO-octadecylamide, protected; the conditions used for this NMR and the peak assignments are listed on page 112.

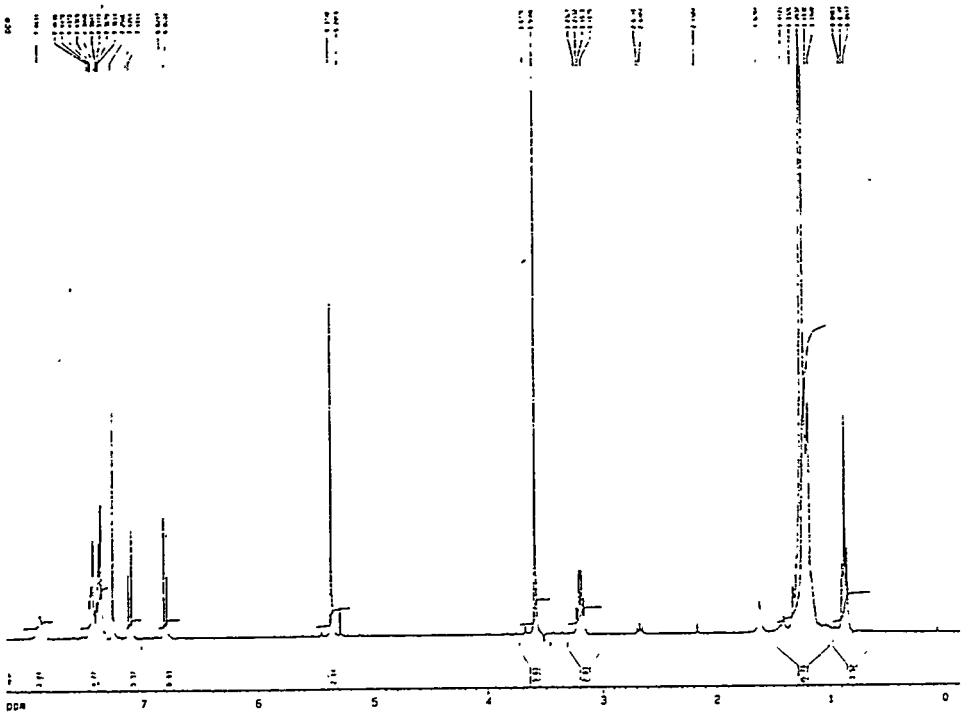

Figure A.37: The ^{1}H NMR of 3,2-HOPO-octadecylamide, protected; the conditions used for this NMR and the peak assignments are listed on page 112.

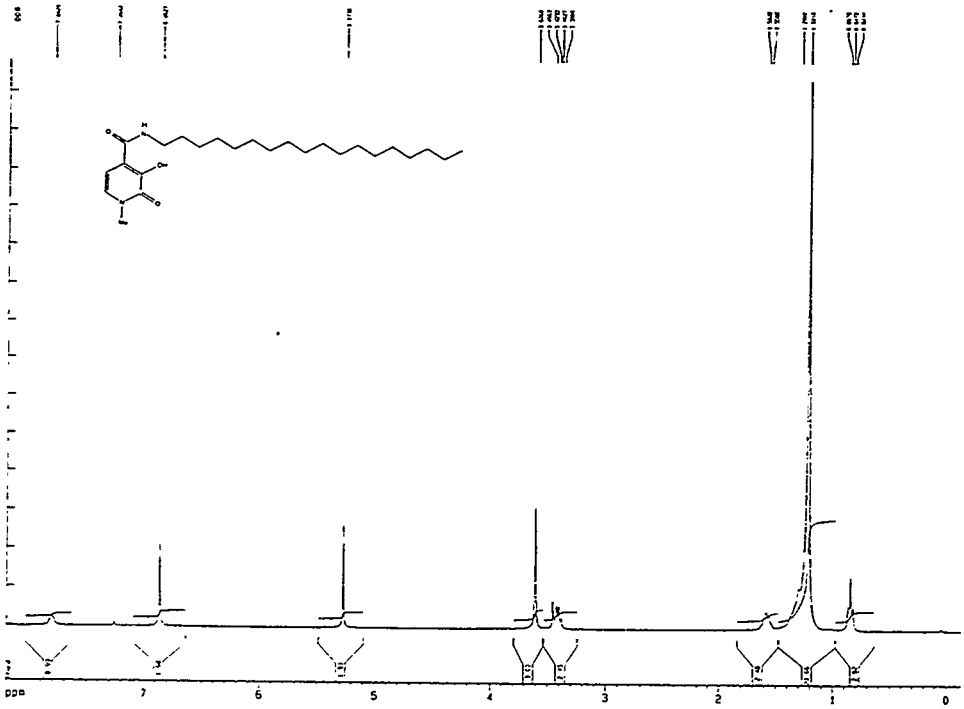

Figure A.38: The ^{1}H NMR of 3,2-HOPO-octadecylamide, deprotected; the conditions used for this NMR and the peak assignments are listed on page 114.

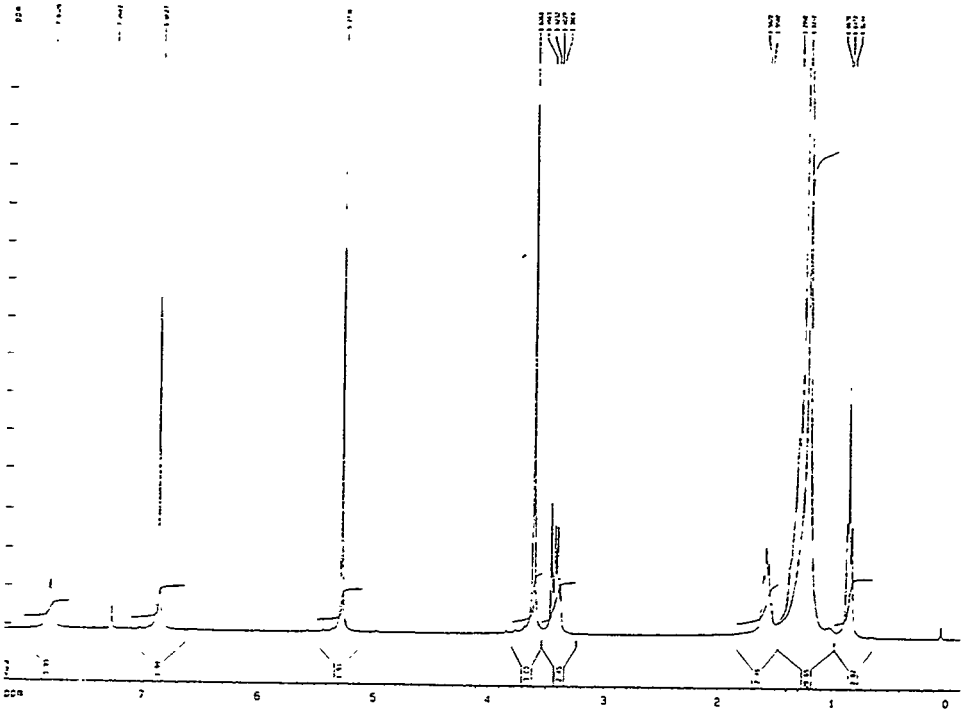

Figure A.39: The ^{1}H NMR of 3,2-HOPO-octadecylamide, deprotected; the conditions used for this NMR and the peak assignments are listed on page 114.

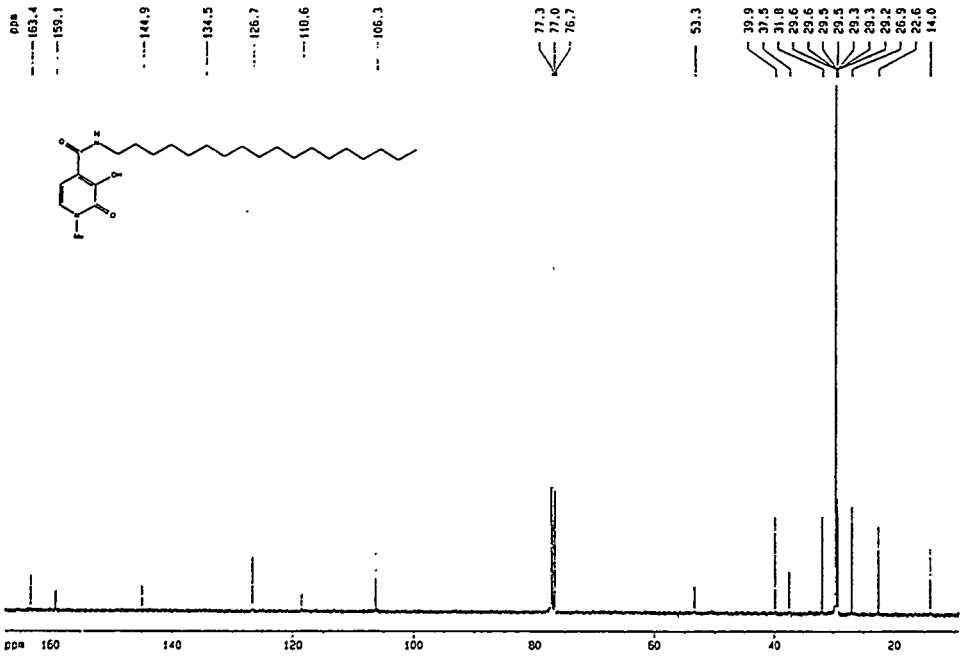

Figure A.40: The ^{13}C NMR of 3,2-HOPO-octadecylamide, deprotected; the conditions used for this NMR and the peak assignments are listed on page 114.

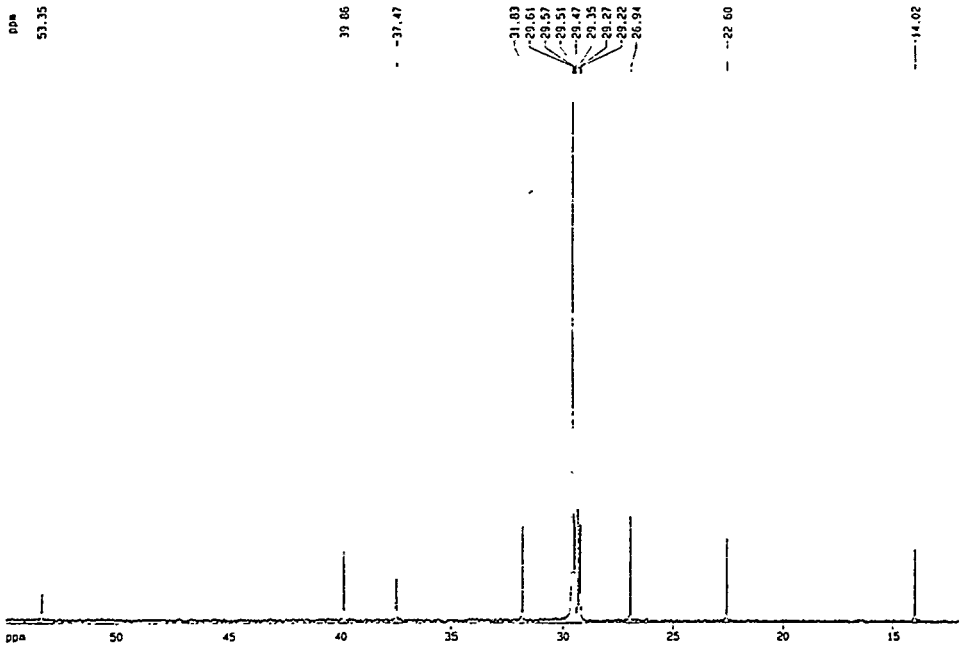

Figure A.41: The ^{13}C NMR of 3,2-HOPO-octadecylamide, deprotected; the conditions used for this NMR and the peak assignments are listed on page 114.

Appendix B

Complete Extraction Data

Table B.1: Pu(IV) extraction data for 1,2-HOPO-hexylamide (Part A).

Org	Aq	Time (min)	% Total Pu(IV)	$\%Ext$	D	$D.F.$
octanol	A	1	98.2	99.4 ± 4.6	179.45 ± 1.95	180.45 ± 1.02
		5	93.3	99.3 ± 4.6	146.79 ± 1.82	147.79 ± 0.96
		10	95.4	99.4 ± 4.6	161.24 ± 1.88	162.24 ± 0.99
		20	94.1	99.0 ± 4.6	102.35 ± 1.73	103.35 ± 0.92
		60	91.2	99.4 ± 4.6	166.38 ± 1.82	167.38 ± 0.96
	B	1	87.8	96.5 ± 4.5	27.77 ± 1.15	28.77 ± 0.62
		5	88.1	97.0 ± 4.5	31.89 ± 1.22	32.89 ± 0.66
		10	87.7	97.0 ± 4.5	32.40 ± 1.22	33.40 ± 0.66
		20	94.9	97.5 ± 4.5	38.62 ± 1.37	39.62 ± 0.74
		60	89.1	98.4 ± 4.6	59.88 ± 1.52	60.88 ± 0.81
MIBK	A	1	103.3	98.6 ± 4.6	72.40 ± 1.73	73.40 ± 0.91
		5	96.4	99.8 ± 4.6	469.02 ± 2.07	470.02 ± 1.08
		10	97.8	99.2 ± 4.6	127.33 ± 1.86	128.33 ± 0.98
		20	95.1	99.5 ± 4.6	188.07 ± 1.91	189.07 ± 1.00
		60	97.3	99.7 ± 4.6	328.72 ± 2.04	329.72 ± 1.07
	B	1	100.8	94.0 ± 4.4	15.76 ± 0.90	16.76 ± 0.50
		5	103.2	99.8 ± 4.6	417.03 ± 2.27	418.03 ± 1.18
		10	103.4	97.5 ± 4.5	39.32 ± 1.45	40.32 ± 0.78
		20	99.2	99.9 ± 4.6	681.16 ± 2.24	682.16 ± 1.17
		60	96.3	99.8 ± 4.6	568.44 ± 2.16	569.44 ± 1.13

Table B.2: Pu(IV) extraction data for 1,2-HOPO-hexylamide (Part B).

Org	**Aq**	**Time (min)**	**% Total Pu(IV)**	*%Ext*	*D*	*D.F.*
kerosene	A	1	56.7	40.6 ± 2.1	0.68 ± 0.07	1.68 ± 0.09
		5	43.0	71.0 ± 3.4	2.45 ± 0.19	3.45 ± 0.15
		10	24.0	83.9 ± 3.9	5.22 ± 0.26	6.22 ± 0.19
		20	21.1	91.7 ± 4.2	11.03 ± 0.32	12.03 ± 0.22
		60	17.1	79.1 ± 3.6	3.79 ± 0.18	4.79 ± 0.15
	B	1	60.0	85.3 ± 4.0	5.82 ± 0.40	6.82 ± 0.25
		5	66.1	91.5 ± 4.3	10.77 ± 0.61	11.77 ± 0.36
		10	89.0	37.3 ± 1.9	0.59 ± 0.06	1.59 ± 0.08
		20	22.8	86.4 ± 4.0	6.37 ± 0.28	7.37 ± 0.20
		60	35.2	61.3 ± 3.0	1.59 ± 0.13	2.59 ± 0.12
dodecane	A	1	46.7	26.4 ± 1.4	0.36 ± 0.04	1.36 ± 0.08
		5	23.6	53.9 ± 2.7	1.17 ± 0.10	2.17 ± 0.11
		10	14.1	31.7 ± 1.7	0.46 ± 0.04	1.46 ± 0.10
		20	18.6	36.2 ± 1.9	0.57 ± 0.05	1.57 ± 0.09
		60	31.2	63.5 ± 3.1	1.74 ± 0.14	2.74 ± 0.13
	B	1	32.0	85.9 ± 4.1	6.09 ± 0.33	7.09 ± 0.22
		5	37.0	80.0 ± 3.8	4.01 ± 0.27	5.01 ± 0.19
		10	21.0	34.2 ± 1.8	0.52 ± 0.05	1.52 ± 0.09
		20	8.9	15.4 ± 0.9	0.18 ± 0.02	1.18 ± 0.12
		60	15.0	78.1 ± 3.5	3.58 ± 0.17	4.58 ± 0.14

Table B.3: Pu(IV) extraction data for 1,2-HOPO-octylamide (Part A).

Org	**Aq**	**Time (min)**	**% Total Pu(IV)**	*%Ext*	*D*	*D.F.*
octanol	A	1	98.9	98.1 ± 4.5	51.97 ± 1.52	52.97 ± 0.81
		5	96.0	98.5 ± 4.6	65.65 ± 1.60	66.65 ± 0.85
		10	95.9	99.2 ± 4.6	130.37 ± 1.83	131.37 ± 0.96
		20	91.5	99.0 ± 4.6	101.49 ± 1.69	102.49 ± 0.89
		60	92.5	98.8 ± 4.6	85.37 ± 1.65	86.37 ± 0.87
	B	1	93.0	93.0 ± 4.3	13.32 ± 0.79	14.32 ± 0.44
		5	89.5	98.2 ± 4.6	53.82 ± 1.48	54.82 ± 0.79
		10	92.2	98.2 ± 4.6	56.08 ± 1.53	57.08 ± 0.81
		20	90.0	98.4 ± 4.6	61.47 ± 1.54	62.47 ± 0.82
		60	93.5	98.9 ± 4.6	87.21 ± 1.73	88.21 ± 0.91
MIBK	A	1	100.4	99.1 ± 4.6	116.57 ± 1.87	117.57 ± 0.98
		5	107.1	89.8 ± 4.2	8.76 ± 0.61	9.76 ± 0.35
		10	97.0	100.1 ± 4.6	inf ± 0.00	inf ± 0.00
		20	97.0	100.1 ± 4.6	inf ± 0.00	inf ± 0.00
		60	95.9	99.9 ± 4.6	1027.10 ± 2.11	1028.10 ± 1.11
	B	1	100.0	98.1 ± 4.5	51.92 ± 1.58	52.92 ± 0.84
		5	101.3	97.5 ± 4.5	38.84 ± 1.43	39.84 ± 0.76
		10	97.8	99.4 ± 4.6	154.11 ± 1.97	155.11 ± 1.04
		20	96.7	100.0 ± 4.6	7595.68 ± 2.26	7596.68 ± 1.18
		60	96.8	100.0 ± 4.6	inf ± 0.00	inf ± 0.00

Table B.4: Pu(IV) extraction data for 1,2-HOPO-octylamide (Part B).

Org	**Aq**	**Time (min)**	**% Total Pu(IV)**	*%Ext*	*D*	*D.F.*
kerosene	A	1	86.3	46.1 ± 2.3	0.86 ± 0.08	1.86 ± 0.09
		5	74.3	79.8 ± 3.8	3.96 ± 0.31	4.96 ± 0.20
		10	87.1	93.7 ± 4.4	14.96 ± 0.82	15.96 ± 0.46
		20	82.1	98.4 ± 4.6	61.55 ± 1.40	62.55 ± 0.75
		60	92.3	98.7 ± 4.6	76.75 ± 1.61	77.75 ± 0.85
	B	1	35.1	77.4 ± 3.7	3.43 ± 0.24	4.43 ± 0.17
		5	55.5	96.1 ± 4.5	24.32 ± 0.83	25.32 ± 0.47
		10	56.1	87.5 ± 4.1	7.03 ± 0.44	8.03 ± 0.27
		20	95.3	99.0 ± 4.6	103.03 ± 1.81	104.03 ± 0.95
		60	91.3	99.8 ± 4.6	603.16 ± 2.06	604.16 ± 1.08
dodecane	A	1	85.5	36.7 ± 1.8	0.58 ± 0.06	1.58 ± 0.08
		5	65.6	73.6 ± 3.5	2.79 ± 0.23	3.79 ± 0.16
		10	46.5	92.1 ± 4.3	11.72 ± 0.54	12.72 ± 0.32
		20	40.8	100.0 ± 4.7	inf ± 0.00	inf ± 0.00
		60	39.6	99.7 ± 4.6	290.48 ± 0.87	291.48 ± 0.49
	B	1	62.2	68.2 ± 3.3	2.14 ± 0.18	3.14 ± 0.14
		5	66.7	71.5 ± 3.4	2.51 ± 0.21	3.51 ± 0.16
		10	68.9	96.8 ± 4.5	29.99 ± 1.03	30.99 ± 0.56
		20	47.3	99.8 ± 4.7	479.40 ± 1.09	480.40 ± 0.60
		60	51.3	99.2 ± 4.6	128.79 ± 1.10	129.79 ± 0.60

Table B.5: Pu(IV) extraction data for 3,2-HOPO-hexylamide.

Org	Aq	Time (min)	% Total Pu(IV)	$\%Ext$	D	$D.F.$
octanol	A	1	99.0	89.8 ± 4.4	8.76 ± 0.85	9.76 ± 0.47
		5	95.2	88.0 ± 4.3	7.31 ± 0.71	8.31 ± 0.41
		10	86.4	85.6 ± 4.2	5.95 ± 0.59	6.95 ± 0.34
		20	93.1	81.8 ± 4.0	4.48 ± 0.44	5.48 ± 0.27
		60	64.5	33.0 ± 1.8	0.49 ± 0.05	1.49 ± 0.08
	B	1	89.6	80.2 ± 3.8	4.06 ± 0.32	5.06 ± 0.21
		5	90.0	79.7 ± 3.7	3.92 ± 0.31	4.92 ± 0.21
		10	90.6	81.8 ± 3.8	4.49 ± 0.35	5.49 ± 0.23
		20	87.9	78.4 ± 3.7	3.64 ± 0.29	4.64 ± 0.20
		60	86.6	68.8 ± 3.3	2.20 ± 0.19	3.20 ± 0.15
MIBK	A	1	100.4	96.4 ± 4.5	26.75 ± 1.18	27.75 ± 0.64
		5	95.7	99.1 ± 4.6	104.36 ± 1.76	105.36 ± 0.93
		10	97.9	99.3 ± 4.6	137.29 ± 1.88	138.29 ± 0.99
		20	94.9	98.2 ± 4.6	53.89 ± 1.50	54.89 ± 0.80
		60	96.3	94.3 ± 4.4	16.62 ± 0.90	17.62 ± 0.50
	B	1	98.3	87.3 ± 4.1	6.89 ± 0.50	7.89 ± 0.30
		5	96.1	99.0 ± 4.6	102.27 ± 1.82	103.27 ± 0.96
		10	99.5	99.2 ± 4.6	120.82 ± 1.93	121.82 ± 1.01
		20	98.0	99.3 ± 4.6	152.82 ± 1.98	153.82 ± 1.04
		60	95.6	98.9 ± 4.6	89.71 ± 1.77	90.71 ± 0.93

Table B.6: Pu(IV) extraction data for 3,2-HOPO-octylamide.

Org	**Aq**	**Time (min)**	**% Total Pu(IV)**	$\%Ext$	D	$D.F.$
octanol	A	1	97.1	97.8 ± 4.5	44.22 ± 1.43	45.22 ± 0.76
		5	93.3	97.4 ± 4.5	36.91 ± 1.30	37.91 ± 0.70
		10	93.5	95.2 ± 4.4	19.78 ± 0.98	20.78 ± 0.54
		20	89.6	91.4 ± 4.3	10.69 ± 0.67	11.69 ± 0.38
		60	93.1	74.7 ± 3.5	2.95 ± 0.25	3.95 ± 0.17
	B	1	88.4	94.4 ± 4.4	16.83 ± 0.89	17.83 ± 0.50
		5	90.9	94.5 ± 4.4	17.10 ± 0.91	18.10 ± 0.50
		10	88.6	92.1 ± 4.3	11.71 ± 0.72	12.71 ± 0.41
		20	92.7	91.2 ± 4.2	10.32 ± 0.67	11.32 ± 0.38
		60	94.7	84.8 ± 4.0	5.57 ± 0.42	6.57 ± 0.26
MIBK	A	1	100.0	98.8 ± 4.6	79.22 ± 1.72	80.22 ± 0.91
		5	98.2	98.2 ± 4.6	53.99 ± 1.54	54.99 ± 0.82
		10	100.0	96.4 ± 4.5	26.82 ± 1.18	27.82 ± 0.64
		20	95.8	83.9 ± 3.9	5.20 ± 0.40	6.20 ± 0.25
		60	99.2	97.1 ± 4.5	33.62 ± 1.30	34.62 ± 0.70
	B	1	99.6	95.6 ± 4.4	21.90 ± 1.09	22.90 ± 0.59
		5	104.0	91.8 ± 4.3	11.22 ± 0.73	12.22 ± 0.41
		10	98.6	96.8 ± 4.5	30.07 ± 1.26	31.07 ± 0.68
		20	77.6	96.5 ± 4.5	27.56 ± 1.07	28.56 ± 0.58
		60	98.4	92.4 ± 4.3	12.14 ± 0.76	13.14 ± 0.43

Table B.7: Pu(IV) extraction data for 3,2-HOPO-decylamide.

Org	Aq	Time (min)	% Total Pu(IV)	$\%Ext$	D	$D.F.$
octanol	A	1	100.0	98.3 ± 4.6	56.64 ± 1.58	57.64 ± 0.84
		5	91.4	96.4 ± 4.5	26.98 ± 1.13	27.98 ± 0.62
		10	93.9	93.6 ± 4.4	14.74 ± 0.83	15.74 ± 0.47
		20	94.9	88.3 ± 4.1	7.51 ± 0.53	8.51 ± 0.31
		60	97.4	57.4 ± 2.8	1.35 ± 0.12	2.35 ± 0.11
	B	1	95.3	68.9 ± 3.3	2.22 ± 0.19	3.22 ± 0.15
		5	90.9	96.2 ± 4.5	25.39 ± 1.12	26.39 ± 0.61
		10	93.4	95.2 ± 4.4	19.71 ± 1.00	20.71 ± 0.55
		20	94.3	92.4 ± 4.3	12.11 ± 0.75	13.11 ± 0.42
		60	92.4	78.2 ± 3.7	3.58 ± 0.29	4.58 ± 0.20
MIBK	A	1	100.5	97.9 ± 4.5	46.00 ± 1.48	47.00 ± 0.79
		5	94.9	97.9 ± 4.5	46.62 ± 1.43	47.62 ± 0.76
		10	95.2	95.8 ± 4.5	22.87 ± 1.07	23.87 ± 0.58
		20	94.4	81.9 ± 3.8	4.52 ± 0.35	5.52 ± 0.23
		60	94.6	97.1 ± 4.5	33.99 ± 1.27	34.99 ± 0.69
	B	1	100.5	98.2 ± 4.5	53.63 ± 1.60	54.63 ± 0.85
		5	102.8	95.9 ± 4.4	23.40 ± 1.14	24.40 ± 0.62
		10	95.8	97.7 ± 4.5	42.43 ± 1.43	43.43 ± 0.76
		20	97.1	93.2 ± 4.3	13.63 ± 0.82	14.63 ± 0.46
		60	95.7	85.7 ± 4.0	5.97 ± 0.45	6.97 ± 0.27

Table B.8: Pu(IV) extraction data for 3,2-HOPO-octadecylamide.

Org	**Aq**	**Time (min)**	**% Total Pu(IV)**	*%Ext*	*D*	*D.F.*
octanol	A	1	104.0	97.7 ± 4.5	42.48 ± 1.47	43.48 ± 0.78
		5	102.9	97.2 ± 4.5	35.19 ± 1.36	36.19 ± 0.73
		10	99.0	94.9 ± 4.4	18.53 ± 0.97	19.53 ± 0.53
		20	94.1	89.9 ± 4.2	8.91 ± 0.60	9.91 ± 0.35
		60	96.9	62.6 ± 3.0	1.67 ± 0.15	2.67 ± 0.12
	B	1	93.6	49.3 ± 2.4	0.97 ± 0.09	1.97 ± 0.10
		5	92.5	95.1 ± 4.4	19.45 ± 0.99	20.45 ± 0.54
		10	89.3	95.6 ± 4.4	21.61 ± 1.03	22.61 ± 0.56
		20	91.0	93.8 ± 4.4	15.19 ± 0.85	16.19 ± 0.47
		60	92.4	80.2 ± 3.8	4.05 ± 0.32	5.05 ± 0.21

Table B.9: Pu(IV) extraction data for 3,2-HOPO-phenylpropylamide.

Org	**Aq**	**Time (min)**	**% Total Pu(IV)**	*%Ext*	*D*	*D.F.*
octanol	A	1	107.1	94.9 ± 4.4	18.63 ± 1.01	19.63 ± 0.55
		5	94.1	91.6 ± 4.3	10.90 ± 0.69	11.90 ± 0.39
		10	94.1	89.2 ± 4.2	8.27 ± 0.57	9.27 ± 0.33
		20	96.8	86.5 ± 4.0	6.40 ± 0.47	7.40 ± 0.28
		60	98.3	44.7 ± 2.2	0.81 ± 0.08	1.81 ± 0.09
	B	1	93.7	88.8 ± 4.1	7.93 ± 0.55	8.93 ± 0.33
		5	94.2	88.9 ± 4.1	7.98 ± 0.56	8.98 ± 0.33
		10	94.1	85.1 ± 4.0	5.70 ± 0.43	6.70 ± 0.26
		20	95.0	80.4 ± 3.8	4.09 ± 0.33	5.09 ± 0.21
		60	92.6	73.0 ± 3.5	2.70 ± 0.23	3.70 ± 0.16
MIBK	A	1	98.9	97.5 ± 4.5	39.67 ± 1.39	40.67 ± 0.74
		5	96.9	99.2 ± 4.6	127.24 ± 1.84	128.24 ± 0.97
		10	96.9	99.3 ± 4.6	139.55 ± 1.87	140.55 ± 0.98
		20	99.0	94.8 ± 4.4	18.24 ± 0.96	19.24 ± 0.53
		60	94.8	95.6 ± 4.4	21.87 ± 1.04	22.87 ± 0.57
	B	1	100.0	91.0 ± 4.2	10.17 ± 0.67	11.17 ± 0.39
		5	100.1	99.4 ± 4.6	177.99 ± 2.05	178.99 ± 1.07
		10	98.1	99.3 ± 4.6	151.19 ± 1.98	152.19 ± 1.04
		20	91.2	100.0 ± 4.6	13758.80 ± 2.14	13759.80 ± 1.12
		60	97.1	99.1 ± 4.6	113.62 ± 1.87	114.62 ± 0.98

Table B.10: Pu(IV) extraction data for 3,4-HOPO-hexylamide.

Org	**Aq**	**Time (min)**	**% Total Pu(IV)**	$\%Ext$	D	$D.F.$
octanol	A	1	102.0	12.2 ± 0.7	0.14 ± 0.02	1.14 ± 0.07
		5	103.1	11.8 ± 0.7	0.13 ± 0.02	1.13 ± 0.07
		10	102.7	12.5 ± 0.7	0.14 ± 0.02	1.14 ± 0.07
		20	103.6	11.6 ± 0.7	0.13 ± 0.01	1.13 ± 0.07
		60	104.5	13.3 ± 0.7	0.15 ± 0.02	1.15 ± 0.07
	B	1	100.6	1.5 ± 0.1	0.02 ± 0.00	1.02 ± 0.09
		5	102.7	1.5 ± 0.1	0.02 ± 0.00	1.02 ± 0.09
		10	101.4	1.5 ± 0.1	0.02 ± 0.00	1.02 ± 0.09
		20	91.4	0.3 ± 0.0	0.00 ± 0.00	1.00 ± 0.14
		60	100.4	1.5 ± 0.1	0.02 ± 0.00	1.02 ± 0.09
MIBK	A	1	99.5	85.0 ± 4.0	5.66 ± 0.43	6.66 ± 0.26
		5	96.9	76.1 ± 3.6	3.18 ± 0.26	4.18 ± 0.18
		10	99.2	83.0 ± 3.9	4.87 ± 0.38	5.87 ± 0.24
		20	97.2	83.2 ± 3.9	4.97 ± 0.38	5.97 ± 0.24
		60	97.2	78.3 ± 3.7	3.61 ± 0.30	4.61 ± 0.20
	B	1	95.8	7.1 ± 0.4	0.08 ± 0.01	1.08 ± 0.07
		5	95.5	5.6 ± 0.4	0.06 ± 0.01	1.06 ± 0.07
		10	95.8	6.5 ± 0.4	0.07 ± 0.01	1.07 ± 0.07
		20	97.8	6.2 ± 0.4	0.07 ± 0.01	1.07 ± 0.07
		60	111.8	17.5 ± 0.9	0.21 ± 0.02	1.21 ± 0.07

Table B.11: Pu(IV) extraction data for 3,4-HOPO-octylamide.

Org	Aq	Time (min)	% Total Pu(IV)	$\%Ext$	D	$D.F.$
octanol	A	1	103.7	12.4 ± 0.7	0.14 ± 0.02	1.14 ± 0.07
		5	102.6	12.7 ± 0.7	0.15 ± 0.02	1.15 ± 0.07
		10	102.4	12.9 ± 0.7	0.15 ± 0.02	1.15 ± 0.07
		20	104.5	12.2 ± 0.7	0.14 ± 0.02	1.14 ± 0.07
		60	102.9	13.4 ± 0.7	0.15 ± 0.02	1.15 ± 0.07
	B	1	102.4	1.7 ± 0.1	0.02 ± 0.00	1.02 ± 0.09
		5	104.0	1.7 ± 0.1	0.02 ± 0.00	1.02 ± 0.09
		10	103.0	1.6 ± 0.1	0.02 ± 0.00	1.02 ± 0.09
		20	102.6	1.7 ± 0.1	0.02 ± 0.00	1.02 ± 0.09
		60	103.3	1.8 ± 0.1	0.02 ± 0.00	1.02 ± 0.09
MIBK	A	1	102.3	82.9 ± 3.9	4.84 ± 0.38	5.84 ± 0.24
		5	97.8	81.8 ± 3.8	4.50 ± 0.36	5.50 ± 0.23
		10	95.7	81.4 ± 3.8	4.37 ± 0.35	5.37 ± 0.22
		20	95.8	81.1 ± 3.8	4.30 ± 0.34	5.30 ± 0.22
		60	97.9	79.1 ± 3.7	3.78 ± 0.31	4.78 ± 0.20
	B	1	96.6	15.8 ± 0.9	0.19 ± 0.02	1.19 ± 0.07
		5	98.4	17.6 ± 1.0	0.21 ± 0.02	1.21 ± 0.07
		10	99.1	17.2 ± 0.9	0.21 ± 0.02	1.21 ± 0.07
		20	94.4	16.2 ± 0.9	0.19 ± 0.02	1.19 ± 0.07
		60	97.7	13.3 ± 0.7	0.15 ± 0.02	1.15 ± 0.07

Table B.12: Pu(IV) extraction data for 3,4-HOPO-decylamide.

Org	Aq	Time (min)	% Total Pu(IV)	$\%Ext$	D	$D.F.$
octanol	A	1	105.8	13.7 ± 0.8	0.16 ± 0.02	1.16 ± 0.07
		5	103.7	14.0 ± 0.8	0.16 ± 0.02	1.16 ± 0.07
		10	103.9	13.5 ± 0.7	0.16 ± 0.02	1.16 ± 0.07
		20	103.6	13.3 ± 0.7	0.15 ± 0.02	1.15 ± 0.07
		60	104.3	13.4 ± 0.7	0.15 ± 0.02	1.15 ± 0.07
	B	1	103.2	2.9 ± 0.2	0.03 ± 0.00	1.03 ± 0.08
		5	102.9	2.7 ± 0.2	0.03 ± 0.00	1.03 ± 0.08
		10	101.2	2.7 ± 0.2	0.03 ± 0.00	1.03 ± 0.08
		20	102.3	2.6 ± 0.2	0.03 ± 0.00	1.03 ± 0.08
		60	103.9	2.5 ± 0.2	0.03 ± 0.00	1.03 ± 0.08
MIBK	A	1	100.1	84.6 ± 4.0	5.51 ± 0.42	6.51 ± 0.26
		5	95.8	83.2 ± 3.9	4.97 ± 0.38	5.97 ± 0.24
		10	96.8	83.3 ± 3.9	4.98 ± 0.39	5.98 ± 0.24
		20	95.8	81.6 ± 3.8	4.43 ± 0.35	5.43 ± 0.22
		60	101.0	80.7 ± 3.8	4.17 ± 0.33	5.17 ± 0.22
	B	1	96.4	26.4 ± 1.4	0.36 ± 0.04	1.36 ± 0.07
		5	97.7	25.7 ± 1.3	0.35 ± 0.04	1.35 ± 0.07
		10	94.5	25.3 ± 1.3	0.34 ± 0.03	1.34 ± 0.07
		20	96.2	25.4 ± 1.3	0.34 ± 0.03	1.34 ± 0.07
		60	97.6	22.7 ± 1.2	0.29 ± 0.03	1.29 ± 0.07

Table B.13: Pu(IV) extraction data for 3,4-HOPO-octadecylamide.

Org	Aq	Time (min)	% Total Pu(IV)	$\%Ext$	D	$D.F.$
octanol	A	1	103.5	11.0 ± 0.6	0.12 ± 0.01	1.12 ± 0.07
		5	103.1	11.7 ± 0.7	0.13 ± 0.01	1.13 ± 0.07
		10	104.9	11.1 ± 0.6	0.12 ± 0.01	1.12 ± 0.07
		20	104.6	11.2 ± 0.6	0.13 ± 0.01	1.13 ± 0.07
		60	104.0	11.9 ± 0.7	0.14 ± 0.02	1.14 ± 0.07
	B	1	103.9	1.2 ± 0.1	0.01 ± 0.00	1.01 ± 0.09
		5	102.0	1.5 ± 0.1	0.02 ± 0.00	1.02 ± 0.09
		10	101.6	1.6 ± 0.1	0.02 ± 0.00	1.02 ± 0.09
		20	102.5	1.4 ± 0.1	0.01 ± 0.00	1.01 ± 0.09
		60	103.9	1.4 ± 0.1	0.01 ± 0.00	1.01 ± 0.09

Table B.14: Pu(IV) extraction data for 3,4-HOPO-phenylpropylamide.

Org	**Aq**	**Time (min)**	**% Total Pu(IV)**	*%Ext*	*D*	*D.F.*
octanol	A	1	105.7	12.7 ± 0.7	0.15 ± 0.02	1.15 ± 0.07
		5	105.3	13.0 ± 0.7	0.15 ± 0.02	1.15 ± 0.07
		10	102.6	13.4 ± 0.7	0.15 ± 0.02	1.15 ± 0.07
		20	103.9	12.9 ± 0.7	0.15 ± 0.02	1.15 ± 0.07
		60	104.7	0.2 ± 0.0	0.00 ± 0.00	1.00 ± 0.18
	B	1	101.3	1.8 ± 0.1	0.02 ± 0.00	1.02 ± 0.09
		5	103.9	1.8 ± 0.1	0.02 ± 0.00	1.02 ± 0.09
		10	102.2	1.8 ± 0.1	0.02 ± 0.00	1.02 ± 0.09
		20	102.8	1.9 ± 0.2	0.02 ± 0.00	1.02 ± 0.08
		60	100.6	1.6 ± 0.1	0.02 ± 0.00	1.02 ± 0.09

Table B.15: Pu(IV) extraction data for 1,2-HOPO-octylamide competition study with ~ 100:1 Fe(III):Pu(IV).

Org	**Aq**	**Time (min)**	**% Total Pu(IV)**	*%Ext*	*D*	*D.F.*
MIBK	A	1	98.7	99.6 ± 4.6	221.52 ± 2.08	222.52 ± 1.09
		5	97.7	100.1 ± 4.6	inf ± 2.34	inf ± 1.22
		10	98.7	99.7 ± 4.6	324.82 ± 2.15	325.82 ± 1.12
		20	99.3	98.1 ± 4.5	52.02 ± 1.57	53.02 ± 0.83
		60	98.7	99.0 ± 4.6	96.67 ± 1.84	97.67 ± 0.97

Table B.16: Pu(IV) extraction data for 1,2-HOPO-octylamide competition study with $\sim$ 1000:1 Fe(III):Pu(IV).

Org	**Aq**	**Time (min)**	**% Total Pu(IV)**	$\%Ext$	D	$D.F.$
MIBK	A	1	92.4	98.3 $\pm$ 4.6	58.92 $\pm$ 1.55	59.92 $\pm$ 0.82
		5	96.5	93.6 $\pm$ 4.4	14.59 $\pm$ 0.85	15.59 $\pm$ 0.47
		10	92.5	97.7 $\pm$ 4.5	42.82 $\pm$ 1.41	43.82 $\pm$ 0.75
		20	93.8	98.0 $\pm$ 4.5	49.12 $\pm$ 1.49	50.12 $\pm$ 0.79
		60	87.9	97.6 $\pm$ 4.5	41.18 $\pm$ 1.34	42.18 $\pm$ 0.72

Table B.17: Pu(IV) extraction data for 1,2-HOPO-octylamide competition study with ~ 3:1 EDTA:HOPO.

Org	**Aq**	**Time (min)**	**% Total Pu(IV)**	*%Ext*	*D*	*D.F.*
MIBK	A	1	95.9	98.6 ± 4.6	71.53 ± 1.68	72.53 ± 0.89
		5	97.5	99.6 ± 4.6	225.53 ± 2.06	226.53 ± 1.08
		10	93.8	99.7 ± 4.6	289.74 ± 2.03	290.74 ± 1.07
		20	96.7	99.8 ± 4.6	489.83 ± 2.16	490.83 ± 1.13
		60	94.1	99.4 ± 4.6	153.19 ± 1.91	154.19 ± 1.00

Table B.18: Pu(IV) extraction data for 1,2-HOPO-octylamide concentration study.

Org	**Aq**	**Ratio [L]/[M]**	**% Total Pu(IV)**	*%Ext*	*D*	*D.F.*
MIBK	A	1	96.3	90.5 ± 4.2	9.57 ± 0.64	10.57 ± 0.37
		3.1	97.0	99.0 ± 4.6	101.83 ± 1.83	102.83 ± 0.96
		6.2	97.4	99.8 ± 4.6	533.71 ± 2.18	534.71 ± 1.14
		15.5	91.7	99.9 ± 4.6	684.48 ± 2.08	685.48 ± 1.09
		31	97.4	99.2 ± 4.6	124.63 ± 1.91	125.63 ± 1.00

Table B.19: Fe(III) extraction data for 1,2-HOPO-hexylamide (Part A).

Org	**Aq**	**Time (min)**	**% Total Pu(IV)**	*%Ext*	*D*	*D.F.*
octanol	A	1	94.1	32.8 ± 3.0	0.49 ± 0.09	1.49 ± 0.14
		5	85.1	90.6 ± 8.3	9.64 ± 1.76	10.64 ± 0.97
		10	84.7	97.5 ± 8.9	39.29 ± 7.18	40.29 ± 3.68
		20	86.1	98.3 ± 9.0	58.18 ± 10.63	59.18 ± 5.41
		60	101.0	98.7 ± 9.0	76.36 ± 13.95	77.36 ± 7.06
	B	1	90.3	32.7 ± 3.1	0.49 ± 0.09	1.49 ± 0.14
		5	83.9	74.4 ± 6.8	2.91 ± 0.53	3.91 ± 0.36
		10	86.7	91.4 ± 8.4	10.61 ± 1.94	11.61 ± 1.06
		20	84.7	98.0 ± 9.0	48.22 ± 8.83	49.22 ± 4.51
		60	85.2	99.3 ± 9.1	135.28 ± 24.76	136.28 ± 12.47
MIBK	A	1	86.2	51.6 ± 4.8	1.06 ± 0.20	2.06 ± 0.19
		5	82.2	93.2 ± 8.5	13.79 ± 2.52	14.79 ± 1.35
		10	80.9	98.8 ± 9.0	82.45 ± 15.08	83.45 ± 7.63
		20	82.1	99.5 ± 9.1	213.34 ± 39.01	214.34 ± 19.60
		60	92.2	99.0 ± 9.0	94.66 ± 17.31	95.66 ± 8.75
	B	1	85.2	74.0 ± 6.8	2.85 ± 0.52	3.85 ± 0.35
		5	85.3	97.2 ± 8.9	34.28 ± 6.28	35.28 ± 3.23
		10	85.6	98.6 ± 9.0	69.63 ± 12.74	70.63 ± 6.46
		20	86.5	97.1 ± 8.9	33.40 ± 6.11	34.40 ± 3.15
		60	84.0	98.5 ± 9.0	63.74 ± 11.67	64.74 ± 5.93

Table B.20: Fe(III) extraction data for 1,2-HOPO-hexylamide (Part B).

Org	Aq	Time (min)	% Total Pu(IV)	$\%Ext$	D	$D.F.$
kerosene	A	1	96.9	71.1 ± 6.5	2.46 ± 0.45	3.46 ± 0.32
		5	92.1	98.8 ± 9.0	81.82 ± 14.96	82.82 ± 7.57
		10	93.2	97.9 ± 9.0	46.73 ± 8.54	47.73 ± 4.36
		20	86.4	99.1 ± 9.1	105.93 ± 19.38	106.93 ± 9.78
		60	98.1	98.7 ± 9.0	73.50 ± 13.43	74.50 ± 6.81
	B	1	71.4	85.7 ± 7.9	5.99 ± 1.10	6.99 ± 0.64
		5	80.1	93.6 ± 8.6	14.62 ± 2.68	15.62 ± 1.43
		10	98.0	96.4 ± 8.8	26.49 ± 4.84	27.49 ± 2.51
		20	86.6	98.4 ± 9.0	60.82 ± 11.13	61.82 ± 5.66
		60	89.9	94.0 ± 8.6	15.62 ± 2.86	16.62 ± 1.52
dodecane	A	1	96.1	70.7 ± 6.5	2.42 ± 0.44	3.42 ± 0.31
		5	95.1	97.7 ± 8.9	42.53 ± 7.77	43.53 ± 3.98
		10	94.0	98.9 ± 9.0	86.20 ± 15.76	87.20 ± 7.97
		20	95.9	98.6 ± 9.0	68.05 ± 12.44	69.05 ± 6.31
		60	98.5	98.5 ± 9.0	64.45 ± 11.77	65.45 ± 5.98
	B	1	65.9	91.4 ± 8.4	10.67 ± 1.96	11.67 ± 1.07
		5	93.3	93.2 ± 8.5	13.72 ± 2.51	14.72 ± 1.35
		10	87.5	96.7 ± 8.8	28.89 ± 5.29	29.89 ± 2.74
		20	80.4	97.9 ± 9.0	47.02 ± 8.61	48.02 ± 4.40
		60	82.7	96.1 ± 8.8	24.34 ± 4.46	25.34 ± 2.32

Table B.21: Fe(III) extraction data for 1,2-HOPO-octylamide.

Org	**Aq**	**Time (min)**	**% Total Pu(IV)**	*%Ext*	*D*	*D.F.*
octanol	A	1	78.7	18.8 ± 1.8	0.23 ± 0.04	1.23 ± 0.12
		5	71.7	80.5 ± 7.5	4.14 ± 0.77	5.14 ± 0.48
		10	69.2	96.5 ± 8.9	27.43 ± 5.09	28.43 ± 2.64
		20	69.9	98.8 ± 9.1	79.78 ± 14.78	80.78 ± 7.48
		60	93.0	98.1 ± 9.0	51.68 ± 9.44	52.68 ± 4.81
	B	1	95.3	5.3 ± 0.6	0.06 ± 0.01	1.06 ± 0.11
		5	94.1	17.4 ± 1.7	0.21 ± 0.04	1.21 ± 0.12
		10	92.4	32.6 ± 3.1	0.48 ± 0.09	1.48 ± 0.14
		20	87.8	57.2 ± 5.4	1.34 ± 0.25	2.34 ± 0.22
		60	83.3	94.5 ± 8.7	17.08 ± 3.13	18.08 ± 1.66
MIBK	A	1	74.2	15.0 ± 1.5	0.18 ± 0.03	1.18 ± 0.12
		5	72.9	38.8 ± 3.7	0.63 ± 0.12	1.63 ± 0.15
		10	72.5	50.8 ± 4.8	1.03 ± 0.19	2.03 ± 0.19
		20	70.5	87.1 ± 8.1	6.73 ± 1.25	7.73 ± 0.72
		60	83.4	99.4 ± 9.1	163.06 ± 29.81	164.06 ± 15.00
	B	1	85.5	15.4 ± 1.5	0.18 ± 0.04	1.18 ± 0.12
		5	87.6	34.9 ± 3.3	0.54 ± 0.10	1.54 ± 0.15
		10	84.2	56.8 ± 5.3	1.31 ± 0.25	2.31 ± 0.22
		20	81.3	79.0 ± 7.4	3.75 ± 0.70	4.75 ± 0.44
		60	87.0	97.5 ± 8.9	39.35 ± 7.20	40.35 ± 3.69

Table B.22: Fe(III) extraction data for 3,2-HOPO-hexylamide.

Org	Aq	Time (min)	% Total Pu(IV)	$\%Ext$	D	$D.F.$
octanol	A	1	100.6	14.9 ± 1.4	0.17 ± 0.03	1.17 ± 0.11
		5	91.5	78.0 ± 7.2	3.55 ± 0.65	4.55 ± 0.42
		10	89.3	93.1 ± 8.5	13.42 ± 2.46	14.42 ± 1.32
		20	88.9	97.7 ± 9.0	42.30 ± 7.75	43.30 ± 3.97
		60	98.5	98.3 ± 9.0	58.47 ± 10.72	59.47 ± 5.45
	B	1	99.1	3.7 ± 0.4	0.04 ± 0.01	1.04 ± 0.11
		5	96.8	14.2 ± 1.4	0.17 ± 0.03	1.17 ± 0.11
		10	94.5	24.6 ± 2.3	0.33 ± 0.06	1.33 ± 0.12
		20	92.4	43.9 ± 4.1	0.78 ± 0.15	1.78 ± 0.17
MIBK	A	1	96.0	16.5 ± 1.6	0.20 ± 0.04	1.20 ± 0.11
		5	92.8	55.2 ± 5.1	1.23 ± 0.23	2.23 ± 0.21
		10	94.4	83.4 ± 7.7	5.03 ± 0.92	6.03 ± 0.55
		20	92.9	87.9 ± 8.1	7.25 ± 1.33	8.25 ± 0.76
		60	98.9	99.0 ± 9.1	103.35 ± 18.91	104.35 ± 9.55
	B	1	91.5	17.9 ± 1.7	0.22 ± 0.04	1.22 ± 0.12
		5	93.0	50.6 ± 4.7	1.02 ± 0.19	2.02 ± 0.19
		10	92.3	69.3 ± 6.4	2.26 ± 0.42	3.26 ± 0.30
		20	91.8	88.7 ± 8.1	7.88 ± 1.45	8.88 ± 0.81
		60	92.6	97.6 ± 8.9	40.97 ± 7.50	41.97 ± 3.84

Table B.23: Fe(III) extraction data for 3,2-HOPO-octylamide.

Org	Aq	Time (min)	% Total Pu(IV)	$\%Ext$	D	$D.F.$
octanol	A	1	101.4	11.1 ± 1.1	0.13 ± 0.02	1.13 ± 0.11
		5	94.2	64.6 ± 6.0	1.83 ± 0.34	2.83 ± 0.26
		10	88.9	88.5 ± 8.1	7.72 ± 1.42	8.72 ± 0.80
		20	89.7	97.6 ± 8.9	40.18 ± 7.37	41.18 ± 3.77
		60	99.2	97.7 ± 9.0	43.01 ± 7.89	44.01 ± 4.04
	B	1	101.5	0.4 ± 0.0	0.00 ± 0.00	1.00 ± 0.13
		5	101.8	1.4 ± 0.1	0.01 ± 0.00	1.01 ± 0.11
		10	99.1	2.8 ± 0.3	0.03 ± 0.01	1.03 ± 0.11
		20	99.5	5.3 ± 0.5	0.06 ± 0.01	1.06 ± 0.11
MIBK	A	1	97.2	5.2 ± 0.5	0.05 ± 0.01	1.05 ± 0.11
		2	97.2	8.9 ± 0.9	0.10 ± 0.02	1.10 ± 0.11
		5	96.1	33.6 ± 3.1	0.51 ± 0.09	1.51 ± 0.14
		10	94.4	45.5 ± 4.2	0.83 ± 0.15	1.83 ± 0.17
		20	92.1	27.9 ± 2.6	0.39 ± 0.07	1.39 ± 0.13
		60	93.8	62.6 ± 5.8	1.68 ± 0.31	2.68 ± 0.25
	B	1	90.1	1.1 ± 0.1	0.01 ± 0.00	1.01 ± 0.11
		2	90.2	1.9 ± 0.2	0.02 ± 0.00	1.02 ± 0.11
		5	91.9	7.3 ± 0.7	0.08 ± 0.02	1.08 ± 0.11
		10	97.4	10.2 ± 1.0	0.11 ± 0.02	1.11 ± 0.11

Table B.24: Fe(III) extraction data for 3,2-HOPO-decylamide.

Org	Aq	Time (min)	% Total Pu(IV)	*%Ext*	*D*	*D.F.*
octanol	A	1	101.0	12.3 ± 1.2	0.14 ± 0.03	1.14 ± 0.11
		5	93.8	52.5 ± 4.9	1.10 ± 0.20	2.10 ± 0.19
		10	91.5	82.0 ± 7.5	4.56 ± 0.84	5.56 ± 0.51
		20	89.9	97.5 ± 8.9	39.60 ± 7.26	40.60 ± 3.72
		60	96.4	97.9 ± 9.0	46.50 ± 8.51	47.50 ± 4.35
	B	1	101.7	0.1 ± 0.0	0.00 ± 0.00	1.00 ± 0.15
		5	100.4	0.5 ± 0.1	0.01 ± 0.00	1.01 ± 0.12
		10	99.5	0.8 ± 0.1	0.01 ± 0.00	1.01 ± 0.12
		20	100.7	1.5 ± 0.2	0.02 ± 0.00	1.02 ± 0.11
MIBK	A	1	92.4	5.1 ± 0.5	0.05 ± 0.01	1.05 ± 0.11
		5	96.3	18.5 ± 1.8	0.23 ± 0.04	1.23 ± 0.12
		10	96.2	40.7 ± 3.8	0.69 ± 0.13	1.69 ± 0.16
		20	96.4	54.8 ± 5.1	1.21 ± 0.22	2.21 ± 0.20
		60	89.9	81.9 ± 7.5	4.52 ± 0.83	5.52 ± 0.51
	B	1	90.3	0.2 ± 0.0	0.00 ± 0.00	1.00 ± 0.15
		5	91.9	0.5 ± 0.1	0.01 ± 0.00	1.01 ± 0.12
		10	95.0	1.0 ± 0.1	0.01 ± 0.00	1.01 ± 0.11
		20	86.7	2.2 ± 0.2	0.02 ± 0.00	1.02 ± 0.11
		60	92.8	5.8 ± 0.6	0.06 ± 0.01	1.06 ± 0.11

Table B.25: Fe(III) extraction data for 3,2-HOPO-octadecylamide.

Org	**Aq**	**Time (min)**	**% Total Pu(IV)**	*%Ext*	*D*	*D.F.*
octanol	A	1	99.7	28.5 ± 2.7	0.40 ± 0.07	1.40 ± 0.13
		5	93.6	67.9 ± 6.3	2.11 ± 0.39	3.11 ± 0.29
		10	90.4	87.7 ± 8.0	7.11 ± 1.31	8.11 ± 0.74
		20	94.0	88.4 ± 8.1	7.65 ± 1.40	8.65 ± 0.79
		60	98.0	97.7 ± 8.9	43.00 ± 7.87	44.00 ± 4.03
	B	1	102.1	0.2 ± 0.0	0.00 ± 0.00	1.00 ± 0.14
		5	100.4	0.4 ± 0.0	0.00 ± 0.00	1.00 ± 0.13
		10	102.6	0.6 ± 0.1	0.01 ± 0.00	1.01 ± 0.12
		20	101.1	1.1 ± 0.1	0.01 ± 0.00	1.01 ± 0.11

Table B.26: Fe(III) extraction data for 3,2-HOPO-phenylpropylamide.

Org	Aq	Time (min)	% Total Pu(IV)	$\%Ext$	D	$D.F.$
octanol	A	1	100.5	16.2 ± 1.5	0.19 ± 0.04	1.19 ± 0.11
		5	95.4	49.9 ± 4.6	0.99 ± 0.18	1.99 ± 0.19
		10	93.4	75.5 ± 7.0	3.08 ± 0.57	4.08 ± 0.38
		20	92.6	93.5 ± 8.6	14.32 ± 2.63	15.32 ± 1.41
		60	101.0	98.2 ± 9.0	55.52 ± 10.18	56.52 ± 5.18
	B	1	100.8	6.9 ± 0.7	0.07 ± 0.01	1.07 ± 0.11
		5	98.9	22.8 ± 2.1	0.30 ± 0.06	1.30 ± 0.12
		10	96.2	41.6 ± 3.9	0.71 ± 0.13	1.71 ± 0.16
		20	94.4	62.4 ± 5.8	1.66 ± 0.31	2.66 ± 0.25
MIBK	A	1	96.6	11.5 ± 1.1	0.13 ± 0.03	1.13 ± 0.11
		5	95.3	33.4 ± 3.1	0.50 ± 0.09	1.50 ± 0.14
		10	94.8	58.1 ± 5.4	1.39 ± 0.26	2.39 ± 0.22
		20	92.0	82.2 ± 7.5	4.61 ± 0.85	5.61 ± 0.51
		60	92.1	98.6 ± 9.0	68.42 ± 12.54	69.42 ± 6.36
		120	92.3	98.4 ± 9.0	61.63 ± 11.29	62.63 ± 5.74
	B	1	90.9	11.2 ± 1.1	0.13 ± 0.02	1.13 ± 0.11
		5	91.1	32.7 ± 3.1	0.49 ± 0.09	1.49 ± 0.14
		10	90.9	56.8 ± 5.2	1.32 ± 0.24	2.32 ± 0.21
		20	93.6	80.6 ± 7.4	4.16 ± 0.76	5.16 ± 0.47
		60	102.1	97.5 ± 8.9	39.46 ± 7.21	40.46 ± 3.70
		120	95.7	94.5 ± 8.7	17.31 ± 3.17	18.31 ± 1.68

Table B.27: Fe(III) extraction data for 3,4-HOPO-hexylamide.

Org	Aq	Time (min)	% Total Pu(IV)	$\%Ext$	D	$D.F.$
octanol	A	1	101.9	11.3 ± 1.1	0.13 ± 0.02	1.13 ± 0.11
		5	98.5	25.5 ± 2.4	0.34 ± 0.06	1.34 ± 0.13
		10	97.7	28.2 ± 2.6	0.39 ± 0.07	1.39 ± 0.13
		20	98.5	28.3 ± 2.7	0.39 ± 0.07	1.39 ± 0.13
	B	1	101.0	2.2 ± 0.2	0.02 ± 0.00	1.02 ± 0.11
		5	99.1	6.2 ± 0.6	0.07 ± 0.01	1.07 ± 0.11
		10	99.3	7.9 ± 0.8	0.09 ± 0.02	1.09 ± 0.11
		20	99.2	8.3 ± 0.8	0.09 ± 0.02	1.09 ± 0.11
MIBK	A	1	99.3	1.7 ± 0.2	0.02 ± 0.00	1.02 ± 0.11
		5	97.1	2.6 ± 0.3	0.03 ± 0.01	1.03 ± 0.11
		10	97.9	2.6 ± 0.3	0.03 ± 0.01	1.03 ± 0.11
		20	96.2	2.6 ± 0.3	0.03 ± 0.01	1.03 ± 0.11
	B	1	92.2	0.2 ± 0.0	0.00 ± 0.00	1.00 ± 0.15
		5	89.8	0.3 ± 0.0	0.00 ± 0.00	1.00 ± 0.14
		10	91.5	0.2 ± 0.0	0.00 ± 0.00	1.00 ± 0.15
		20	94.2	0.2 ± 0.0	0.00 ± 0.00	1.00 ± 0.15

Table B.28: Fe(III) extraction data for 3,4-HOPO-octylamide.

Org	**Aq**	**Time (min)**	**% Total Pu(IV)**	$\%Ext$	D	$D.F.$
octanol	A	1	102.5	5.3 ± 0.5	0.06 ± 0.01	1.06 ± 0.11
		5	99.7	21.4 ± 2.0	0.27 ± 0.05	1.27 ± 0.12
		10	98.7	24.6 ± 2.3	0.33 ± 0.06	1.33 ± 0.12
		20	100.1	25.2 ± 2.4	0.34 ± 0.06	1.34 ± 0.13
	B	1	97.7	1.0 ± 0.1	0.01 ± 0.00	1.01 ± 0.11
		5	98.2	3.9 ± 0.4	0.04 ± 0.01	1.04 ± 0.11
		10	100.0	7.2 ± 0.7	0.08 ± 0.02	1.08 ± 0.11
		20	99.0	11.9 ± 1.1	0.13 ± 0.03	1.13 ± 0.11
MIBK	B	1	89.9	1.8 ± 0.2	0.02 ± 0.00	1.02 ± 0.11
		2	92.9	2.0 ± 0.2	0.02 ± 0.00	1.02 ± 0.11
		5	86.9	4.2 ± 0.4	0.04 ± 0.01	1.04 ± 0.11
		10	89.9	5.5 ± 0.5	0.06 ± 0.01	1.06 ± 0.11
		20	88.3	6.4 ± 0.6	0.07 ± 0.01	1.07 ± 0.11

Table B.29: Fe(III) extraction data for 3,4-HOPO-decylamide.

Org	Aq	Time (min)	% Total Pu(IV)	$\%Ext$	D	$D.F.$
octanol	A	1	101.6	10.7 ± 1.0	0.12 ± 0.02	1.12 ± 0.11
		5	101.8	23.5 ± 2.2	0.31 ± 0.06	1.31 ± 0.12
		10	97.2	27.4 ± 2.6	0.38 ± 0.07	1.38 ± 0.13
		20	98.5	26.0 ± 2.4	0.35 ± 0.07	1.35 ± 0.13
		60	101.7	25.5 ± 2.4	0.34 ± 0.06	1.34 ± 0.13
	B	1	100.6	0.3 ± 0.0	0.00 ± 0.00	1.00 ± 0.13
		5	100.8	1.4 ± 0.2	0.01 ± 0.00	1.01 ± 0.11
		10	99.2	2.4 ± 0.3	0.02 ± 0.01	1.02 ± 0.11
		20	98.9	4.1 ± 0.4	0.04 ± 0.01	1.04 ± 0.11
MIBK	A	1	97.6	1.6 ± 0.2	0.02 ± 0.00	1.02 ± 0.11
		5	98.4	4.3 ± 0.4	0.05 ± 0.01	1.05 ± 0.11
		10	96.6	5.6 ± 0.6	0.06 ± 0.01	1.06 ± 0.11
		20	98.8	5.7 ± 0.6	0.06 ± 0.01	1.06 ± 0.11
		60	97.6	5.6 ± 0.6	0.06 ± 0.01	1.06 ± 0.11
	B	1	93.2	1.9 ± 0.2	0.02 ± 0.00	1.02 ± 0.11
		5	93.2	6.6 ± 0.7	0.07 ± 0.01	1.07 ± 0.11
		10	93.7	12.3 ± 1.2	0.14 ± 0.03	1.14 ± 0.11
		20	91.9	19.6 ± 1.9	0.24 ± 0.05	1.24 ± 0.12
		60	91.8	28.0 ± 2.6	0.39 ± 0.07	1.39 ± 0.13

Table B.30: Fe(III) extraction data for 3,4-HOPO-octadecylamide.

Org	**Aq**	**Time (min)**	**% Total Pu(IV)**	*%Ext*	*D*	*D.F.*
octanol	A	1	100.8	9.6 ± 0.9	0.11 ± 0.02	1.11 ± 0.11
		5	99.5	18.6 ± 1.8	0.23 ± 0.04	1.23 ± 0.12
		10	100.0	20.4 ± 1.9	0.26 ± 0.05	1.26 ± 0.12
		20	99.6	21.0 ± 2.0	0.27 ± 0.05	1.27 ± 0.12
	B	1	100.8	0.1 ± 0.0	0.00 ± 0.00	1.00 ± 0.15
		5	99.9	0.5 ± 0.1	0.00 ± 0.00	1.00 ± 0.13
		10	99.4	1.7 ± 0.2	0.02 ± 0.00	1.02 ± 0.11
		20	100.3	3.0 ± 0.3	0.03 ± 0.01	1.03 ± 0.11

Table B.31: Fe(III) extraction data for 3,4-HOPO-phenylpropylamide.

Org	Aq	Time (min)	% Total Pu(IV)	$\%Ext$	D	$D.F.$
octanol	A	1	102.2	14.0 ± 1.3	0.16 ± 0.03	1.16 ± 0.11
		5	97.7	35.5 ± 3.3	0.55 ± 0.10	1.55 ± 0.15
		10	98.5	41.3 ± 3.9	0.70 ± 0.13	1.70 ± 0.16
		20	99.1	42.4 ± 3.9	0.74 ± 0.14	1.74 ± 0.16
	B	1	102.0	5.4 ± 0.5	0.06 ± 0.01	1.06 ± 0.11
		5	102.3	9.9 ± 1.0	0.11 ± 0.02	1.11 ± 0.11
		10	101.0	10.7 ± 1.0	0.12 ± 0.02	1.12 ± 0.11
		20	101.0	10.9 ± 1.0	0.12 ± 0.02	1.12 ± 0.11

Bibliography

[1] H. Becquerel. *Compt. Rend.*, 122:501, 1896.

[2] G. Friedlander, J.W. Kennedy, E.S. Macias, et al. *Nuclear and Radiochemistry.* John Wiley and Sons, New York, 1981.

[3] A.M. Poskanzer, G.W. Butler, and E.K. Hyde. *Phys. Rev. C*, 3:882, 1971.

[4] L.G. Moretto. *Nucl. Phys.*, A247:211, 1975.

[5] R. Vandenbosch and J. Huizenga. *Nuclear Fission.* Academic Press, New York, 1973.

[6] U.L. Businaro and S. Gallone. *Nuovo Cim.*, 1:629, 1955.

[7] U.L. Businaro and S. Gallone. *Nuovo Cim.*, 1:1277, 1955.

[8] K.T. Davies and A.J. Sierk. *Phys. Rev. C*, 31:915, 1985.

[9] D.S. Burnett, R.C. Gatti, F. Plasil, et al. *Phys. Rev.*, 134:952, 1964.

[10] G.M. Raispeck and J.W. Cobble. *Phys. Rev.*, 153:1270, 1967.

[11] L.G. Moretto, S.G. Thompson, J. Routti, et al. *Phys. Lett.*, B38:471, 1972.

[12] W.D. Myers. *Droplet Model of Atomic Nuclei.* Plenum, New York, 1977.

[13] B.B. Back, O. Hansen, H.C. Britt, et al. *Physics and Chemistry of Fission, vol. 1.* IAEA, Vienna, 1974.

[14] S. Cohen, F. Plasil, and W.J. Swiatecki. *Ann. of Phys.*, 82:557, 1974.

[15] M. Beckerman and M. Blann. *Phys. Rev.*, C17:1615, 1985.

[16] F. Plasil, R.L. Ferguson, R.L. Hann, et al. *Phys. Rev. Lett.*, 45:1615, 1980.

[17] M. Blann and T. Komoto. *Phys. Rev.*, C26:472, 1982.

[18] D.J. Hinde, J.O. Newton, J.R. Leigh, et al. *Nucl. Phys.*, A398:308, 1983.

[19] R.J. Charity, J.R. Leigh, J.J.M. Bokhorst, et al. *Nucl. Phys.*, A457:441, 1986.

[20] A.J. Sierk. *Phys. Rev.*, C33:2039, 1986.

[21] A.J. Sierk. *Phys. Rev. Lett.*, 55:582, 1985.

[22] J. van der Plicht, H.C. Britt, M.M. Fowler, et al. *Phys. Rev.*, C28:2022, 1983.

[23] F. Plasil, T.C. Awes, B. Cheynis, et al. *Phys. Rev.*, C29:1145, 1984.

[24] D.N. Delis, Y. Blumenfeld, D.R. Bowman, et al. *Nucl. Phys.*, A534:403, 1991.

[25] D.N. Delis, Y. Blumenfeld, D.R. Bowman, et al. *Z. Phys.*, A339:279, 1991.

[26] M.A. McMahan, L.G. Moretto, M.L.Padgett, et al. *Phys. Rev. Lett.*, 54:1995, 1985.

[27] G. Royer and F. Haddad. *Phys. Rev.*, C51:2813, 1995.

[28] G.V.R. Prasad, V.S. Ramamurthy, and R.T. Radav. *Phys. Rev.*, C51:2833, 1995.

[29] J. Boger and J.M. Alexander. *Phys. Rev.*, C50:1006, 1994.

[30] W.D. Myers and W.J. Swiatecki. Technical Report LBL-36557, Lawrence Berkeley Laboratory, 1994.

[31] K.X. Jing, L.G. Moretto, A.C. Veeck, et al. Submitted for publication in *Physical Review C.*

[32] N. Bohr and J.A. Wheeler. *Phys. Rev.*, 56:426, 1939.

[33] Z.Q. Xie, C.M. Lyneis, R.S. Lam, et al. *Rev. Sci. Instrum.*, 62:775, 1991.

[34] D.J. Clark and G.J. Wozniak. *Nucl. Instr. Meth.*, A295:34, 1990.

[35] J.T. Walton, H.A. Sommer, G.J. Wozniak, et al. *IEEE Trans. Nucl. Sci.*, 37:1578, 1990.

[36] M.A. McMahan, G.J. Wozniak, C.M. Lyneis, et al. *Nucl. Instr. Meth.*, A253:1, 1986.

[37] J.B. Moulton, J.E. Stephenson, R.P. Schmitt, et al. *Nucl. Instr. Meth.*, 157:325, 1978.

[38] M.A. McMahan, R.F. Lebed, and B. Feinberg. The 1989 ieee particle accelerator conference. Chicago, IL, March 1989.

[39] R.J. Charity, M.A. McMahan, G.J. Wozniak, et al. *Nucl. Phys.*, A483:371, 1988.

[40] A.C. Veeck, K.X. Jing, Q. Sui, et al. *Nucl. Instr. Meth.*, B108:159, 1996.

[41] W.K. Chu, J.W. Mayer, and M.A. Nicolet. *Backscattering Spectrometry.* Academic Press, New York, 1978.

[42] J. Stoner. Arizona Carbon Foil Inc., private communication.

[43] D. Balzer and G. Bonani. *Nucl. Instr. Meth.*, 167:129, 1979.

[44] Y. Haruyama H. Ogawa, I. Katayama, et al. *Nucl. Instr. Meth.*, B48:130, 1990.

[45] L.K. Fifield and N.A. Orr. *Nucl. Instr. Meth.*, A288:360, 1990.

[46] D.L. Weathers, J.L. Duggan, R.B. Escue, et al. *Nucl. Instr. Meth.*, A303:69, 1991.

[47] R. Pulley. Specialty Minerals Inc., private communication.

[48] R.J. Charity, D.R. Bowman, Z.H. Liu, et al. *Nucl. Phys.*, A476:516, 1988.

[49] R.J. Charity, M.A. McMahan, D.R. Bowman, et al. *Phys. Rev. Lett.*, 56:1354, 1986.

[50] H.Y. Han, K.X. Jing, E. Plagnol, et al. *Nucl. Phys.*, A492:138, 1989.

[51] R.J. Charity, K.X. Jing, D.R. Bowman, et al. *Nucl. Phys.*, A511:59, 1990.

[52] V.E. Viola, K. Kwiatkowski, and M. Walker. *Phys. Rev.*, C31:1550, 1985.

[53] G.J. Mathews, J.B. Moulton, G.J. Wozniak, et al. *Phys. Rev.*, C25:300, 1982.

[54] L.G. Moretto, S.K. Kataria, R.C. Jared, et al. *Nucl. Phys.*, A255:491, 1975.

[55] R. Babinet, L.G. Moretto, J. Galin, et al. *Nucl. Phys.*, A258:172, 1976.

[56] R. Schmitt, G. Bizard, G.J. Wozniak, et al. *Phys. Rev. Lett.*, 46:522, 1981.

[57] L.G. Moretto. Fission probabilities in lighter nuclei: A theoretical and experimental investigation of the shell and pairing effects in fissioning nuclei. In *Physics and Chemistry of Fission 1973*, volume I, page 329, Vienna, 1974. IAEA.

[58] L.G. Moretto and G.J. Wozniak. *Prog. Part. Nucl. Phys.*, 21:401, 1988.

[59] V.F. Weisskopf and P.H. Ewing. *Phys. Rev.*, 57:472, 1940.

[60] W.E. Parker, M. Kaplan, D.J. Moses, et al. *Phys. Rev.*, C44:774, 1991.

[61] A.J. Sierk. Private communication.

[62] R.Bass. *Nucl. Phys.*, A231:45, 1974.

[63] R.Bass. *Phys. Rev. Lett.*, 39:265, 1977.

[64] B. Haas, G. Duchene, F.A. Beck, et al. *Phys. Rev. Lett.*, 54:398, 1985.

[65] D. Cha and G.F. Bertsch. *Phys. Rev.*, C46:306, 1992.

[66] J.P. Lestone. *Phys. Rev. Lett.*, 70:2245, 1993.

[67] L.G. Moretto, K.X. Jing, and G.J. Wozniak. *Phys. Rev. Lett.*, 74:3557, 1995.

[68] *St Louis Post-Dispatch*, Oct 1903.

[69] *Washington Post*, Dec 1993.

[70] *New York Times*, Jun 1993.

[71] *New York Times*, Dec 1992.

[72] *New York Times*, Jan 1992.

[73] *Washington Post*, Dec 1991.

[74] *New York Times*, Aug 1990.

[75] *Los Angeles Times*, Aug 1994.

[76] W.G. Sutcliffe, R.H. Condit, W.G. Mansfield, et al. A perspective on the dangers of plutonium. Technical Report UCRL-ID-118825, Center for Security and Technology Studies, LLNL, 1995.

[77] B. Hileman. *Chemical and Engineering News*, 72(24):12, 1994.

[78] *New York Times*, Nov 1994.

[79] *Nuclear Wastes: Technologies for Separations and Transmutations.* National Academy Press, Washington DC, 1996.

[80] D.L. Illman. *Chemical and Engineering News*, 71(25):9, 1993.

[81] G.K. Allen. Estimated inventory of chemicals added to underground waste tanks, 1944-1975. Technical Report ARH-CD-6108, Research and Engineering Division, Hanford, WA, 1976.

[82] F.W. Walker, J.R. Parrington, and F. Feiner, editors. *Nuclides and Isotopes.* GE Nuclear Energy, San Jose, fourteenth edition, 1989.

[83] E.M. McMillan and P.H. Abelson. *Phys. Rev.*, 57:1185, 1940.

[84] G.T. Seaborg, E.M. McMillan, J.W. Kennedy, et al. *Phys. Rev.*, 69:366, 1946.

[85] G.T. Seaborg, A.C. Wahl, and J.W. Kennedy. *Phys. Rev.*, 69:367, 1946.

[86] G.T. Seaborg. *Nuclear Milestones.* W.H. Freeman and Sons, San Francisco, 1972.

[87] J.J. Katz, G.T. Seaborg, and L.R. Morss. *Chemistry of the Actinide Elements.* Chapman and Hall, New York, second edition, 1986.

[88] E. Segre. *Enrico Fermi: Physicist.* University of Chicago, Chicago, 1970.

[89] L.R. Groves. *Now It Can Be Told.* Harper & Brothers, New York, 1962.

[90] *Historical Perspectives: Dawn of the Nuclear Age*, La Grange Park, IL, 1982. American Nuclear Society.

[91] R.L. Bates and J.A. Jackson. *Glossary of Geology.* American Geological Institute, Falls Church, VA, 1980.

[92] Bechtel National Inc. Results of Fall 1994 Sampling of Gunite and Associated Tanks at the Oak Ridge National Laboratory. Technical Report ORNL/ER/Sub/87-99053/74, Environmental Restoration Program, Oak Ridge, TN, 1995.

[93] K.N. Raymond, W.L. Smith, F.L. Weitl, et al. Specific sequestering agents for the actinides. In *Lanthanide and Actinide Chemistry and Spectroscopy*, number 131 in ACS Symposium Series. American Chemical Society, Washington DC, 1980.

[94] J.R. Telford. *Synthesis, Structural, and Thermodynamic Characterization of Bis-catecholate Siderophores and a Novel Enterobactin Analog.* PhD thesis, University of California, Berkeley, 1995.

[95] K.N. Raymond. Private communication.

[96] G.N. Stradling, S.A. Gray, J.C. Moody, et al. *International Journal of Radiation Biology*, 64:133, 1993.

[97] J.L. Poncy, G. Rateau, R. Burgada, et al. *International Journal of Radiation Biology*, 64:431, 1993.

[98] V. Volf, R. Burgada, K.N. Raymond, et al. *International Journal of Radiation Biology*, 63:785, 1993.

[99] P.W. Durbin, B. Kullgren, J. Xu, et al. *Radiation Protection Dosimetry*, 53:305, 1994.

[100] J. Xu, B. Kullgren, P.W. Durbin, et al. *J. Med. Chem.*, 38:2606, 1995.

[101] G.H. Morrison and H. Freiser. *Solvent Extraction in Analytical Chemistry*. John Wiley and Sons, New York, 1957.

[102] Y. Marcus and A.S. Kertes. *Ion Exchange and Solvent Extraction of Metal Complexes*. Wiley Interscience, London, 1969.

[103] D.W. Whisenhunt, M.P. Neu, Z. Hou, et al. *Inorg. Chem.*, 35:4128, 1996.

[104] D.J. White. Progress report for Ken Raymond, University of California, Berkeley, 1996.

[105] D.W. Whisenhunt. *Synthesis and Evaluation of Chelating Agents and Resins Specific for the Actinides*. PhD thesis, University of California, Berkeley, 1994.

[106] G.J. Lumetta, M.J. Wagner, and C.D. Carlson. *Solvent Extraction and Ion Exchange*, 14:35, 1996.

[107] E.P. Horowitz, H. Diamond, R.C. Gatrone, et al. In *Proceedings of the International Solvent Extraction Conference*, New York, 1990. Elsevier.

[108] C. Musikas and H. Hubert. In *Proceedings of the International Solvent Extraction Conference*, New York, 1983. Elsevier.

[109] C. Musikas and W.W. Schulz. Solvent extraction in nuclear science and technology. In J. Rydberg, C. Musikas, and G.R. Choppin, editors, *Principles and Practices of Solvent Extration*, chapter 11. Dekker Inc, New York, 1992.

[110] L. Nunez, B.A. Buchholz, M. Kaminski, et al. *Sep. Sci. Tech.*, 31:1393, 1996.

[111] Y. Wada and K. Morimoto. *Rad. Acta*, 72:195, 1996.

[112] J.P. Shukla, J.V. Sonawane, A. Kumar, et al. *Rad. Acta*, 72:189, 1996.

[113] *Bus. Week*, page 54, Feb 1996.

[114] *New York Times*, Jul 1996.

[115] B. Hileman. *Chemical and Engineering News*, 74(32):14, 1996.

[116] L.C. Uhlir. *Mixed Functionality Actinide Sequestering Agents.* PhD thesis, University of California, Berkeley, 1992.

[117] J. Xu. From catechol chemistry to HOPO chemistry. Progress report for Ken Raymond, University of California, Berkeley, 1992.

[118] D.L. White, P.W. Durbin, N. Jeung, et al. *J. Med. Chem.*, 31:11, 1988.

[119] D.J. Leggett, editor. *Computational Methods for the Determination of Formation Constants.* Plenum Press, New York, 1985.

[120] F.L. Welcher, editor. *The Analytical Uses of Ethylenediamine Tetraacetic Acid.* D. Van Nostrand Co, Inc, Princeton, NJ, 1985.

[121] M.P. Neu. *Coordination Chemistry of Two Heavy Metals: I. Ligand Preferences in Lead(II) Complexation, Toward the Development of Therapeutic Agents for Lead Poisoning. II. Plutonium Solubility and Speciation Relevant to the Environment.* PhD thesis, University of California, Berkeley, 1993.

[122] R.H. Rainey. Technical Report CF-59-12-95, Oak Ridge National Laboratory, 1959.